UNCLASSIFIED

REPORT DOCUMENTATION PAGE

1a. REPORT SECURITY CLASSIFICATION	1b. RESTRICTIVE MARKINGS
2a. SECURITY CLASSIFICATION AUTHORITY	3. DISTRIBUTION/AVAILABILITY OF REPORT Approved for public release; distribution unlimited.
2b. DECLASSIFICATION/DOWNGRADING SCHEDULE	
4. PERFORMING ORGANIZATION REPORT NUMBER(S) NEAR TR 365	5. MONITORING ORGANIZATION REPORT NUMBER(S) AFWAL-TR-86-3112
6a. NAME OF PERFORMING ORGANIZATION Nielsen Engineering & Research, Inc. 6b. OFFICE SYMBOL (If applicable)	7a. NAME OF MONITORING ORGANIZATION Flight Dynamics Laboratory (AFWAL/FIMG), Air Force Wright Aeronautical Laboratories
6c. ADDRESS (City, State, and ZIP Code) 510 Clyde Avenue Mountain View, CA 94043-2287	7b. ADDRESS (City, State, and ZIP Code) Wright-Patterson AFB, OH 45433-6553
8a. NAME OF FUNDING/SPONSORING ORGANIZATION AFWAL 8b. OFFICE SYMBOL (If applicable) AFWAL/FIMG	9. PROCUREMENT INSTRUMENT IDENTIFICATION NUMBER Contract No. F33615-83-C-3033
8c. ADDRESS (City, State, and ZIP Code) Flight Dynamics Laboratory Wright-Patterson AFB, OH 45433-6553	10. SOURCE OF FUNDING NUMBERS PROGRAM ELEMENT NO.: FY1456 / PROJECT NO.: 0501 / TASK NO.: 30 / WORK UNIT ACCESSION NO.: 05
11. TITLE (Include Security Classification) An Investigation of Wing Lift Augmentation with Spanwise Tip Blowing	
12. PERSONAL AUTHOR(S) Michael R. Mendenhall, Steven C. Caruso, Daniel J. Lesieutre, and Robert E. Childs	
13a. TYPE OF REPORT: Final 13b. TIME COVERED: FROM 09/83 TO 10/86	14. DATE OF REPORT (Year, Month, Day): 1987 April 22 15. PAGE COUNT: 254
16. SUPPLEMENTARY NOTATION	

17. COSATI CODES		
FIELD	GROUP	SUB-GROUP
20	40	

18. SUBJECT TERMS (Continue on reverse if necessary and identify by block number)
Lift Augmentation, Numerical Analysis, Wing Tip Blowing, Experiment

19. ABSTRACT (Continue on reverse if necessary and identify by block number)

Experimental and analytical investigations of lift augmentation on fighter-type wings with wing tip blowing are described. Results of a small-scale wind tunnel test program in the NEAR, Inc. facility are presented for three wings with a wide range of tip nozzle configurations. Effects of nozzle geometry and blowing rate are described, and optimum tip nozzles are selected for further examination in a large-scale test. Results from a large-scale test program in the 7- by 10-foot wind tunnel at the NASA/Ames Research Center are presented for a typical fighter wing with tip blowing. Effects of tip nozzle geometry and blowing rate on lift and drag augmentation, measured pressure distributions, and flow field surveys are discussed. An analytical investigation of a typical fighter-type wing with tip blowing using a modified version of a three dimensional Navier-Stokes code, ARC3D, is presented. Predicted lift coefficients, pressure distributions, and

20. DISTRIBUTION/AVAILABILITY OF ABSTRACT ☒ UNCLASSIFIED/UNLIMITED ☒ SAME AS RPT. ☐ DTIC USERS	21. ABSTRACT SECURITY CLASSIFICATION UNCLASSIFIED
22a. NAME OF RESPONSIBLE INDIVIDUAL Terry Kasten	22b. TELEPHONE (Include Area Code): (513) 255-2803 22c. OFFICE SYMBOL: AFWAL/FIMG

DD FORM 1473, 84 MAR 83 APR edition may be used until exhausted. All other editions are obsolete.

flow field parameters are compared with experiment for purposes of verifying the computer code and understanding the complex flow phenomena associated with wing tip blowing.

Summary

The results of the experimental investigation documented in this report provide an expanded data base of information on lift augmentation on fighter-type wings with wing-tip blowing. The parametric study is suitable for use in future preliminary design efforts involving low-speed lift augmentation concepts for advanced fighter aircraft. The analytical investigation contributes significant understanding to the fluid mechanics of lift augmentation by tip blowing. The computer code has the potential for further development into an analytic preliminary design tool.

ACKNOWLEDGEMENTS

The authors acknowledge the efforts of a number of individuals who contributed to the success of the investigation. Mr. Terry Kasten of AFWAL acted as the Air Force Program Manager, and his cooperation and interest in the program added significantly to its successful completion.

The Low Speed Aerodynamics Branch of the NASA/Ames Research Center contributed the Cray computer time and the funding for the development of the Navier-Stokes code in the analytical investigation. Special thanks to Mr. David H. Hickey and Mr. James E. Eshleman for their assistance in this portion of the study. The cooperation of Mr. Eshleman and the 7- by 10-foot wind tunnel staff during the large-scale test program is also appreciated.

Special acknowledgement is due for Dr. J. M. Wu and Dr. A. Vakali of the University of Tennessee Space Institute who acted as consultants to the experimental program. They contributed the designs of the discrete slot nozzles for both the small- and large-scale test programs. Dr. Wu's comments on the results of the small-scale test program were also very useful to the authors.

Other members of the NEAR staff contributed to the program in many ways. Dr. Robert E. Reed was instrumental in the success of the small-scale test at NEAR, and he made a substantial contribution to the NASA test. Mr. Gary P. Johnson and his staff conducted the small-scale test program and modified and assembled the hardware and associated electronics for the flowfield survey traverse rig mechanism. Mrs. Susana M. Nazario contributed the software necessary for the operation of the traverse rig. Finally, special thanks are due Mrs. Cathy A. Clenner and Mrs. Judy A. Faltz for their efforts and patience in assisting the authors in the construction of this document.

TABLE OF CONTENTS

TABLE OF CONTENTS (concluded)

LIST OF FIGURES

LIST OF FIGURES (continued)

LIST OF FIGURES (continued)

LIST OF FIGURES (continued)

LIST OF FIGURES (concluded)

LIST OF TABLES

AN INVESTIGATION OF WING LIFT AUGMENTATION WITH SPANWISE TIP BLOWING

1. INTRODUCTION

The quest for improved STOL capability and low-speed aerodynamic characteristics of modern fighter aircraft has involved the use of high-energy jets in various schemes for boundary layer and circulation control. One such concept that has not received wide attention is the blowing of high-pressure air jets in a spanwise direction from wing tips (Fig. 1). Experimental investigations have shown significant increases in wing lift with moderate amounts of blowing; for example, see References 1 through 5. Preliminary studies preceding the current efforts (Refs. 6 and 7) verified the enhanced aerodynamic characteristics achieved with wing tip blowing.

The fluid mechanic process of tip blowing is not fully understood, but there are several proposed answers to the apparent success of the approach. For example, the jet sheet from the wing tip will support a pressure gradient during its deformation; therefore, the illusion of a wing with higher aspect ratio is present. Also, the blowing may interact with the tip vortex to reduce three-dimensional effects and effectively increase the aspect ratio. An alternative solution is that the tip jet entrainment induces a spanwise flow on the top surface of the wing thus lowering pressure and increasing lift. All of the above suggestions may play a part in the effectiveness of tip blowing on fighter-wing aerodynamics.

The purpose of the investigation reported herein is manifold. First, a small-scale test program to extend the preliminary tests in References 6 and 7 is reported. In these tests, a number of parameters such as wing aspect ratio, sweep, camber,

tip-jet geometry, and blowing rate were varied to determine their effects on wing lift augmentation, and if possible, optimum tip-jet nozzle geometries were to be selected for a large-scale investigation.

Second, the optimum nozzles identified in the small-scale tests were to be designed and fabricated for a large-scale wing for examination as part of a NASA/Ames Research Center tip-blowing investigation in the 7- by 10-foot wind tunnel. In this large-scale test program, details of the lift augmentation were investigated through wing pressure measurements and flow field surveys at various blowing rates. Major objectives were to increase understanding of the mechanism of lift augmentation via tip blowing and to provide detailed experimental data suitable for verification of the numerical method under concurrent development.

Finally, an analytical investigation of wing-tip blowing lift augmentation based on solution of the Navier-Stokes equations was conducted to provide a means to gain more detailed understanding of the fluid mechanics of the phenomena involved. The objectives were to modify an existing NASA wing code to include effects of a tip jet, verify the code with experimental data, and use the detailed predicted results to gain better understanding of the lift-augmentation process.

The remainder of this report is divided into three major sections for the small-scale test program, the large-scale test program, and the analytical investigation. Each section is autonomous; however, they do refer to one another on occasion. The report closes with some general remarks and recommendations for additional work.

2. SMALL-SCALE TEST PROGRAM

2.1 Background

In a previous investigation reported in Reference 6, a series of eight semispan wing models with tip blowing were tested with the purpose of extending the information data base to low aspect ratio wings. The aspect ratios varied from 0.62 to 4.0 with taper ratios of 0.25 to 1.0. Each wing planform area was approximately 0.5 sq. ft., and a NACA 0015 airfoil section was used throughout. The tip jet for each wing was nearly the full length of the tip chord for all wings. A summary of the results from this initial test program is presented in Reference 7. In general, the experimental results showed significant lift augmentation with blowing at low angles of attack, but the amount of augmentation decreased in inverse proportion with wing angle of attack.

In the current test program, three wings, each with aspect ratio 2.0 and each with several tip nozzle geometries, are considered. Two wings are uncambered NACA 0015 sections, one planform rectangular, the other with a swept leading edge (Λ = 33.8°). The third wing has the same planform as the swept wing, but a cambered airfoil section based on a NACA 64-series mean line. A more complete calibration procedure in the current series of tests revealed inaccuracies in the data reported in Reference 6, although the trends are consistent.

2.2 Test Program

2.2.1 Scope

The tests were conducted in the NEAR low-speed wind tunnel facility at a tunnel speed of 195 ft./sec. (Reynolds number of

1.1×10^6/ft., q_∞ = 45 psf). A few runs were made at lower tunnel speeds to see if the momentum coefficient was an appropriate parameter to measure augmentation effectiveness. The semispan wings were attached to a 5-component balance which in turn was attached to a motor-driven rotary table which varied the angle of attack through a range of 0° to 18°. Although the balance measures all components of forces and moments, except for the force in the spanwise direction, only the lift and drag forces are of primary interest in this study.

2.2.2 Models

The three semispan wings are shown in Figure 2, and their dimensional characteristics are given in Table 1. The wings have zero twist and are cast of aluminum. Several tips with different slot configurations were fabricated for each wing as shown in Figures 3, 4 and 5. The tips with three discrete jets are based on suggested designs by Prof. J. Wu (Ref. 1). The sweep and dihedral angles of the slots were cut to the specified flow angles shown in Table 2; however, the flow did not always conform to these angles. The measured flow angles with no freestream velocity are also shown in Table 2.

2.2.3 Facility

Each wing is mounted in the NEAR tunnel as shown in Figure 6. The test section of the tunnel is 14 x 20 inches (20 in. vertical) and has a maximum wind speed of 220 ft./sec. The flow loop contains two honeycomb flow straighteners (one in the plenum), four turbulence-damping screens in the plenum, and an 8:1 area-ratio nozzle. The typical inlet test section flow distortion in velocity is ±0.2 percent and ±0.2° in flow angle. Very little inlet flow degradation is anticipated with the models at maximum angle of attack due to the relatively high flow loss

around the circuit and the extra honeycomb and screens for flow straightening. Standard wind tunnel wall corrections for blockage (for the semispan wings tested) at maximum lift are 1 percent for velocity and 2 percent for the lift coefficient.

The blowing air is supplied by a 550 cfm roots-type blower driven by a 75-hp motor. The blowing system is illustrated in Figure 7. The after cooler keeps the blowing air at about 71° F. The air blower runs at a constant speed and has constant output. To allow variable flow to the wing tips, a bypass loop is included with this configuration as shown. The flow rate ejected from the wing is the same as the inlet flow rate measured at the orifice regardless of the proportion of air circulated in the bypass loop. Because the orifice is at the upstream end of the system, leaks in the blowing system produced errors in the mass flow computations; therefore, considerable effort was made to reduce leakage to a negligible level. The mass flow rate of the air is measured by an ASME orifice (Ref. 8) placed in the line near the entrance (Fig. 7). Two orifices (diameter of 1 and 2 inches) are used to cover the range of the momentum coefficient. The blowing air is ducted into the wing through a bellows surrounding the balance in the base of the wing (Fig. 6).

Operation at the high tunnel velocity heated the tunnel air rather quickly and was the limiting factor on the length of each test run. The tunnel was shut down when the tunnel air temperature reached 130° F.

2.2.4 Data Acquisition

Each data point was obtained by sampling each data channel at 500 samples/sec. for 1 second, digitizing, and averaging the 500 values to obtain a single value. The data channels are listed in Table 3. Channels 8 to 12 recorded the balance data in

a coordinate system fixed in the balance or the wing, whereas the final lift and drag coefficients are defined in a system fixed to the tunnel. These coordinate systems are shown in Figure 8.

2.2.5 System Calibration

2.2.5.1 Orifice Calibration

Since it was desired to test a wider range of tip flow rates than those used in the previous test (Ref. 6), it was necessary to calibrate the different orifices required. A 6-ft. weather balloon was used to measure the flow rate of the system. It was filled from the air supply system with the wing replaced by a pipe with cross sectional area approximately the same as the tip slots. Filling times were approximately 100 seconds to inflate the balloon to 5-ft. diameter. The air inside the balloon was at room temperature and nearly at atmospheric pressure (less than 0.05 psig), and the balloon was close to neutral bouyancy. The volume of the balloon was determined by measuring the perimeter around different great circles, and the variation in these measurements were typically one part in two hundred. Comparison between the measured flow rate of air and the computed value, with the orifice located between the blower and the wing, was poor and varied with the flow rate. This result places the blowing rates reported in Reference 6 in some doubt.

Next, dynamic measurements were made to determine the quality of flow in the system. It was found that the pump, a Roots blower, positive displacement pump, put out a highly pulsating flow with amplitudes of ±1.2 psi at the orifice when the orifice mean value of Wp was about 0.5 psi. A dominant frequency of 240 Hz (traceable to the number of lobes in the pump) existed with certain higher frequencies. Under these unsteady conditions, the use of an orifice as a flow measuring device is not feasible.

Reference 8 notes that, under pulsating loads, no known relation exists between flow rate and orifice Δp. To avoid this problem, the configuration was modified by placing the orifice upstream of the pump near the inlet of the system and installing mufflers between the orifice and the pump. A muffler was also installed upstream of the wing to steady the flow entering the wing. The fluctuations at the orifice were reduced to about ± 0.03 psi. Subsequent comparisons of the flow rate derived from the balloon measurements and each of two orifices (diameters of 1 and 2 inches) were within about 3-percent using the book values (Ref. 8) for the orifice discharge coefficients. This accuracy was considered to be in the same range as that of the balloon measurements themselves.

2.2.5.2 Balance Calibration

In the Phase I test program, it was recognized that the calibration of the wing-balance-bellows system could change with each wing. The bellows provided a path parallel to the balance through which unmeasured loads could be transmitted. Because the bellows was quite stiff both in torsion and in the directions of normal and side forces, self-equilibrating loads could exist between the balance and the bellows. The five-component balance was calibrated for each wing on a test fixture that housed the actual wing-balance-bellows assembly.

To account for a possible effect of the internal pressure produced by the jet blowing, the balance was calibrated at two values of the pressure denoted by PTC. This was accomplished by sealing the wing tips and statically pressurizing the wing-bellows cavity. The variation between the two calibration matrices was slight with variations in normal and side force being approximately 1 to 2 percent. Linear interpolation of these two matrices was used to obtain the calibration matrix for the value of PTC that existed for each data point during testing.

2.2.5.3 Jet Momentum

The momentum coefficient is based on jet momentum which requires knowledge of mass flow rate and the velocity, or velocity and density. To obtain a direct measure of jet momentum, the wing was mounted in the test fixture on load cells acting in the spanwise direction. The thrust loads were measured as a function of mass flow rate of the blowing air. This direct measurement of momentum avoided the difficult task of integrating the density and velocity distributions over the area of the jet to obtain the momentum coefficient C_μ. Only the spanwise component of momentum, perpendicular to the root chord, is used to define C_μ, because the other components of thrust (balance forces from blowing air) may contain self-equilibrating loads between the bellows and balance.

2.2.5.4 Balance Forces

It is necessary to know the balance forces as functions of tip jet mass flow rate. These forces due to the blowing air are removed from the balance readings to give net external aerodynamic loads acting on the wing. This portion of the calibration was carried out with the wing installed in the tunnel with zero tunnel velocity. It was determined that this calibration was not significantly affected by the tunnel walls, and it did not change as long as the wing was not removed from the balance. The forces being measured were small, but they had a significant effect on the change in drag due to blowing. The present scheme for calibration indicate an upper bound of error of about 0.1 lb. for Fx and 0.2 lb. for Fz. This represents an increment in C_L of about 0.01 and in C_D of 0.005.

2.3 Test Results

All lift and drag coefficients presented herein are based on the external aerodynamic forces acting on the wing; that is, the thrust components from the blowing air have been removed from the total forces and moments measured by the balance. The lift and drag coefficients versus momentum coefficient, C_μ, are presented with angle of attack as a parameter. In the data, small differences in values of α for each configuration exist because of variations in manually setting α and because the correction applied to α depended on the lift coefficient.

An upper bound on experimental error has been estimated to be about 0.01 on C_L and 0.005 on C_D. The error on C_D may be a large percentage at low values of angle of attack, but more accurate drag measurements are beyond the capability of the instrumentation and facilities used in this study. Small differences between different tips should not necessarily be attributed solely to experimental error; for example, it is observed that lift and drag for a given wing appear to be somewhat dependent on the port configuration even when $C_\mu = 0$.

To show a reason why differences may actually exist, the wing cavity pressure was measured when $C_\mu = 0$ with the wing cavity sealed except for the opening of the tip port(s). The negative pressure in the wing cavity varied between configurations that are identical except for the geometry of the ports. This variation in pressure at the same value of α must be caused by changes in the flow around the different tips; for example, a chordwise pressure gradient at the tip will produce a local flow in and out of the multiple ports. These changes can produce variations in the lift and drag for different port configurations.

In the following sections, the measured lift and drag coefficients on each wing and tip combination are presented. Comments on the data are provided as part of the discussion for each wing.

2.3.1 Wing No. 1

The results of measured lift and drag coefficients at various blowing rates for the rectangular wing are shown in Figures 9 through 12. Tips 1, 2, and 3 show small gains in lift up to C_μ = 0.04. In Figure 9, the lift coefficient of a single port, (the forward two ports in Tip 1 were sealed) shows a decrease in lift. In Figure 12, Tip 4 shows a gain in lift of 20 percent at α = 18° and approximately 60 percent at α = 3° at a value of C_μ = 0.12.

The drag coefficients measured on the rectangular wing with multiple tip jets (Tips 1, 2, and 3) are uncertain at best. The trends are consistent; that is, blowing either has little effect on drag or it increases drag slightly. The experimental error in the drag measurements are the same order of magnitude as the change in drag. The long slot, Tip 4, causes a significant increase in drag with increased blowing as shown in Figure 12(b).

All tips on Wing No. 1 are compared in Figure 13 at constant blowing coefficients. The no-blowing condition in Figure 13(a) illustrates the small effect of tip geometry on the baseline condition as described in a previous section. Within the expected scatter in the data, there is virtually no tip effect on drag with no blowing. At a constant blowing rate, C_μ = 0.035, in Figure 13(b), there are some small effects of geometry. Comparison of parts (a) and (b) illustrates increased lift and drag due to tip blowing over the entire range of angle of attack.

2.3.2 Wing No. 2

The measured results of lift and drag coefficient at various blowing rates for the uncambered swept wing are shown in Figures 14 through 17. The results for Tips 1 and 2, each having three discrete slots, are shown in Figures 14 and 15. Both tips exhibit increases in both lift and drag at the larger angles of attack. Tips 3 and 4 in Figures 16 and 17 have long slots extending over most of the tip chords. It is seen in Figures 16 and 17 that the lift at C_μ = 0.10 for both tips is increased about 18 percent at α = 12°. At angles of attack, Tip 4 has a higher increase in lift than Tip 3. As shown in previous results, the drag increase due to blowing is greater for the longer slots.

The different tips on Wing No. 2 are compared with and without tip blowing in Figure 18. Without blowing, there are small tip geometry effects on lift and drag, but for practical purposes, the results lie within the normal scatter in the measurements. With blowing, the lift curves show no tip effects until large angles of attack. There seems to be a significant tip effect on the drag coefficient over the entire angle range.

In Figure 19, the average values of lift and drag of all the tips are shown for C_μ = 0.0 and 0.04 to illustrate the increases with blowing. The average curve for lift coefficient is more meaningful than that for drag coefficient since there is little lift variation between tips. There is more variation in drag between tips at C_μ = 0.04, but the average values are still useful in showing the trend of drag increasing with C_μ. The increase in lift at C_μ = 0.04 is about 8 percent.

2.3.3 Wing No. 3

This wing has the same planform as Wing No. 2, but the section is cambered (NACA 64 Mean Line). The measured results for lift and drag coefficient for different levels of tip blowing are shown in Figures 20 through 23. The effect of camber is largely an added increment of angle of attack of almost 6 degrees or an increment of lift of about $\Delta C_L = 0.25$. If the effects of camber are removed such that C_L at $\alpha = 3°$ equals C_L for Wing No. 2, Tip 4 at $\alpha = 3°$, the results at other values of α are similar to those described previously. A summary of the effect of tip blowing for all tips together is shown in Figure 24, and the averaged values are shown in Figure 25. It appears the drag coefficient is not affected by blowing, and the lift coefficient is increased approximately 5 percent at $\alpha = 18°$.

2.3.4 Tunnel Velocity

Several runs were made at lower tunnel velocities to test the validity of using C_μ as a measure of the blowing effectiveness. Shown in Figure 26 are results for $V_\infty = 100$ and 195 ft./-sec. The agreement between runs is good. From the definition of C_μ, a lower tunnel velocity allows a higher C_μ, and it is apparent that the lift continues to increase at the higher blowing rates for $\alpha = 12$ and 18 degrees. The higher tunnel velocity was chosen for most of the testing to ensure that the jet is swept aft to prevent reflections from the opposite tunnel wall from impinging on the wing.

2.3.5 General Comparisons

Comparisons of the improvement in lift due to tip blowing are shown in Figure 27 for $\alpha = 3°$, 12°, and 18°. The tip considered for each wing has the long slot covering most of the tip

chord. The cambered wing (No. 3) shows less improvement in lift than the other wings, especially at low angles of attack, and the lift improvement on the cambered wing is nearly independent of α.

The effect of camber on the relationship between lift and drag for the swept wings is seen in Figure 28. The effect of blowing is about the same for each wing.

2.4 Discussion of Results

The different tips for a given wing exhibit similar aerodynamic characteristics at the same values of momentum coefficient. The lift coefficient generally increases with increasing values of momentum coefficient. The location of the tip jet is critical to the lift augmentation; although, the one tip made up of a small jet near the trailing edge of the wing actually decreased the lift with blowing. This particular jet had a large sweep angle (about 60°) which may have been too large for optimum efficiency.

The angles of the blowing jet deserve more investigation to determine their effect on the performance of the wing. Also, the effect of camber is important and represents another parameter to be investigated. The lower improvement in lift and its relative independence of α suggests that camber basically affects the process by which lift is improved.

The jet momentum coefficient is controlled by two parameters, the mass flow rate and the pressure ratio. To obtain comparable values of C_μ, a small port using a low flow rate requires a high pressure ratio whereas a large jet uses a large flow rate and a lower pressure ratio. The more important parameter may be tip-jet velocity ratio for correlation of induced lift

with blowing; however, it is difficult to use this additional parameter when tip geometry is also changing. This area needs further investigation.

3. LARGE-SCALE TEST PROGRAM

3.1 Background

NASA/Ames Research Center has an interest in tip blowing for lift augmentation that extends back to 1960, including an unpublished tip-blowing test program from that period. A briefing at NASA/Ames Research Center on the small-scale tests described above brought to light a planned tip-blowing test in the Ames 7- by 10-foot wind tunnel. Through a cooperative agreement between Ames and the Air Force, NEAR was allowed to participate in this large-scale test program which would permit tests on a larger scale wing at higher pressure ratio tip jets than was possible in the NEAR facility. The NEAR participation included the fabrication of an experimental apparatus to measure flow field information in the vicinity of the wing with tip blowing, design and fabrication of interesting tips identified in the small-scale test program, and participation in the actual test program at NASA to monitor the preliminary data and provide any experience gained during the small-scale tests.

NASA/Ames Research Center contributed the experimental data on tip blowing presented herein. These data are to be published by NASA at a later date.

3.2 Test Program

3.2.1 Scope

The NASA test program involved the design, fabrication, and testing of a wing with planform similar to the small-scale swept wing described above. The wing was instrumented for overall force and moment measurements and pressure measurements on the wing surface. A computer-controlled traversing system for measuring static and dynamic pressures in the flow field in the vicinity of the wing was available for flow field surveys.

The tests were conducted for a number of different tip nozzle configurations over a range of angles of attack and blowing rates. To obtain desired blowing coefficients, the tip nozzle pressure ratio and the freestream velocity were varied. The freestream velocity ranged from 160 to 285 ft./sec. during the tests, and the tip pressure ratio was between 4.8 and 6.3. This velocity range provided a Reynolds number range of 0.93 x 10^6 to 1.70 x 10^6/ft. and a dynamic pressure range of 30 to 90 psf. For a single run (angle of attack sweep) the tip pressure ratio and the freestream velocity were held nearly constant. They were changed between runs to obtain different blowing rates.

3.2.2 Model

A sketch of Wing C-BT is shown in Figure 29 where the spanwise location of pressure ports are shown. The locations of the pressure ports on each surface are given in Tables 4 and 5 where the chordwise locations are measured from the local leading edge, and each is normalized by the local chord length.

The basic wing dimensions are

semispan, $b/2 = 30.4$ in.
root chord, $c_R = 36.0$ in.
tip chord, $c_T = 10.8$ in.

A total of five tips with different blowing slots were considered. In addition, a solid tip was included as a reference for the case of no blowing. The tip numbers and the corresponding slot geometries are defined in Figures 30(a) and (b) where the length of each single slot jet is determined by the location of the end points given in percent of the tip chord. The area of each slot is 0.24 sq. in; therefore, the constant area is achieved by varying the width of the slot for each tip. The slots for tips five and six have splay (dihedral) angles of 30 and 60 degrees, respectively; that is, the jets blow downward at an angle measured from a horizontal reference. These tips blow outward at a sweep angle equal to zero.

Tip 8 was designed by Dr. J. M. Wu of the University of Tennessee Space Institute. The three slots have sweep and splay angles as shown in Figure 30(b). Although the slots were cut to these angles, the actual flow angles sometimes varied from these values. The total area of the three slots, measured perpendicular to the flow channels within the wing is 0.36 sq. in. which is slightly greater than the other tips.

3.2.3 Facility

The NASA/Ames Research Center 7- by 10-foot wind tunnel is a closed circuit, atmospheric, subsonic (0 to 220 knots) tunnel having an external balance for measuring loads on the model. The balance consists of scales connected with the appropriate linkages to measure the six components of load. Semispan models can

be attached to a floorplate which is attached to the scales, and the floorplate rotates about a vertical axis to change the angle of attack of the model.

A large supply of high pressure air is available for tip blowing. The hoses carrying this air have couplings that form a flexible "trapeze" to eliminate variable resultant loads in the hoses that could be applied to the balance.

The flowfield traverse rig is a structure that moves a probe along three orthogonal axes throughout the test section. The degrees of freedom can be increased by adding the rotation capability to the probe unit. The unit is computer controlled through software that allows either movement to single locations or automatic movement through an array of locations for flow field surveys.

3.2.4 Data Acquisition and Reduction

The data consist of the six components of resultant forces and moments obtained from the external balance system, wing surface pressures from the array of taps, parameters of both the tunnel and the blowing air, and airstream pressures from the traversing probe.

The force data are reduced to net forces, in coefficient form, produced by the external aerodynamic forces acting on the wing; that is, the forces produced by the blowing air internally within the wing system are removed. These tare forces were obtained by a two-step procedure. First, the wing tare forces at angle of attack for the wing with no blowing and the tunnel off were measured. Then, each tip was tested with blowing and the tunnel off. The wing tares were subtracted from these data to obtain the net tip tares. Note that the tip tares should be

included in some cases; for example, when comparing the effect on lift and drag of a jet blowing at different sweep or splay angles, the thrust portion of the tare may contribute lift and drag forces that exist in an actual application.

The pressure data are reduced to pressure-coefficient form, and the resulting pressure distribution is integrated to obtain the aerodynamic contribution to the lift force. This is useful for comparing to the balance-measured lift force. The blowing coefficient is obtained from thrust measurements with zero tunnel velocity and from measurements taken in the blowing-air lines. The mass flow rate is measured with an orifice, and the tip momentum is calculated from the mass flow rate and the measured pressure ratio at the tip. Because the pressure ratio is greater than two, sonic velocity exists at the tip nozzle for all blowing conditions.

3.3 Test Results

Preliminary lift and drag data from the large-scale test of Wing C-BT at the NASA/Ames Research Center are presented in this section. These data have not received extensive analysis, and they are presented herein for illustration purposes. A formal test report will be forthcoming from Ames in the near future; therefore, this section should not be considered as wind tunnel test documentation.

The lift and drag coefficients to follow are corrected for tip jet tares as described above; therefore, the forces are the external aerodynamic forces acting on the wing. The results are presented with jet momentum coefficient and angle of attack as parameters. A sample of the measured results on each tip configuration are presented, and brief comments on the data are provided as part of the discussion for each configuration.

3.3.1 Tip 2

Measured lift and drag coefficients on Wing C-BT with Tip 2 are shown in Figure 31 for a range of blowing coefficients and angle of attack. The solid tip is shown on each curve as a reference for the basic wing. Tip 2, the long straight slot jet, produces increased lift and lift curve slope with blowing. The maximum lift coefficient is significantly higher at the large blowing rates, but the stall angle is unchanged. Drag coefficients shown in Figure 31 (b) indicate increased minimum drag with blowing, but the measured drag at higher lift coefficients appears to decrease with blowing. The decrease in drag at a given lift coefficient is likely caused by the lower angle of attack required to produce a specified lift coefficient with tip blowing activated.

3.3.2 Tip 4

Tip 4 has a slot length approximately equal to 25-percent of the tip chord. Measured lift and drag coefficients for a range of blowing coefficients are shown in Figure 32. These results are similar to those discussed above; however, it appears the lift increment due to blowing may be slightly less than that observed for Tip 2 at the same momentum coefficient. Drag also seems to decrease with blowing, but the total increment is less for this tip.

3.3.3 Tip 5

Tip 5 is the same size as Tip 4, but Tip 5 is blowing downward at a 30-degree dihedral angle. Direct lift from the jet momentum has been removed from these results shown in Figure 33. At low angles of attack, the lift increment due to blowing is greater than that measured on Tip 4 without dihedral; however,

at higher angles of attack, the lift increment due to blowing appears to be less with dihedral. The drag coefficient shown in Figure 33 (b) is apparently decreased with blowing at higher lift coefficients, but at low values of lift, the increment in drag is the same order as the scatter in the measurements.

3.3.4 Tip 6

Tip 6 (Figure 34) is the same tip described above, but it has a 60-degree dihedral angle. In general, the results with blowing show higher lift at low angles of attack than that measured on the previous tip; however, the maximum lift coefficients with blowing are nearly identical to the other tips. The measured drag coefficients are virtually identical to those described above.

3.3.5 Tip 8

The measured lift and drag coefficients on this tip with three individual slots, illustrated in Figure 30 (b), is shown in Figure 35. Tip blowing increases the lift coefficient at the high angles of attack, but the amount of increase appears to be slightly less than that produced by the other tips. The lift increment due to blowing is less at low angles of attack. The drag data appear to be questionable as if the thrust components of the jets have not been removed from the measurements. These data should be investigated further before comparisons with other tips are considered.

3.3.6 Pressure Distributions

Details of the effects of tip blowing on the chordwise pressure distribution on Wing C-BT are available from the large-scale NASA test for selected configurations and flow conditions. In

Figure 36, measured pressure distributions on the wing with Tip 2 at 5 degrees angle of attack and C_μ = 0.02 are compared to the unblown wing at the same angle. The tip jet tends to lower the suction pressure on the wing upper surface over the entire span; however, the jet-induced effects are small inboard of the mid semispan. On the lower surface, the tip jet causes an increase in the pressure, but the effect is small inboard of the 80-percent semispan station. Thus the total effect of tip blowing is to increase the lift over the semispan of the wing with the largest increases occurring at the tip as expected.

Measured pressure distributions on Wing C-BT with Tip 4 under similar flow conditions are shown in Figure 37. Though Tip 4 is a shorter slot, the jet-induced effects are nearly the same as for Tip 2. The inboard lower-surface pressures seem to exhibit slightly lower jet-induced effects as do the lower surface pressures over the entire semispan.

Similar pressure measurements are shown in Figure 38 for the wing with Tip 8 with three discrete slots (Fig. 30(b)) at various sweep and dihedral angles. Though the inboard pressure measurements are omitted because of instrumentation difficulties, the outboard pressure distributions exhibit some distinct differences from the previous results. For example, the jet-induced lower pressure on the upper surface is concentrated toward the trailing edge of the wing with smaller effects near the leading edge. Also, the jet-induced effects on the lower surface are smaller than those observed in the previous figures. These results are not unexpected since the tip jets are concentrated near the trailing edge.

3.3.7 Flow Field Surveys

Preliminary velocity field measurements at two stations (1 inch and 10 inches) aft of the wing trailing edge are available from traverse surveys. These qualitative measurements clearly illustrate the trailing vortex as shown in Figure 39. Figures 39 (a) and (b) show the vortex for Wing C-BT at 8 degrees angle of attack and no tip blowing. The origin of the coordinate system is located at the tip trailing edge, and the wing trailing edge line is shown to illustrate the wing position. With tip blowing on, a significant change in trailing vortex position is shown in Figures 39 (c) and (d). It is clear the vortex is moved outboard and upward, and from the relative magnitude of the individual vectors, it appears the vortex is dispersed over a greater area. Furthermore, it appears the tip vortex with tip blowing is stronger than the vortex without blowing.

The results from the flowfield measurements indicate significant effects of tip blowing on the trailing vortex. These results are preliminary and have suffered minimum analysis; therefore, some caution is advised in developing conclusions based on the above observations.

3.7.8 General Results

The tip blowing results described above provide sufficient data for a number of parametric studies. Detailed analysis of these data is beyond the scope of the current investigation; however, several interesting comparisons follow to illustrate general trends of the experiment.

The effect of tip nozzle geometry is shown in Figures 40, 41, and 42 where the measured lift and drag coefficient on each tip is compared for nearly constant blowing rates. The first

observation is that Tip 2 provides the highest lift augmentation at high angles of attack, but Tip 6 provides higher augmentation at low angles of attack. Discounting the possible problem with the drag data for Tip 8, the measured drag results highlight Tips 2 and 6 as providing more drag reduction at a constant lift coefficient than the other tips. However, the difficulty in measuring drag and the scatter in the data make this result tentative at best.

An alternate means of comparing tip geometry effects is to compare relative lift increments induced by tip blowing. In Figure 43, the incremental lift attributed to tip blowing, normalized by the baseline lift on the wing without blowing, is shown for each tip at constant blowing coefficients over the entire range of angles of attack. Although these results have not been smoothed or curve fit for easier visualization, several interesting results appear. Tip 2 produces the greatest lift augmentation at high angles, but Tip 6 is marginally better at low angles. Tip 8 consistently produces the lowest lift augmentation at angles below maximum lift. As expected, the lift augmentation increases with increased blowing rates.

Another means to quantify lift augmentation at varying blowing rates is shown in Figure 44 where the lift augmentation is shown as a function of blowing rate for constant angles of attack. In general, these results indicate increased lift augmentation with increased blowing; however, the rate of increase decreases at higher angles of attack. As noted previously, Tip 6 provides the greatest lift augmentation at low angles of attack, but at 16 degrees, Tip 2 is marginally better.

3.4 Discussion of Results

As described above, tip blowing from any of the nozzles considered has an effect on lift augmentation, although some nozzles appear to be more efficient than others. The pressure distributions illustrate that the lift augmentation due to tip blowing is concentrated at the tip; however, there is some effect over most of the wing, both upper and lower surfaces. The flow field studies illustrate a significant effect on the location and strength of the wing trailing vortex.

The investigation reported in this section permitted only a cursory study of the wealth of data obtained in the NASA/Ames large scale test program, and additional analysis of these data may add more understanding to a complex flow phenomenon. Therefore, it is important that firm conclusions be delayed until all the measurements have been examined with care. In particular, it is important that the measurements be studied in the context of the theoretical analysis reported in the following sections.

4. ANALYTICAL INVESTIGATION

4.1 Background

The fluid phenomena responsible for providing lift augmentation with wing tip blowing are not well understood. The purpose of the analytical investigation is to study the effects of tip blowing by using a Navier-Stokes code to predict the flowfields about a realistic wing with variable blowing conditions (jet geometry and blowing coefficients). Spanwise blowing from near the root of the wing is also investigated. Analysis of the simulated flowfields can provide further understanding into the mechanisms and parameters affecting lift augmentation.

There are few previous analytical studies of the wing/tip-jet problem. The complexity of the flowfield makes a theoretical approach difficult; consequently, only inviscid models have been attempted. For example, Wu et al. (Ref. 1) uses a vortex lattice-model for the wing and tip jet. The computed spanwise distribution of normal-force coefficients and chordwise loadings are in fair agreement with experimental data, although the agreement deteriorates near the tip.

Assuming the jet is an inviscid sheet and acts as a fluid extension of the wing tip, Tavella and Roberts (Ref. 9) derive scaling laws for lift augmentation as a function of blowing coefficient and angle of attack. Using these scaling relations, data taken from different blowing experiments with rectangular wings are correlated (within a fairly large band). Based on the correlation, the authors conclude (Refs. 10 and 11) that lift augmentation is primarily the result of inviscid phenomena.

Neither of the above approaches explicitly accounts for any viscous lift augmentation mechanism. The Navier-Stokes method was purposely selected for simulating this flow because it includes both viscous and inviscid effects. As part of the current effort, a preliminary numerical study of the flow over a rectangular wing having spanwise tip blowing was accomplished (Ref. 12). A summary of these preliminary calculations and results are discussed in the following section.

4.2 Preliminary Analytical Study

To identify the important mechanisms influencing lift augmentation, and also to demonstrate the feasibility of performing a Navier-Stokes simulation of the wing/tip-jet flowfield, a preliminary numerical study was conducted. The numerical model used

and the important results of the study are summarized in this section. Further details are presented in Reference 12.

The simulated wing model has a rectangular planform with an aspect ratio of one. The cross-section is 10 percent thick, having circular arc upper and lower surfaces and 2 percent camber. The leading and trailing edges are sharp, and the wing tip profile is rectangular. The tip jet consists of a thin slot, approximately 70-percent chord in length and centered vertically and horizontally on the tip. This geometry provides blowing in the spanwise direction (normal to the free stream flow direction) with zero dihedral or splay angle.

The Reynolds-averaged, compressible, Navier-Stokes equations are solved using second-order central differencing with fourth-order numerical dissipation terms added for stability. MacCormack's explicit algorithm (Ref. 13) is used as the solution algorithm. The turbulence model consists of a constant mixing-length based on the jet-slot width and is described in detail in a later section.

The selected grid, Cartesian and nonboundary fitting, has 32 x 32 x 16 points in the streamwise, wing-surface normal, and spanwise directions, respectively. The grid density across the tip jet is necessarily coarse for this preliminary study.

Boundary conditions applied at the nonblowing surfaces of the wing and the wing root wall are inviscid, tangency conditions. The wing boundary layer is neglected because proper grid resolution cannot be provided. All cases consider a freestream Mach number of 0.5 and subsonic jet velocities. Inflow boundary conditions are specified and outflow conditions are extrapolated.

Numerical simulations with parametric variations of angle of attack and jet blowing coefficient are shown. The jet blowing coefficient is defined as

$$C_\mu = \frac{\dot{m}_j V_j}{q_\infty S} \qquad (1)$$

and varies between 0.0 and 0.32. The angle of attack varies between 0 and 6 degrees. The ratio of jet velocity to free-stream velocity varies with C_μ and does not exceed two.

Before discussing the simulation results, two terms are defined to quantify lift augmentation. Lift increment is defined as the difference in lift coefficient with and without blowing, and relative lift increment is defined as the ratio of the lift increment and the lift coefficient without blowing.

The following observations are made with respect to the wing loading. At a constant angle of attack, the relative lift increment increases rapidly at intermediate blowing coefficients, then more slowly at higher C_μ (Fig. 45(a)). Holding the blowing coefficient constant, Figure 45(b) shows the relative lift increment rises and then falls off as the angle of attack increases. The falloff is primarily due to the increase in the baseline lift coefficient at higher angles of attack. Similar lift augmentation behavior is found in experimental studies described in References 4, 14, and 15.

Based on predicted results, spanwise loading with tip blowing increases over the entire semi-span. The largest increases in lift occur near the tip, but some augmentation occurs near the root. Generally, the upper surface pressures are lower with tip blowing, and the lower surface pressures are nearly unchanged. The location of the minimum pressure on the

upper surface shifts rearward with tip blowing as noted in Reference 15.

The predicted flowfield in the vicinity of the wing tip reveals additional insight into the mechanisms of lift augmentation. The trailing vortex with blowing is shifted upwards and outwards from the wing tip as shown in Figure 46; consequently, the induced velocity on the wing upper surface near the tip has an outboard component. This is in contrast to the no-blowing case where the velocity has an inboard component. Observations of the outward movement of the tip vortex is also described in Reference 15.

A view of the pressure field at 104-percent semi-span (Fig. 47) reveals a distinct pressure difference across the jet. At 80-percent chord (Fig. 48) the pressure field exhibits a pocket of low pressure adjacent to and just outboard of the tip in the vicinity of the tip vortex core. This pocket of low pressure is responsible for lowering the pressure on the wing upper surface near the wing tip thus accounting for part of the lift augmentation.

To assess the influence of this low pressure region on the augmentation effect, an additional simulation holding the angle of attack and blowing coefficients fixed was investigated; however, jet velocity was reduced and jet density was increased to maintain the constant blowing coefficient, as discussed in Reference 12, the resulting tip vortex is weaker, the pressure in the vortex region is higher, and the lift increment is smaller.

The following picture emerges from these observations. A primary augmentation mechanism appears to be the generation of a low pressure region associated with the tip vortex core. With

blowing, the tip vortex has greater swirl and lower core pressure. Energizing the tip vortex is a result of jet-induced shear stresses acting on the surrounding fluid; therefore, the jet velocity appears to be an important parameter, more so than the blowing coefficient. Because of the close proximity of the low pressure region to the tip, greater suction pressure is induced on the upper surface near the tip and decreasing towards the root. The wing's lower surface pressure remains essentially unchanged. The net result is a gain in lift.

The results of this preliminary study indicate viscous effects are a key ingredient to lift augmentation by tip blowing. Since viscous effects have been neglected in previous theoretical approaches, it is important they be included to gain complete understanding of the fluid mechanics of the complex flow field.

4.3 Analytical Method

This section describes the details of the analytical method used for simulating tip-jet flows. The governing equations are presented, followed by descriptions of the numerical algorithm, wing and grid, turbulence models, and boundary conditions.

4.3.1 Governing Equations

The Reynolds-averaged Navier-Stokes equations in generalized curvilinear coordinates in strong conservation law form are

$$\partial_\tau \hat{Q} + \partial_\xi(\hat{E} - \hat{E}_v) + \partial_\eta(\hat{F} - F_v) + \partial_\zeta(\hat{G} - \hat{G}_v) = 0 \qquad (2)$$

where the conserved variables and convective fluxes are

$$\hat{Q} = J^{-1}\begin{bmatrix} \rho \\ \rho u \\ \rho v \\ \rho w \\ e \end{bmatrix} \qquad \hat{E} = J^{-1}\begin{bmatrix} \rho U \\ \rho uU + \xi_x p \\ \rho vU + \xi_y p \\ \rho wU + \xi_z p \\ U(e + p) - \xi_\tau p \end{bmatrix}$$

(3a)

$$\hat{F} = J^{-1}\begin{bmatrix} \rho V \\ \rho uV + \eta_x p \\ \rho vV + \eta_y p \\ \rho wV + \eta_z p \\ V(e + p) - \eta_\tau p \end{bmatrix} \qquad \hat{G} = J^{-1}\begin{bmatrix} \rho W \\ \rho uW + \zeta_x p \\ \rho vW + \zeta_y p \\ \rho wW + \zeta_z p \\ W(e + p) - \zeta_\tau p \end{bmatrix}$$

(3b)

The contravariant velocity components, U, V, and W are given in terms of the Cartesian components

$$U = \xi_t + \xi_x u + \xi_y v + \xi_z w \tag{4a}$$

$$V = \eta_t + \eta_x u + \eta_y u + \eta_z w \tag{4b}$$

$$W = \zeta_t + \zeta_x u + \zeta_y v + \zeta_z w \tag{4c}$$

Using the ideal-gas equation of state, pressure is related to the conserved variables as

$$p = (\gamma - 1)\left[e - \frac{1}{2}\rho\,(u^2 + v^2 + w^2)\right] \tag{5}$$

The viscous flux terms are

$$\hat{E}_v = J^{-1}\begin{bmatrix} 0 \\ \xi_x\tau_{xx} + \xi_y\tau_{xy} + \xi_z\tau_{xz} \\ \xi_x\tau_{yx} + \xi_y\tau_{yy} + \xi_z\tau_{yz} \\ \xi_x\tau_{zx} + \xi_y\tau_{zy} + \xi_z\tau_{zz} \\ \xi_x\beta_x + \xi_y\beta_y + \xi_z\beta_z \end{bmatrix} \tag{6a}$$

$$\hat{F}_v = J^{-1}\begin{bmatrix} 0 \\ \eta_x\tau_{xx} + \eta_y\tau_{xy} + \eta_z\tau_{xz} \\ \eta_x\tau_{yx} + \eta_y\tau_{yy} + \eta_z\tau_{yz} \\ \eta_x\tau_{zx} + \eta_y\tau_{zy} + \eta_z\tau_{zz} \\ \eta_x\beta_x + \eta_y\beta_y + \eta_z\beta_z \end{bmatrix} \tag{6b}$$

$$\hat{G}_v = J^{-1}\begin{bmatrix} 0 \\ \zeta_x\tau_{xx} + \zeta_y\tau_{xy} + \zeta_z\tau_{xz} \\ \zeta_x\tau_{yx} + \zeta_y\tau_{yy} + \zeta_z\tau_{yz} \\ \zeta_x\tau_{zx} + \zeta_y\tau_{zy} + \zeta_z\tau_{zz} \\ \zeta_x\beta_x + \zeta_y\beta_y + \zeta_z\beta_z \end{bmatrix} \tag{6c}$$

with

$$\tau_{xx} = \frac{2}{3}\mu[2(\xi_x u_\xi + \eta_x u_\eta + \zeta_x u_\zeta) - (\xi_y v_\xi + \eta_y v_\eta + \zeta_y v_\zeta) - (\xi_z w_\xi + \eta_z w_\eta + \zeta_z w_\zeta)] \tag{7a}$$

$$\tau_{yy} = \frac{2}{3}\mu[2(\xi_y v_\xi + \eta_y v_\eta + \zeta_y v_\zeta) - (\xi_x u_\xi + \eta_x u_\eta + \zeta_x u_\zeta) - (\xi_z w_\xi + \eta_z w_\eta + \zeta_z w_\zeta)] \tag{7b}$$

$$\tau_{zz} = \frac{2}{3}\mu[2(\xi_z w_\xi + \eta_z w_\eta + \zeta_z w_\zeta) - (\xi_x u_\xi + \eta_x u_\eta + \zeta_x u_\zeta) - (\xi_y v_\xi + \eta_y v_\eta + \zeta_y v_\zeta)] \quad (7c)$$

$$\tau_{xy} = \mu(\xi_y u_\xi + \eta_y u_\eta + \zeta_y u_\zeta + \xi_x v_\xi + \eta_x v_\eta + \zeta_x v_\zeta) \quad (7d)$$

$$\tau_{xz} = \mu(\xi_z u_\xi + \eta_z u_\eta + \zeta_z u_\zeta + \xi_x w_\xi + \eta_x w_\eta + \zeta_x w_\zeta) \quad (7e)$$

$$\tau_{yz} = \mu(\xi_z v_\xi + \eta_z v_\eta + \zeta_z v_\zeta + \xi_y w_\xi + \eta_y w_\eta + \zeta_y w_\zeta) \quad (7f)$$

and

$$\beta_x = \gamma\kappa Pr^{-1}\partial_x e_I + u\tau_{xx} + v\tau_{xy} + w\tau_{xz} \quad (8a)$$

$$\beta_y = \gamma\kappa Pr^{-1}\partial_y e_I + u\tau_{yx} + v\tau_{yy} + w\tau_{yz} \quad (8b)$$

$$\beta_z = \gamma\kappa Pr^{-1}\partial_z e_I + u\tau_{zx} + v\tau_{zy} + w\tau_{zz} \quad (8c)$$

$$e_I = e\rho^{-1} - 0.5(u^2 + v^2 + w^2) \quad (8d)$$

The effective viscosity, μ, is the sum of the molecular and turbulent viscosities described in Section 4.3.4.

The transformation metric terms are

$$\xi_x = J(y_\eta z_\zeta - y_\zeta z_\eta) \qquad \eta_x = J(z_\xi y_\zeta - y_\xi z_\zeta)$$

$$\xi_y = J(z_\eta x_\zeta - x_\eta z_\zeta) \qquad \eta_y = J(x_\xi z_\zeta - x_\zeta z_\xi)$$

$$\xi_z = J(x_\eta y_\zeta - y_\eta x_\zeta) \qquad \eta_z = J(y_\xi x_\zeta - x_\xi y_\zeta) \qquad (9)$$

$$\zeta_x = J(y_\xi z_\eta - z_\xi y_\eta) \qquad \xi_t = -x_\tau \xi_x - y_\tau \xi_y - z_\tau \xi_z$$

$$\zeta_y = J(x_\eta z_\xi - x_\xi z_\eta) \qquad \eta_t = -x_\tau \eta_x - y_\tau \eta_y - z_\tau \eta_z$$

$$\zeta_z = J(x_\xi y_\eta - y_\xi x_\eta) \qquad \zeta_t = -x_\tau \zeta_x - y_\tau \zeta_y - z_\tau \zeta_z$$

and the inverse Jacobian is:

$$J^{-1} = x_\xi y_\eta z_\zeta + x_\zeta y_\xi z_\eta + x_\eta y_\zeta z_\xi - x_\xi y_\zeta z_\eta - x_\eta y_\xi z_\zeta - x_\zeta y_\eta z_\xi \qquad (10)$$

The thin-layer approximation to the Navier-Stokes equations (Ref. 16) is commonly used for calculating wing flowfields. The major assumptions in this model are that the Reynolds number is large, shear layers are thin, and the grid is sufficiently clustered in the shear layers. Viscous terms associated only with derivatives normal to the shear layers are retained in the flux terms given in Equation (6). The resulting thin-layer equations are considerably simpler and, consequently, more economical to solve than the full Navier-Stokes equations.

The thin-layer approximation is applicable to jet flows; however, with spanwise blowing, it must be modified to account for the fact the jet is blowing in a direction normal to the freestream flow direction. Applying the thin-layer assumption in all three directions, the viscous fluxes $\hat{E}_v$, $\hat{F}_v$, and $\hat{G}_v$ become $\tilde{E}_v$, $\tilde{F}_v$, and $\tilde{G}_v$, respectively, and are

$$\tilde{E}_v = J^{-1} \begin{bmatrix} 0 \\ \mu a_1 u_\xi + (\mu/3) a_2 \xi_x \\ \mu a_1 v_\xi + (\mu/3) a_2 \xi_y \\ \mu a_1 w_\xi + (\mu/3) a_2 \xi_z \\ \mu a_1 a_3 + (\mu/3) a_2 (\xi_x u + \xi_y v + \xi_z w) \end{bmatrix} \tag{11a}$$

$$\tilde{F}_v = J^{-1} \begin{bmatrix} 0 \\ \mu b_1 u_\eta + (\mu/3) b_2 \eta_x \\ \mu b_1 v_\eta + (\mu/3) b_2 \eta_y \\ \mu b_1 w_\eta + (\mu/3) b_2 \eta_z \\ \mu b_1 b_2 + (\mu/3) b_2 (\eta_x u + \eta_y v + \eta_z w) \end{bmatrix} \tag{11b}$$

$$\tilde{G}_v = J^{-1} \begin{bmatrix} 0 \\ \mu c_1 u_\zeta + (\mu/3) c_2 \zeta_x \\ \mu c_1 v_\zeta + (\mu/3) c_2 \zeta_y \\ \mu c_1 w_\zeta + (\mu/3) c_2 \zeta_z \\ \mu c_1 c_2 + (\mu/3) c_2 (\zeta_x u + \zeta_y v + \zeta_z w) \end{bmatrix} \tag{11c}$$

where

$$a_1 = \xi_x^2 + \xi_y^2 + \xi_z^2 \tag{12a}$$

$$a_2 = \xi_x u_\xi + \xi_y v_\xi + \xi_z w_\xi \tag{12b}$$

$$a_3 = (u^2 + v^2 + w^2)_\xi / 2 + P_r^{-1} (\gamma - 1)^{-1} (a^2)_\xi \tag{12c}$$

$$b_1 = \eta_x^2 + \eta_y^2 + \eta_z^2 \tag{13a}$$

$$b_2 = \eta_x u_\eta + \eta_y v_\eta + \eta_z w_\eta \tag{13b}$$

$$b_3 = (u^2 + v^2 + w^2)_\eta / 2 + P_r^{-1} (\gamma - 1)^{-1} (a^2)_\eta \tag{13c}$$

$$c_1 = \zeta_x^2 + \zeta_y^2 + \zeta_z^2 \qquad (14a)$$

$$c_2 = \zeta_x u_\zeta + \zeta_y v_\zeta + \zeta_z w_\zeta \qquad (14b)$$

$$c_3 = (u^2 + v^2 + w^2)_\zeta/2 + P_r^{-1}(\gamma-1)^{-1}(a^2)_\zeta \qquad (14c)$$

For incompressible flow in an orthogonal coordinate system, the full Navier-Stokes viscous terms in Equation (6) reduce to Equation (11). Most calculations in this study are made at $M_\infty = 0.25$ and on a grid which is orthogonal in the viscous regions of the flowfield.

4.3.2 Numerical algorithm

The NASA/Ames Research Center code, ARC3D, forms the basis of the code used to compute the wing/tip-jet flowfields. ARC3D solves the thin-layer Navier-Stokes equations in generalized coordinates. To compute the tip-jet flows, the following changes are necessary:

(1) The thin-layer approximation is implemented in all three directions.
(2) The tip jet is simulated by specifying the jet flow on the wing tip surface.
(3) The turbulence model is modified in the tip-jet region.

These changes are described in this and the following sections.

A full description of the algorithms contained in ARC3D is found in Reference 17. To illustrate the particular version of

the algorithm used in this study, the numerical method is presented without elaboration, except where it is necessary to indicate any changes.

The solution method in the current version of ARC3D is derived from the Beam and Warming implicit approximation-factorization algorithm (Ref. 18). When second-order central differencing is used for all spatial operators, the Beam and Warming method requires the inversion of block tridiagonal systems of equations. A diagonal form of the algorithm (Ref. 19) requires the inversion of scalar pentadiagonal matrices (using fourth-order implicit dissipation terms) and is more economical than the Beam and Warming method.

The diagonal form is given by:

$$T_\xi(I + h\delta_\xi \Lambda_\xi^n + hD_i|_\xi)\hat{N}(I + h\delta_\eta \Lambda_\eta^n + hD_i|_\eta)\hat{P}(I + n\delta_\zeta \Lambda_\zeta^n + hD_i|_\zeta)T_\xi^{-1}\Delta\hat{Q}^n = \hat{R}^n \qquad (15)$$

and

$$\hat{R}^n = -h(\delta_\xi \hat{E}^n + \delta_\eta \hat{F}^n + \delta_\zeta \hat{G}^n - Re^{-1}\delta_\zeta \hat{S}^n + D_e \hat{Q}^n) \qquad (16)$$

where Λ_ξ, Λ_η and Λ_ξ are diagonal matrices consisting of the eigenvalues of the Jacobians of $\hat{E}$, $\hat{F}$, and $\hat{G}$. T_ξ, $\hat{N}$, $\hat{P}$, and T_ξ^{-1} are matrices related to the similarity transformations, D_i and D_e are the implicit and explicit dissipation operators, respectively. Note the explicit right-hand-side vector, $\hat{R}$, contains the thin-layer viscous flux terms, $\hat{S}$. The three-dimensional thin-layer approximation is implemented by augmenting $\hat{S}$ to include the viscous terms given in Equation (11).

The dissipation terms are a combination of second- and fourth-order differences which are shown in Equation (7.8) of Reference 20. In the current study, the coefficient of the second-order term, κ_2, is set to zero. The fourth-order coefficient, κ_4, is made as small as possible while not destroying the stability of the solution algorithm. $\kappa_4 = 1/256$ is used for most calculations shown herein.

All spatial differences are second-order central, including the metric differences. This version of the code uses freestream subtraction (Ref. 16) to maintain exact freestream flow.

All calculations are run with a spatially-variable time step,

$$h = \min\left(\frac{\Delta x}{|u| + a}, \frac{\Delta y}{|v| + a}, \frac{\Delta z}{|w| + a}\right) CFL \qquad (17)$$

and constant CFL number.

4.3.3 Wing Model and Grid

The wing chosen for this study is a low aspect ratio, swept wing having twist, taper, and camber that has been extensively studied both experimentally (Refs. 21 through 23) and computationally (Refs. 24 through 27). Commonly referred to as WING C, it has a planform similar to the large-scale wing tested in the current program (see Section 3 above), but it has a different airfoil section. A schematic of WING C is given in Figure 49.

A boundary-conforming curvilinear mesh with a C-O-type topology was constructed about the wing model. The "C" part of the mesh wraps around the upper and lower wing surfaces at constant spanwise stations (Fig. 50(a)). Two-dimensional C-grids are constructed at the root, mid-span and tip locations, where

the wing geometry is known, using a hyperbolic grid generation algorithm. A spanwise distribution, which clusters grid lines near the tip, is constructed. Three-dimensional grids are created by linearly interpolating in the previously generated two dimensional grids at the desired spanwise stations.

The "O" part of the mesh, shown in Figure 50(b), wraps around the tip. It is generated by rotating the upper- and lower-half planes of the C-mesh at the tip about a curved line consisting of the grid line normal to the wing at the leading edge, the tip camber line, and the wake cut. A segment of the axis of rotation is shown as line a-b-c-d in Figure 50(c).

Construction of the grid topology in this manner creates singularities and cuts in the mesh. Pole singularities exist in the tip plane along the wake-cut line and the line emanating from the leading edge. The "tip cut" (Fig. 50(b)) occurs where the upper- and lower-half tip planes coincide at the maximum value of η. Treatment of the solution at grid cuts and singularities is described in Section 4.3.5 below.

The grid has 85 x 23 x 30 points in the ξ, η, and ζ directions, respectively, with 58 points distributed on the chord. (ξ, η, and ζ refer to the streamwise, spanwise, and wing-surface normal directions, respectively, in Fig. 50). This is the largest number of grid points which permit the code (approximately 2 million words in length) to run fully in central memory on a Cray X-MP/48 without reducing job priority.

In the x-z plane, the far-field mesh boundary varies from four to five root chords from the trailing edge. In the y-z plane, the boundary is four to five root chords from the wing tip.

The mesh on the wing surface is illustrated in Figure 51(a). Grid points are clustered at the leading edge to give a minimum grid spacing of approximately 1-percent chord. Clustering is also required at the trailing edge to ensure a smooth transition of lower and upper surface pressures.

At constant chord, the grid is equally spaced on the wing tip. To maintain a reasonable variation of grid spacing (in the spanwise direction) at the transition between the wing surfaces and the tip, grid lines on the upper and lower surfaces are clustered at the wing tip. This clustering also provides for additional resolution in a critical region of the flowfield when the tip-jet is on. Due to the thickness variation of the airfoil, it is necessary to bend grid lines near the tip as indicated in Figure 51(b). This adjustment considerably reduces the variation in mesh spacing at the surface-tip transition where the airfoil is thin, as illustrated in Figure 52. In Figure 52(a), the original grid is illustrated to show the problem area near the tip. The grid spacing is much more reasonable with the bent grid lines on the wing surface as shown in Figure 52(b).

In the direction normal to the wing surface, the grid is tightly clustered to resolve the boundary layer. Although not sufficient for high accuracy, an attempt is made to maintain a minimum of eight to ten points in the boundary layer.

4.3.4 Turbulence Models

Turbulence closure in ARC3D is provided by the Baldwin-Lomax model (Ref. 28), where the eddy viscosity is given as the product of an algebraically-defined mixing length and the magnitude of the local vorticity

$$\nu_t = \ell_m^2 |\omega| \qquad (18)$$

The Baldwin-Lomax model has been shown to be accurate for attached boundary layers and simple mixing layers.

The mixing-length in the model is formulated in terms of a normal distance through the shear layer; consequently, it is easily applied to a boundary-conforming mesh having coordinate lines normal to the wing surface, as is the case with the C-O-type grid. Equation (18) has been used at all locations on the wing surface, but not in the tip-jet and the wake.

A crude approximation is used in the wake region because the wake flow exerts a small influence on the wing flow field. The eddy-viscosity distribution in the trailing edge boundary layers is applied at all locations downstream of the trailing edge in the wake region. Reprogramming of ARC3D is required to implement the Baldwin-Lomax model in the wake region.

The tip-jet is modeled as a planar slot in the tip (Fig. 53). A common mixing-length model for a planar-jet (Ref. 29) assumes the mixing length is constant across the shear layer and is given by

$$\ell_{in} = 0.9\delta \qquad (19)$$

where δ is the distance from the jet centerline to the point where the velocity differs from the free stream by 1 percent. Equations (18) and (19) are used to model turbulence in the tip-jet, with δ taken as one-half of the jet-slot width. Since the thickness of a turbulent jet grows slowly (Ref. 30), streamwise variation of the mixing-length is neglected. This jet mixing-length is applied along all grid lines normal to the tip-jet opening. Thus, the turbulence model is accurate in the near field of the jet, but inaccurate in the far field where the flow is largely inviscid.

4.3.5 Boundary Conditions

In nearly all simulations, the flowfield is subsonic everywhere (except in the tip-jet exit plane), and appropriate boundary conditions are applied. All normal-gradient approximations are first-order differences. The boundary conditions are explicitly applied after each solution update.

At the farfield boundary, freestream conditions are imposed where the flow is into the domain. Otherwise, zero normal gradients of the conservative variables are specified, except for the total energy. Pressure is linearly extrapolated to the outer boundary, and energy is calculated from the equation of state.

At the wing-root wall an inviscid, impermeable boundary is approximated by setting the normal velocity component to zero and imposing zero normal gradients for the other variables. Since the root-wall boundary layer is neglected, computed inboard-wing surface pressures are expected to deviate slightly from experimental data.

On the wing surface, no-slip conditions are specified, and zero gradients are imposed on the density and pressure. The latter conditions provide an adiabatic wall, along with the boundary layer approximation.

The tip jet is a sonic or supersonic inflow boundary, and jet density, velocity, and pressure are all specified.

At grid singularities and also at the tip and wake cuts (Fig. 50), the solution is taken as an average of the neighboring grid point values. Since the pole singularities are internal to

the computational domain, these averages are also applied explicitly after the solution is updated.

4.4 Results

Results of the numerical simulations are discussed in this section. First, normal nonblowing calculations are presented to establish the code's accuracy and a baseline case for the tip-blowing simulations. Results of the tip-jet-on cases are discussed, followed by a description of a preliminary calculation made with spanwise blowing.

All calculations were run on the NASA/Ames Research Center Cray X-MP/48 computer. The code ran 1.8 cpu seconds per time step, with each run requiring about 45 minutes of cpu time.

For both blowing and nonblowing runs, approximately 1500 steps are required to reduce the residual two orders of magnitude, while converging the total lift coefficient to three significant figures. The rms right-hand-side residual is defined as

$$r = \left\{ \frac{\sum_{j,k,\ell,m} \left\{ \frac{\hat{R}}{h}(j,k,\ell,m) \right\}^2}{N_j \; N_k \; N_\ell} \right\}^{1/2} \qquad (20)$$

where the short-hand notation implies summation over the spatial indices j, k, and l, and the dependent variable index, m. $\hat{R}$ is given by Equation (16), h is the variable time step from Equation (17), and N_j, N_k, and N_ℓ are the number of mesh points, respectively, in the three directions.

4.4.1 No-blowing Wing Calculations

The first simulation on Wing C is for $M_\infty = 0.7$ and $\alpha = 5°$. Comparisons of measured and predicted chordwise pressure distribution and spanwise loading are shown in Figures 54 and 55, respectively. Experimental values from Reference 22 are shown as symbols alone, and the solid line represents predicted results. The predictions show very good agreement with experimental chordwise and spanwise pressure variations. As shown in the table below, the total lift coefficient is within 2 percent of the experimental value.

Measured and Predicted Lift and Drag Coefficient on Wing C
$M_\infty = 0.7$, $\alpha = 5°$

	C_L	C_L
experimental	0.447	.037
predicted	0.438	.031
Δ%	-2%	-16%

Navier-Stokes results are compared to experimental data and calculations made with the full potential FLO22 code on Wing C at $M_\infty = 0.25$ and $\alpha = 5°$ (Ref. 23). Figures 56 and 57 illustrate the chordwise pressure variations and spanwise loading where the dashed line represents the FLO22 calculations, the solid line the current Navier-Stokes calculations, and the open symbols the experimental data. The Navier-Stokes chordwise pressure variations agree well with both the experimental data and the inviscid FLO22 calculations; however, the accuracy of the spanwise loading is not as good as the previous case at the higher Mach number. Both calculations underpredict the experimental data. The cause for this discrepancy is not known.

Due to the reasonable agreement between the Navier-Stokes predictions and experimental data for Wing C, it is concluded that the code has sufficient accuracy for the nonblowing wing. The latter case at $M_\infty = 0.25$ is used as the baseline case for the blowing simulations described in the following sections.

4.4.2 Wing Tip-Blowing Calculations

4.4.2.1 Introduction

An initial goal of this study is to simulate the tip-jet geometry and test parameters used in the large-scale experiments described in Section 3. The experimental jet consists of a thin rectangular slot machined in the wing tip, as illustrated in Figure 30. Because of the limitation on the maximum number of grid points (Section 4.3.3), the grid in the vicinity of the tip-jet is rather coarse, and it is not possible to accurately model the slot width of the experimental jet. The length of the jet is approximately maintained; therefore, the simulated jet exit-plane areas are considerably larger than the respective experimental values. The jet length is considered to be a more important parameter than its width.

The geometry of the simulated tip-jet is illustrated in Figure 53. One long and one short jet are considered in this study, and the dimensions and locations of both simulated and actual jets are given in Table 6. Note that five grid lines span the simulated jet width.

Before describing the computational results, it is necessary to discuss two important differences between the simulations and the experiments. As stated in Section 4.3.3, the simulated and experimental wing planforms are similar, but the airfoil sections

are different. This is reflected in the base-line lift coefficients. At $\alpha = 5°$, Wing C has $C_L = 0.42$ (Ref. 23), compared to $C_L = 0.32$ for the large-scale wing (Wing C-BT). The difference in airfoil section is also apparent in the chordwise pressure distributions. The large-scale wing pressures (Fig. 58) are considerably different from those of Wing C (Fig. 56). However, other factors preclude the modeling of the actual airfoil section of Wing C-BT; therefore, comparisons of measured and predicted results will involve lift increments and trends.

The other major difference between experiment and simulation is the condition of the tip-jet. In the experiments, the jet is considerably underexpanded, with jet pressure ratios (jet-stagnation to freestream-static) as high as six. The cyclic shock/expansion-fan pattern, typical of underexpanded jets was noted during the experiments. Because the grid is too coarse to properly resolve such a complicated flowfield, the tip-jet is simulated as a perfectly expanded jet. These two types of jet-exit conditions are expected to produce different levels of lift augmentation through different entrainment and other turbulence-induced effects; however, it is difficult to determine to what extent these differences affect the results.

Because of the aforementioned differences in airfoil section and tip-jet conditions, there is no basis to directly compare simulated and experimental lift augmentation levels. However, the order of magnitude of lift increment and parameter effects are expected to be similar, and the tip-jet-induced flow phenomena should be the same.

All jet-on simulations are shown for $M_\infty = 0.25$ and $\alpha = 5°$ to match experimental conditions unless otherwise noted. The jet-momentum coefficient is determined by specifying the jet velocity and density. Jet-exit plane pressure is set to the freestream

value. A summary of the various cases considered, along with the resulting lift augmentation levels, is given in Table 7, and a set of corresponding experimental cases is shown in Table 8. Case numbers are selected to reflect similar parameter variations.

4.4.2.2 Long Jet

Cases 1 through 4 are calculations made with the long jet described in Table 6. Case 1 is the first jet-on simulation, and it has no turbulence model in the jet. This case shows very little lift augmentation, approximately 3 percent in relative lift increment (Table 7). At the same C_μ, the experiment has 25-percent augmentation. When the turbulence model is incorporated in Case 2, the lift increment doubles, but it still is considerably smaller than that measured.

At the same C_μ and q_∞, the simulated jet has a lower exit-plane velocity, because its area is larger than in the experiment. It is possible that the ratio of jet-to-tree-stream velocity is more important than momentum coefficient alone; therefore, in Case 3, the jet velocity ratio, $v_j/V_\infty = 4$, is increased to better approximate the experimental velocity ratio. The magnitude of the lift increment in Case 3 is in better agreement with experiment, Case 2', though the momentum coefficients are different. Increasing the jet velocity ratio to eight in Case 4 provided only slightly larger lift increment than in Case 3.

A single calculation was made at $\alpha = 10°$ (Case 3a) with the same blowing coefficient and jet velocity ratio as Case 3. Lift variation versus angle of attack is compared with experimental data (Cases 0' and 3') in Figure 59. Although the baseline and lift-augmentation levels differ, the predicted lift-curve slopes are similar to experiment. This is expected since both wings

have the same planform. The slight increase in lift-curve slope caused by tip blowing is also in good agreement with experiment.

The predicted chordwise pressure distributions and spanwise loadings for the wing with and without tip blowing are compared in Figures 60 and 61, respectively. Surface pressures inboard of 50-percent semispan show little effect of tip-jet blowing; however, at 90-percent semispan, the upper surface pressure is significantly lower over most of the chord with the jet on. The jet-induced effects on the lower surface are small, but they do increase toward the tip. The spanwise loading comparisons show a lift gain over the entire span, with the largest gain occuring near the tip, and gains decreasing inboard. The high loading exhibited at the tip with blowing is caused by numerical oscillations in the pressure near the jet. Also note that $2y/b = 1$ corresponds to a station on the wing surface (Fig. 51) slightly inboard of the actual tip.

Experimental chordwise pressure distributions with and without blowing are shown in Figure 62 to illustrate tip-jet-induced effects. Jet-on data are from experimental conditions similar to Case 2'. The experimental pressures display qualitative behavior very similar to the computational pressures shown in Figure 60. There is little difference between the blowing and nonblowing pressures inboard of 50-percent semispan. At 90-percent semispan, with blowing, the upper surface pressures are lower over the full chord. Small pressure increases on the lower wing surface near the tip are observed.

The complete wing surface pressure contours for computed jet-on and jet-off cases are compared in Figure 63. These contours indicate the lower surface pressure is largely unaffected by blowing. The upper surface pressure contours are shifted rearward over the entire wing (also noted experimentally,

Ref. 15) and a low pressure region appears near the tip for the jet-on case. The redistribution of upper surface pressures provides the lift augmentation observed.

The cause of upper surface pressure changes is explained by viewing the predicted wing tip flowfield. Figure 64 compares the predicted pressure field at 35-percent chord. For the wing without blowing, Figure 64(a) illustrates the small pressure gradient that exists around the wing tip. This gradient is, of course, responsible for the spilling of fluid around the tip which eventually leads to the formation of the tip vortex. When the tip jet is on, a pocket of low pressure exists just outboard and above the tip and extends to the upper wing surface as shown in Figure 64(b).

Figure 65 is a close-up of the flowfield at the 35-percent chord station. The pressure oscillations shown in Figure 65(a) are discussed at the end of this section. The tip-jet spreads rapidly (Fig. 65(b)) and bends upward as it progresses outboard of the tip. A relatively strong vortex is formed above the jet, its core located within the pocket of low pressure. The vortex appears to be created by shear stresses generated by the jet, and its strength is enhanced by the curved, upward jet trajectory. The prevailing global circulation around the tip also serves to increase vorticity. A weaker vortex, with opposite rotation is faintly visible beneath the jet. Note also that the velocity on the upper surface near the tip has an outboard component. For a nonblowing wing, the flow is always inboard at this location.

The chordwise extent of the outboard low pressure region is illustrated in Figure 66, where normalized pressure is shown at the 100-percent semispan station. This pressure-field pattern is consistent with the notion that the jet acts as a fluid extension of the wing. It is plausible that the acceleration of the

oncoming flow, as fluid deflects around the jet, is partially responsible for the creation of this pressure field.

The wing flowfield, illustrated above, is consistent with that observed in the preliminary analytical study described in Section 4.2. The current results support the picture of the lift-augmentation process previously described. The shearing effect of the tip-jet creates a relatively strong vortex above and outboard of the wing tip, oncoming freestream fluid is accelerated as it passes through the core of the vortex, and some fluid accelerates to deflect around the jet. The induced flow and the latter two acceleration effects create a region of low pressure that extends to the upper wing surface producing a net gain in lift.

To complete the discussion of the long jet results, the wake flowfield is considered. The streamwise component of vorticity at 150-percent chord is shown in Figure 67 for the jet-off and two jet-on cases (Cases 0, 3, and 4) corresponding to jet-velocity ratios of 0, 4, and 8, respectively. For the nonblowing wing, the location of the tip vortex is apparent by the concentration of vorticity at $y/c_R \sim 0.8$ in Figure 67(a). When the tip blowing is on, the tip vortex is displaced outboard and upward with respect to the nonblowing tip vortex. A secondary region of weaker vorticity with opposite rotation is located below the jet. Grid coarseness in the wake region distorts the shape of the wake vortices.

The localized pressure oscillations near the jet exit (Fig. 65) are numerical in nature, caused by the central differencing scheme. Oscillations typically occur where there is insufficient grid resolution in a location of large gradients such as occurs at the jet origin. Increasing the numerical dissipation will smooth both the oscillations and the solution. The oscillations

can be eliminated, or at least reduced in magnitude, by refining the grid and/or using a difference method (such as a TVD scheme, Ref. 31) that is not as susceptible to oscillations.

The coarseness of the grid in the tip-jet region is indicated in the velocity vector plot in Figure 65. Each velocity vector emanates from a single grid point. It is clear that the grid spacing radially outboard of the tip becomes coarse very rapidly, and the coarseness causes both the jet and the vortex above it to become over-diffused. Insufficient grid resolution in this critical area is believed to be the primary cause for the low lift augmentation levels in the computations.

4.4.2.3 Short Jet

Case 5 is a calculation made with the short jet to illustrate the effect of jet length on lift augmentation. The jet begins at the same location as the long jet, 13 percent of the tip chord, and ends at 36 percent of the chord, making it approximately one-third the length of the long jet. The jet locations and lengths are similar to those in the Ames experiment (Table 6).

Table 7 shows that the short jet produces a 3-percent relative lift increment compared to the jet-off case. At the same C_μ, the short jet produces only one-half of the long jet's lift augmentation (Case 2), and only one-third of the augmentation for the same jet-velocity ratio (Case 3).

The effect of jet length on lift augmentation is also seen in the experimental data. Table 8 illustrates that the experimental relative lift increment of the short jet is 60 percent of that measured for the long jet.

In case 6, the short jet has the same jet-velocity ratio as the previous case, but the momentum coefficientis doubled, by doubling the jet density. Doubling C_μ while holding the jet velocity ratio constant increases the relative lift increment an insignificant amount. This further supports the conclusion that, for a given wing/jet geometry, the momentum coefficient alone is not sufficient to descrube tip-blowing effects.

The reduction in lift gain for a shorter jet is not surprising considering the mechanisms responsible for lift augmentation. Within the chordwise extent of the jet, long and short jets have similar tip flow fields. Aft of the end of the short jet, the flow around the tip (from lower to upper surface) reestablishes (Fig. 68); consequently, a large pressure difference cannot be supported at the tip. However, the jet-generated vortex and its associated low pressure core persist downstream and serve to lower the upper wing surface pressure beyond the end of the jet, as revealed in the chordwise pressure results shown in Figure 69.

4.4.2.4 Jet with Splay Angle

The last tip-jet simulation, Case 7 in Table 7, considers the long tip jet blowing at a 30-degree splay or dihedral angle (downward with respect to the horizontal). The jet-momentum coefficient and jet-velocity ratio are the same as in Case 4 where the blowing is straight out from the tip. Note that C_μ is based on the total jet velocity.

Blowing in a downward direction provides over twice the aerodynamic lift augmentation compared to blowing straight out. Lift is calculated by integrating wing surface pressures; therefore, the thrust of the jet is not included. In the large-scale

experiments, Case 7' in Table 8, a similarly large increase in augmentation was observed with downward blowing tip jets.

In addition to the augmentation process described earlier, blowing at a splay angle introduces or enhances an additional augmentation effect. To investigate this mechanism, the flowfields for tip blowing with and without a splay angle (Cases 7 and 3, respectively) are compared.

Chordwise surface pressure distributions are compared in Figure 70 for both 0- and 30-degree splay angles. Inboard of 50-percent semispan, the pressures are not influenced by splay angle. At 90-percent semispan, there is increased suction on the upper surface and higher pressure on the lower surface with the downward blowing jet. This is similar to the pressure change that occurs at a slightly higher angle of attack. Compare the results in Figure 70(c) with the measured surface pressures for the large scale wing shown in Figure 71. These measurements at 90-percent semispan for $\alpha = 5°$ and $\alpha = 8°$ illustrate the effect of increasing angle of attack. Predicted velocity vectors just upstream of the leading edge at the tip, shown in Figure 72, reveal that the approaching flow angle is slightly larger with downward blowing thus increasing the angle of attack at the tip.

The spanwise loading in Figure 73 illustrates that augmentation is largest at the tip and decreases inboard, typical of all previous results. The numerical oscillations at the tip, causing the large loading near the tip, are still in evidence at the 30-degree splay angle.

The predicted flowfield at 35-percent chord is illustrated in Figure 74. It is similar to the straight-blowing velocity field (Figs. 64 and 65) except that the low pressure region and outboard vortices are shifted downward to follow the jet path.

This change in position does not significantly alter the outboard upper surface pressures at this chordwise location.

The above observations indicate that downward blowing induces an increased angle of attack at the tip, which in turn produces greater lift augmentation levels compared to straight blowing. The velocity field at a spanwise location beyond the wing tip, presented on the curved surface indicated in Figure 75 because of the grid topology, may indicate jet-induced changes in flow angles. Figures 76(a) and (b) are predicted velocity fields on this curved surface for the cases of straight-out and downward blowing, respectively. The projection of the airfoil section at the tip is included for a reference in these figures.

When the jet is blowing straight out, oncoming freestream fluid deflects symmetrically over the tip jet due to the blockage effect of the jet. When the jet is blowing downward, the deflection becomes asymmetric as some oncoming freestream fluid below the leading edge of the wing is deflected above the jet. This upward movement of fluid causes the flow approaching the wing tip leading edge to have an increased upward velocity component when compared to the straight-blowing case. The resulting increase in flow angle near the tip increases the loading on the forward portion of the airfoil section. There may be an increase in the leading-edge suction in this region of the wing which could have an effect on drag; however, this is beyond the scope of the present investigation.

4.4.3 Spanwise Blowing Calculations

Spanwise blowing from the root wall, also investigated in the large-scale test program, produces lift augmentation levels comparable to those with tip blowing. A simulation of spanwise

blowing was attempted with the same code used for tip blowing, and the results are described in this section.

In the experimental apparatus, blowing is accomplished with a round jet mounted in the root wall. The jet has a diameter equal to 3 percent of the root chord, and it is located at 3 percent of the root chord above the upper wing surface. The jet's chordwise location, a test parameter, is varied between 0-percent and 26-percent chord. Jet pressure ratios are greater than two; therefore, sonic conditions prevail at the jet exit.

The spanwise jet is simulated by specifying jet velocity, density, and pressure at approximately 18 percent of the root chord on the root wall. Because of the grid coarseness at this location, only four grid points identify the jet, resulting in a jet-exit area three times larger than the experimental value. The jet velocity ratio (v_j/V_∞) is four, approximately the same as experimental value. The simulated momentum coefficient, C_μ = 0.14, is approximately twice the experimental result. Jet turbulence is modeled in a manner similar to the tip-jet modeling.

The pressure and velocity fields are illustrated in the x-z plane at 13-percent semispan and in the y-z plane at 20-percent chord in Figures 77 and 78, respectively. Corresponding pressures for the nonblowing wing are shown in Figure 79 for comparison purposes. Large numerical oscillations in the pressure predictions occur because the jet is poorly resolved. Upper surface pressures are significantly distorted, producing a total lift less than the nonblowing wings while experimental results indicate a 13-percent increase in relative lift increment. Grid refinement in the vicinity of the jet is required to improve the simulation accuracy.

Although the accuracy is poor, the predicted results provide some insight into the physics of this flow. As indicated in the velocity plot in Figure 77(b), the flow on the upper surface accelerates as it deflects above the jet (at approximately 20-percent chord) producing a large region of low pressure as seen in Figure 77(a). The spanwise extent of the low pressure region is seen in Figure 78(a). The initial formation of a vortex above the jet is apparent in the velocity vectors on the inboard part of the upper surface at 20-percent chord in Figure 78(b).

The pressure field for a nonblowing wing is plotted at the same spanwise and chordwise locations in Figures 79(a) and (b), respectively. Compared to the nonblowing wing, the pressure field generated with spanwise blowing indicates increased suction over a large portion of the wing upper surface to account for the gain in lift. Spanwise blowing apparently produces lift augmentation phenomena similar to that produced by tip-blowing. Two acceleration effects, the blockage caused by the jet and the formation of a vortex above the jet, contribute to the creation of a low pressure region and thus increased suction on the wing upper surface.

5. CONCLUSIONS

The investigation reported in this document consists of three distinct topics related to wing tip blowing lift augmentation. These are a small-scale test program, a large-scale test program, and an analytical study. Because of the diversity of the three topics, the conclusions are considered separately.

5.1 Small-Scale Test Program

The small-scale test in the NEAR wind tunnel of three semi-span wings with a number of different tip nozzle configurations

is reported herein. The stated objectives of these tests were to determine the influence of the tip nozzle geometry, tip jet momentum, and jet direction on the aerodynamic loads of three wings. Optimum nozzles selected from these tests were to be used in a large-scale test program at NASA/Ames Research Center. Some observations and conclusions based on the results of the three wings tested follow.

The rectangular wing exhibited only small effects of tip nozzle geometry. In general, blowing from the tip did augment lift and modify drag; however, the drag data are uncertain because of the accuracy of the measurements.

The swept wing without camber showed lift increases attributed to tip blowing, and certain nozzle configurations proved better than others. For example, the long slot nozzle covering most of the tip chord was significantly better in lift augmentation than the smaller discrete slots. At low angles of attack, there was little effect of tip nozzle geometry on lift augmentation; however, there was a large effect on drag. This latter effect must be tempered with the knowledge of the difficulty in measuring drag accurately.

The swept wing with camber showed only small increases in lift due to tip blowing and almost no change in drag. In some instances, tip blowing may reduce drag for a constant lift coefficient.

The small-scale test program contributed to the data base and knowledge of tip-blowing effects on the aerodynamic characteristics of fighter-type wings. Based on the measurements, several optimum tip nozzle configurations were suggested to NASA/Ames for further testing in the large-scale test program.

These nozzles included the long slot nozzle and the three discrete nozzle configurations.

5.2 Large-Scale Test Program

The large-scale test program conducted in the NASA/Ames Research Center 7- by 10-foot wind tunnel on a swept and cambered wing with tip blowing is also reported in this document. NEAR, Inc., contributed to the test program by sharing the results and experience gained in the small-scale tests, by suggesting and designing several tip nozzle configurations based on the small-scale results, and by actual participation during the test.

Measured aerodynamic characteristics from the NASA test are presented in a previous section. These results indicate the long slot nozzle provides the greatest lift augmentation, particularly at high angles of attack, but the shorter slot nozzle has some advantage at low angles. In general, the long single slot nozzles proved better than the multiple slot nozzles. Drag coefficient is not as sensitive as lift to nozzle geometry, but it is difficult to make definite statements regarding drag based on the preliminary information reported above. Additional analyses of the data are required to assess its accuracy and consistency.

Perhaps the most important pieces of information from the large-scale test program are the pressure distributions and the flowfield surveys. These data provide heretofore unavailable details of the flow interactions caused by wing tip blowing, and as discussed below, these data coupled with predicted results provide greater understanding of the complex phenomena associated with tip blowing.

5.3 Analytical Investigation

The existing Navier-Stokes code, ARC3D, was modified to simulate the flow about a three-dimensional semispan wing with wing tip blowing. A three-dimensional thin-layer approximation to the full Navier-Stokes equations is solved, and turbulence is modeled with an algebraic turbulent eddy viscosity. The simulated wing model has a similar planform, but different airfoil section, to the wing used in the large-scale test program. Simulated tip jets are modeled as perfectly expanded jets with larger exit-plane areas, but tip jets in the experiment were underexpanded.

The code was verified by comparing calculated and experimental surface pressure distributions and spanwise loadings for the nonblowing wing at $M_\infty = 0.25$ and $M_\infty = 0.7$. Calculations showed good agreement with experimental data at both Mach numbers.

A series of simulations with tip jets were made to investigate the effects of jet turbulence, momentum coefficient, jet-to-freestream-velocity ratio, jet length, and splay angle. The calculated flowfields were analyzed to determine the mechanisms responsible for lift augmentation. Computed results were compared to data from the large-scale test.

Predicted lift augmentation levels are smaller than those measured, but the parametric behavior is similar to experimental observations. A lack of grid resolution in the tip jet region is believed to be the primary cause for shortfalls in lift increment. Inaccurate turbulence modeling is also a source of error in the simulations; for example, lift augmentation doubles when turbulence is modeled in the jet. This indicates that the creation of turbulent shear stresses by the tip-jet, a viscous

effect, is an important mechanism in lift augmentation; therefore, the type of turbulence model selected may also have a significant effect on lift augmentation.

For fixed geometry, increasing C_μ by increasing only jet density has a negligible effect on lift augmentation. The jet-velocity ratio has a stronger influence on jet-induced effects. Increased velocity ratio means stronger jet shear stresses, another indication that viscous effects play an important role in lift augmentation due to tip blowing.

A picture of the source of lift augmentation emerged from the numerical studies. The shearing action of the tip-jet on the surrounding fluid creates a relatively strong vortex above and outboard of the wing tip. Oncoming freestream fluid is accelerated as it passes through the core of the vortex, and some fluid also deflects around the jet in reaction to its blockage effect. These two acceleration effects create a region of low pressure that extends to the upper wing surface producing a net gain in lift.

The experimental observations of the influence of jet nozzle length on lift augmentation is confirmed. A long jet gives at least twice the lift increment of a jet one-third in length, and the short jet imparts less energy into the tip-generated vortex. Also, a large pressure difference cannot be supported at the tip, aft of the end of the short jet, where spilling of fluid around the tip is reestablished.

The measured effect of jet splay angle is also confirmed. In addition to the augmentation effects caused by straight blowing jets, a splay-related mechanism induces a higher angle of attack at the tip which contributes to the augmentation.

A simulation of spanwise blowing is considered in this study, but due to grid coarseness, large oscillations near the jet occur in the pressure field, and numerical convergence cannot be achieved. The preliminary flowfield results show similarities to the phenomena associated with the tip-jet field; however, additional effort is required to gain proper understanding of spanwise blowing lift agumentation.

6. RECOMMENDATIONS

The experimental and analytical investigations reported above have added considerable information and understanding to the pheonomena associated with lift augmentation due to wing tip blowing. In particular, the theoretical effort and preliminary prediction method provide heretofore unavailable capability to calculate details of the flows and interactions. Other investigators are also making significant contributions in this area. It is time to try to assimilate all the available information, new and old, experimental and theoretical, good and bad, into a unified understanding of the fluid mechanisms involved with jet interactions with lifting surfaces. Wing tip blowing and spanwise blowing are just two of many such lift augmentation proposals. This is the basic recommendation of the authors.

The following specific recommendations for extension of the work reported herein are offered. The large quantity of experimental results collected from both the small and large scale tests have not been thoroughly examined. For example, the analytical study indicated that jet velocity ratio may be a more important parameter for data correlation than momentum coefficient. The measured results should be examined in detail for such a correlation.

The large-scale tests provided more data than could be analyzed in this investigation. Additional pressure and flowfield data should be studied and added to the information data base. These data can provide useful comparisons with the theory for code verification as well as contributions to the basic understanding of lift augmentation.

If additional large scale tests are warranted, the results of this investigation can be used to guide a future test program. For example, recommendations for flow conditions, type and location of measurements, and geometry for future tests can be made based on the theoretical method reported above.

It was noted previously that the numerical approach developed for this effort is still of a preliminary nature, and it will require some additional work before it can be considered for use as a design method. Several specific recomendations for additional work on the prediction method follow.

The grid should be refined in the jet flowfield so that accuracy can be brought to an acceptable level. Refinement in the tip region, however, should not be made at the expense of grid coarsening in some other region. Due to the large grid requirement for this problem, the generation of an improved grid is not a simple task; however, one approach would be to use a patched grid (Ref. 27) or a zonal approach.

Due to the strong dependence of lift augmentation on jet shearing, a more accurate turbulence model, such as a $k-\varepsilon$ model should be investigated. Besides being difficult to apply to complex flows, the accuracy of the algebraic turbulence model used in the current code is not adequate for the problems of interest. It is likely the turbulence model used in the comparisons with the large-scale data described above is not adequate

to model the increased turbulence level and mixing present in the supersonic jets of the experiment. Another possibilty for improvement of the prediction method is to tailor a turbulence model, based on the available experimental data, to provide proper augmentation levels. This modified model can be used for further studies and preliminary design work.

The above recommendations will result in an improved code with more general application to lift augmentation problems. Verification can be carried out by comparison with experimental data. In particular, studies at other angles of attack and jet splay angles should be conducted. The improved code will provide the added capability of investigating other phenomena of interest, such as the tip jet effect on wing drag and separation effects near the tip.

The preliminary study of spanwise blowing indicates the possibility of predicting the lift augmentation phenomena; however, as noted above, the grid was too coarse in this initial study to provide definitive results. Additional refinement to the grid for spanwise blowing applications can be accomplished using the knowledge gained in the tip blowing investigation. It is recommended that these modifications be accomplished and the improved code verified by comparison with available experimental information.

The expanded data base and the potential analytical capability resulting from this investigation provide a means to study the effects of tip blowing as a lift augmentation device on an advanced fighter aircraft. Such a preliminary design exercise is recommended to identify the feasibility of using tip blowing during various segments of a proposed mission; for example, there is an obvious use in STOL mission segments, but the concept may

also have interesting aerodynamic stability and control benefits during maneuvers.

REFERENCES

1. Wu, J. M., Vakili, A., and Chen, Z. L.: Investigation on the Effects of Discrete Wing Tip Jets, AIAA 83 0546, Jan. 1983.

2. Wu, J. M., Vakili, A., and Chen, Z. L.: Wing Tip Jets Aerodynamic Performance. 13th Congress of the International Council of the Aeronautical Sciences, Seattle, Wash., Aug. 1982.

3. Waugh, J. G., Kelly, H. R., and Fabula, A. G.: Recent Hydrodynamic Research at the Naval Ordnance Test Station (sub-section on Fin Lift Augmentation by Spanwise Fluid Ejection-Reprise of J.B. Brook's work). ONR-9, Vol. 2, p. 504, presented at 5th Navy Science Symp., Naval Academy, Annapolis, MD., Apr. 1961.

4. Carafoli, E. and Camarsescu, N.: New Researches on Small Span-Chord Ratio Wings with Lateral Jets. Studii si Cercetari de Mecanica Aplicata, 1970, Vol. 29, No. 4, pp. 947-962, also available in English from NTIS as AD-733858.

5. Lloyd, A.: The Effect of Spanwise Blowing on the Aerodynamic Characteristics of Low Aspect Ratio Wings. Von Karman Institute for Fluid Dynamics Project Report 1963-90, 1963.

6. Schwind, R. G. and Briggs, M. M.: Effects of Blowing Spanwise From the Tips of Low-Aspect Ratio Wings of Varying Taper Ratio, with Application to Improving STOL Capability of Fighter Aircraft. AFOSR-TR-83-1045, Feb. 1983.

7. Briggs, M. M. and Schwind, R. G.: Augmentation of Fighter Aircraft Lift and STOL Capability by Blowing Outboard from the Wing Tips, AIAA 83-0078, Jan. 1983.

8. Bean, Howard S., editor: Fluid Meters, 6th ed. ASME, New York, 1971.

9. Tavella, D. A. and Roberts, L.: The Concept of Tip Blowing, AIAA 85-5000, Oct. 1985.

10. Lee, C. S., Tavella, D, Wood, N. J., and Roberts, L.: Flow Structure of Lateral Wing-Tip Blowing, AIAA 86-1810, June 1986.

11. Travella, D. A., Wood, N. J., Lee, S. S., and Roberts, L.: Two Blowing Concepts for Roll and Lateral Control of Aircraft. Stanford University JIAA TR-75, October 1986.

REFERENCES (continued)

12. Childs, R. E.: Lift Augmentation Via Spanwise Tip Blowing: A Numerical Study, AIAA 86-0474, Jan. 1986.

13. MacCormack, R. W.: The Effect of Viscosity in Hypervelocity Impact Cratering, AIAA 69-345.

14. Tavella, D., Wood, N., and Harrits, P. Measurements on Wing-Tip Blowing. Stanford University JIAA TR-64, 1985.

15. Tavella, D. A., Wood, N. J., and Harrits, P.: Influence of Tip Blowing on Rectangular Wings, AIAA 85-5001, Oct. 1985.

16. Pulliam, T. H. and Steger, J. L.: On Implicit Finite-Difference Simulations of Three-Dimensional Flow, AIAA 78-10, Jan. 1978.

17. Pulliam, T. H.: Euler and Thin Layer Navier-Stokes Codes: ARC2D, ARC3D, Notes for Computational Fluid Dynamics User's Workshop, The University of Tennessee Space Institute, Tullahoma, TN., March 12-16, 1984.

18. Beam, R. and Warming, R. F.: An Implicit Factored Scheme for the Compressible Navier-Stokes Equations, AIAA 77-645, June 1977.

19. Pulliam, T. H. and Chaussee, D. S.: A Diagonal Form of an Implicit Approximate-Factorization Algorithm, J. of Comp. Phys., Vol. 39, No. 2, 1981, pp. 347-363.

20. Pulliam, T. H.: Artificial Dissipation Models for the Euler Equations, AIAA 85-0438, Jan. 1985.

21. Hinson, B. L. and Burdges, K. P.: Acquisition and Application of Transonic Wing and Far-Field Test Data for Three-Dimensional Computational Method Evaluation, Lockheed-Georgia, Co., AFOSR-TR 80-0421, 1980.

22. Hinson, B. L. and Burdges, K.P.: Acquisition and Application of Transonic Wing and Far-Field Test Data for Three-Dimensional Computational Method Evaluation, Vol. II, Appendix B, Experimental Data, Lockheed-Georgia Co., AFOSR-TR 80-0422, 1980.

23. Keener, E. R.: Pressure-Distribution Measurements on a Transonic Low-Aspect Ratio Wing., NASA TM 86683, Sept. 1985.

REFERENCES (concluded)

24. Hinson, B. L. and Burdges, K. P.: An Evaluation of Three-Dimensional Transonic Codes Using New Correlation-Tailored Test Data, AIAA 80-0003, Jan. 1980.

25. Mansour, N. N.: Computation of the Tip Vortex Off a Low-Aspect Ratio Wing, AIAA J., Vol. 23, No. 8, 1985, pp. 1143-1149.

26. Kaynak, U., Holst, T., Cantwell, B. J. and Sorenson, R. J.: Numerical Simulation of Transonic Separated Flows Over Low-Aspect Ratio Wings, AIAA 86-0508, Jan. 1986.

27. Srinivasan, G. R., McCroskey, W. J., Baeder, J. D., and Edwards, T. A.: Numerical Simulation of Tip Vortices in Subsonic and Transonic Flows, AIAA 86-1095, May 1986.

28. Baldwin, B. S. and Lomax, H.: Thin Layer Approximation and Algebraic Model for Separated Turbulent Flows, AIAA 78-257, Jan. 1978.

29. Rodi, W.: Turbulence Models and Their Application in Hydraulics, Intl. Assoc. for Hydraulics Research, Delft, 1980.

30. Tennekes, H. and Lumley, J. L.: A First Course in Turbulence., MIT Press, Cambridge, Mass, 1972.

31. Chakravarty, S. R., Szema, K. Y., Goldber, U. C., and Gorski, J. J.: Application of a New Class of High Accuracy TVD Schemes to the Navier-Stokes Equations, AIAA 85-0165, Jan. 1985.

LIST OF SYMBOLS

a	speed of sound
$b/2$	wing semispan
c	local wing chord
c_R	root chord
c_T	tip chord
C_D	wing drag coefficient
C_L	wing lift coefficient
C_{LB}	baseline wing lift coefficient, no blowing
C_{L_o}	wing lift coefficient with no blowing
C_p	pressure coefficient, $(p-p_\infty)/q_\infty$
C_μ	jet momentum coefficient, $\dot{m}_j v_j/(q_\infty S)$
D_e, D_i	explicit, implicit dissipation terms in Eqs. (15,16)
e	total energy
$\hat{E}$, $\hat{F}$, $\hat{G}$	transformed, convective flux vectors in Eq. (2)
$\hat{E}_v$, $\hat{F}_v$, $\hat{G}_v$	transformed, diffusive flux vectors in Eq. (2)
J, J^{-1}	metric and inverse-metric Jacobians, respectively
h	spatially-varying time step
ℓ_m	mixing length
$\dot{m}_j$	jet mass flowrate
M_∞	Mach number
p	static pressure
q_∞	freestream dynamic head, $\frac{1}{2}\rho_\infty\lvert V_\infty^2\rvert$
$\hat{Q}$	conserved-variable vector in Eq. (2)
S	wing area
$\hat{S}$	thin-layer viscous flux vector in Eq. (16)
t, τ	time
v_j	jet exit-plane velocity
u,v,w	Cartesian velocity components in x,y,z-directions, respectively

LIST OF SYMBOLS (concluded)

U, V, W	velocity components in computational space, in x,y,z-directions, respectively
V_∞	free stream velocity
x, y, z	physical coordinates
Λ	wing leading edge sweep angle
α	angle of attack
γ	ratio of specific heats
δ	shear layer thickness parameter
δ_ξ	finite-difference approximation to first derivative in ξ-direction
ΔC_L	increment in lift coefficient
κ_2, κ_4	second- and fourth-order coefficients of dissipation terms in Eqs. (15, 16)
ν_T	turbulent eddy viscosity
ξ, η, ζ	transformed coordinates
ρ	fluid density
ω, Γ	vorticity

TABLE 1. Small Scale Wing Geometry

Description	Wing 1	Wing 2	Wing 3
Planform	Rectangular	Swept	Swept
Section	NACA 0015	NACA 0015	NACA 64 mean line
Semispan, b/2 (in.)	8.40	8.35	8.35
Planform Area, S/2 ($in.^2$)	70.05	69.65	69.65
Rootchord, c_R (in.)	8.36	11.13	11.13
Tip Chord, c_T (in.)	8.36	5.55	5.55
LE. Sweep Angle	0°	33.8°	33.8°
Thickness at Root (in.)	1.25	1.67	1.67
Aspect Ratio	2.0	2.0	2.0

TABLE 2. Measured Blowing Angles for Small-Scale Wings

Wing No.	Sweep Angle, Deg. forward	middle	aft	Dihedral Angle, Deg. forward	middle	aft
1-Tip 1	17	30	58	15	15	15
Tip 2	28	28	58	0	0	15
Tip 3	28	31	55	0	0	-15
Tip 4	-	0	-	-	0	-
2-Tip 1	22	40	62	15	15	15
Tip 2	20	34	65	0	0	15
Tip 3	-	0	-	-	0	-
Tip 4	-	0	-	-	0	-
3	All Angles Zero					

NOTES:

1. Nonzero values of sweep angles for the forward, middle, and aft slots are designed to be 30°, 45°, 60°, respectively.

2. Nonzero values of dihedral angles are ±15°, and the actual blowing angles agreed with the design angle in each case.

3. Positive dihedral angles blow upward, and positive sweep angles blow to the rear.

TABLE 3. Data Channels

Channel No.	Symbol	Function
1	PDB	Orifice Δp
2	PTB	Orifice total pressure
3	TB	Orifice total temperature
4	PTC	Wing cavity pressure
5	PDW	Test section P_{static} relative to plenum
6	PSMA	Test section P_{static} relative to atmosphere
7	TW	Tunnel air temperature
8	Fz	Force normal to chord plane
9	Fy	Force parallel to wing chord line
10	My	Pitching moment about spanwise axis
11	Mz	Yawing moment about normal to chord plane
12	Mx	Root bending moment about chord axis
13	α	Angle of attack
14	-----	Not used
15	Fx2	Spanwise load cell, test fixture
16	Fx1	Spanwise load cell, outside of tunnel

TABLE 4. Pressure Tap Locations on the Wing Upper Surface

	2y/b						
	0.150	0.296	0.500	0.697	0.800	0.894	0.950
x/c	0.02	0.02	0.02	0.02	0.02	0.02	0.02
	0.05	0.05	0.05	0.05	0.05	0.05	0.05
			0.07				
	0.10	0.10	0.10	0.10	0.10	0.10	0.10
	0.15	0.15	0.15	0.15	0.15	0.15	0.15
	0.20	0.20	0.20	0.20	0.20	0.20	0.20
			0.25			0.25	
	0.30	0.30	0.30	0.30	0.30	0.30	0.30
			0.35			0.35	
	0.40	0.40	0.40	0.40	0.40	0.40	0.40
			0.45			0.45	
	0.50	0.50	0.50	0.50	0.50	0.50	0.50
			0.55				
	0.60	0.60	0.60	0.60	0.60	0.60	0.60
			0.65				
	0.70	0.70	0.70	0.70	0.70	0.70	0.70
			0.75				
	0.80	0.80	0.80	0.80	0.80	0.80	0.80
			0.85				
	0.90	0.90	0.90	0.90	0.90	0.90	0.90
			0.95				

TABLE 5. Pressure Tap Locations on The Wing Lower Surface

	2y/b						
	0.150	0.296	0.500	0.697	0.800	0.894	0.950
x/c	0.05	0.05	0.02 0.05 0.07	0.05	0.05	0.05	0.05
	0.10	0.10	0.10 0.15	0.10	0.10 0.15	0.10	0.10
	0.20	0.20	0.20 0.25	0.20	0.20	0.20	0.20
	0.30	0.30	0.30 0.35	0.30	0.30	0.30	0.30
	0.40	0.40	0.40 0.45	0.40	0.40	0.40	0.40
	0.50	0.50	0.50 0.55	0.50	0.50	0.50	0.50
	0.60	0.60	0.60 0.65	0.60	0.60	0.60	0.60
	0.70	0.70	0.70 0.75	0.70	0.70	0.70	0.70
	0.80	0.80	0.80 0.85	0.80	0.80	0.80	0.80
	0.90	0.90	0.90 0.95	0.90	0.90	0.90	0.90

TABLE 6. Simulated and Experimental Tip Jet Geometries*

	Jet	c_j/c_T	ℓ_j/c_T	Jet Area / Wing Area
simulated	Short	0.13	0.23	$1.6\ 10^{-3}$
	Long	0.13	0.65	$3.7\ 10^{-3}$
experiment	Short (Tip #4)	0.28	0.29	$3.3\ 10^{-4}$
	Long (Tip #2)	0.07	0.76	$3.3\ 10^{-4}$

*Refer to Figure 53

TABLE 7. Computational Results for Tip-Jet On*

Case	Jet	C_μ	Velocity Ratio**	C_L	ΔC_L	$\Delta C_L/C_{L_o}$ x 100%	Comments
0	Off	0.0	.0	0.392	0.	0.	Baseline
1	Long	0.052	2.2	0.403	0.011	2.8	Laminar
2	"	0.052	2.2	0.416	0.024	6.1	Velocity Ratio Effect
3	"	0.177	4	0.429	0.037	9.4	" "
3a	"	0.177	4	0.726	0.087	13.6	α = 10° (C_{L_o} = 0.639)
4	"	0.472	8	0.434	0.042	10.7	Velocity Ratio Effect
5	Short	0.052	4	0.404	0.012	3.1	Jet Length Effect
6	"	0.104	4	0.408	0.016	4.1	C_μ Effect
7	Long, Splay = 30°	0.177	4	0.481	0.089	22.7	Splay Effect

**v_{jet}/V_∞

*All cases at α = 5°, except Case 3a.

TABLE 8. Experimental Results for Tip-Jet On

Case	Jet	Tip #	Run #	C_μ	Velocity Ratio	C_L	ΔC_L	$\Delta C_L/C_{L_o}$ x 100%
0'	Off	0	66	0.0	0.0	0.32	0.0	0.0
2'	Long	2	32	0.018	3.4	0.36	0.04	12.5
3'	Long	2	35	0.052	5.5	0.40	0.08	25.0
5'	Short	4	43	0.052	5.5	0.37	0.05	15.6
7'	Short, Splay = 30°	6	57	0.065	5.7	0.46	0.14	44.0

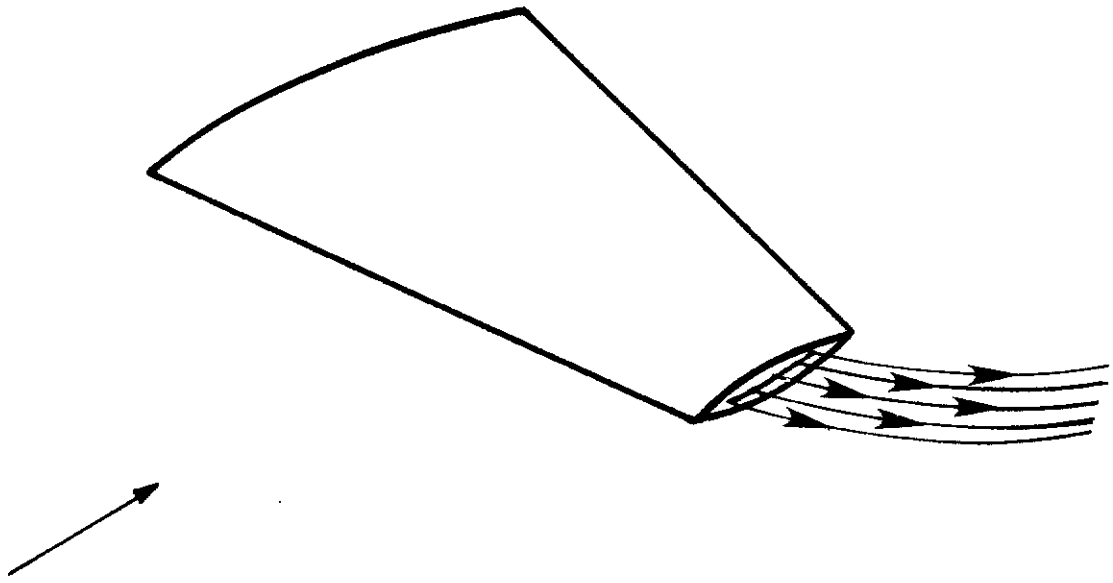

Figure 1.- Wing Tip Blowing.

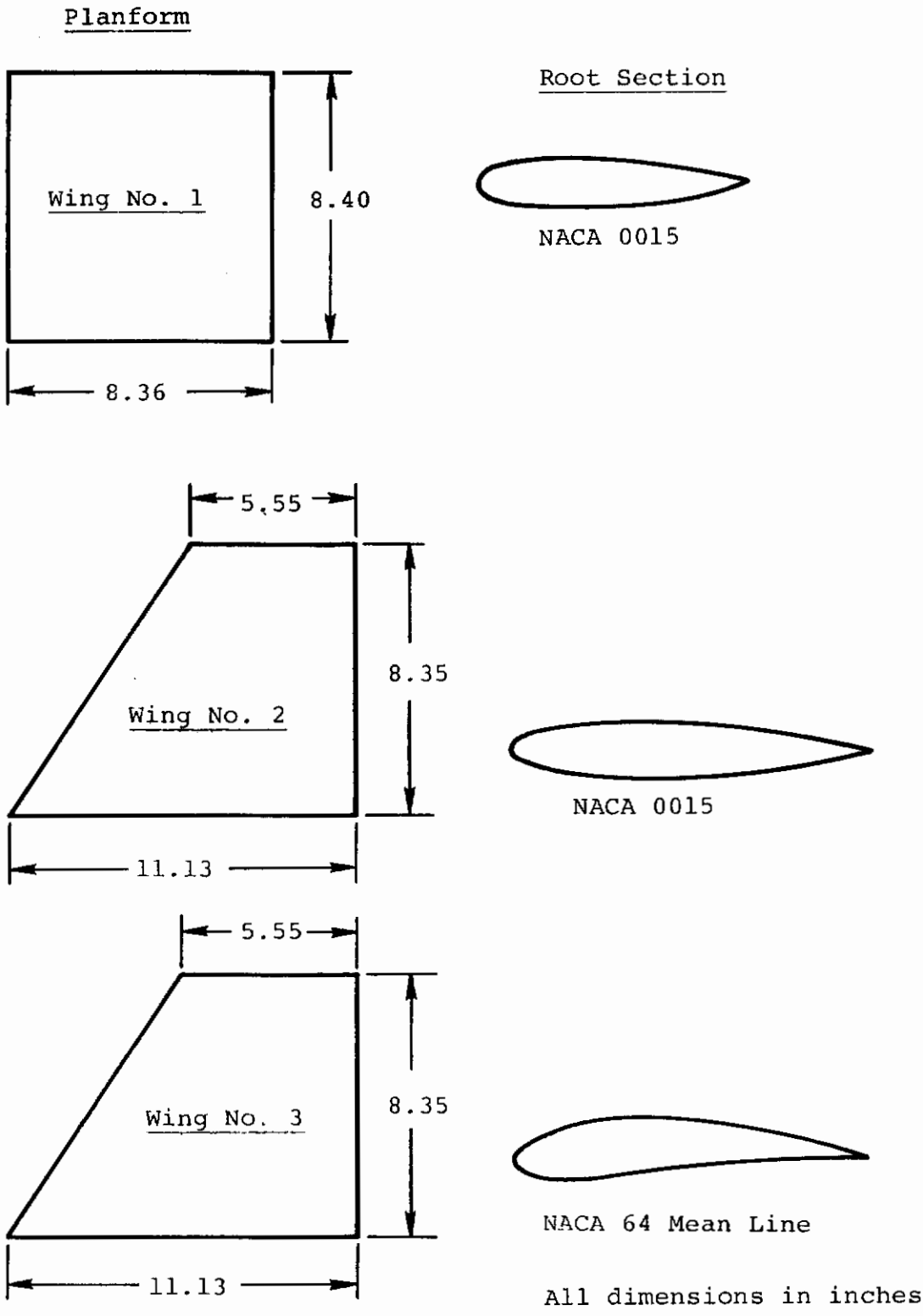

Figure 2.- Sketch of wings tested.

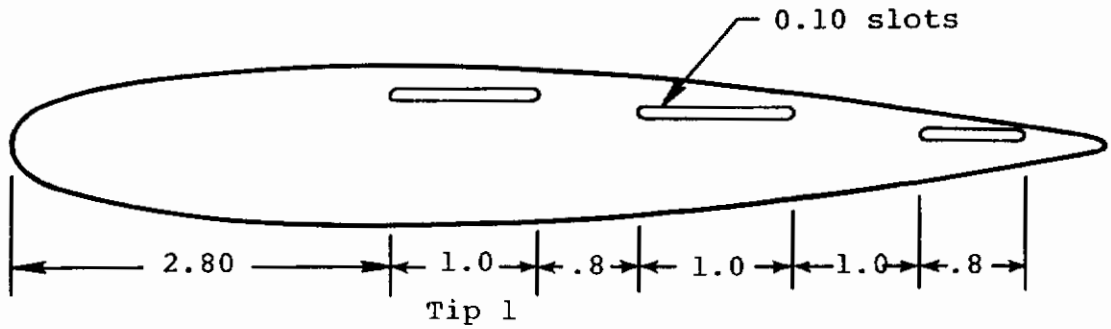

Tip 1

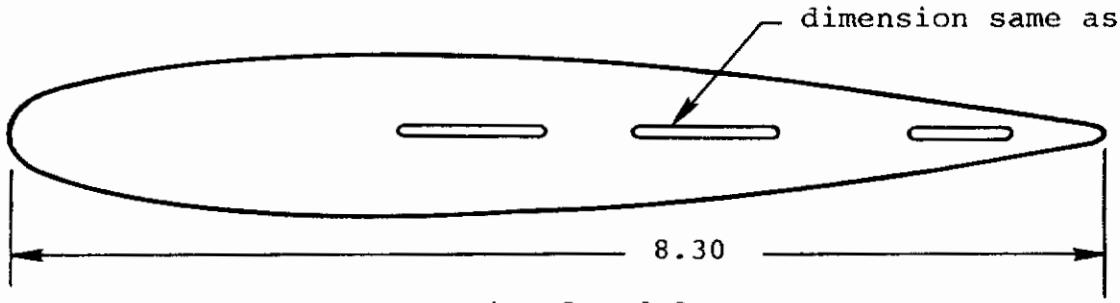

Tips 2 and 3

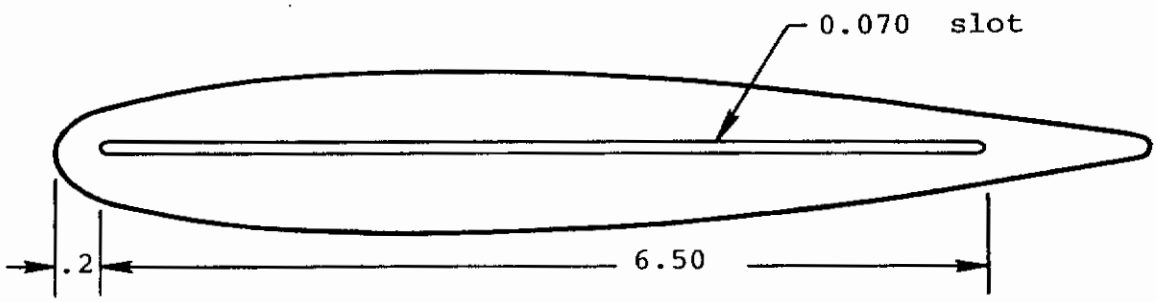

Tip 4

All dimensions in inches

Figure 3.- Tips for rectangular Wing No. 1.

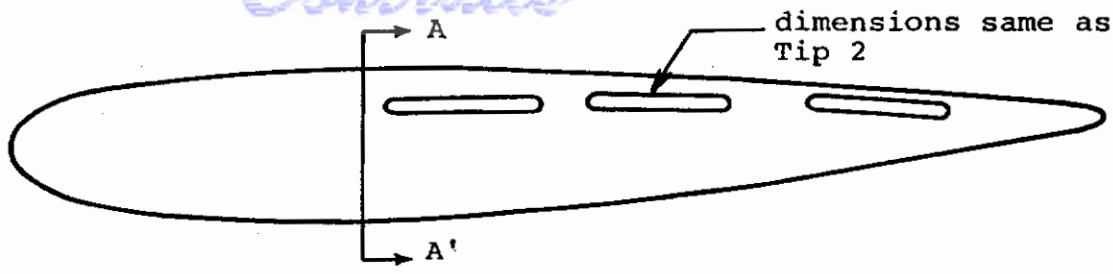

Tip 1

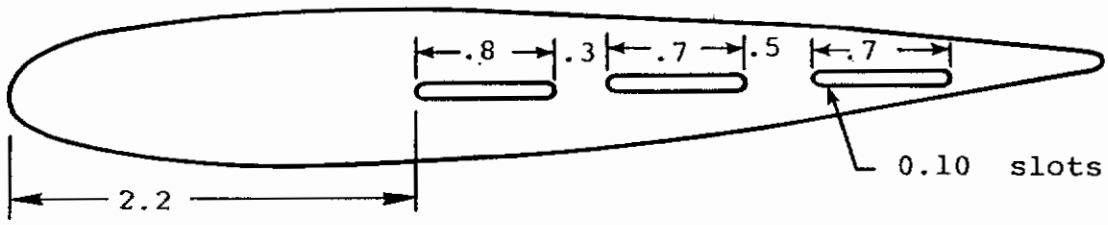

Tip 2

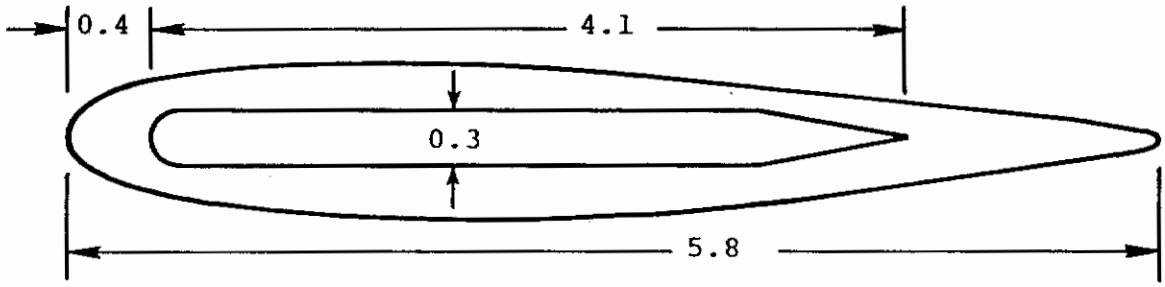

Tip 3

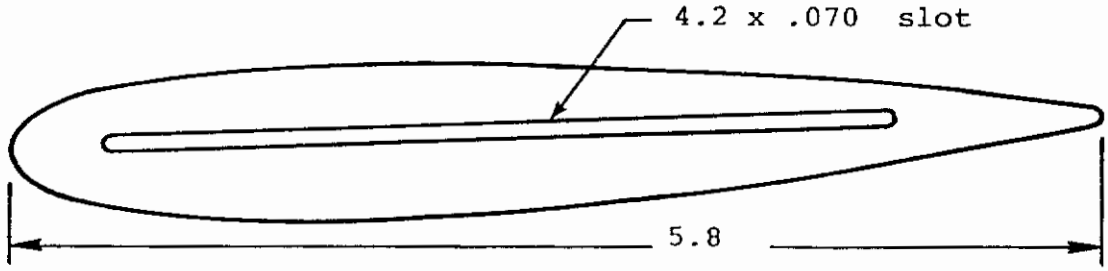

Tip 4

All dimensions in inche

Figure 4.- Tips for swept Wing No. 2

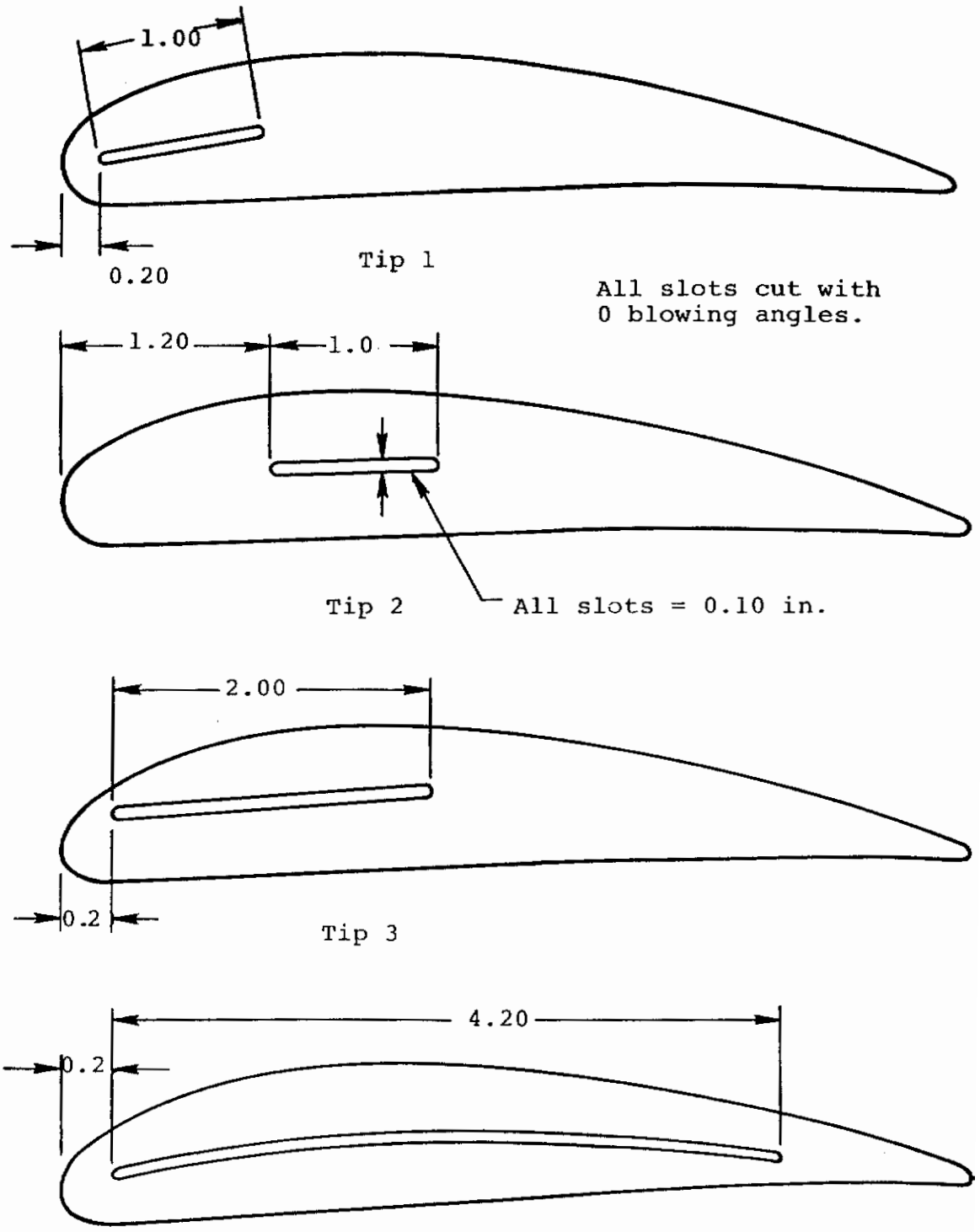

Figure 5.- Tips for swept, cambered Wing No. 3.

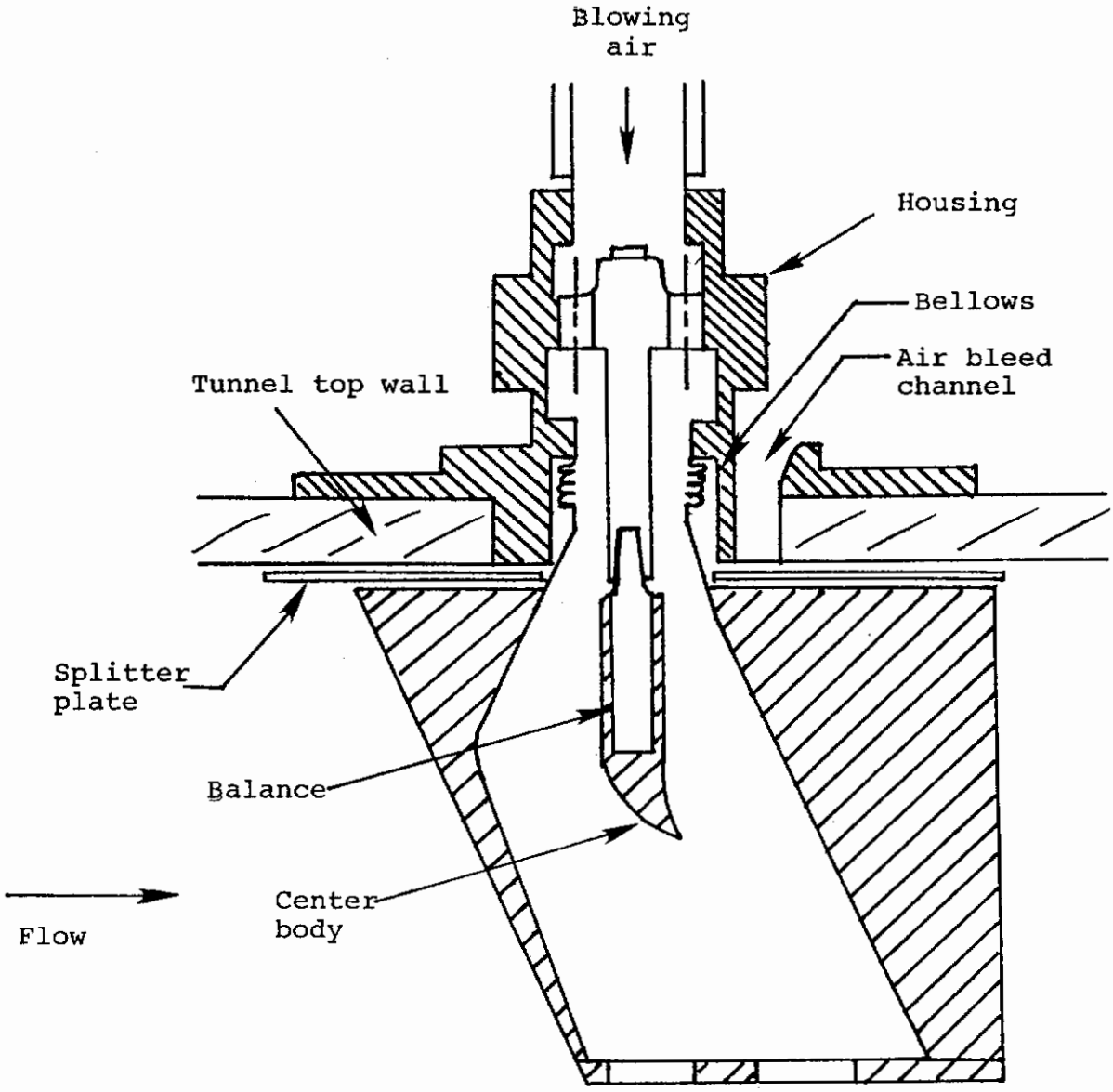

Figure 6.- Tunnel installation of wing and balance

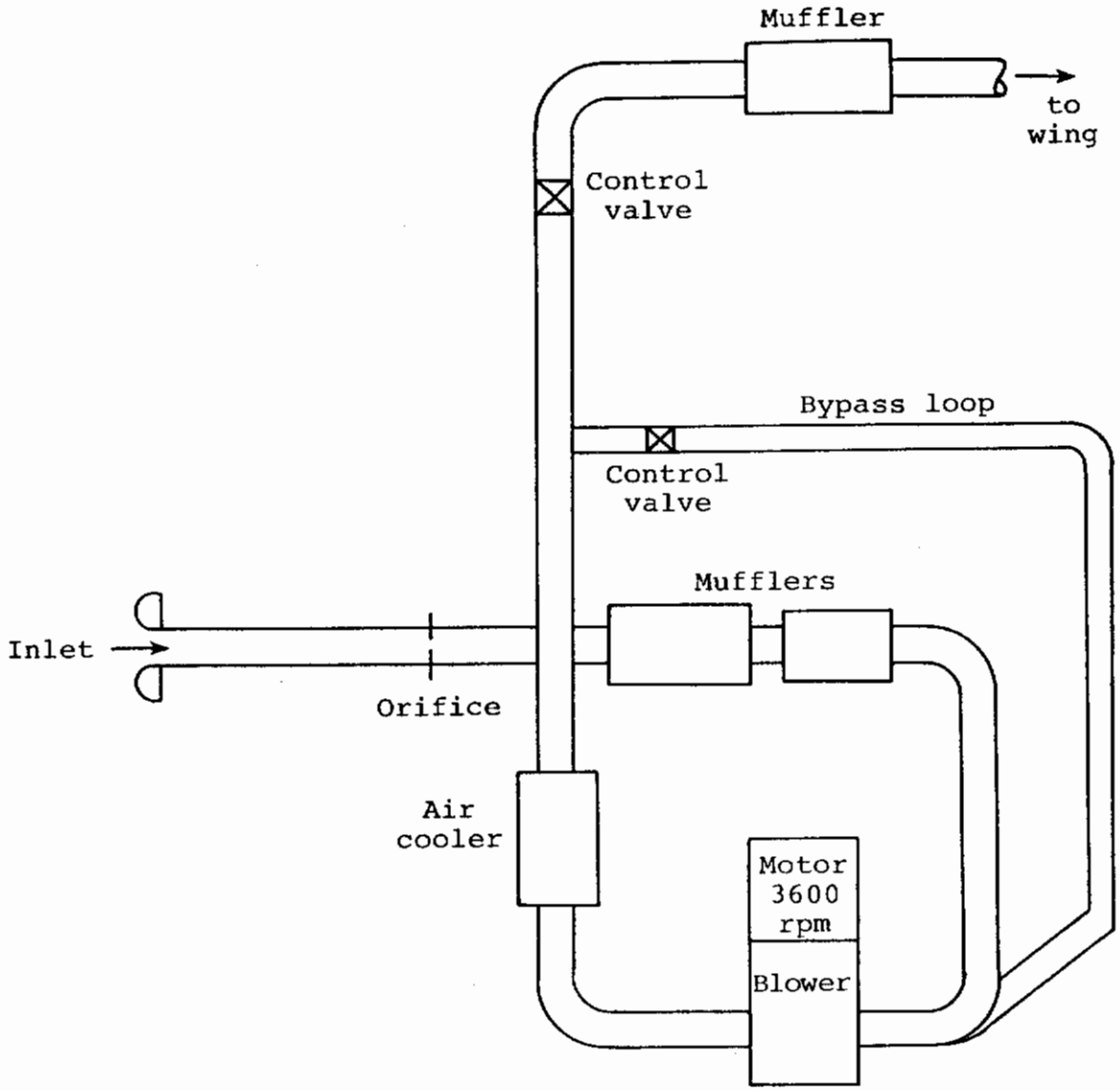

Figure 7.- Configuration of blowing system

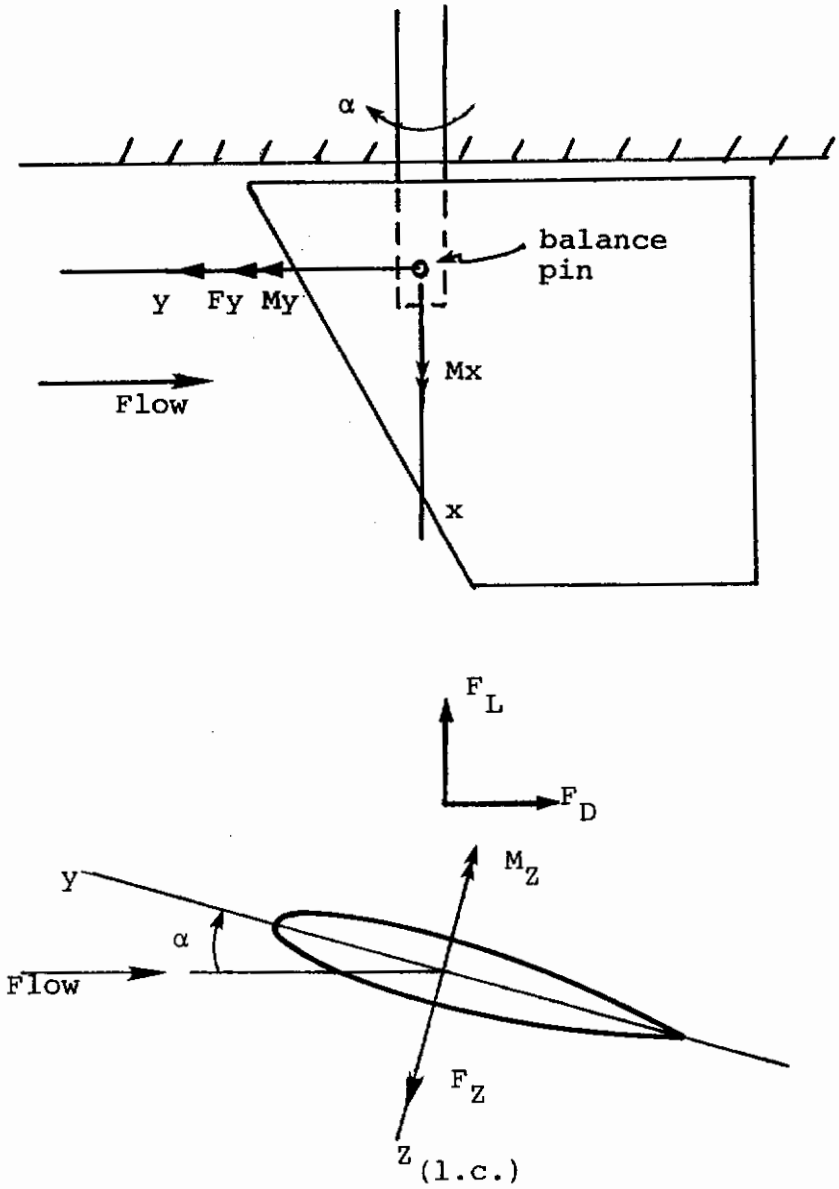

Figure 8.- Force and moment coordinate systems

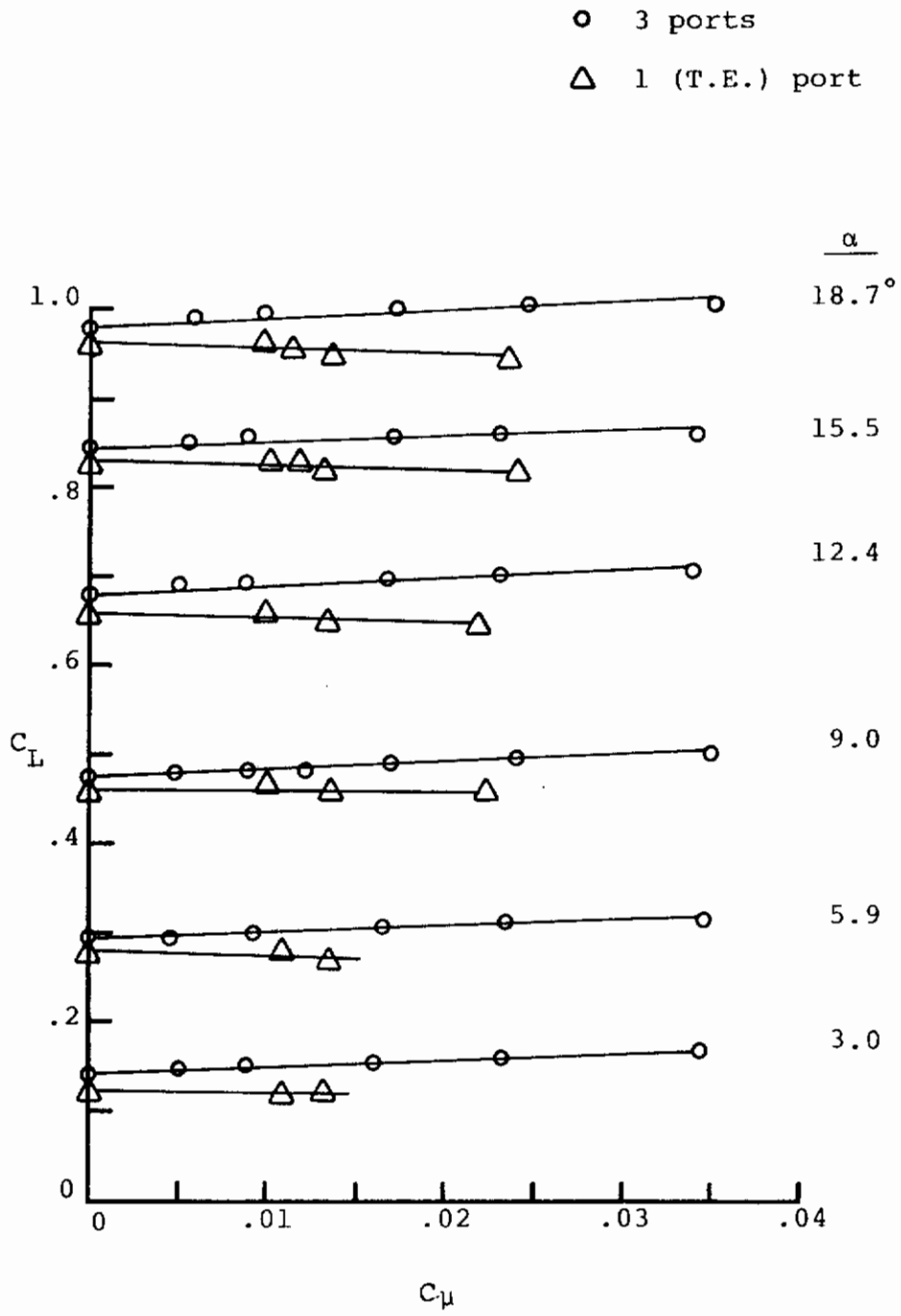

(a) Lift Coefficient

Figure 9.- Measured lift and drag coefficients on Wing No. 1 with Tip 1.

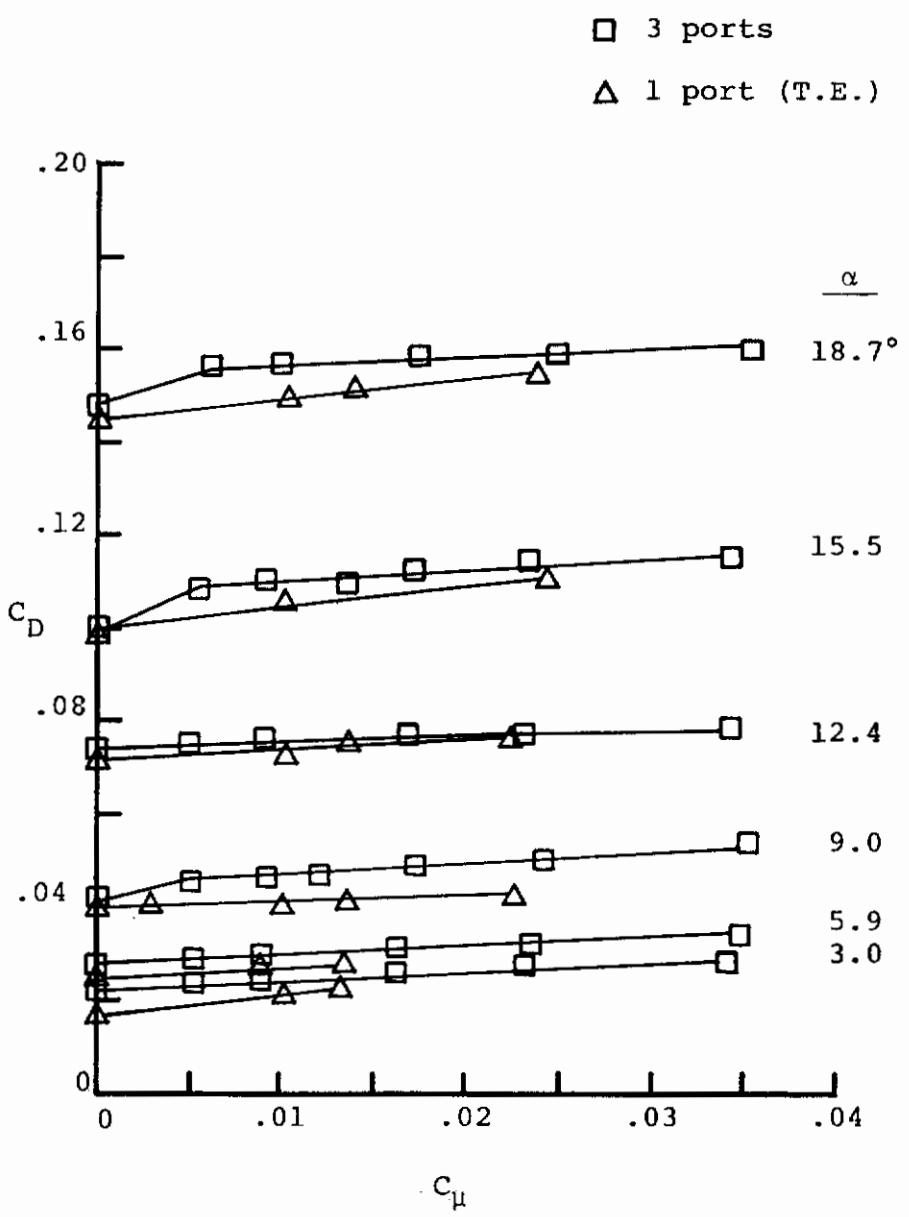

(b) Drag Coefficient

Figure 9.- Concluded.

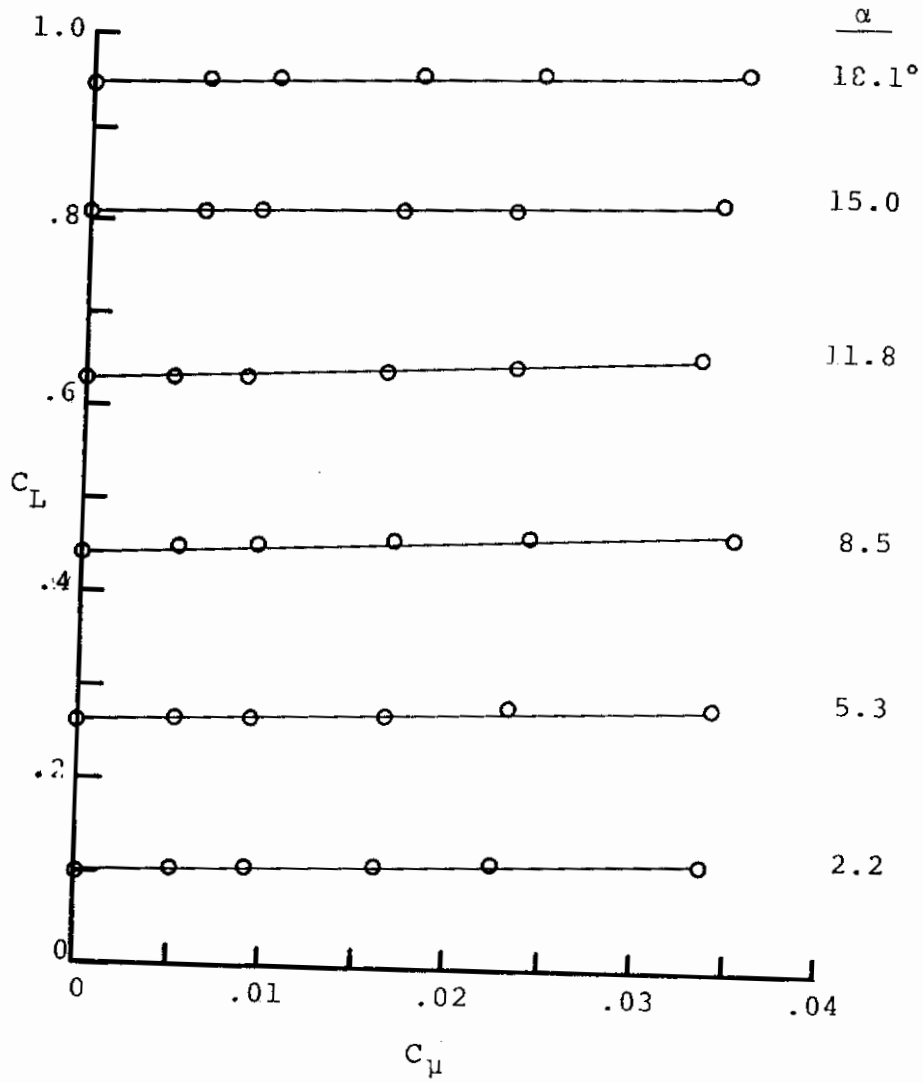

(a) Lift Coefficient

Figure 10.- Measured lift and drag coefficients on Wing No. 1 with Tip 2.

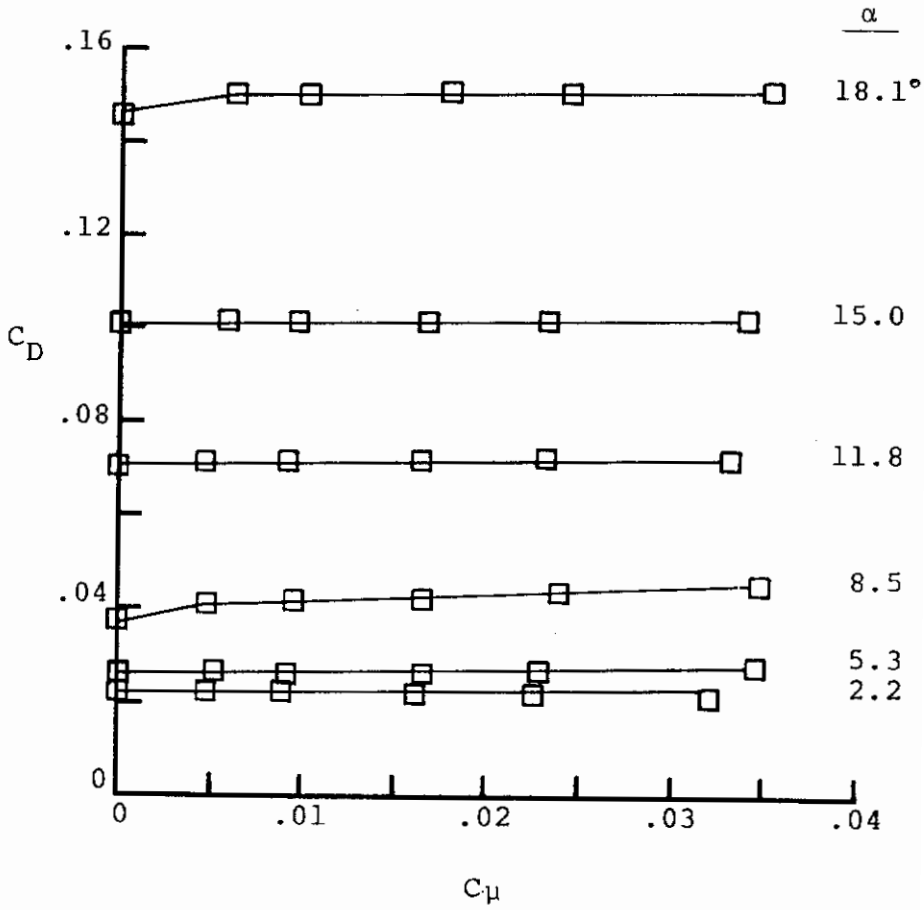

(b) Drag Coefficient

Figure 10.- Concluded.

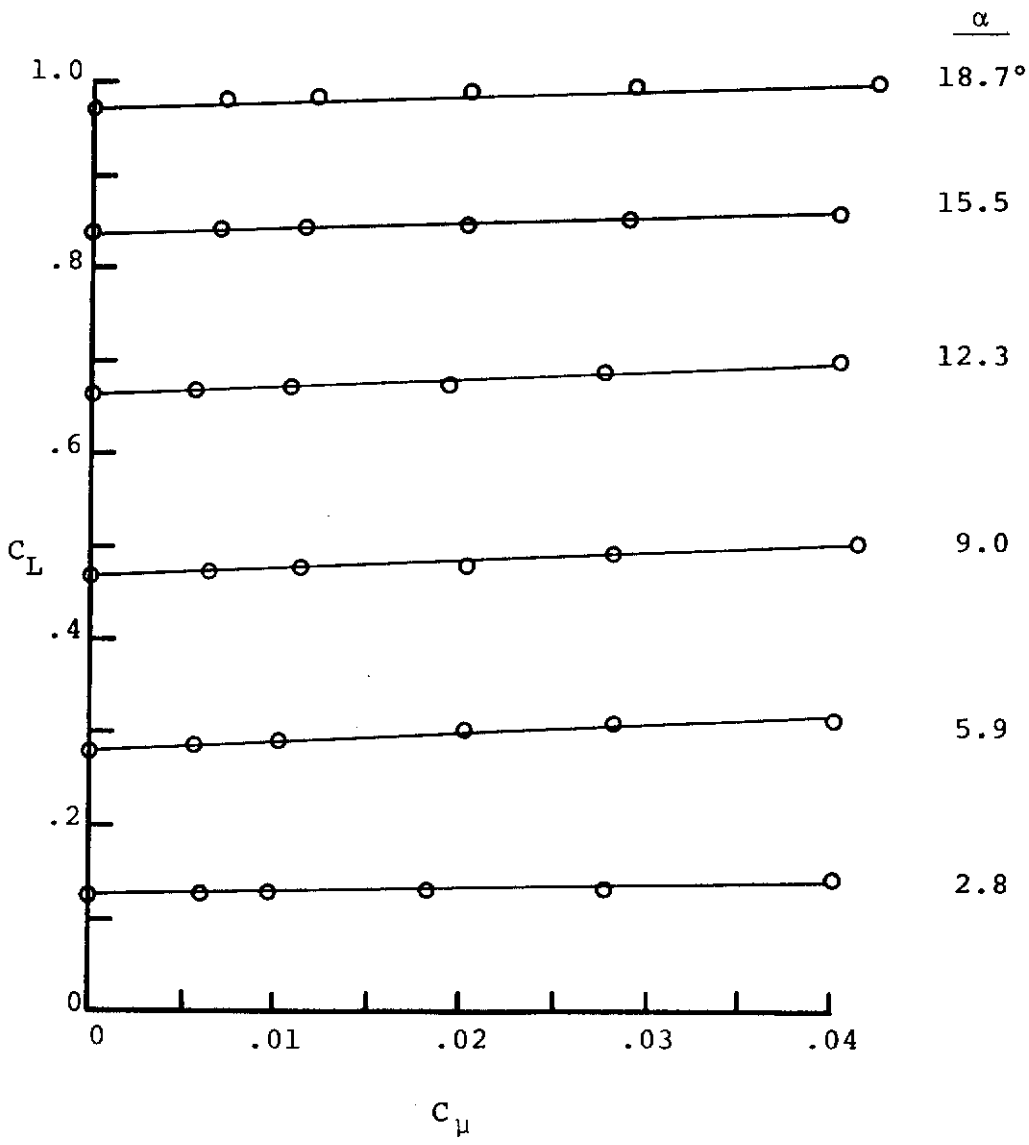

(a) Lift Coefficient

Figure 11.- Measured lift and drag coefficients on Wing No. 1 with Tip 3.

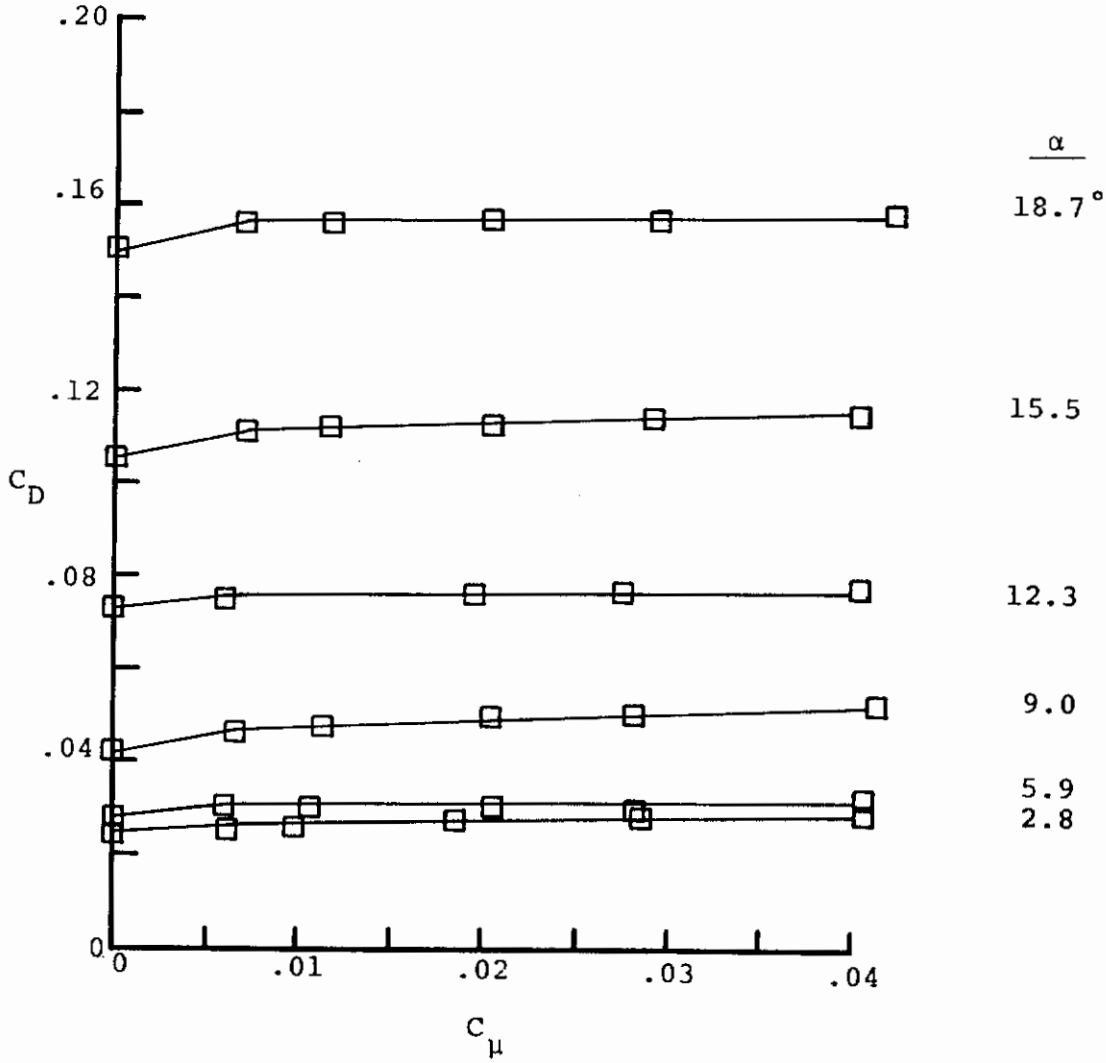

(b) Drag Coefficient

Figure 11.- Concluded.

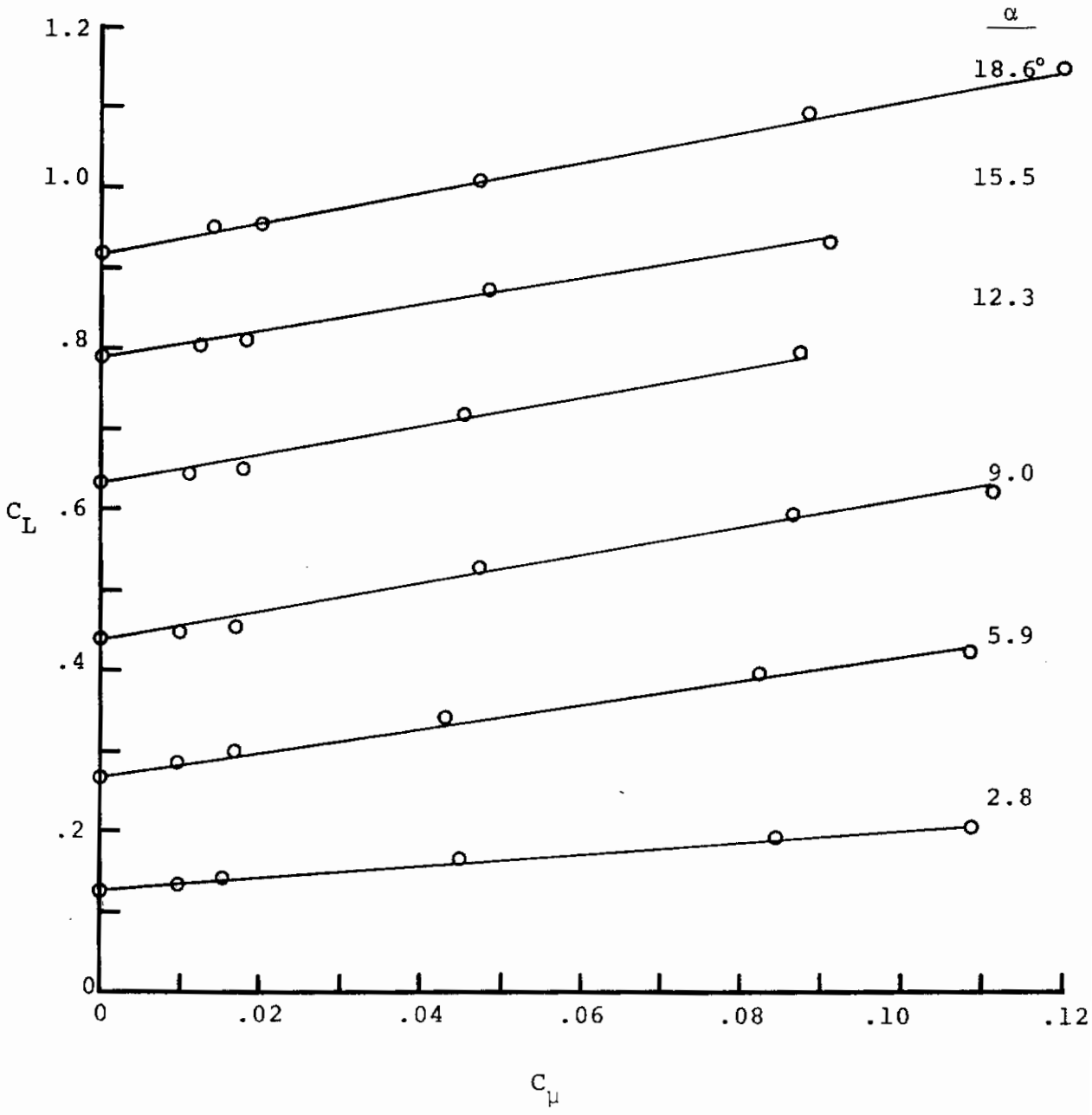

(a) Lift Coefficient

Figure 12.- Measured lift and drag coefficients on Wing No. 1 with Tip 4.

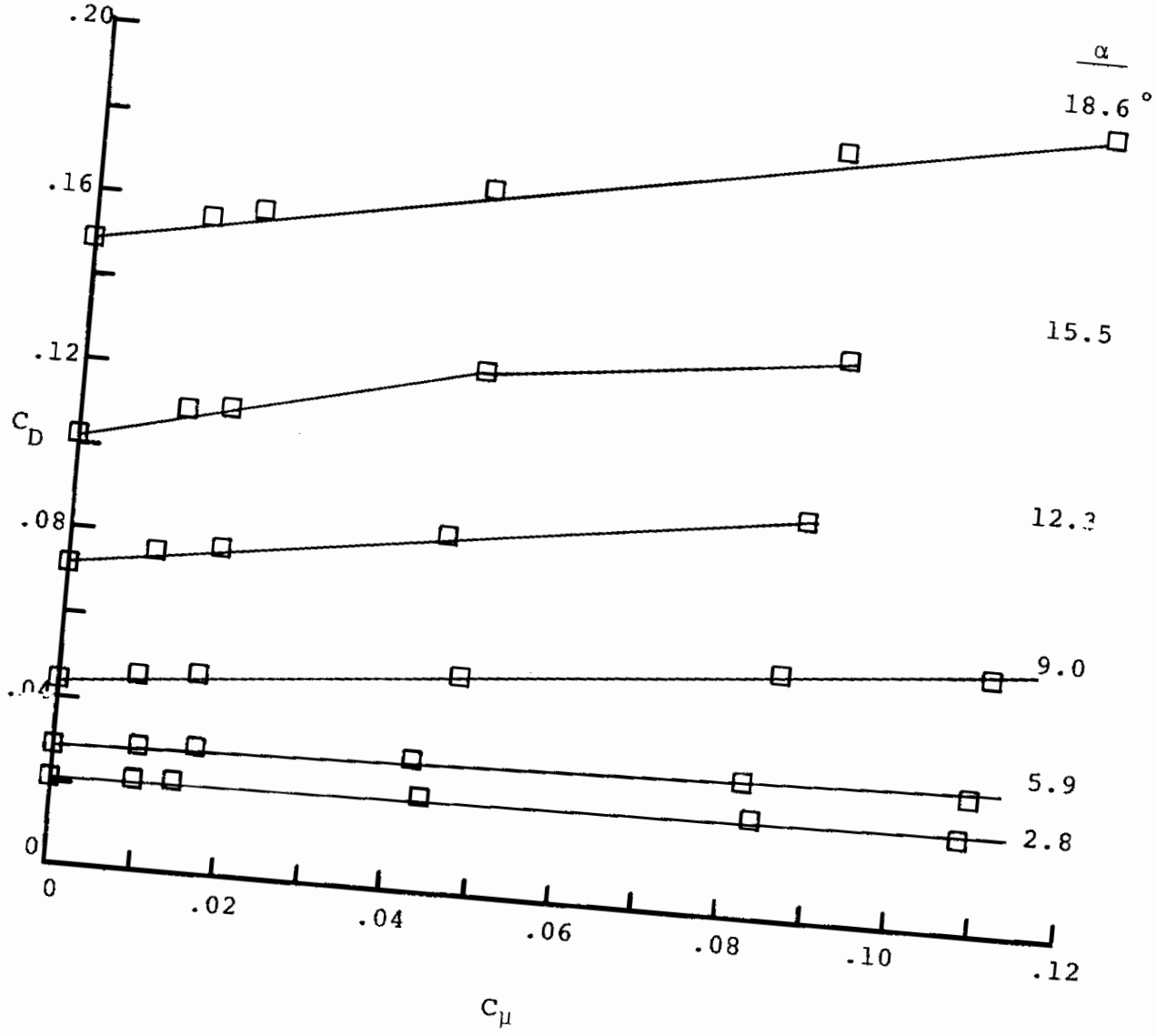

(b) Drag Coefficient

Figure 12.- Concluded.

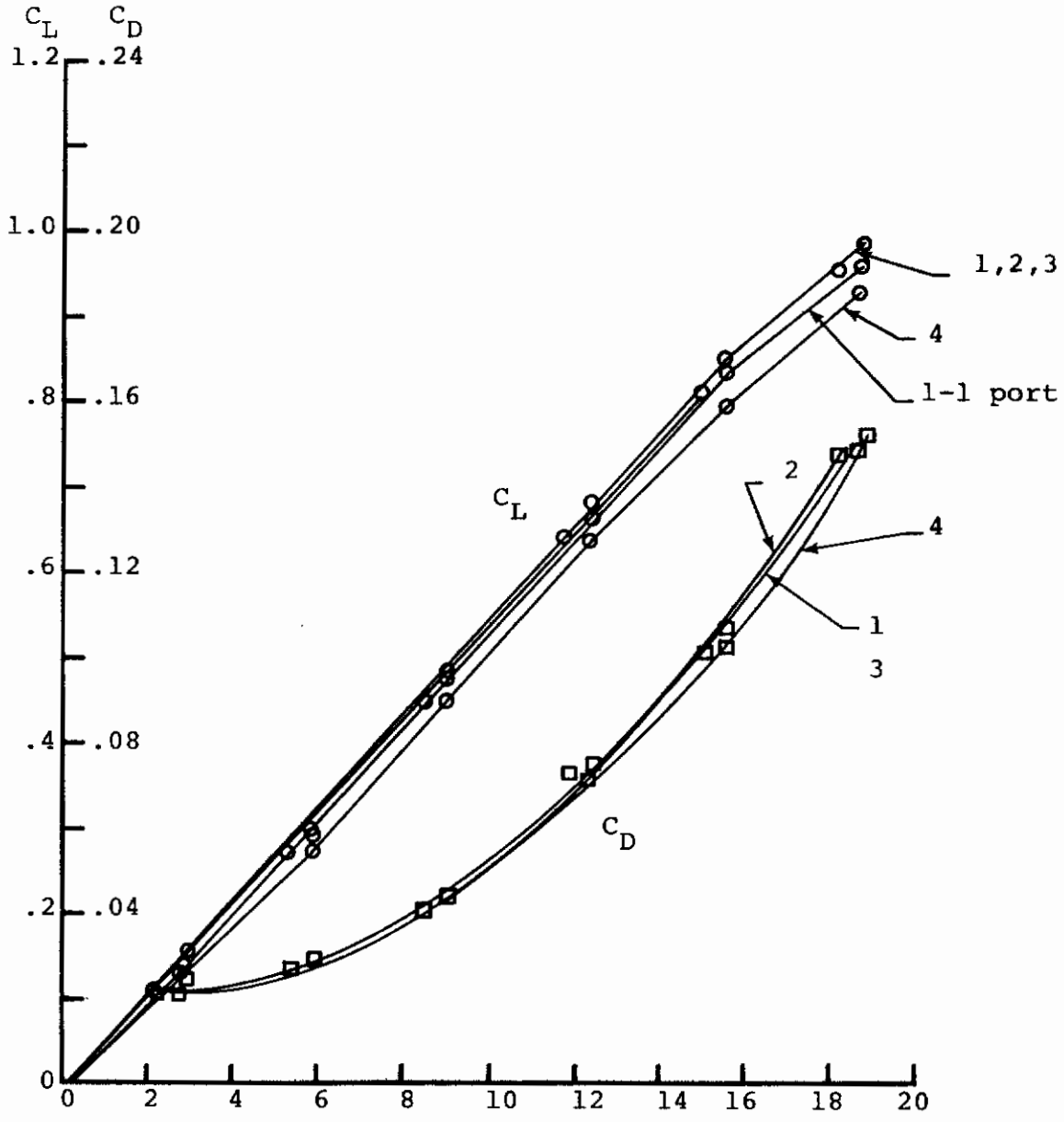

(a) $C_\mu = 0.0$

Figure 13.- Effect of tip geometry on measured lift and and drag coefficients on Wing No. 1.

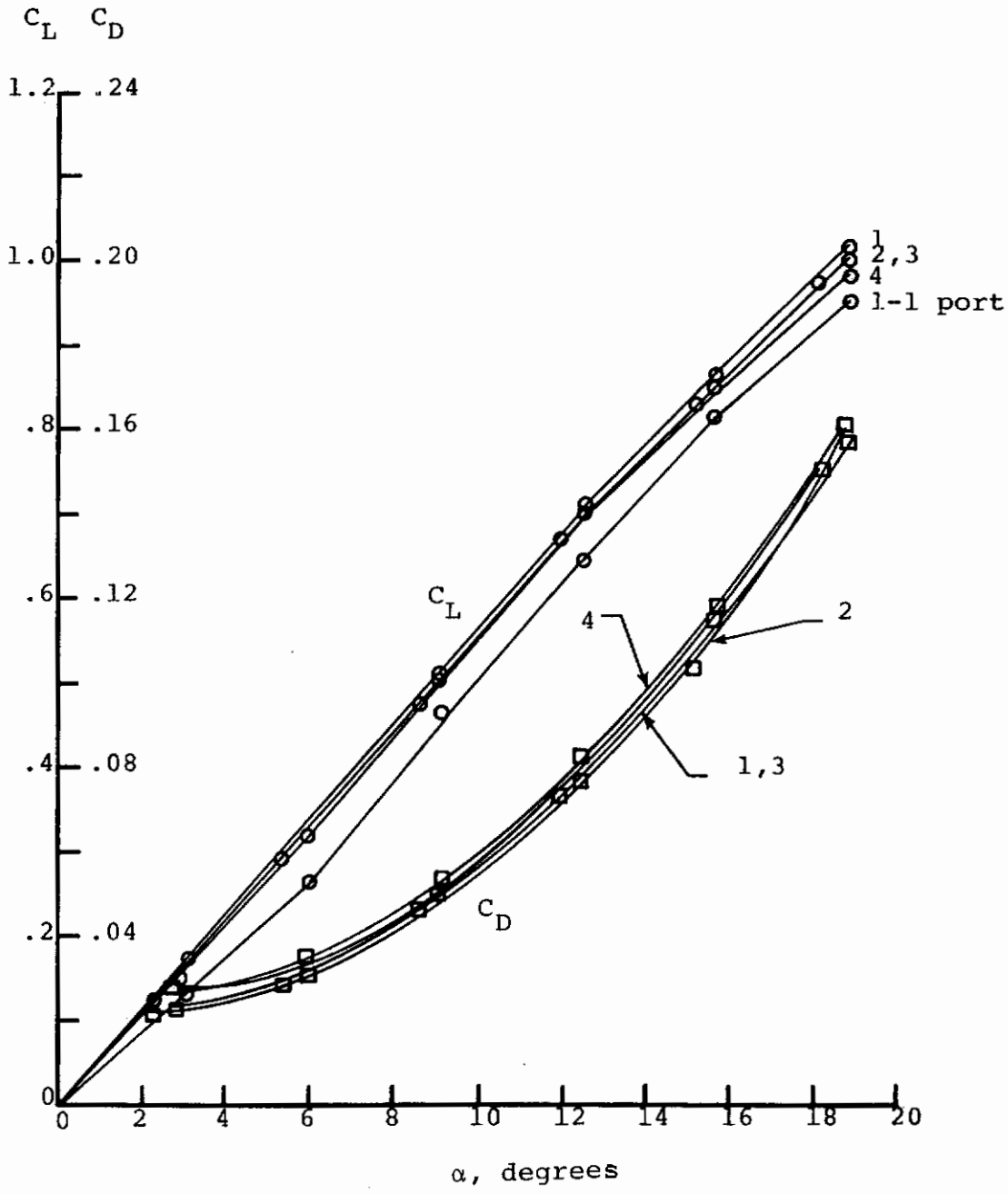

(b) $C_\mu = 0.035$

Figure 13.- Concluded.

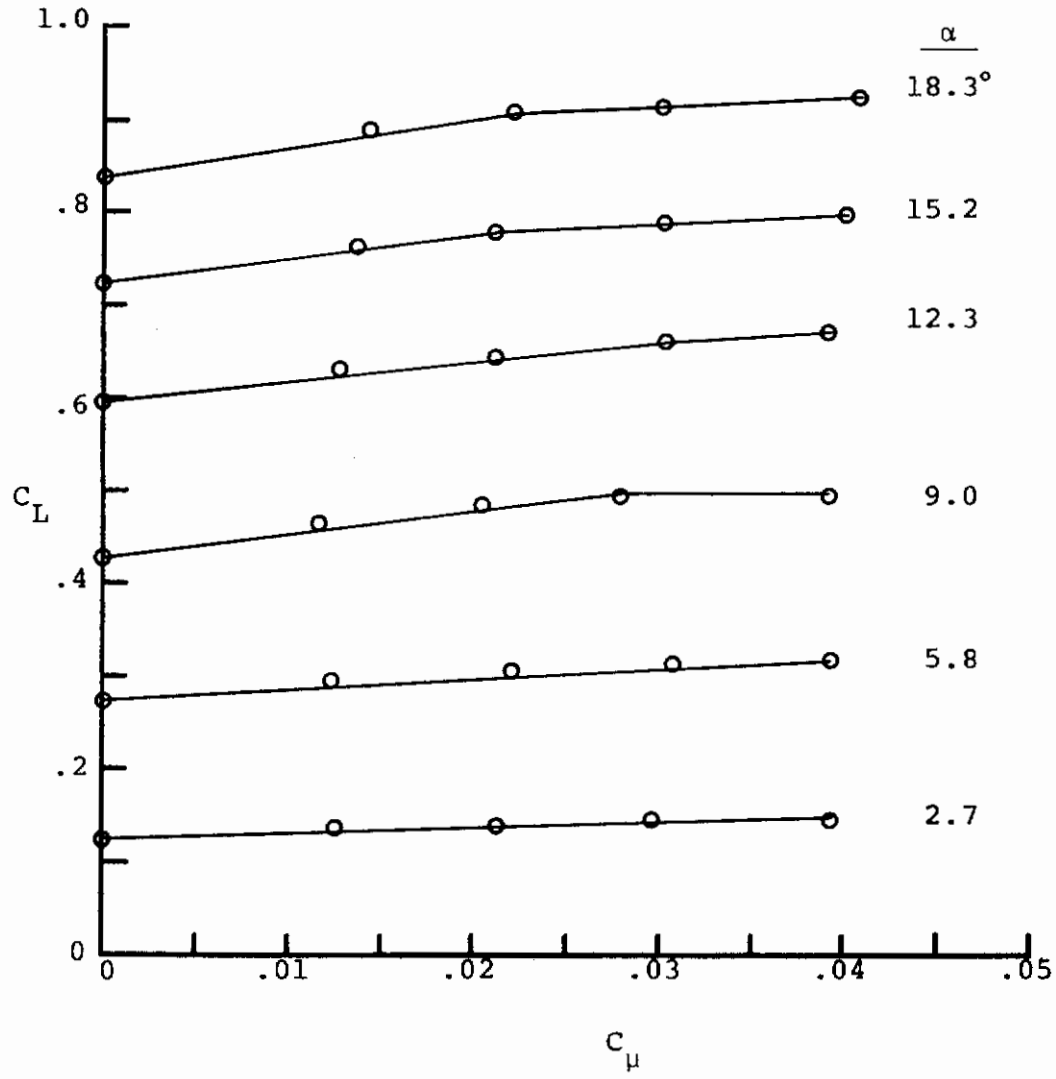

(a) Lift Coefficient

Figure 14.- Measured lift and drag coefficients on Wing No. 2 with Tip 1.

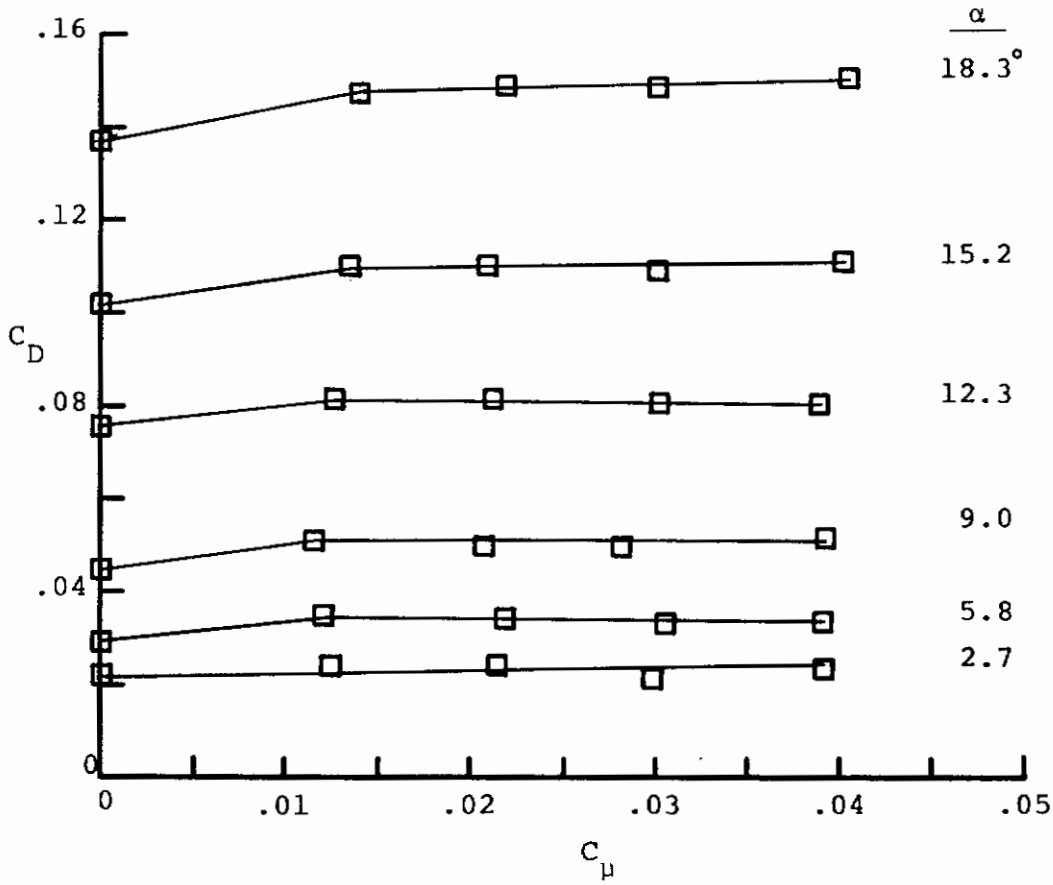

(b) Drag Coefficient

Figure 14.- Concluded.

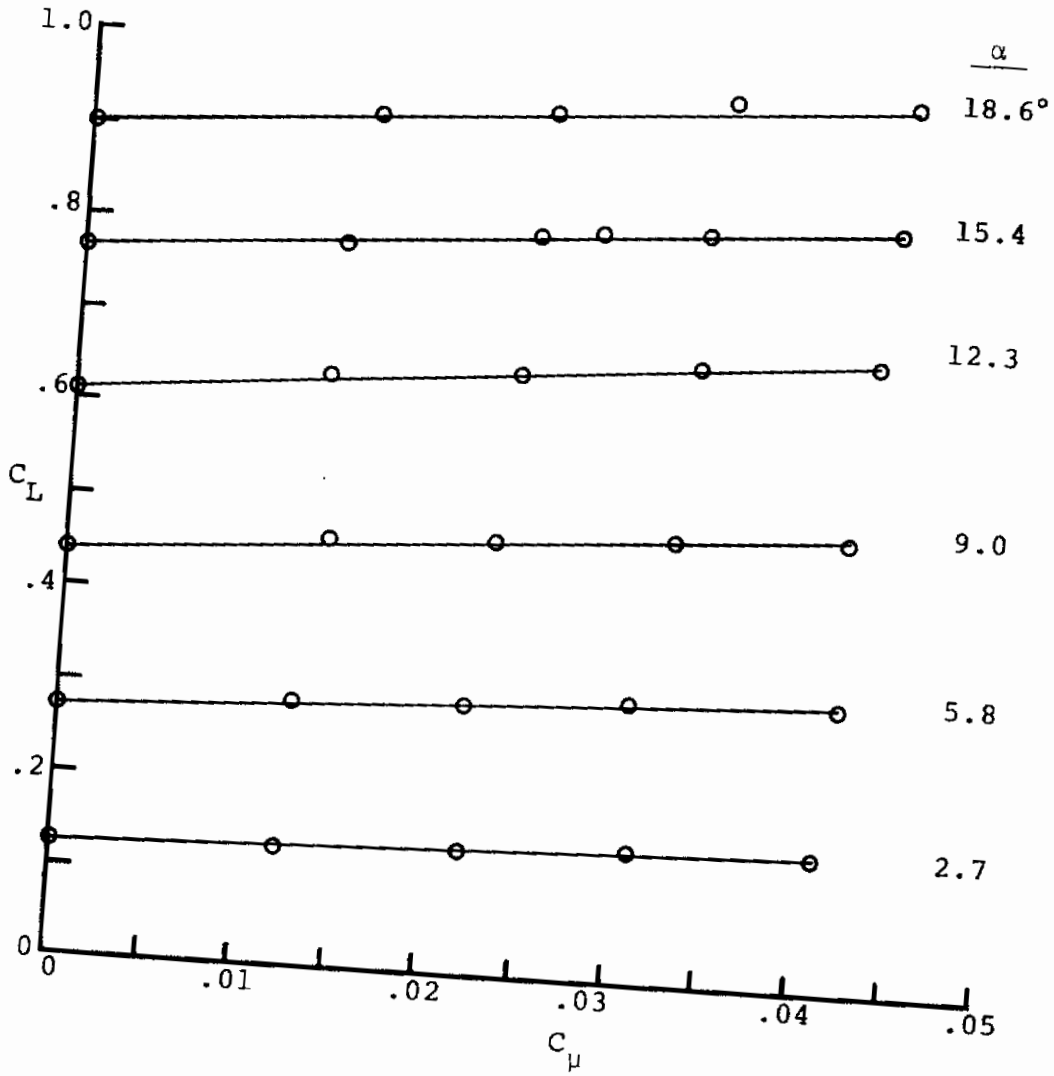

(a) Lift Coefficient

Figure 15.- Measured lift and drag coefficients on Wing No. 2 with Tip 2.

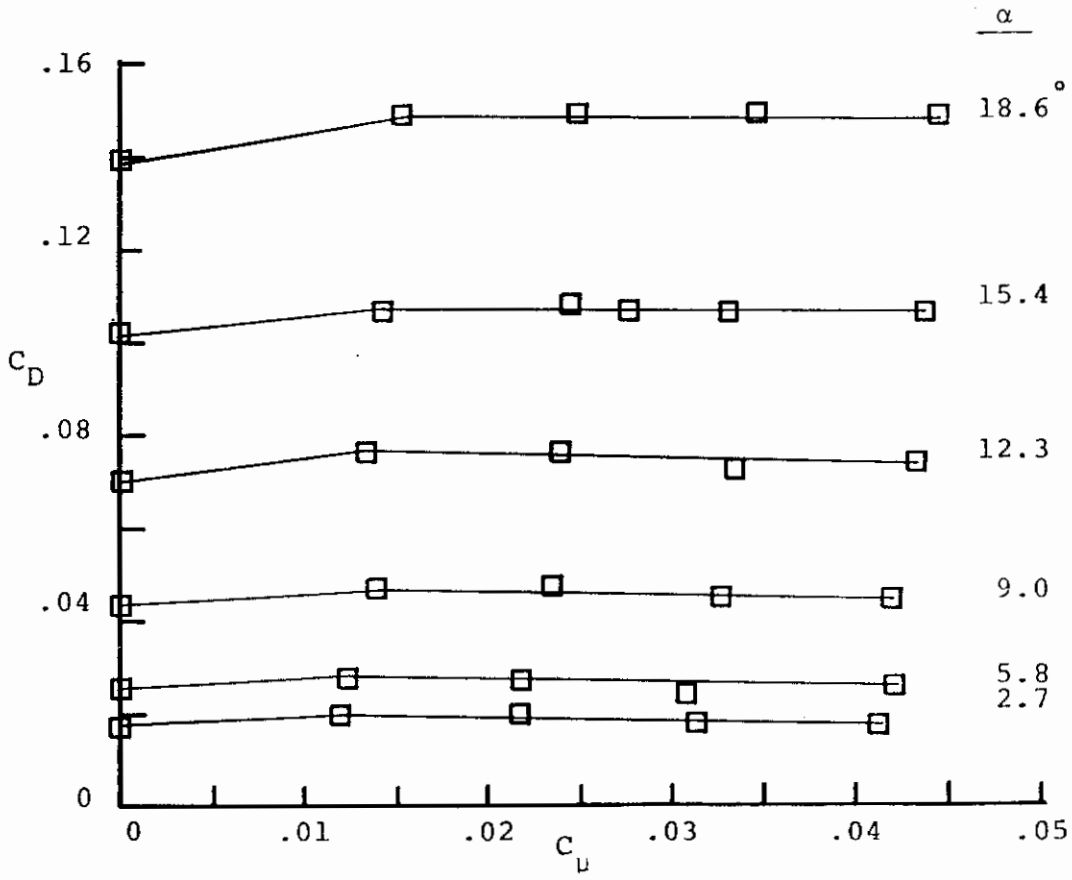

(b) Drag Coefficient

Figure 15.- Concluded.

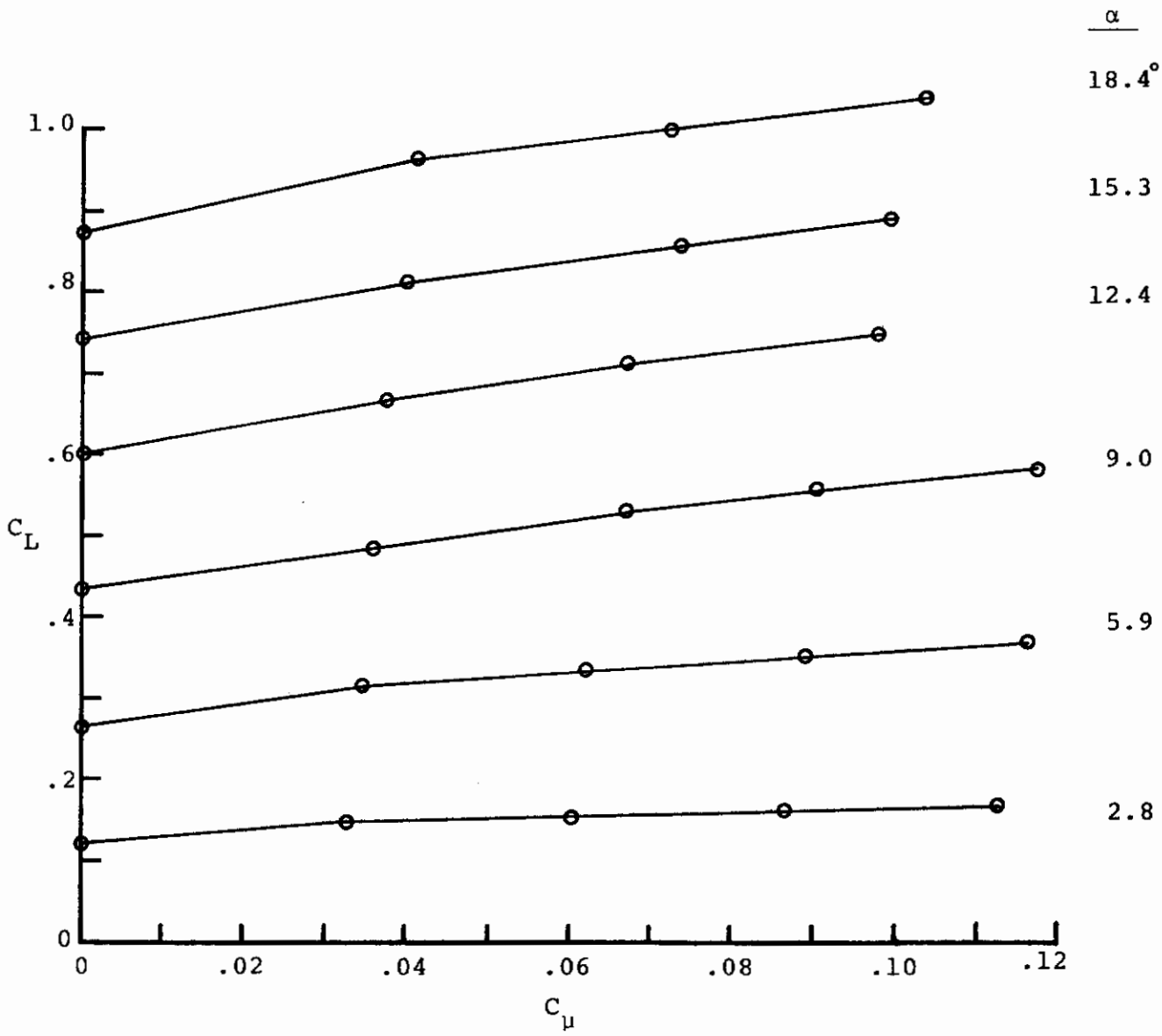

(a) Lift Coefficient

Figure 16.- Measured lift and drag coefficients on Wing No. 2 with Tip 3.

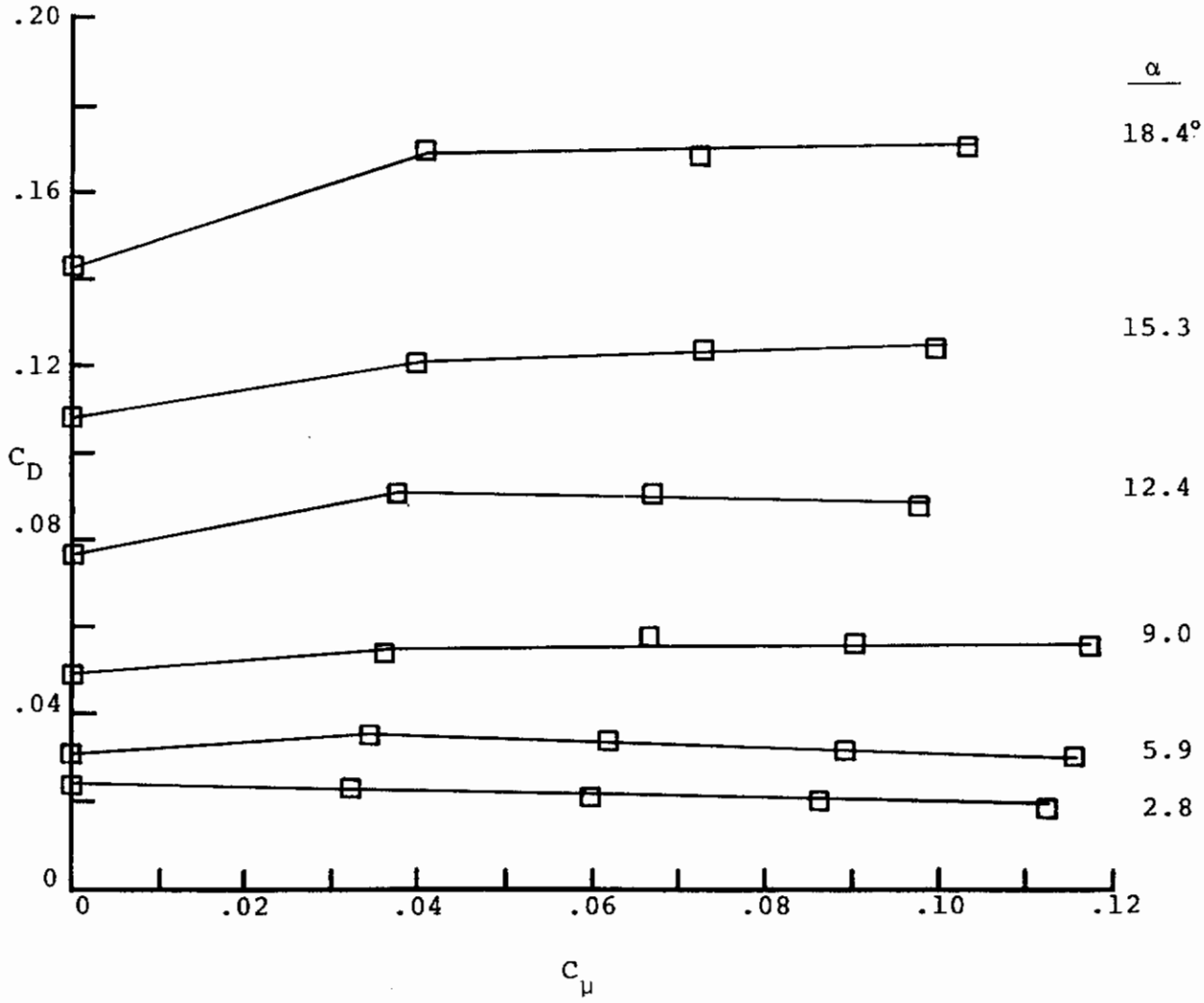

(b) Drag Coefficient

Figure 16.- Concluded.

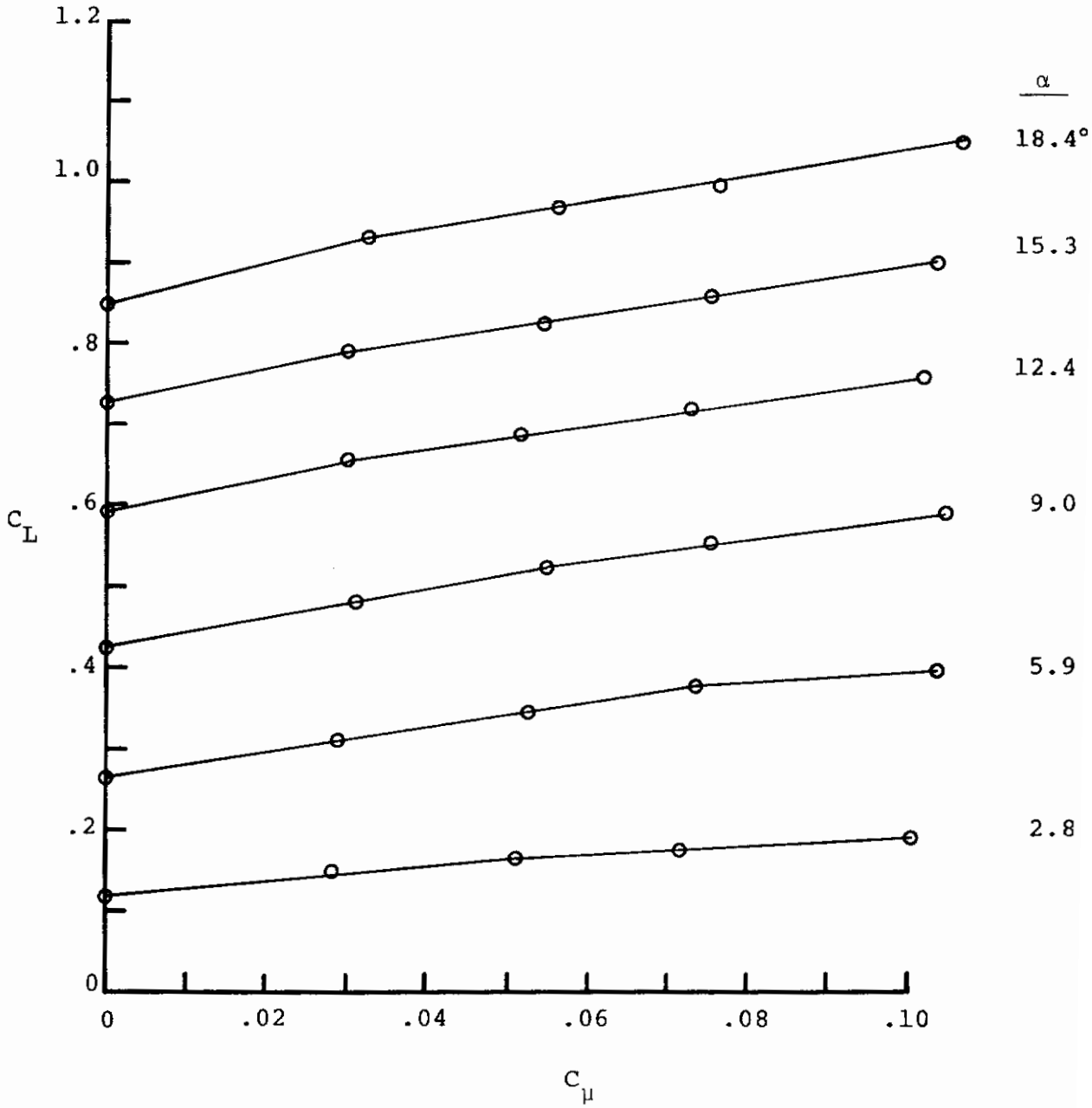

(a) Lift Coefficient

Figure 17.- Measured lift and drag coefficients on Wing No. 2 with Tip 4.

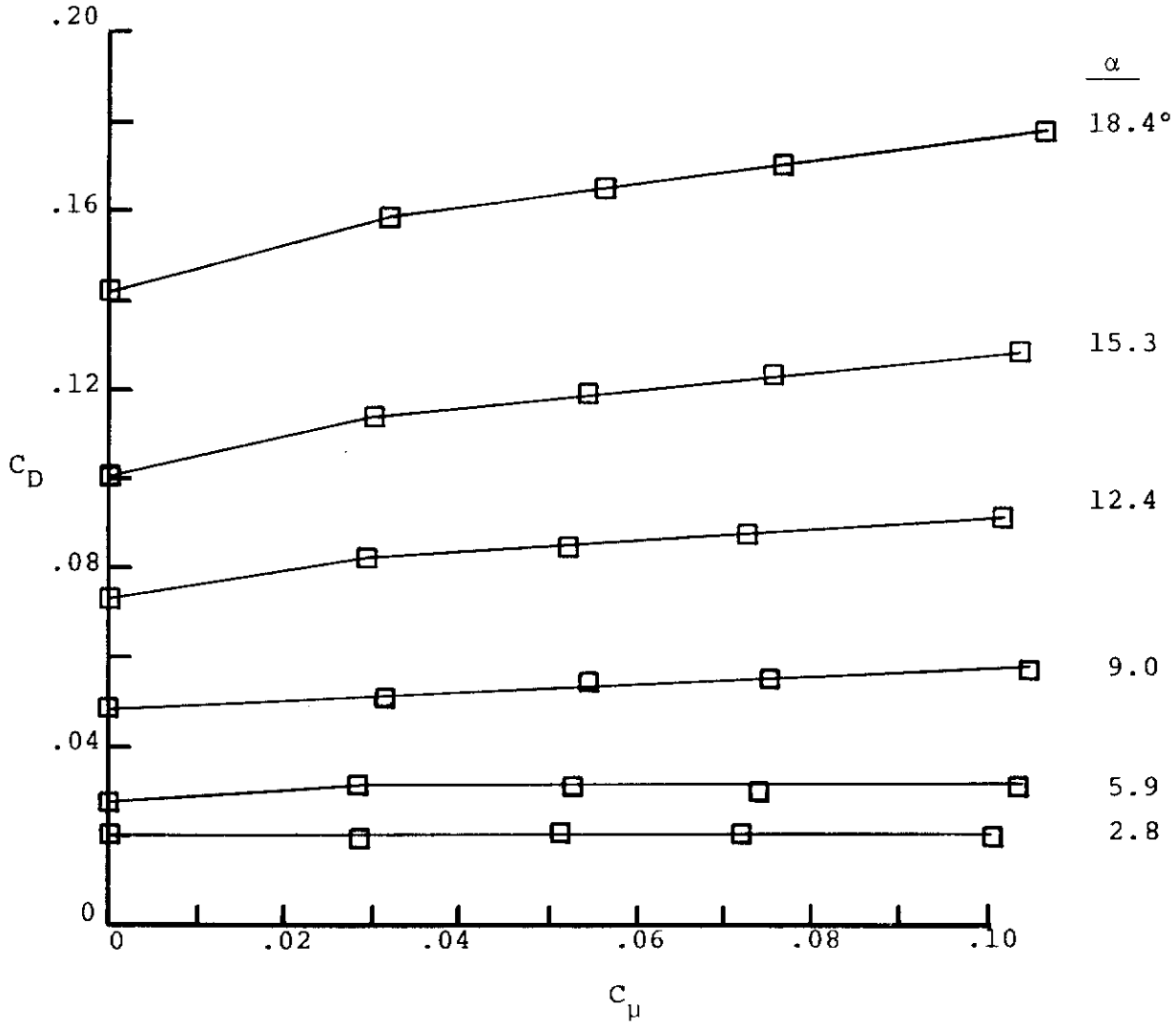

(b) Drag Coefficient

Figure 17.- Concluded.

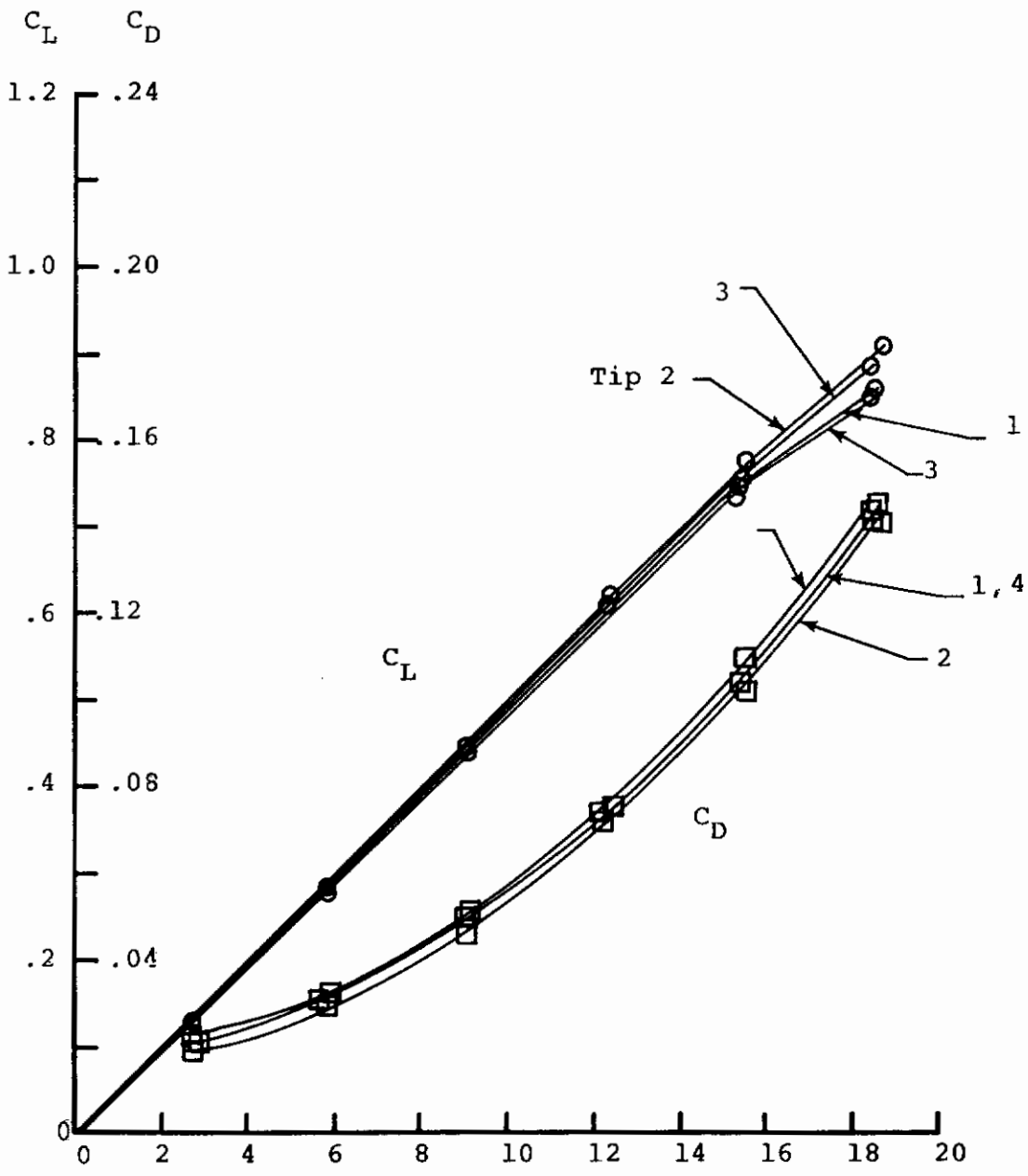

(a) $C_\mu = 0.0$

Figure 18.- Effect of tip geometry on measured lift and drag coefficients on Wing No. 2.

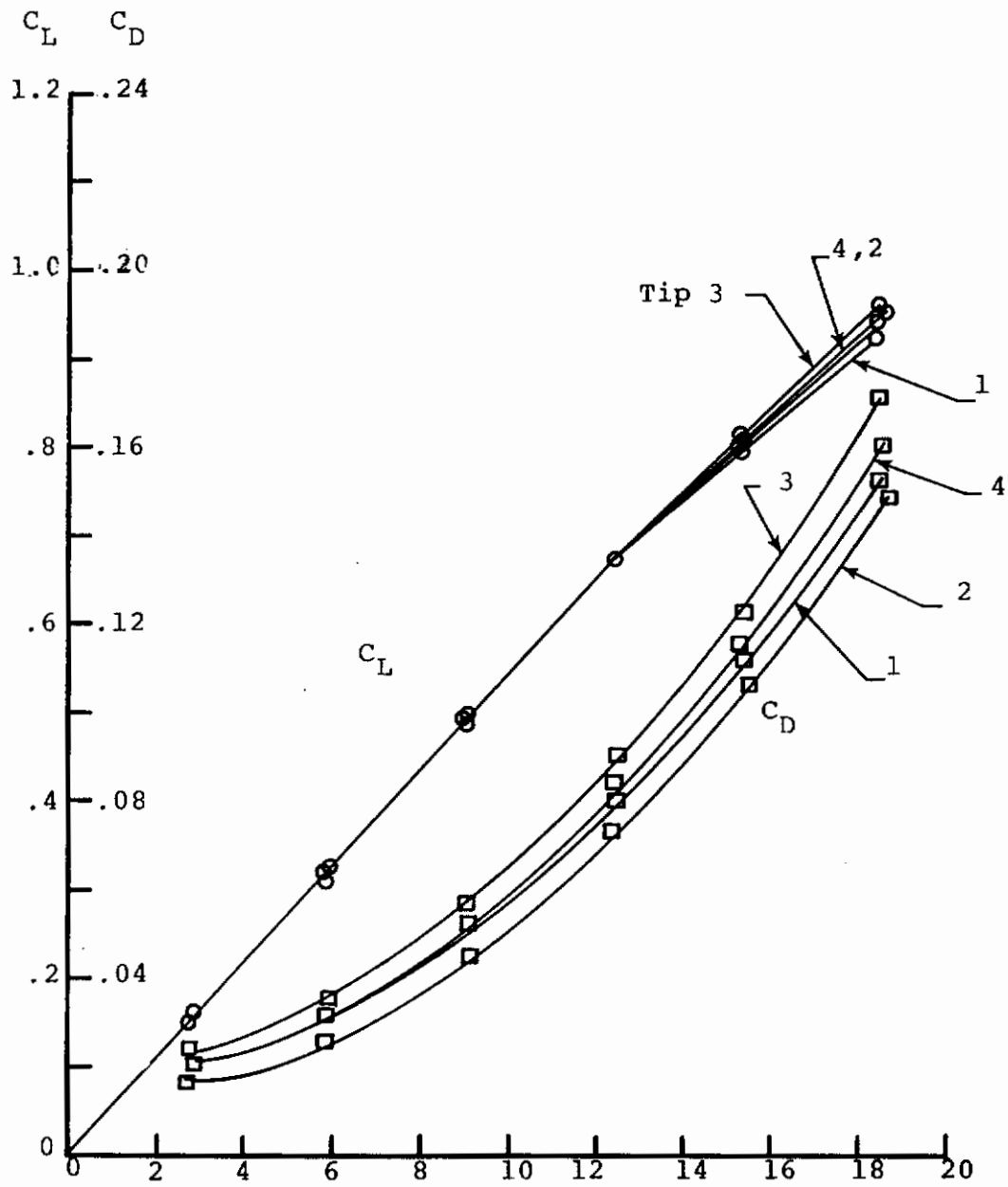

(b) $C_\mu = 0.04$

Figure 18.- Concluded.

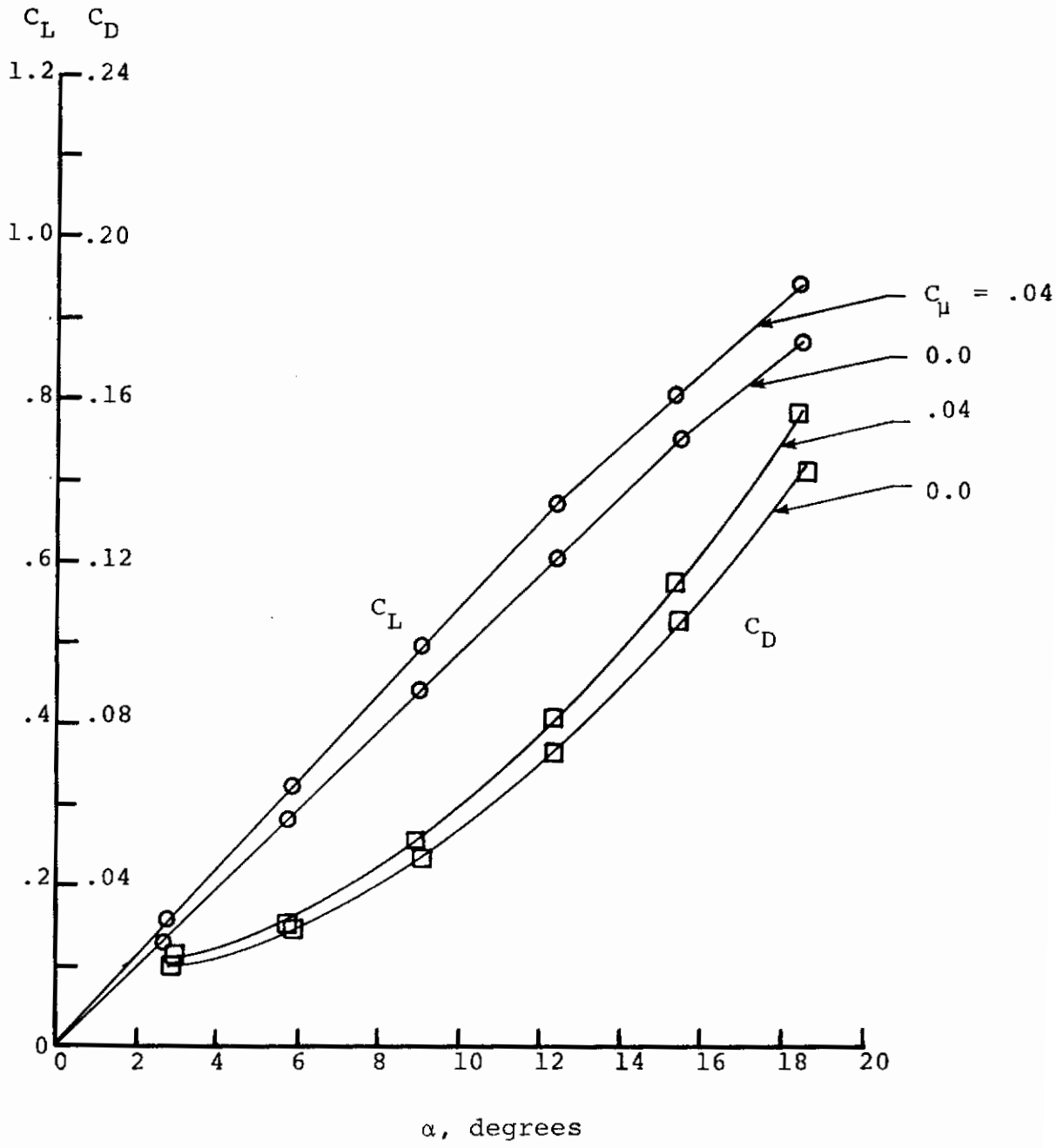

Figure 19.- Average effect of tip blowing on lift and drag characteristics of Wing No. 2.

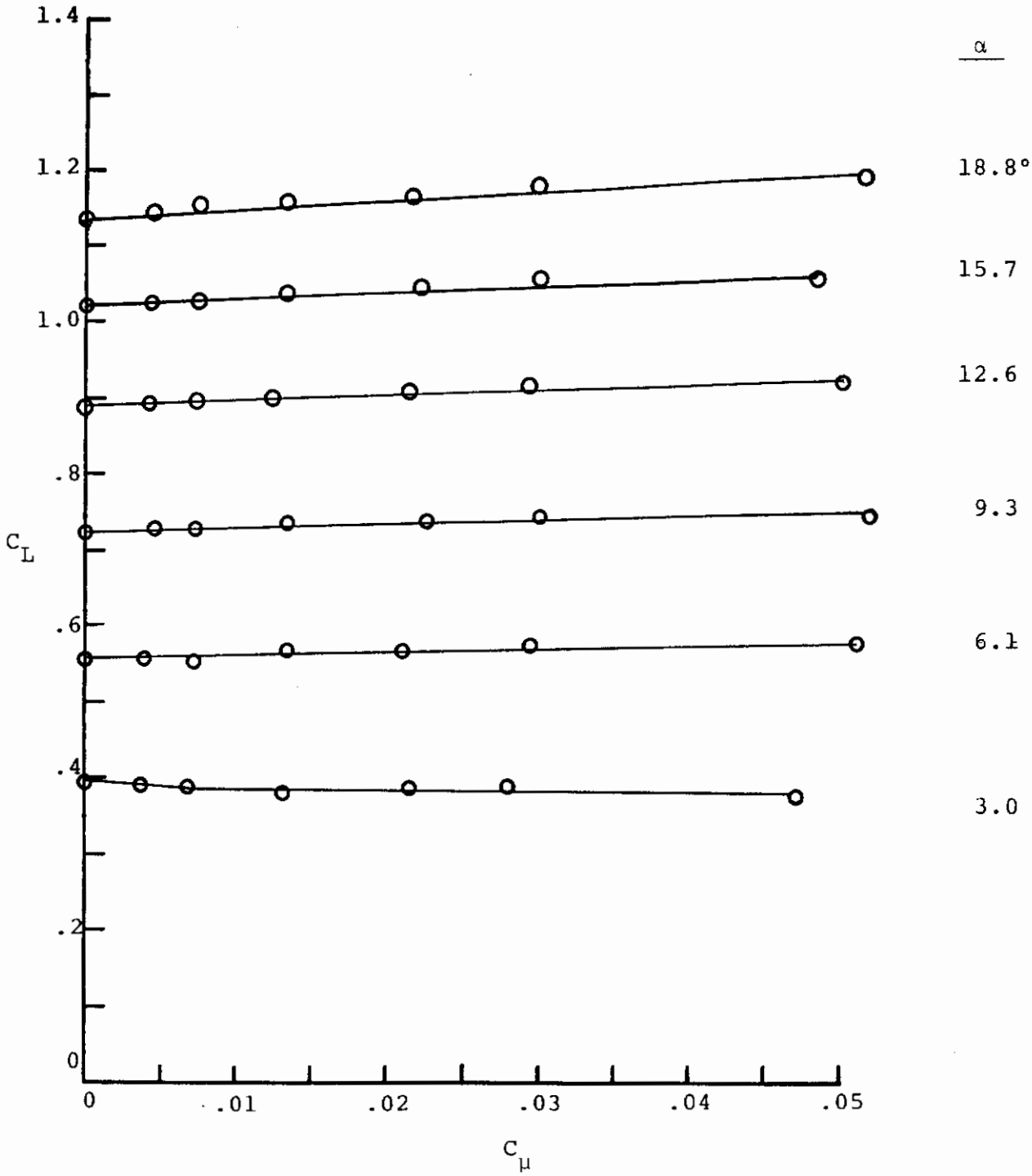

(a) Lift Coefficient

Figure 20.- Measured lift and drag coefficients on Wing No. 3 with Tip 1.

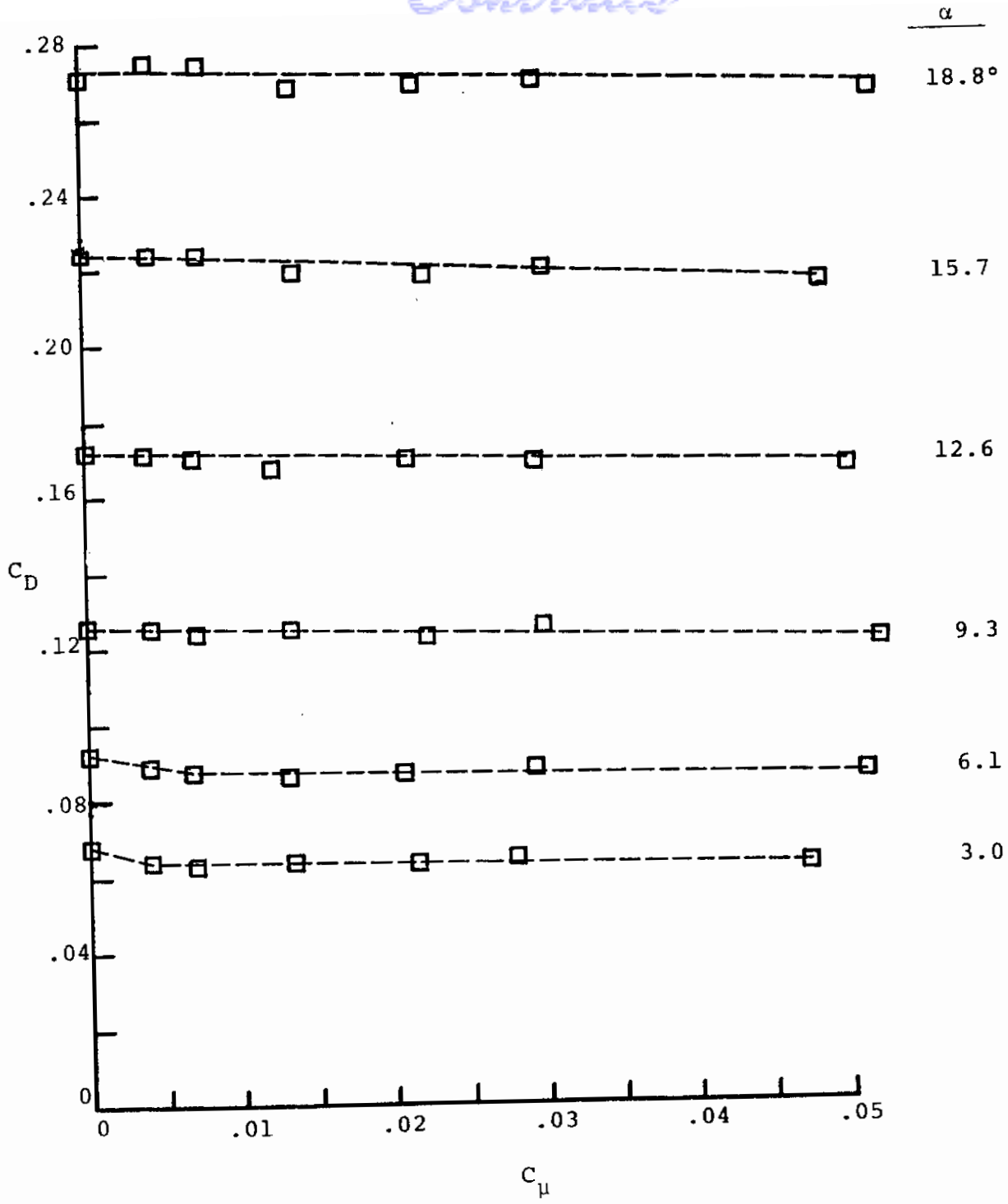

(b) Drag Coefficient

Figure 20.- Concluded.

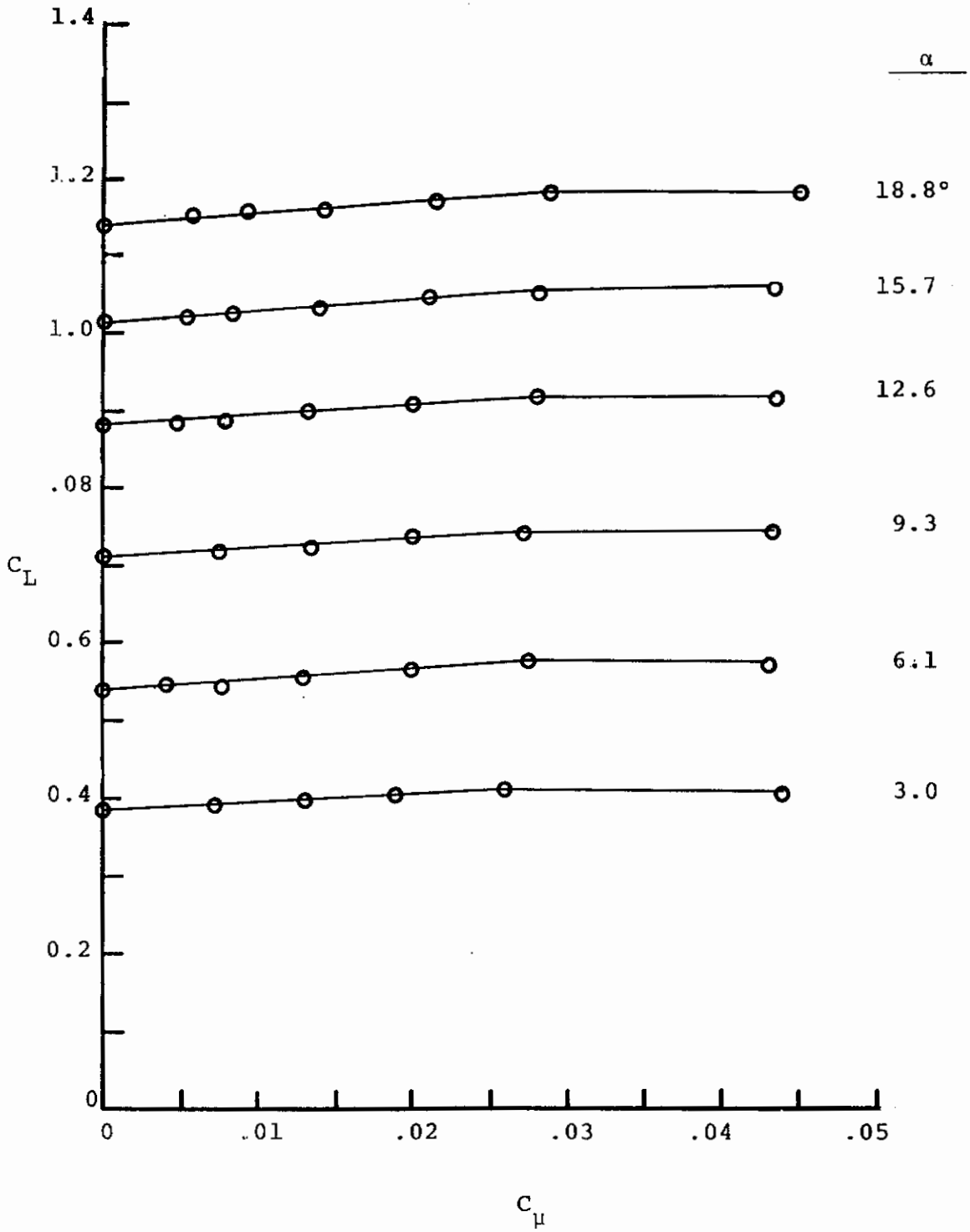

(a) Lift Coefficient

Figure 21.- Measured lift and drag coefficients on Wing No. 3 with Tip 2.

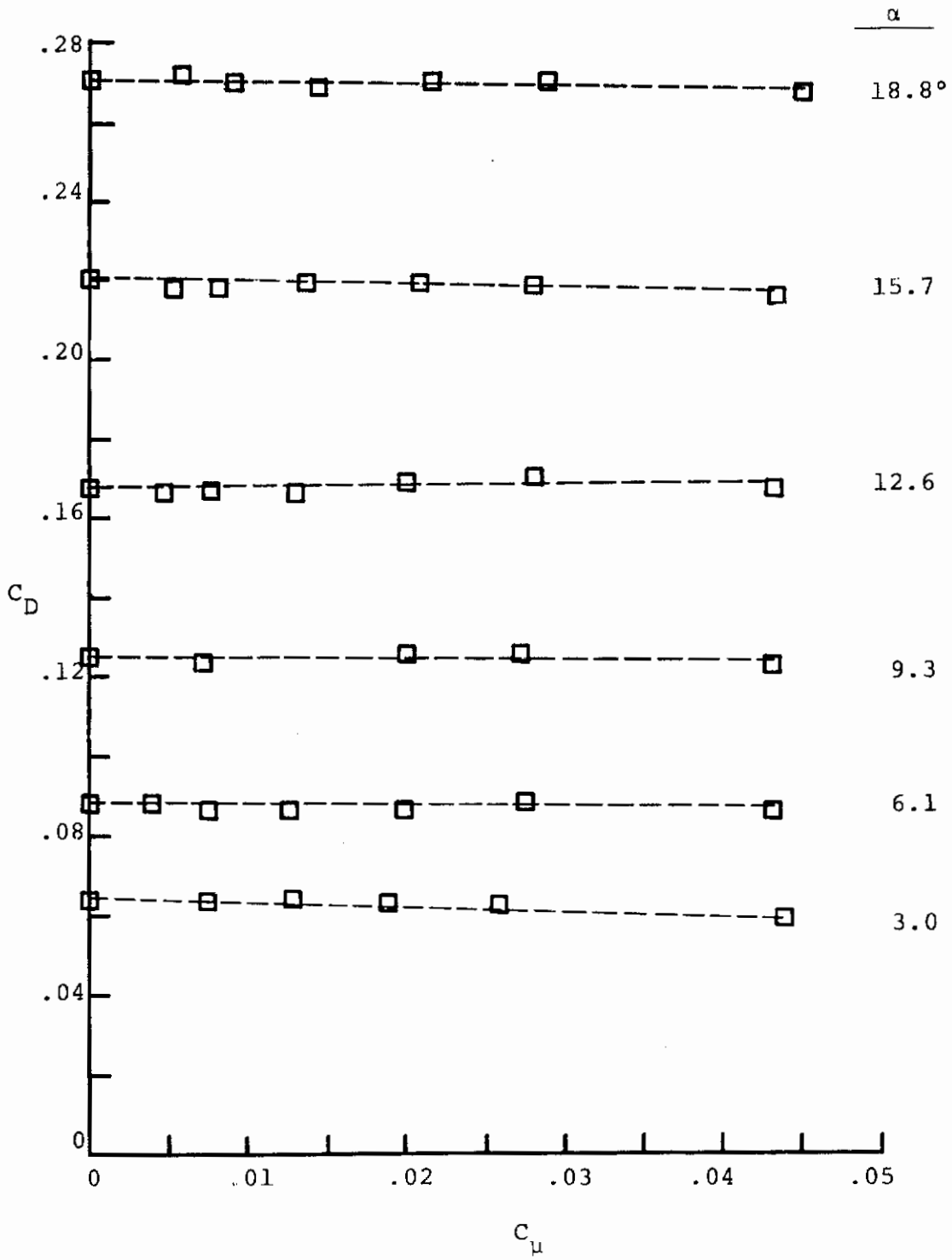

(b) Drag Coefficient

Figure 21.- Concluded.

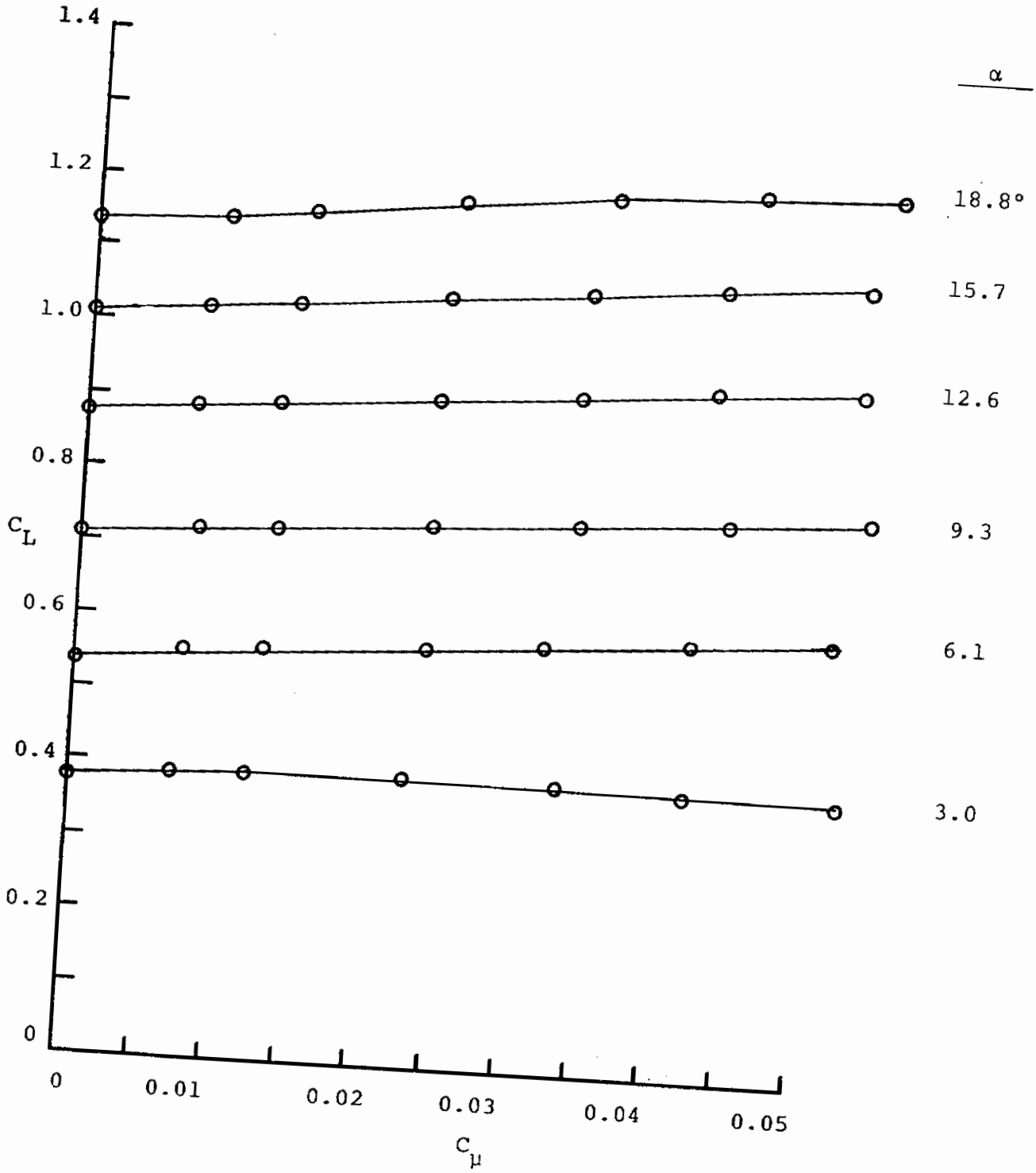

(a) Lift Coefficient

Figure 22.- Measured lift and drag coefficients on Wing No. 3 with Tip 3.

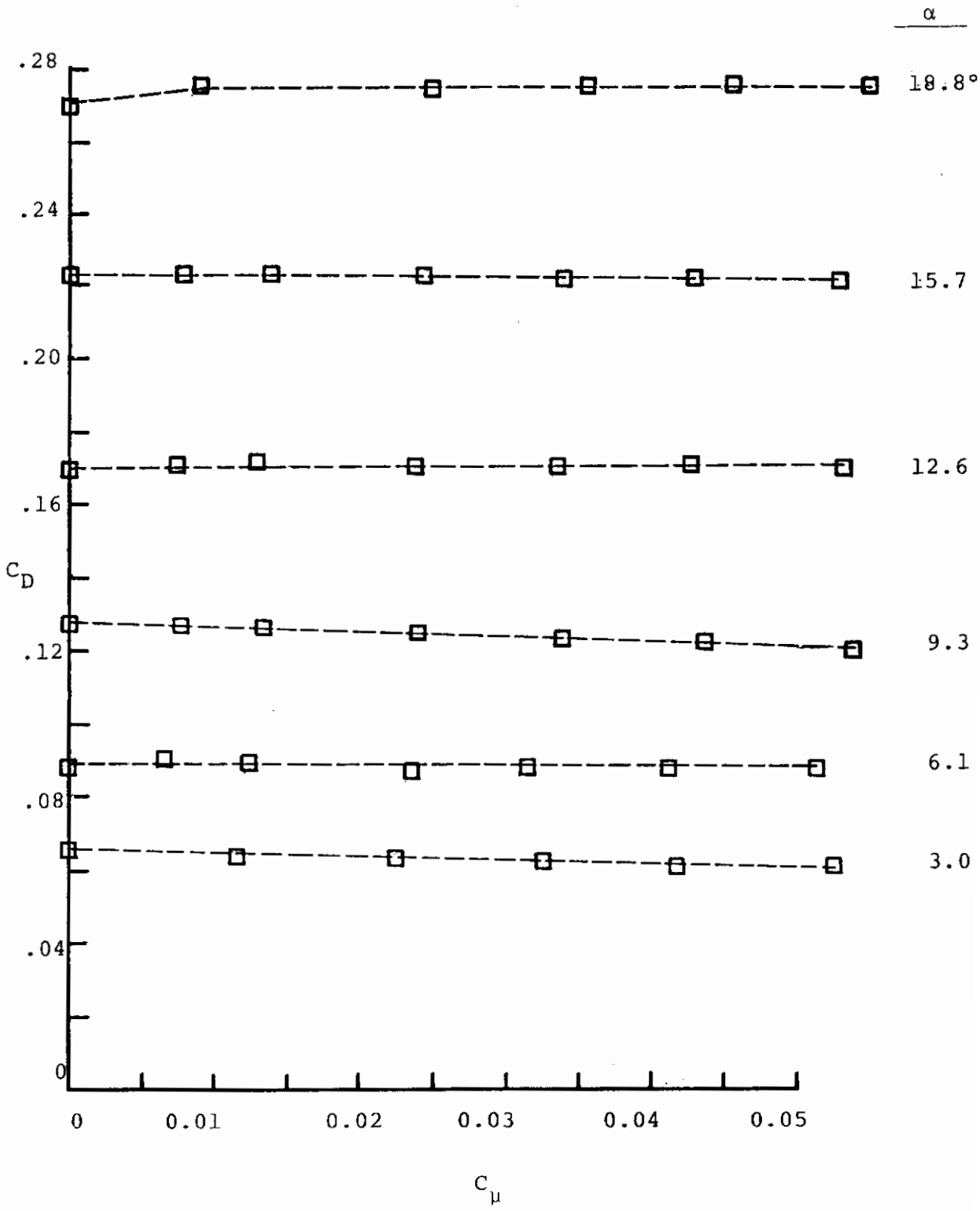

(b) Drag Coefficient

Figure 22.- Concluded.

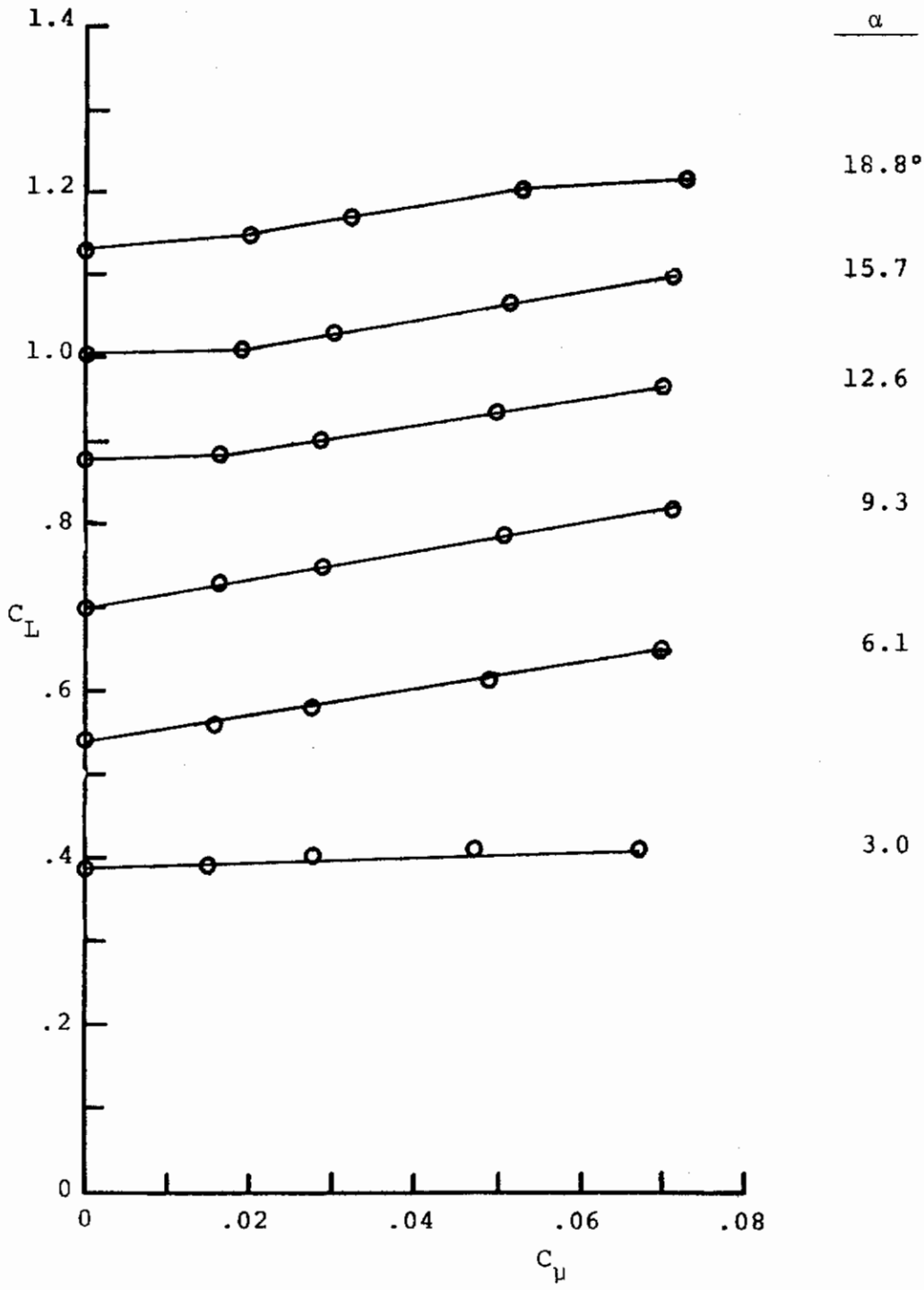

(a) Lift Coefficient

Figure 23.- Measure lift and drag coefficients on Wing No. 3 with Tip 4.

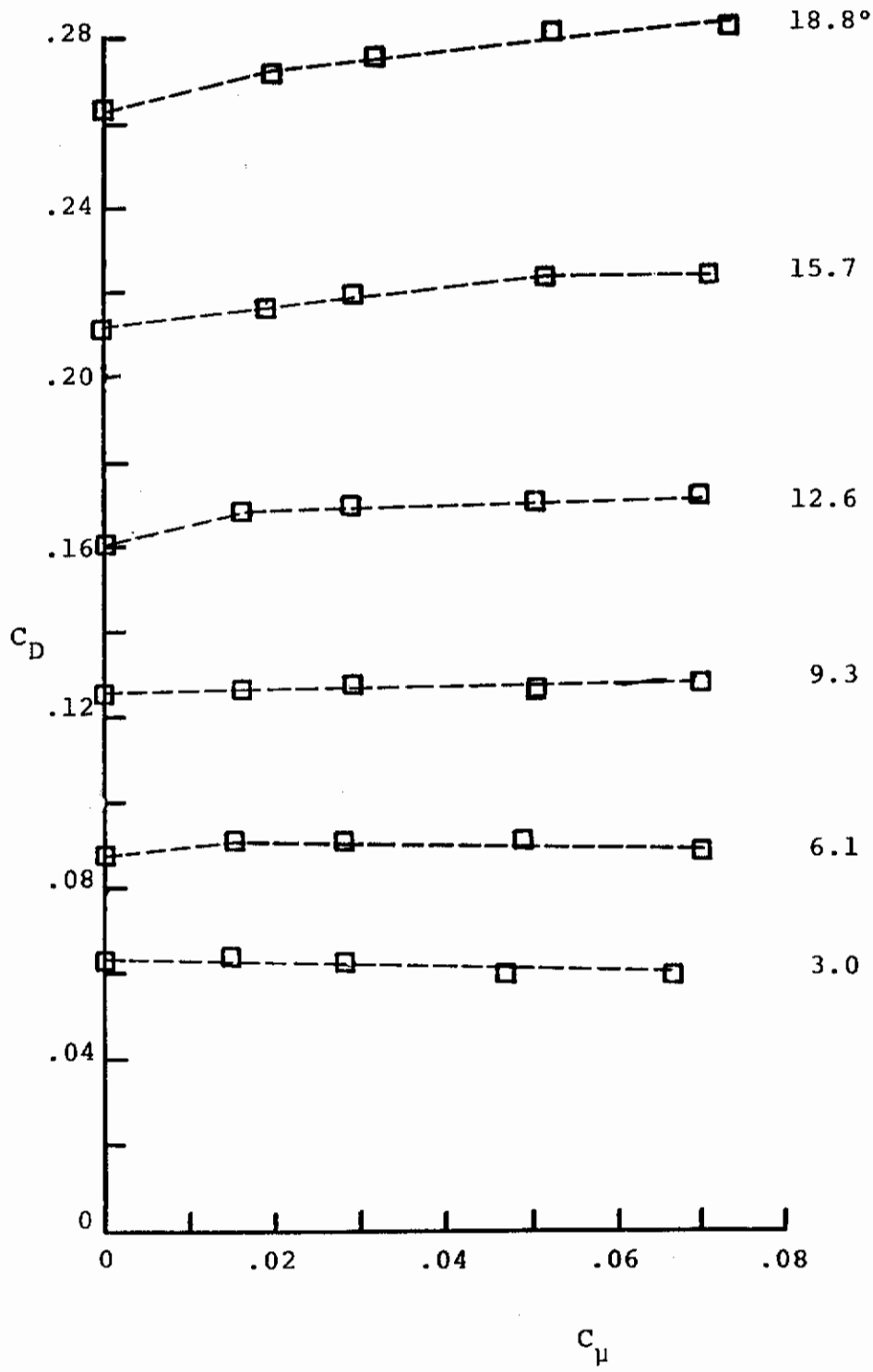

(b) Drag Coefficient

Figure 23.- Concluded.

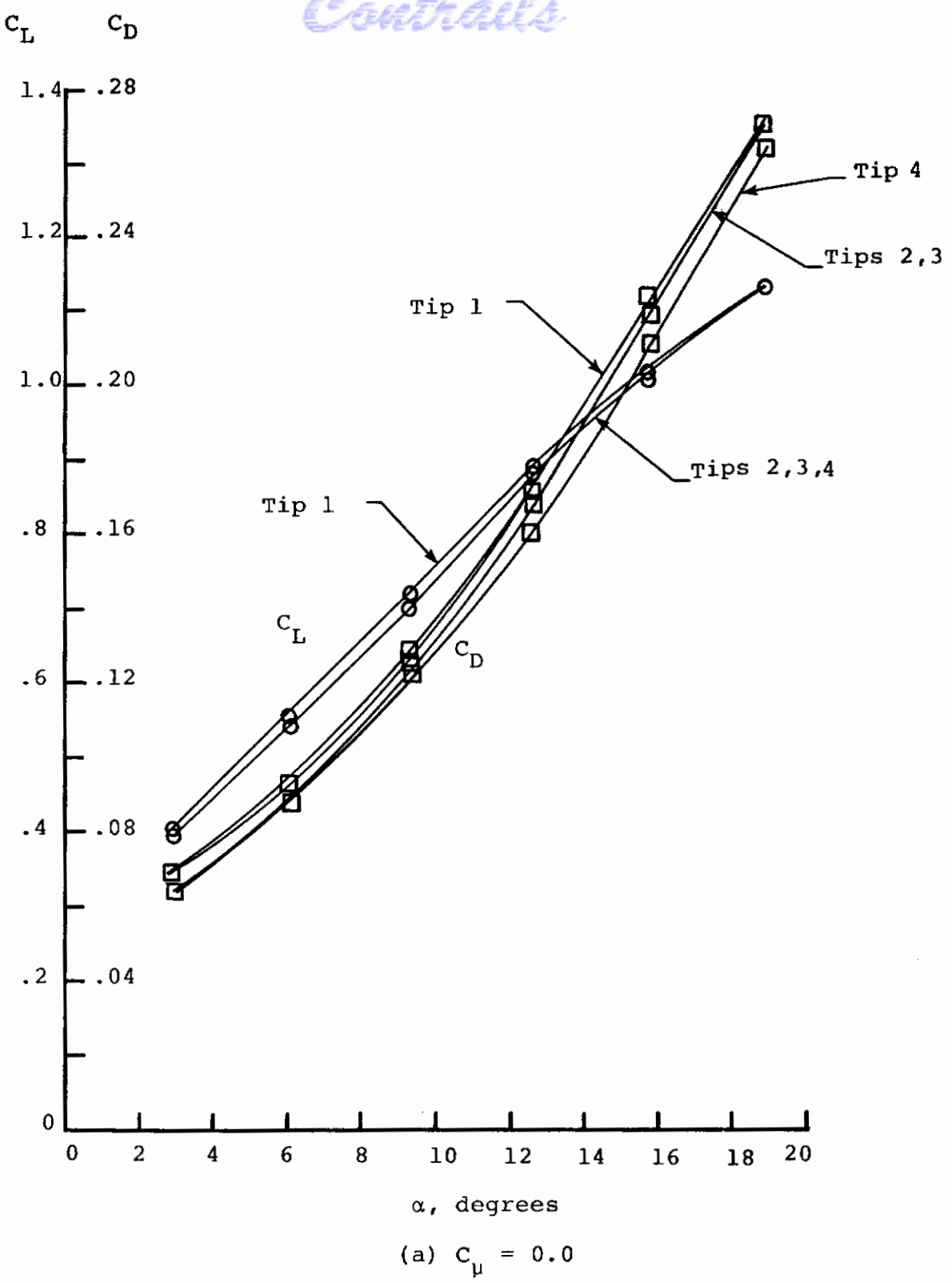

(a) $C_\mu = 0.0$

Figure 24.- Effect of tip geometry on measured lift and drag coefficients on Wing No. 3.

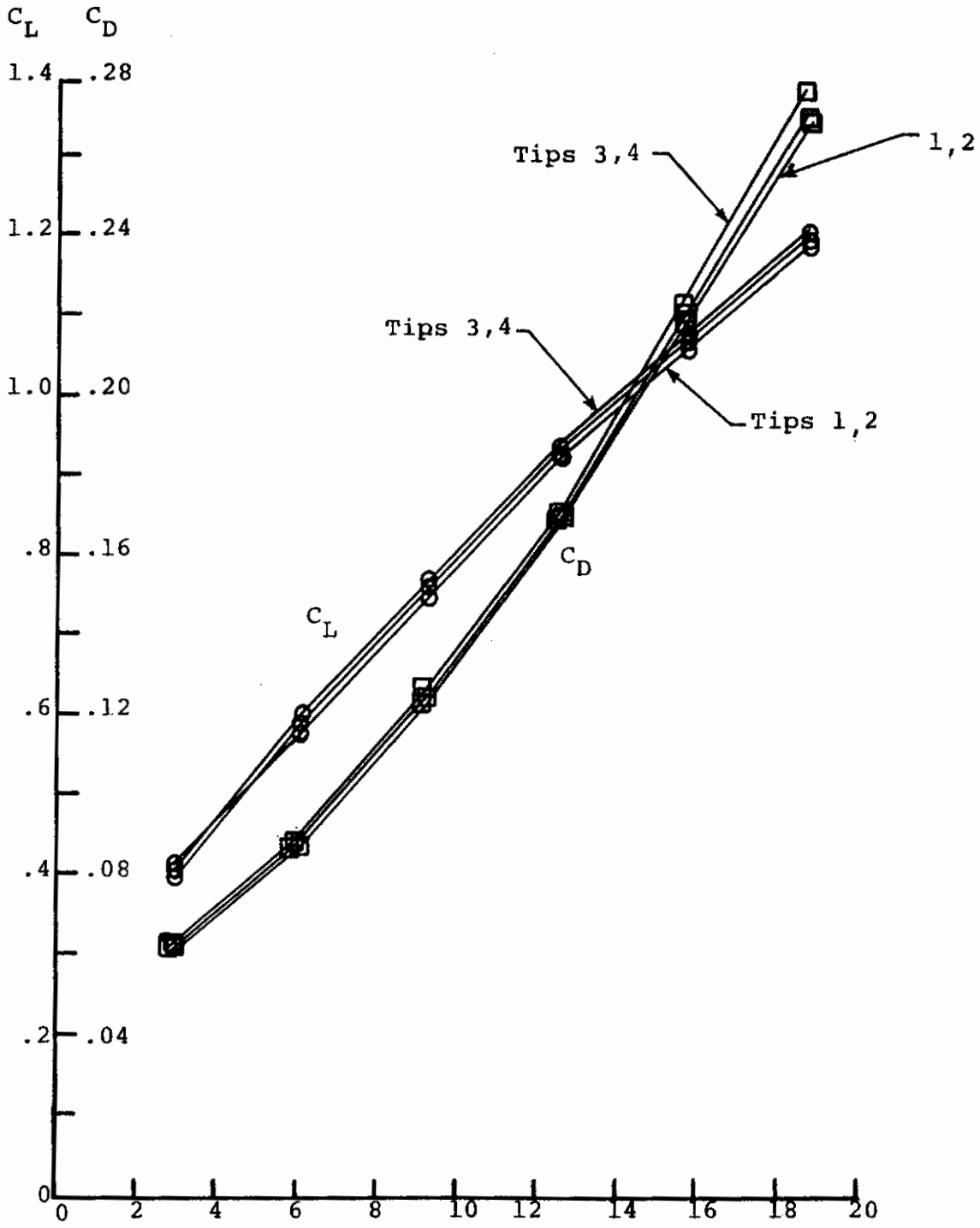

(b) $C_\mu = 0.04$

Figure 24.- Concluded.

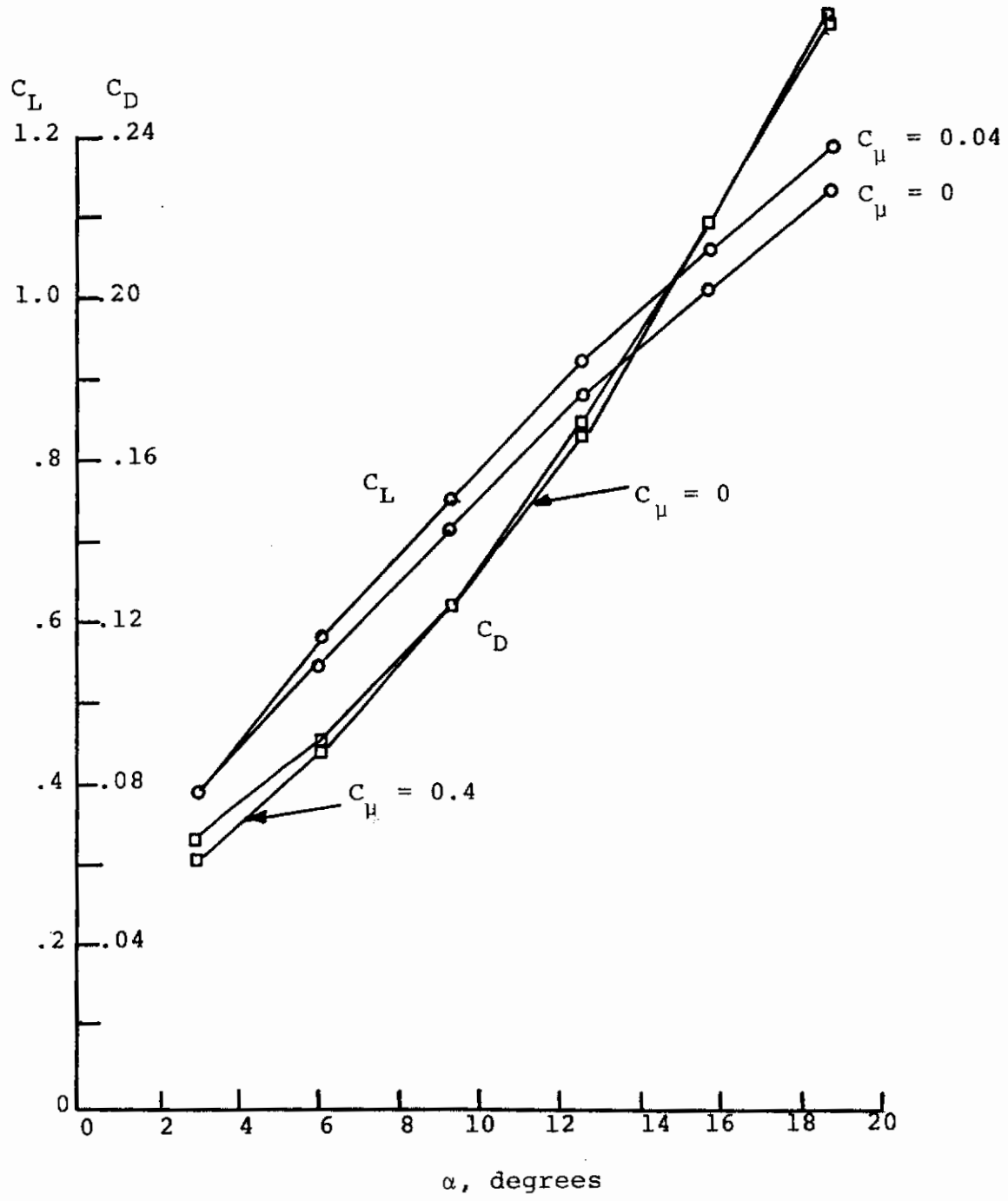

Figure 25.- Average effects of tip blowing on lift and drag coefficients on Wing No. 3.

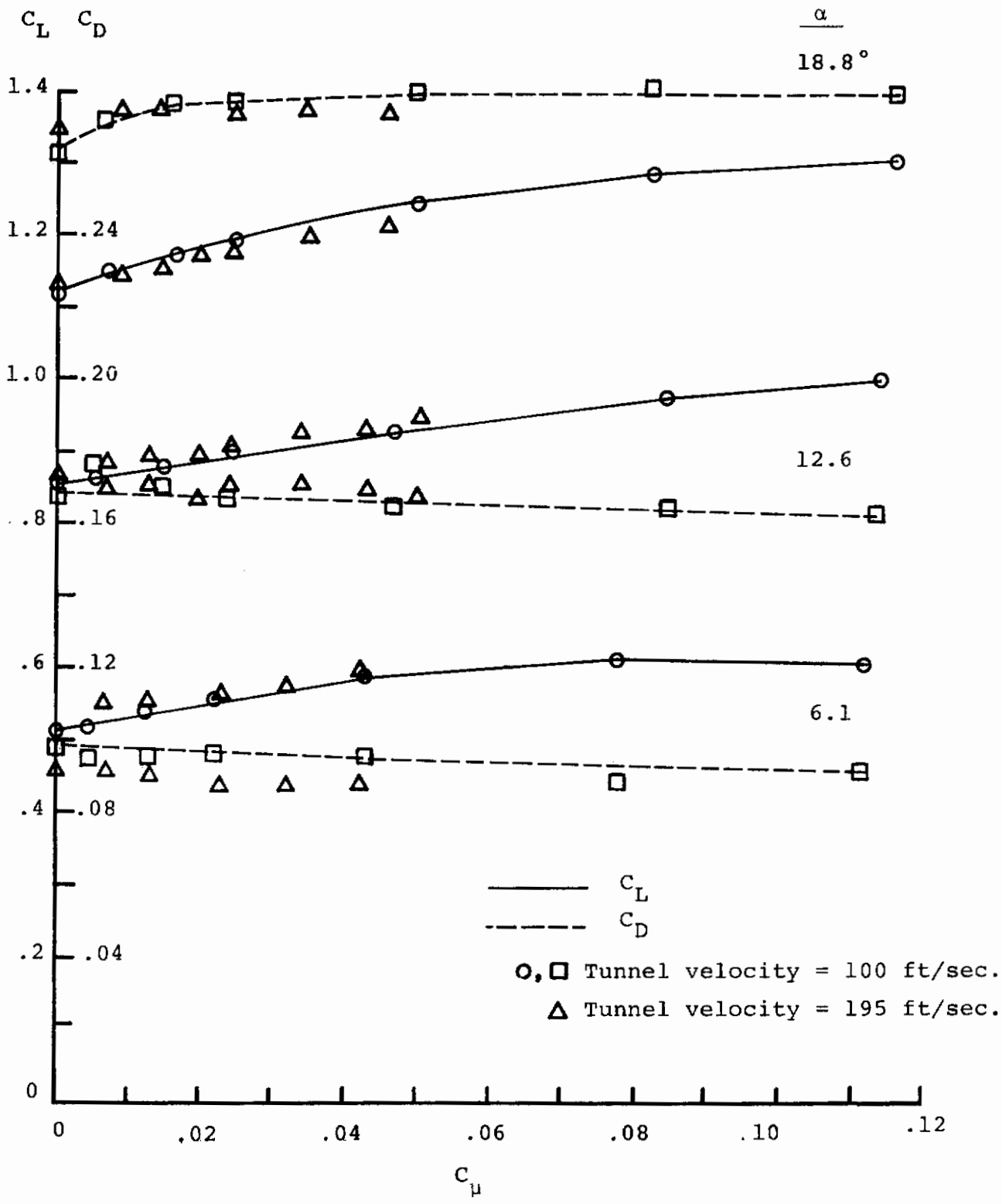

Figure 26.- Effect of tunnel velocity on measured lift and drag coefficients on Wing No. 3 with tip blowing.

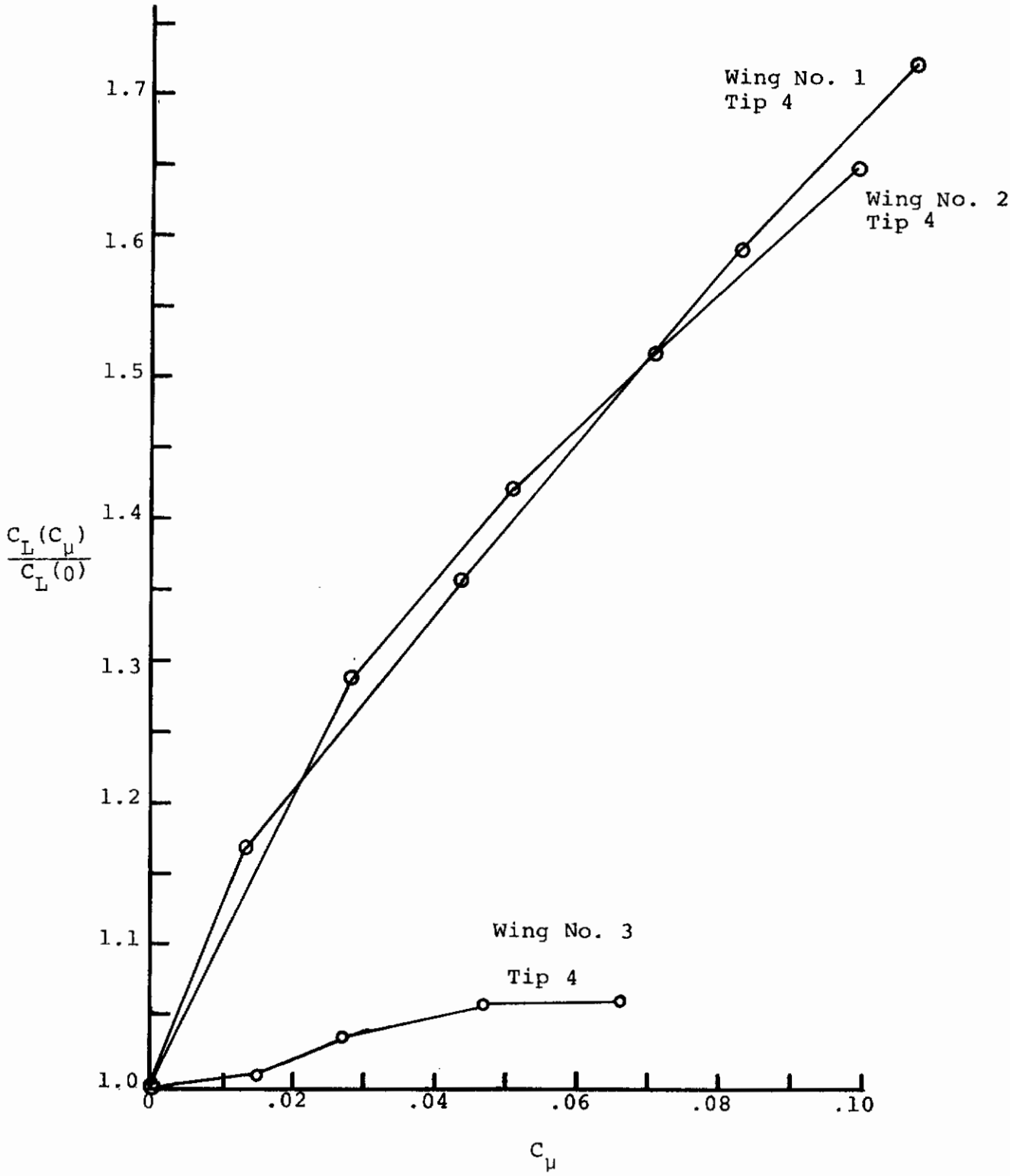

(a) $\alpha = 3°$

Figure 27.- Effect of tip blowing on the measured lift coefficients of three wings with long tip slots.

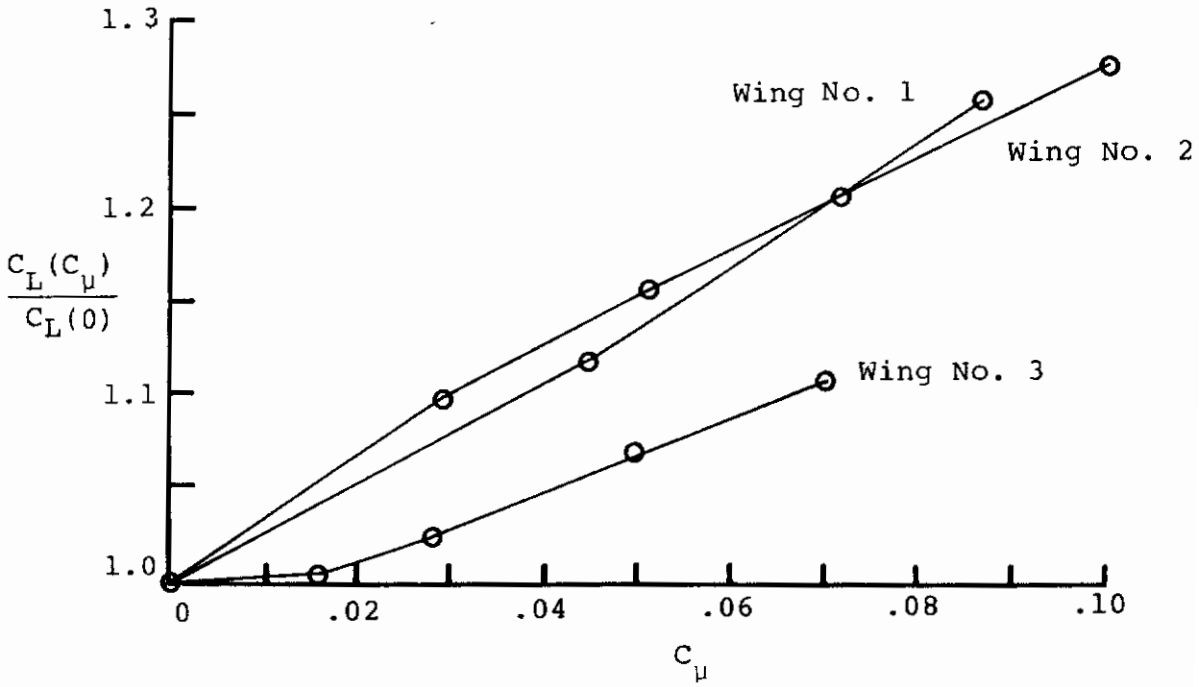

(b) $\alpha = 12°$

Figure 27.- Continued.

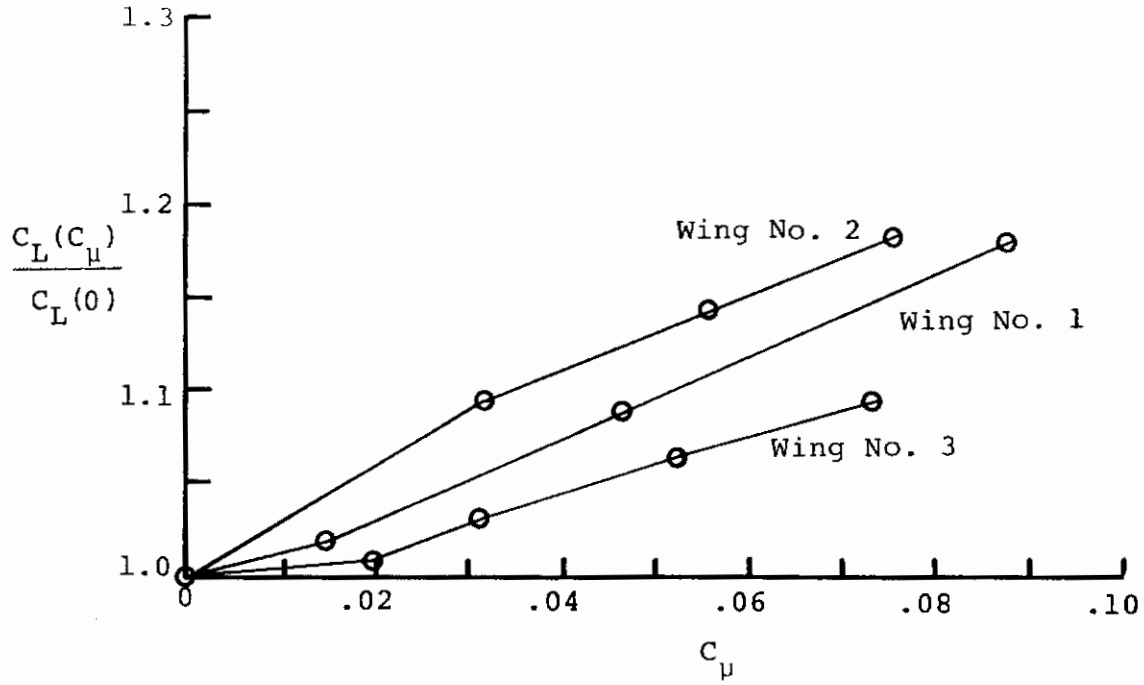

(c) α = 18°

Figure 27.- Concluded.

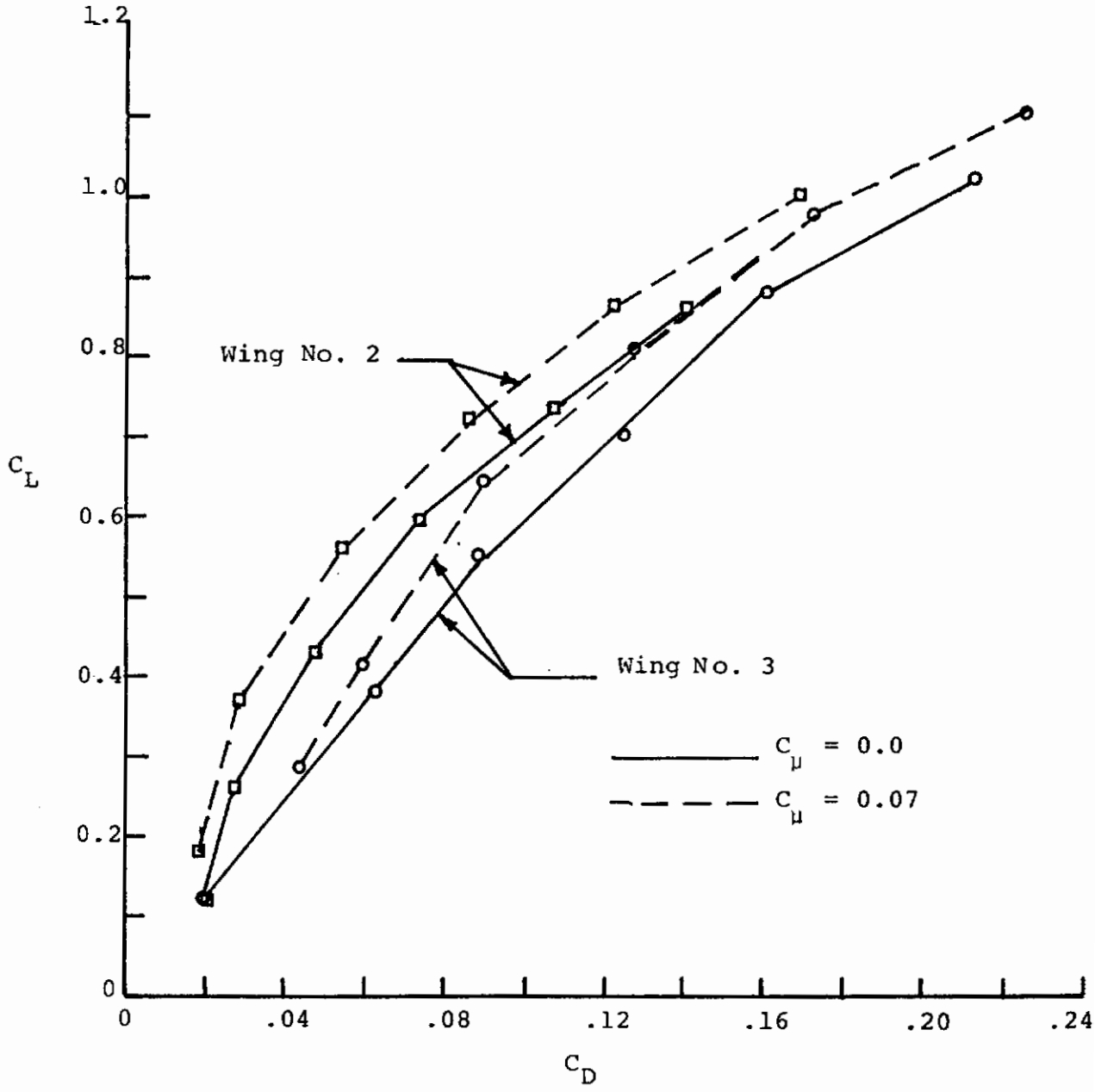

Figure 28.- Effect of camber and tip blowing on the measured aerodynamic characteristics of a swept wing.

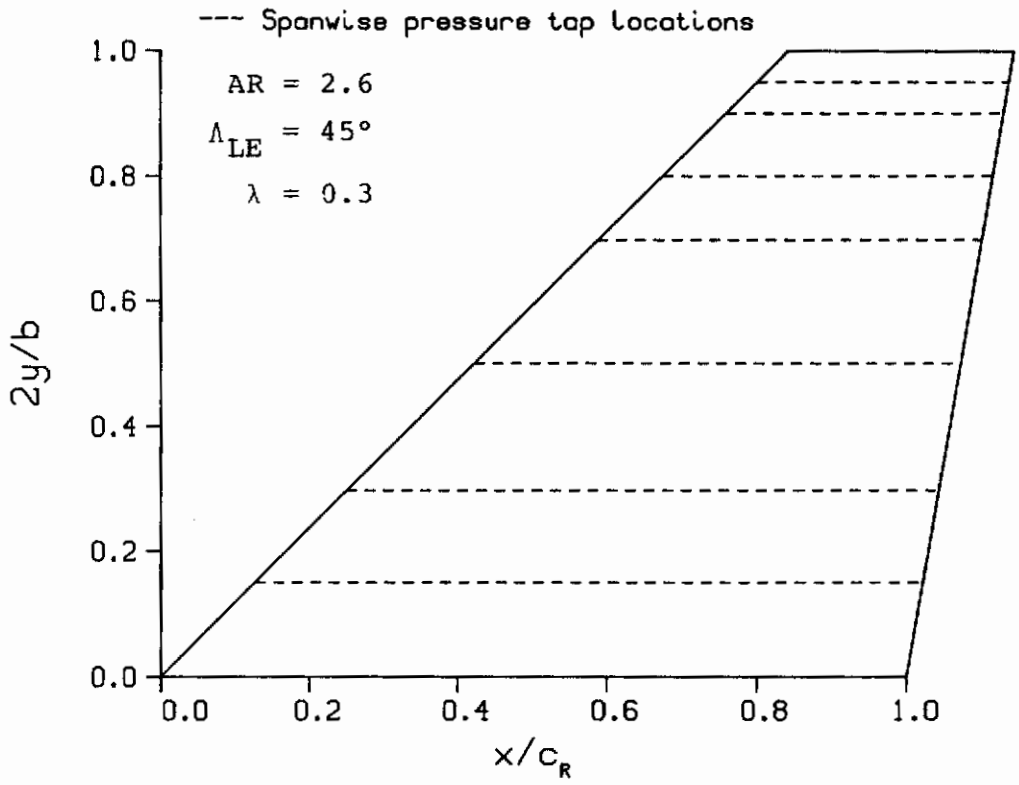

Figure 29.- Large scale wing with tip blowing.

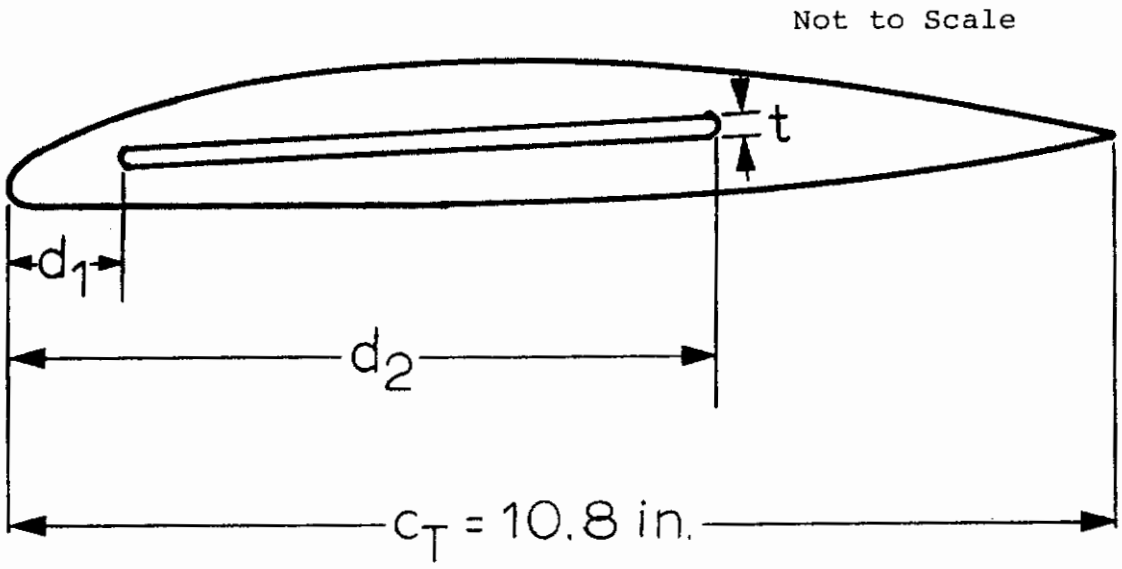

Tip No.	d_1/c_T	d_2/c_T	t in.	Dihedral Angle
0	solid tip (baseline)			
2	.07	.83	.029	0°
4	.28	.57	.077	0°
5	.28	.57	.077	30° ↓
6	.28	.57	.077	60° ↓
8	Wu's tip, see Figure 30 (b)			

(a) Tips 0,2,4,5,6

Figure 30.- Wing tip nozzles for the large-scale wing.

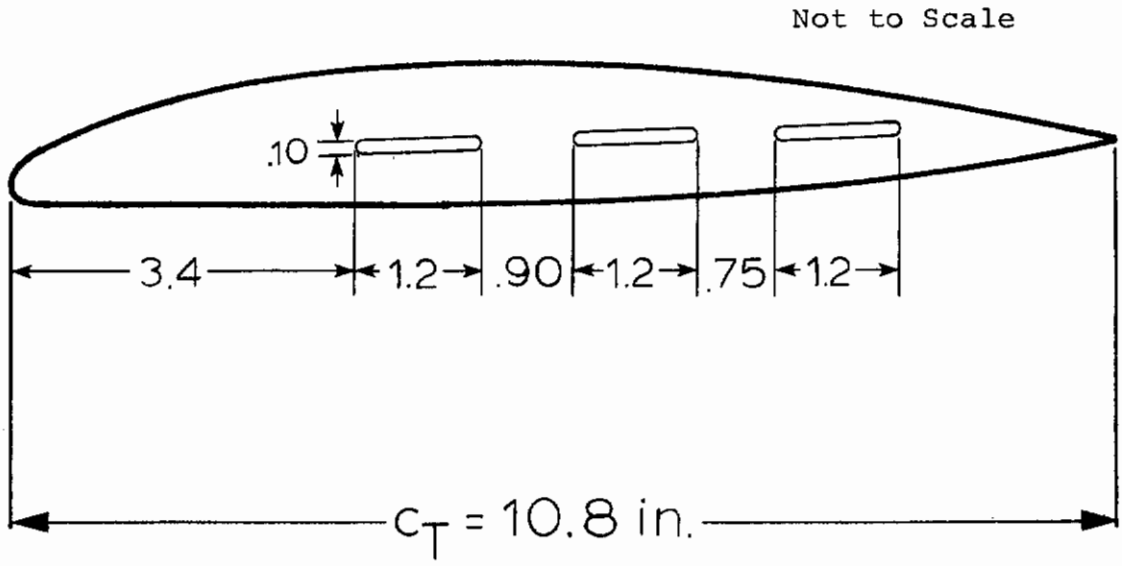

Sweep angle	45°	45°	50° →
Dihedral angle	0°	0°	- 15° ↑

(b) Tip 8

Figure 30.- Concluded.

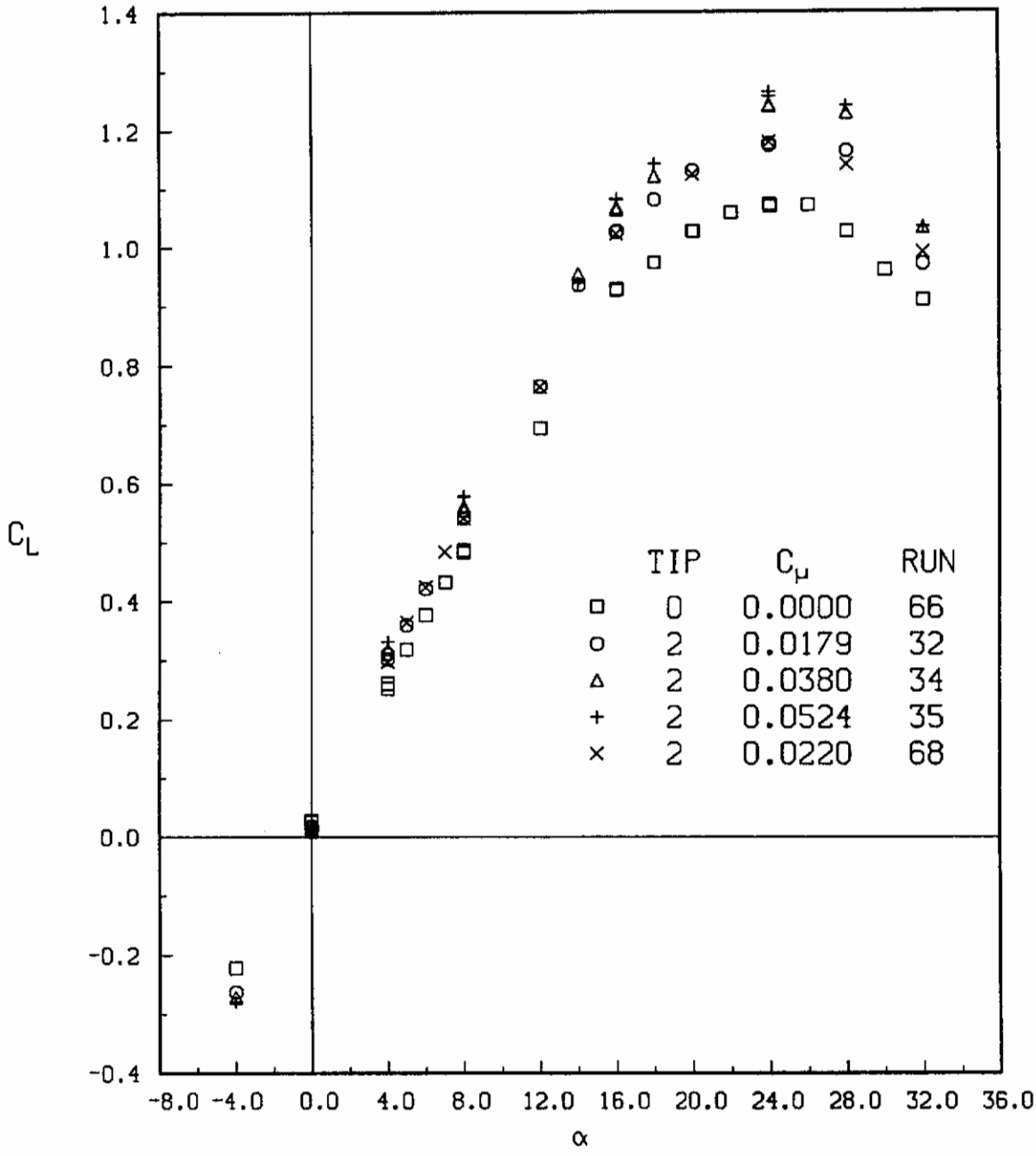

(a) Lift Coefficient

Figure 31.- Measured lift and drag coefficients on Wing C-BT with Tip No. 2.

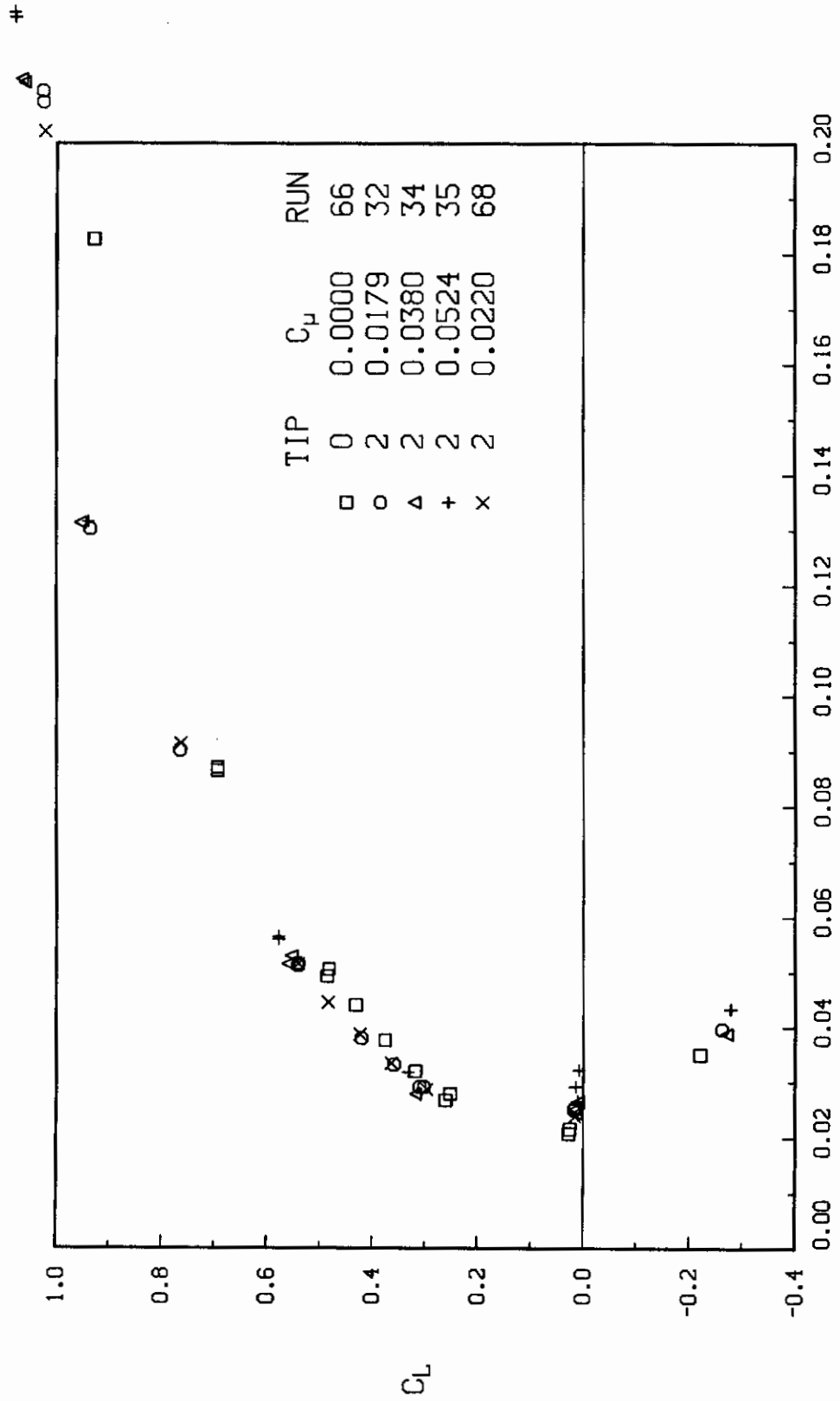

(b) Drag Coefficient

Figure 31.- Concluded.

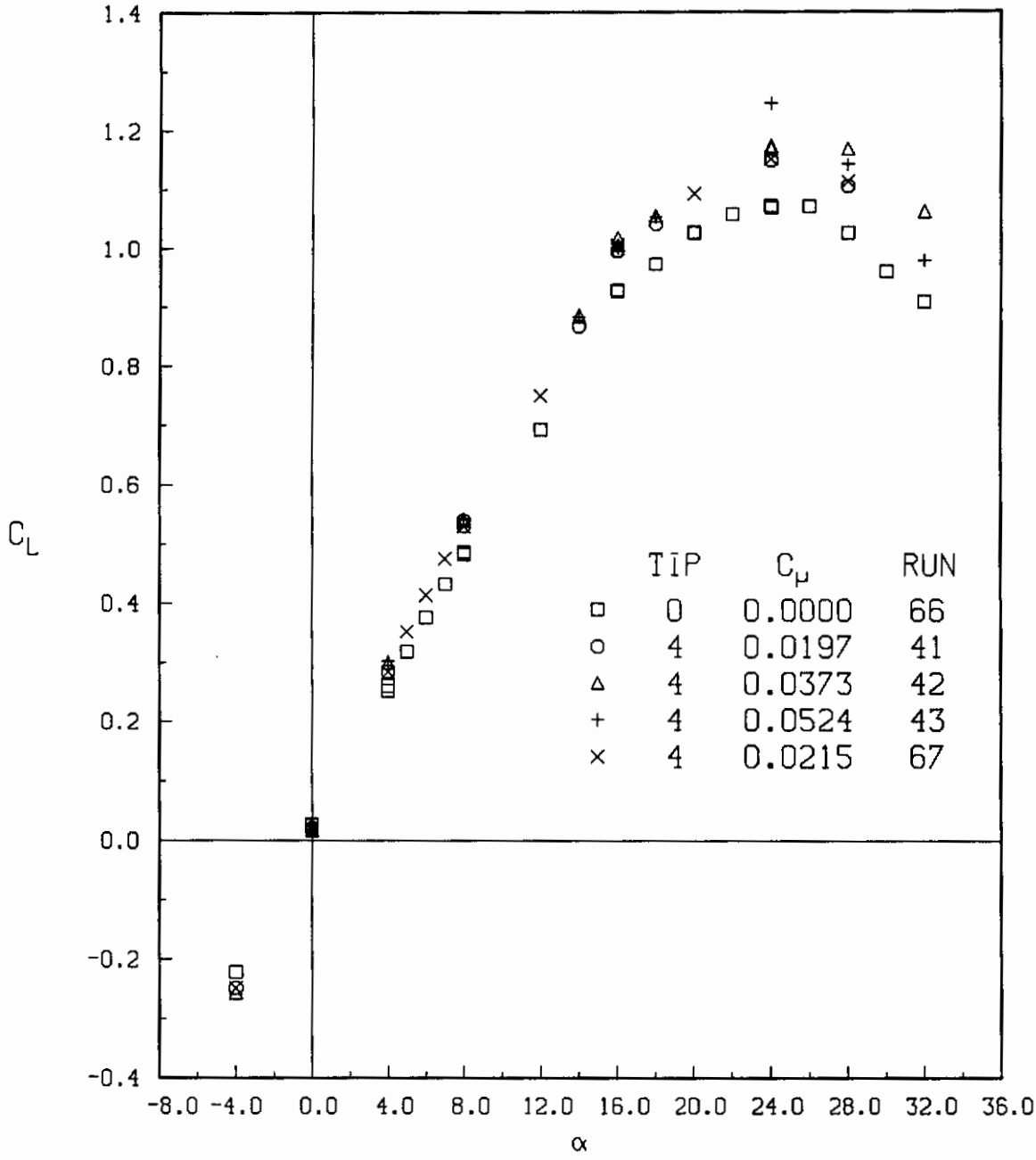

(a) Lift Coefficient

Figure 32.- Measured lift and drag coefficients on Wing C-BT with Tip No. 4.

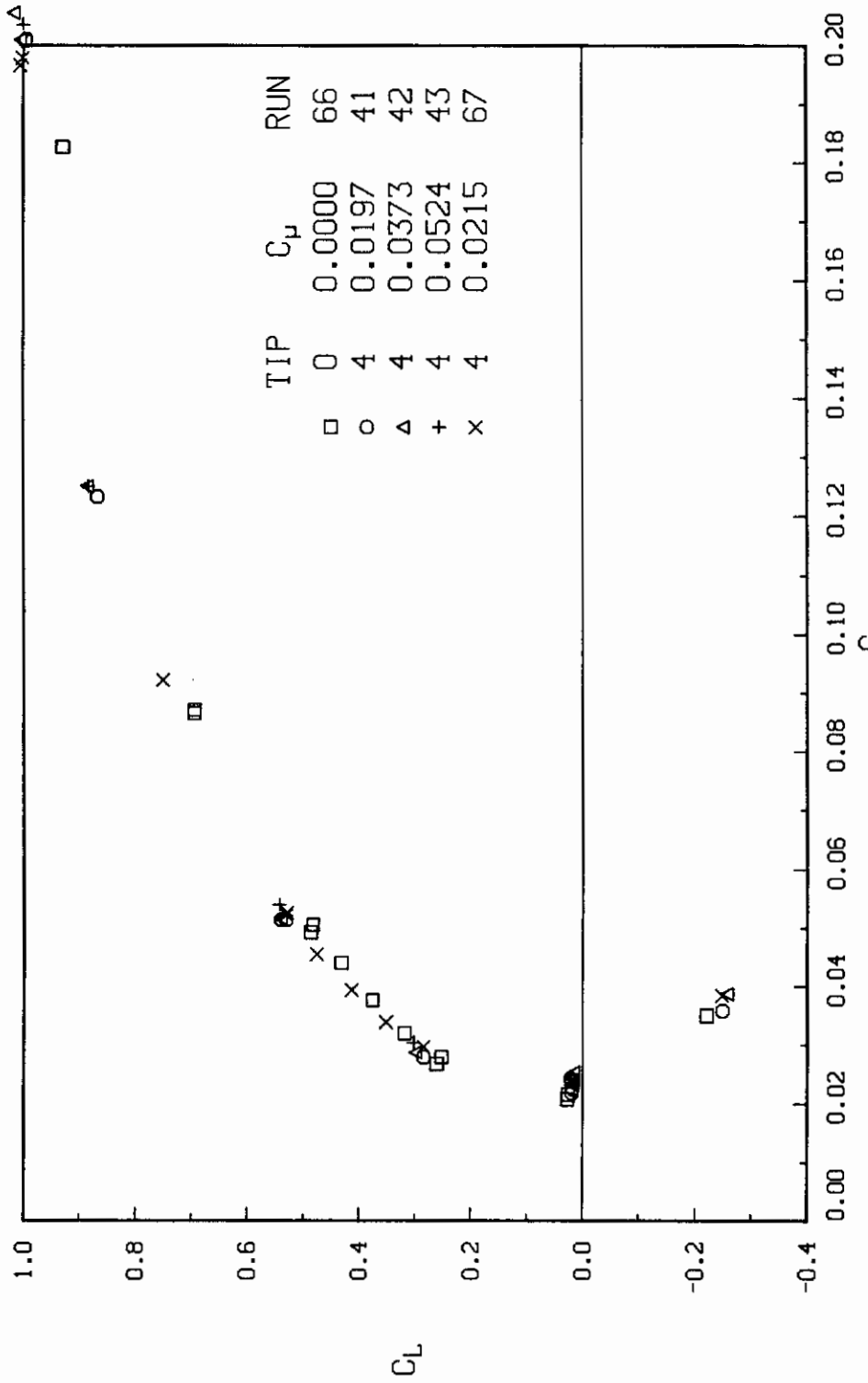

(b) Drag coefficient

Figure 32.- Concluded.

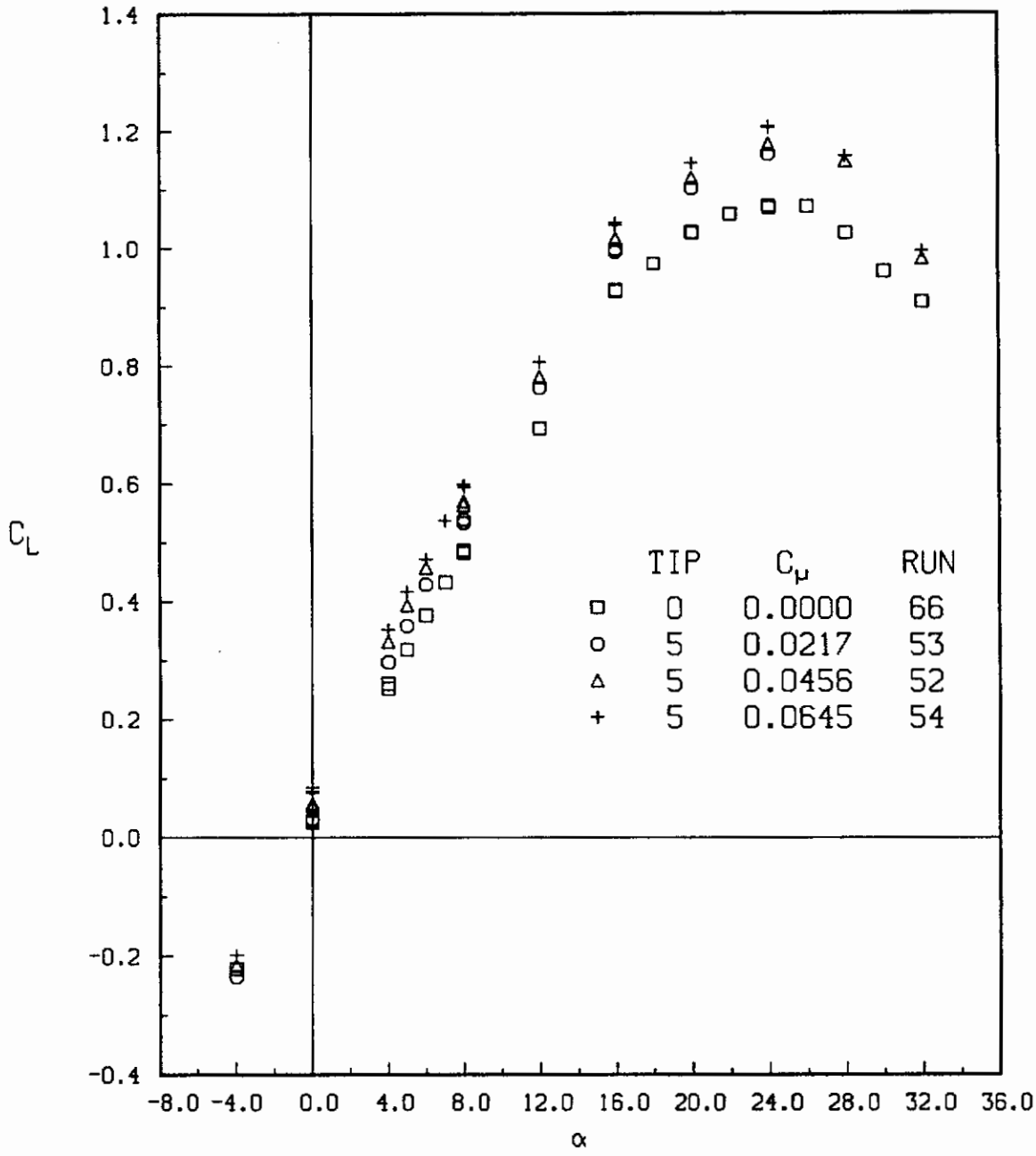

(a) Lift Coefficient

Figure 33.- Measured lift and drag coefficients on Wing C-BT with Tip No. 5.

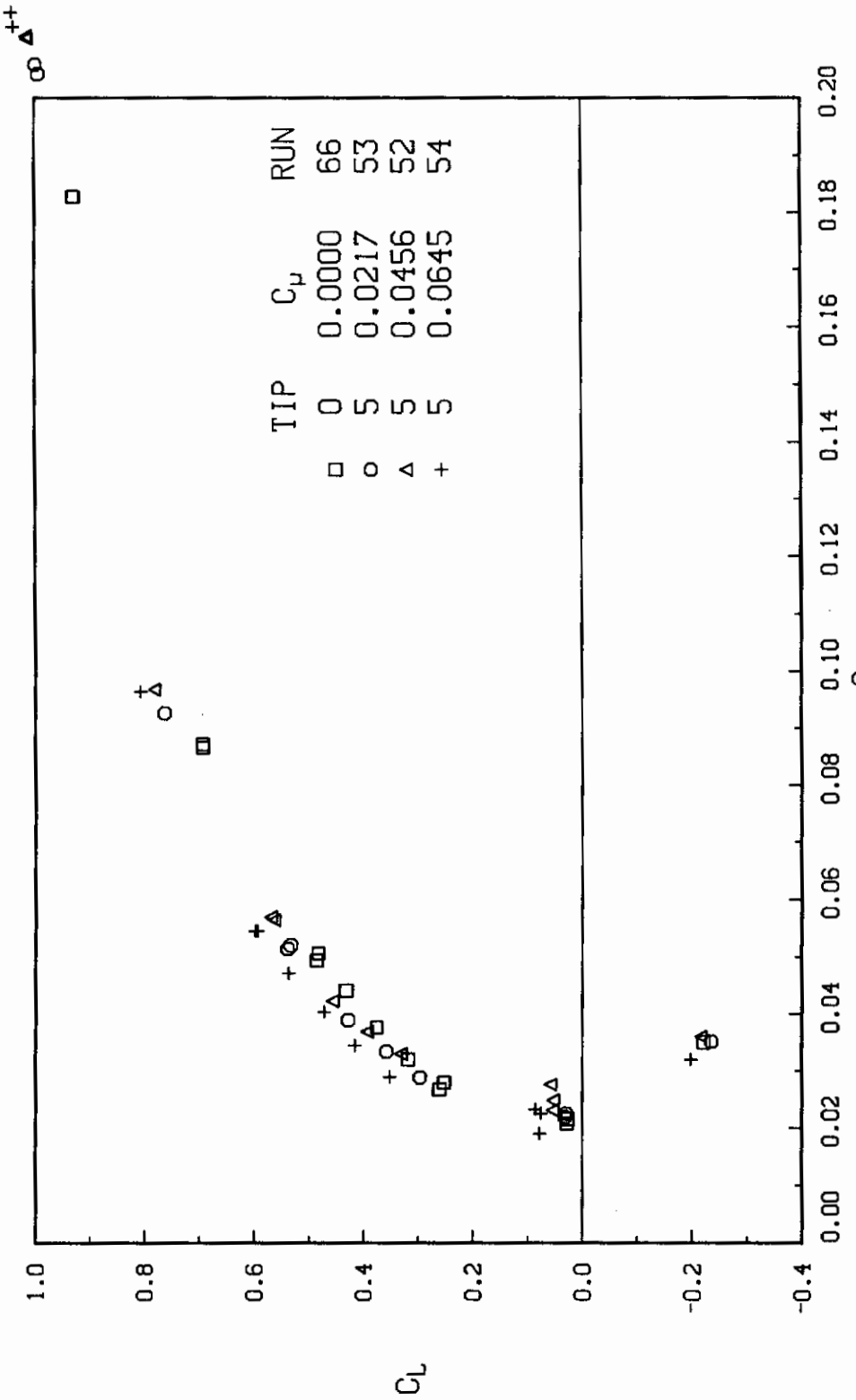

(b) Drag coefficient

Figure 33.- Concluded.

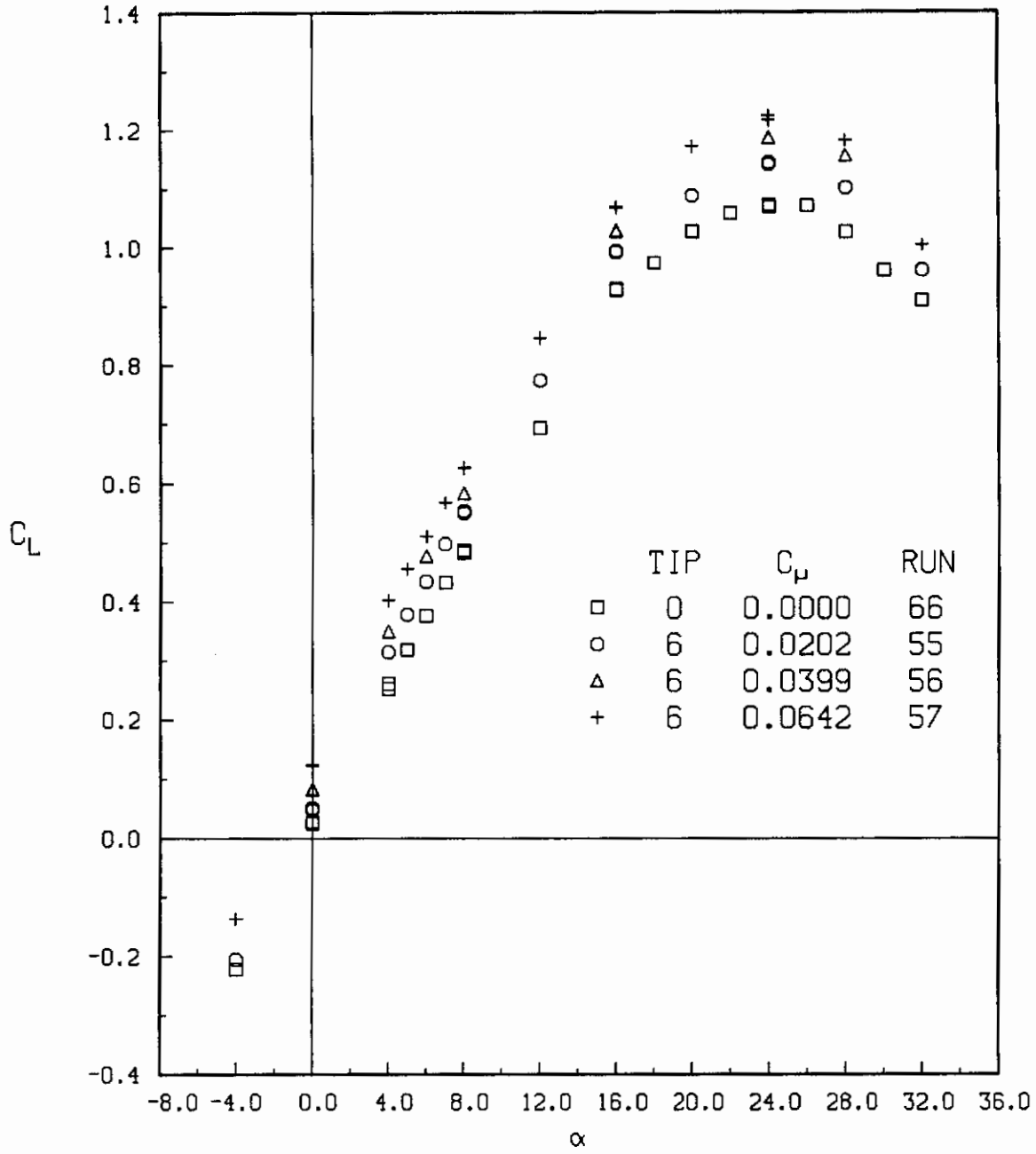

(a) Lift coefficient

Figure 34.- Measured lift and drag coefficients on Wing C-BT with Tip No. 6.

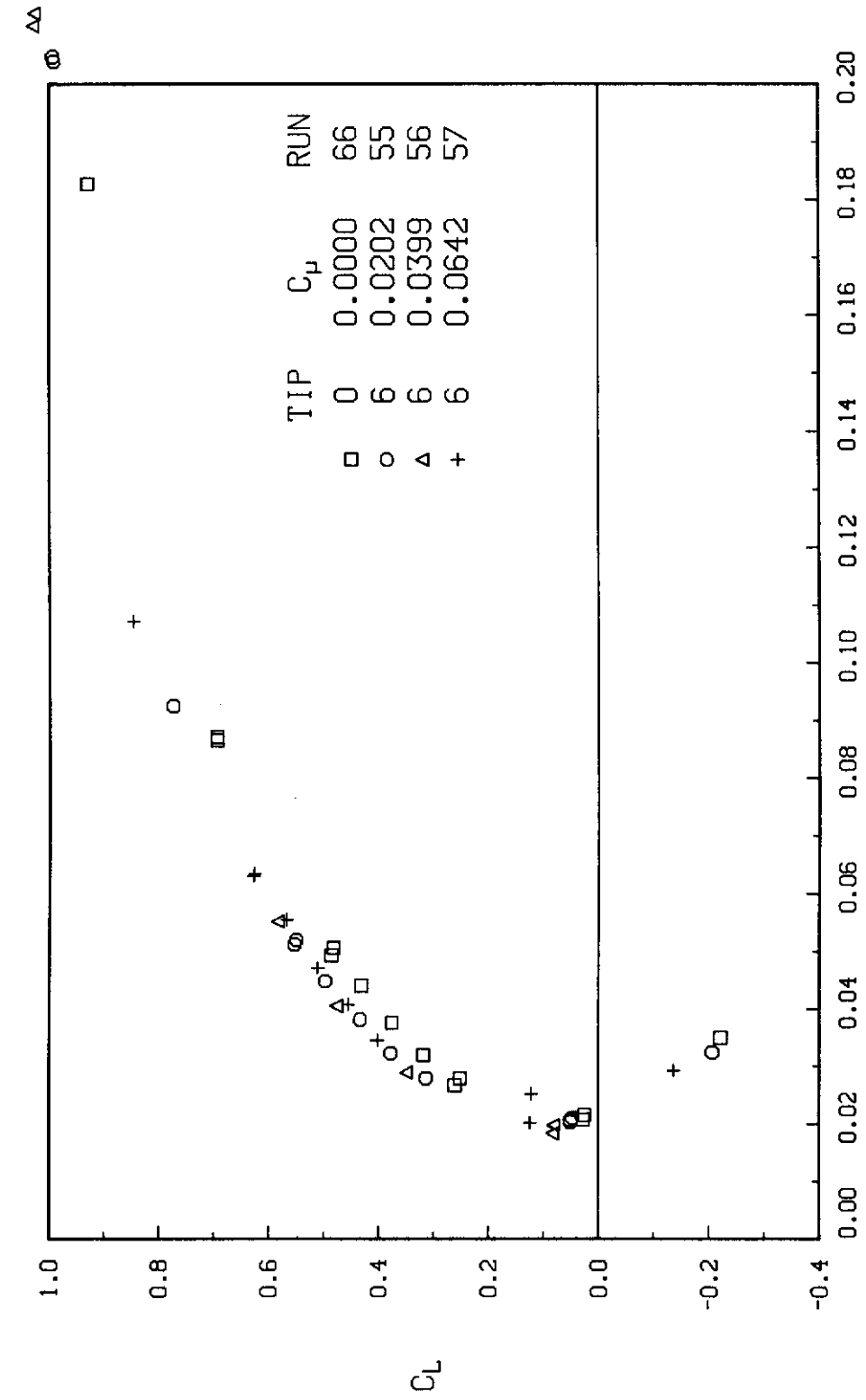

(b) Drag coefficients

Figure 34.- Concluded.

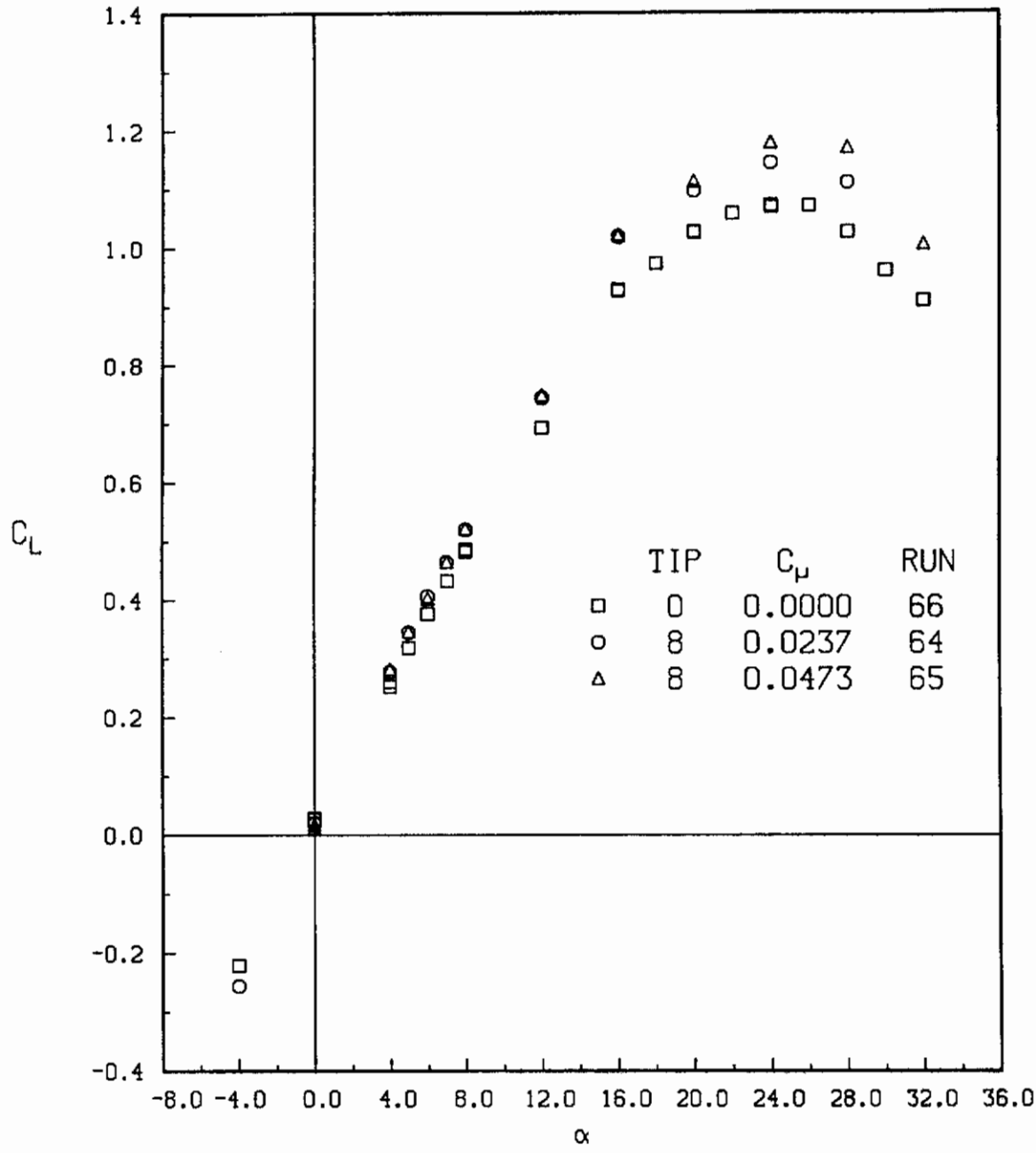

(a) Lift coefficient

Figure 35.- Measured lift and drag coefficients on Wing C-BT with Tip No. 8.

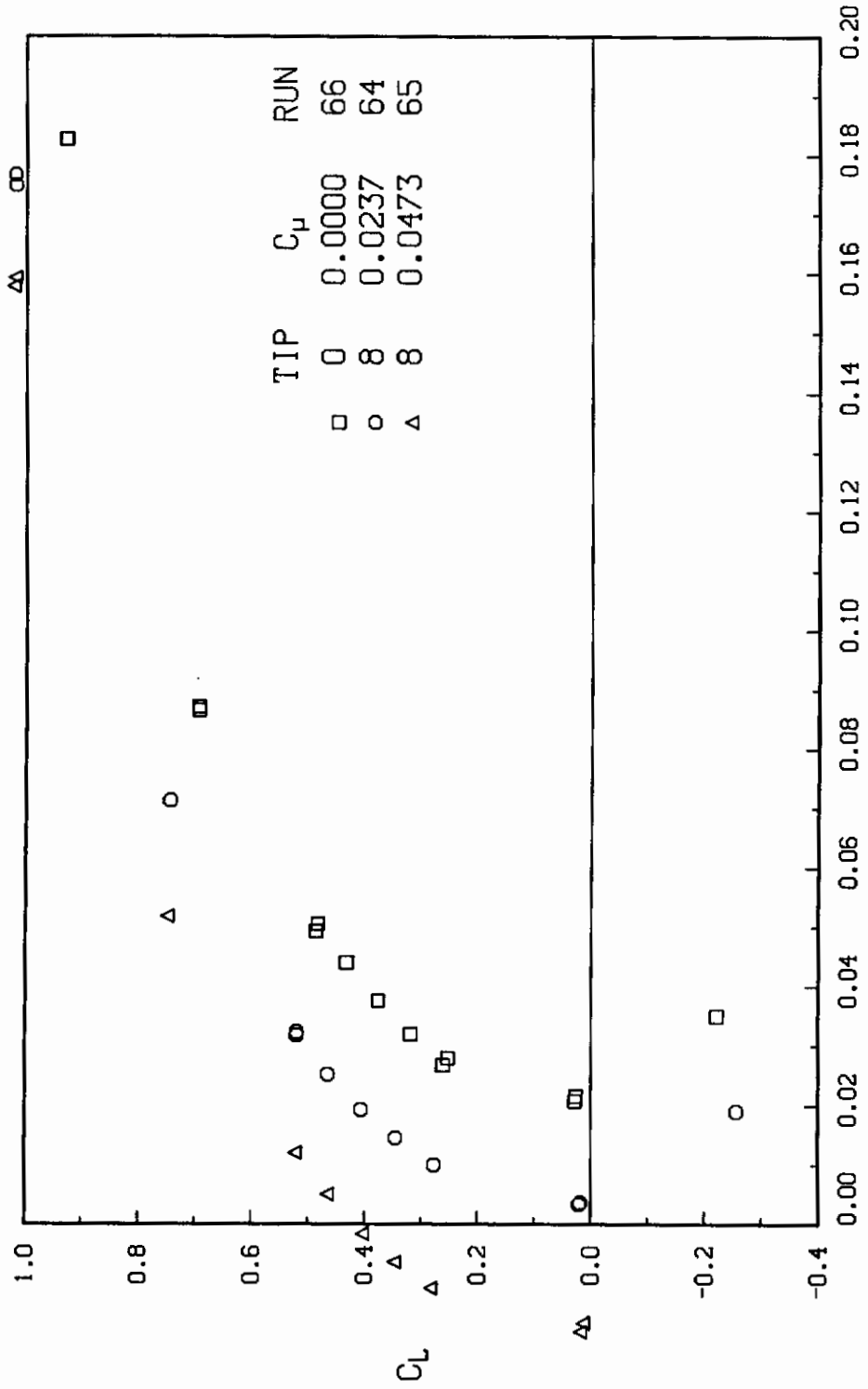

(b) Drag coefficient

Figure 35.- Concluded.

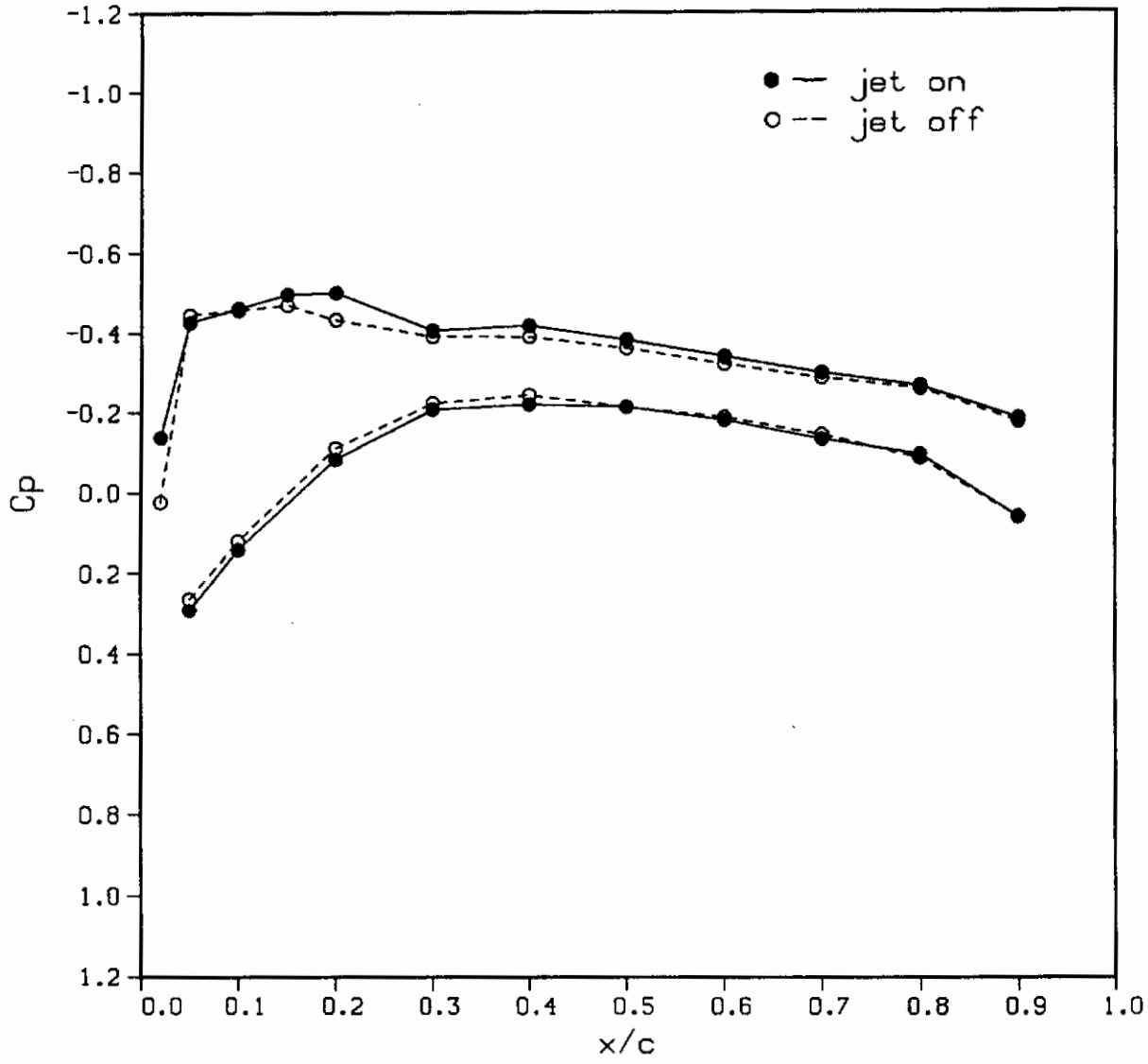

(a) 2y/b = 0.15

Figure 36.- Effect of tip blowing on the measured pressure distribution on Wing C-BT (Tip No. 2) at $\alpha = 5°$, $C_\mu = 0.02$.

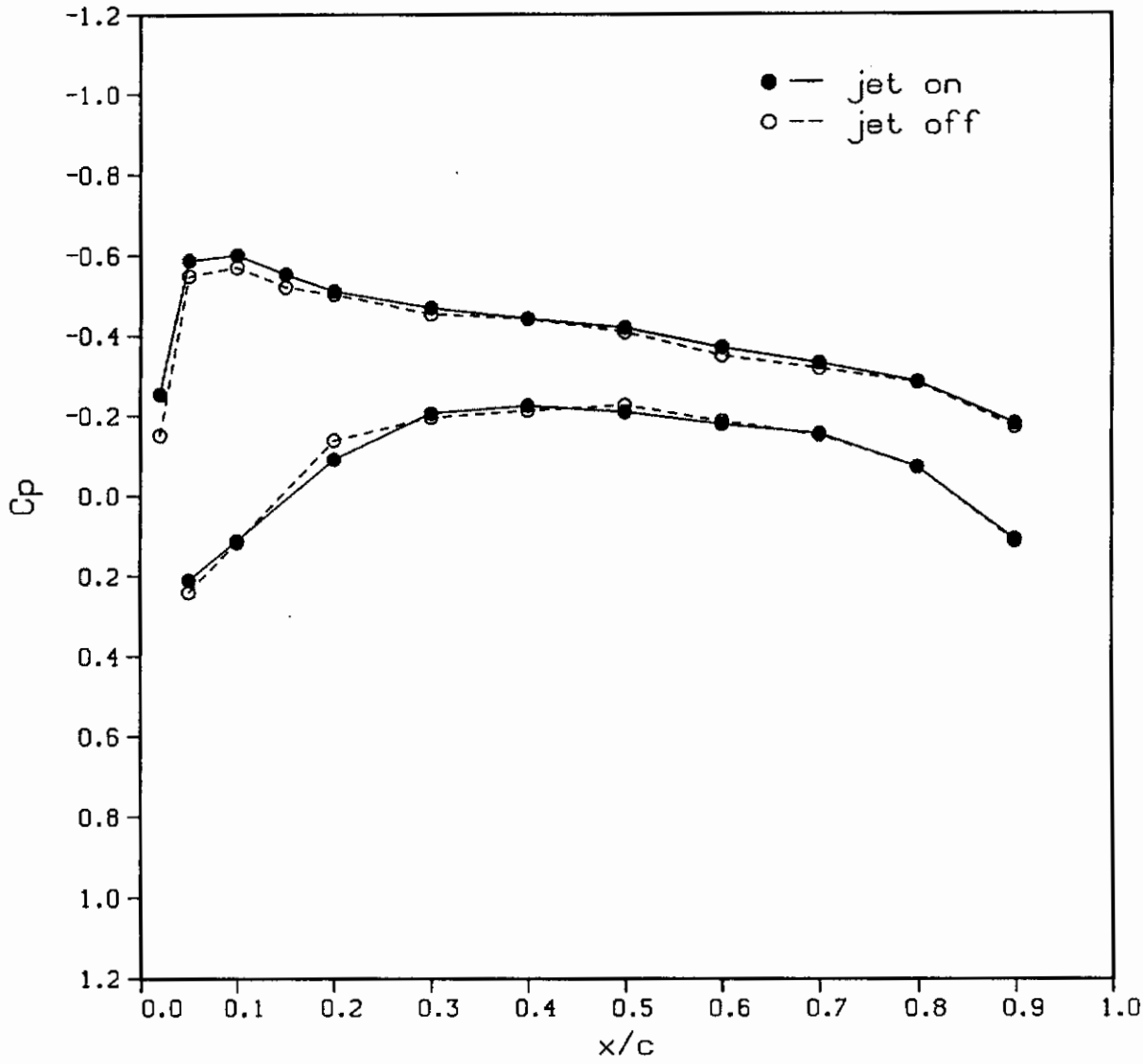

(b) $2y/b = 0.296$

Figure 36.- Continued.

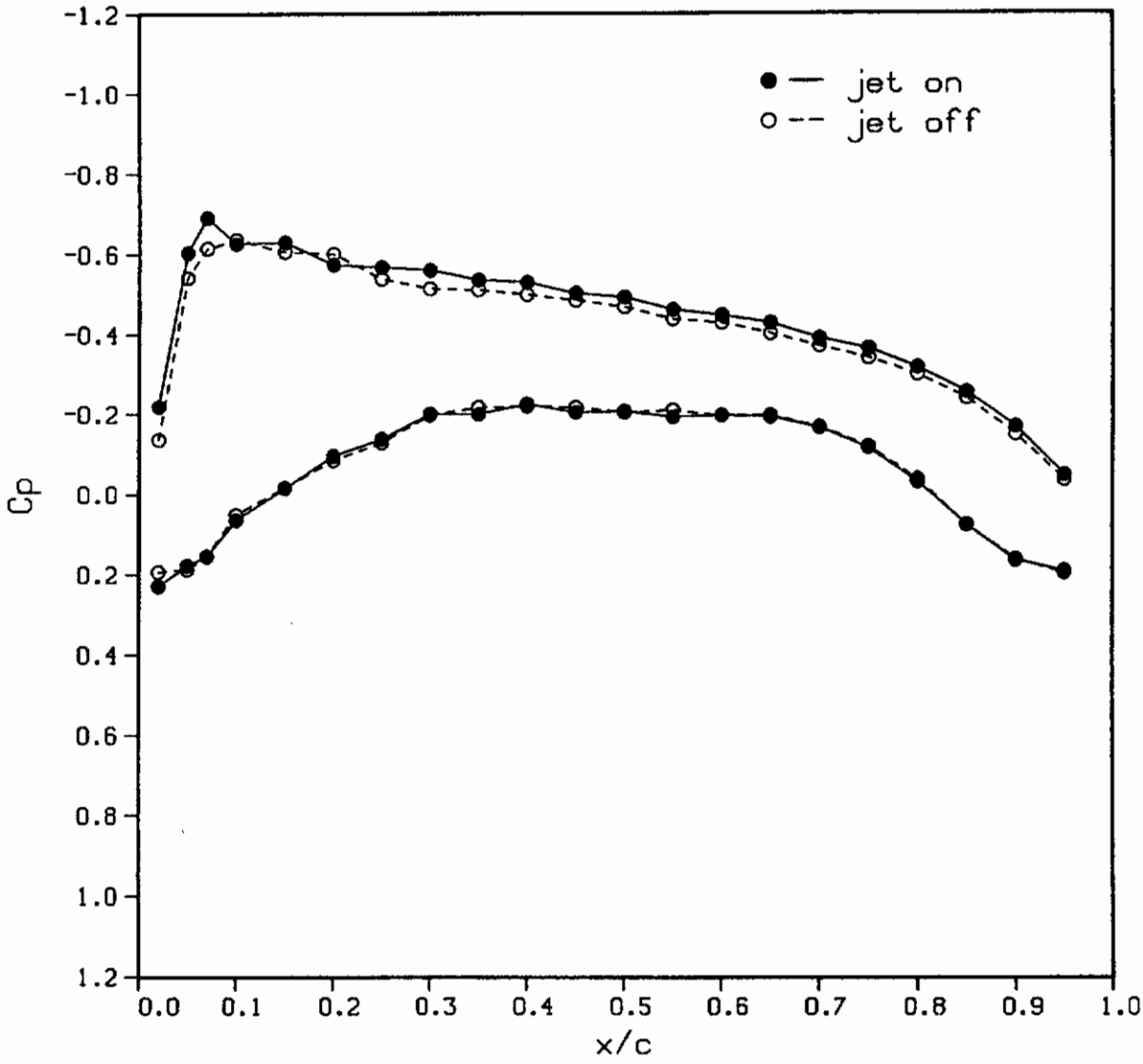

(c) 2y/b = 0.50

Figure 36.- Continued.

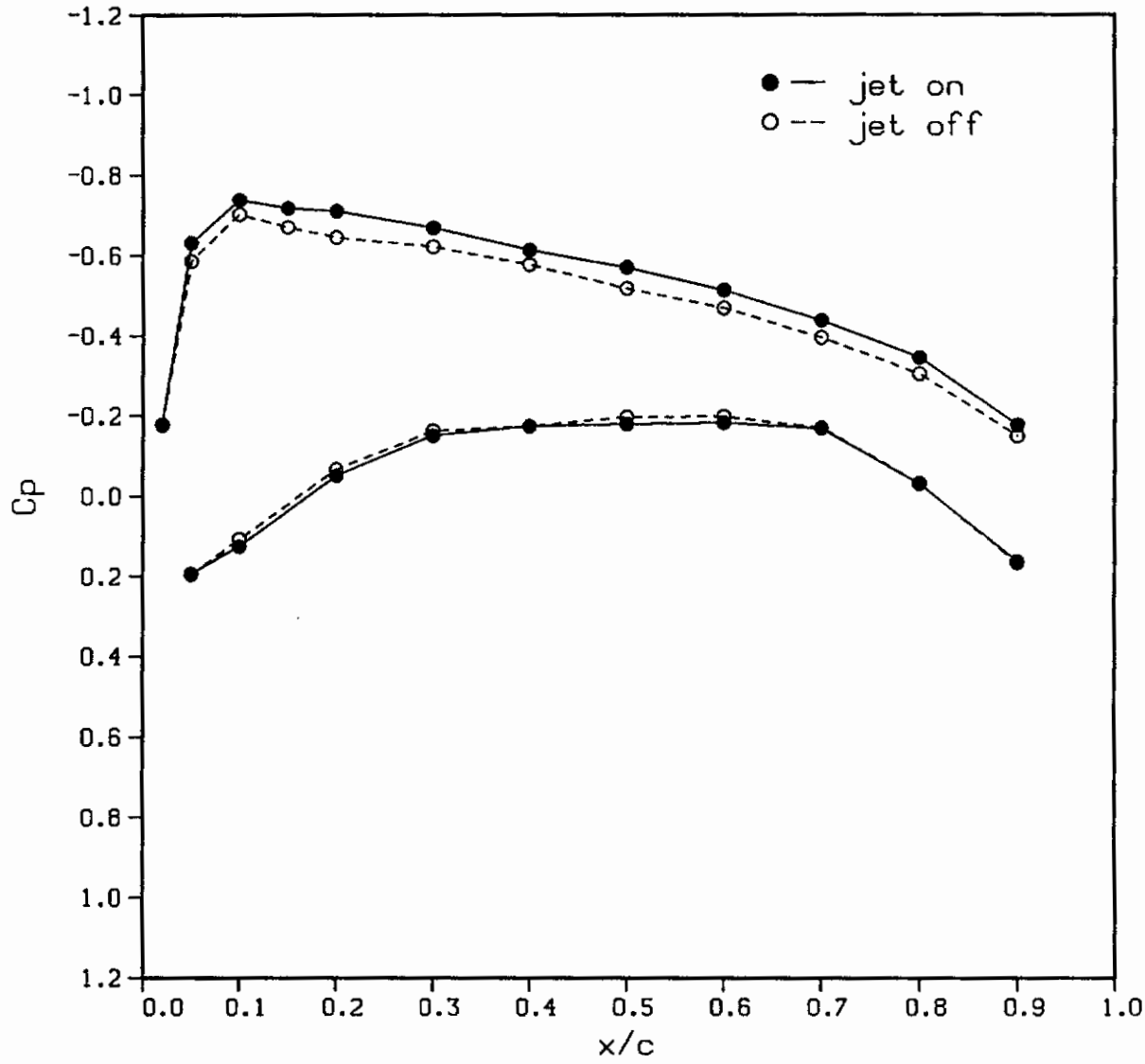

(d) 2y/b = 0.697

Figure 36.- Continued.

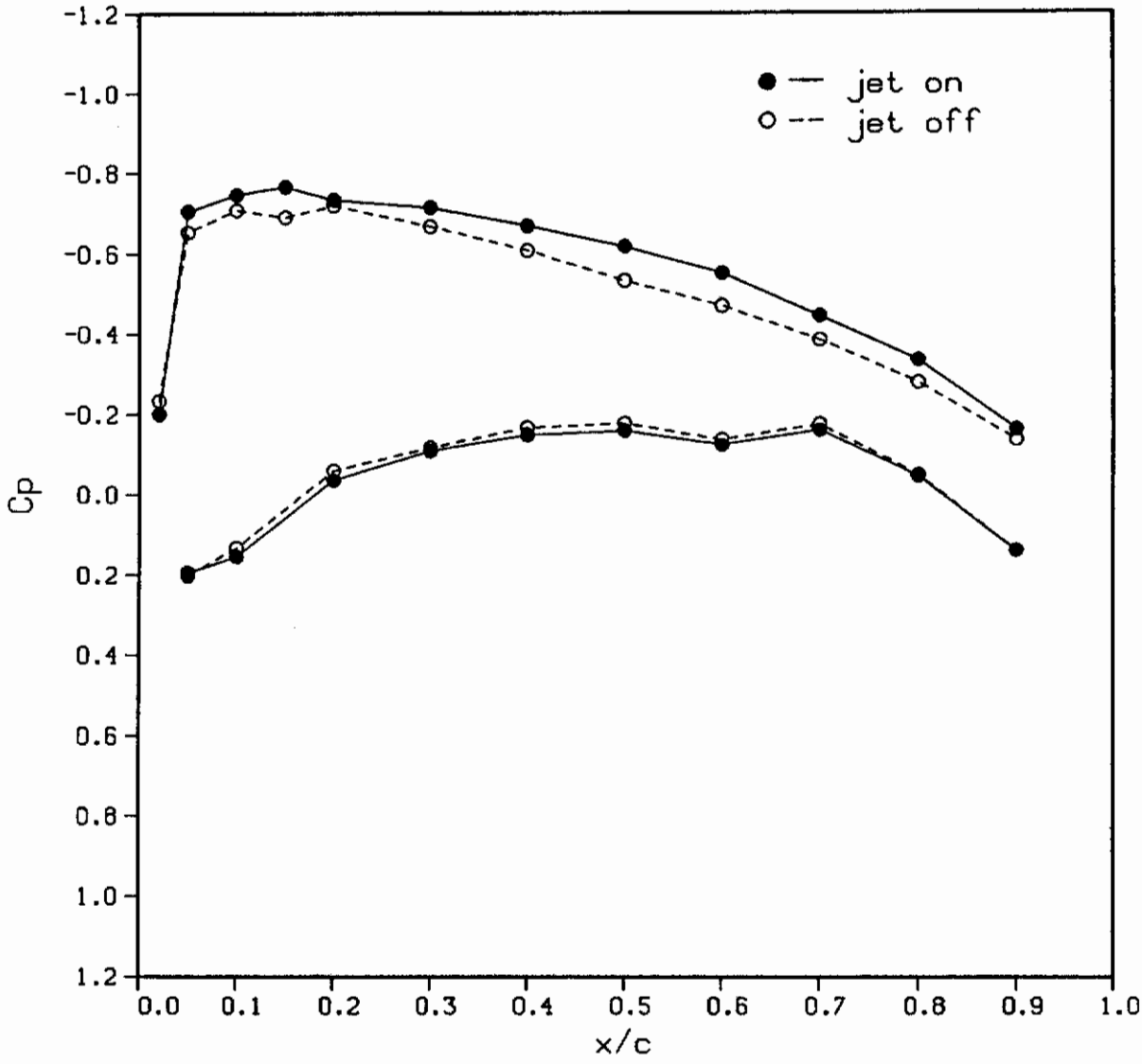

(e) 2y/b = 0.80

Figure 36.- Continued.

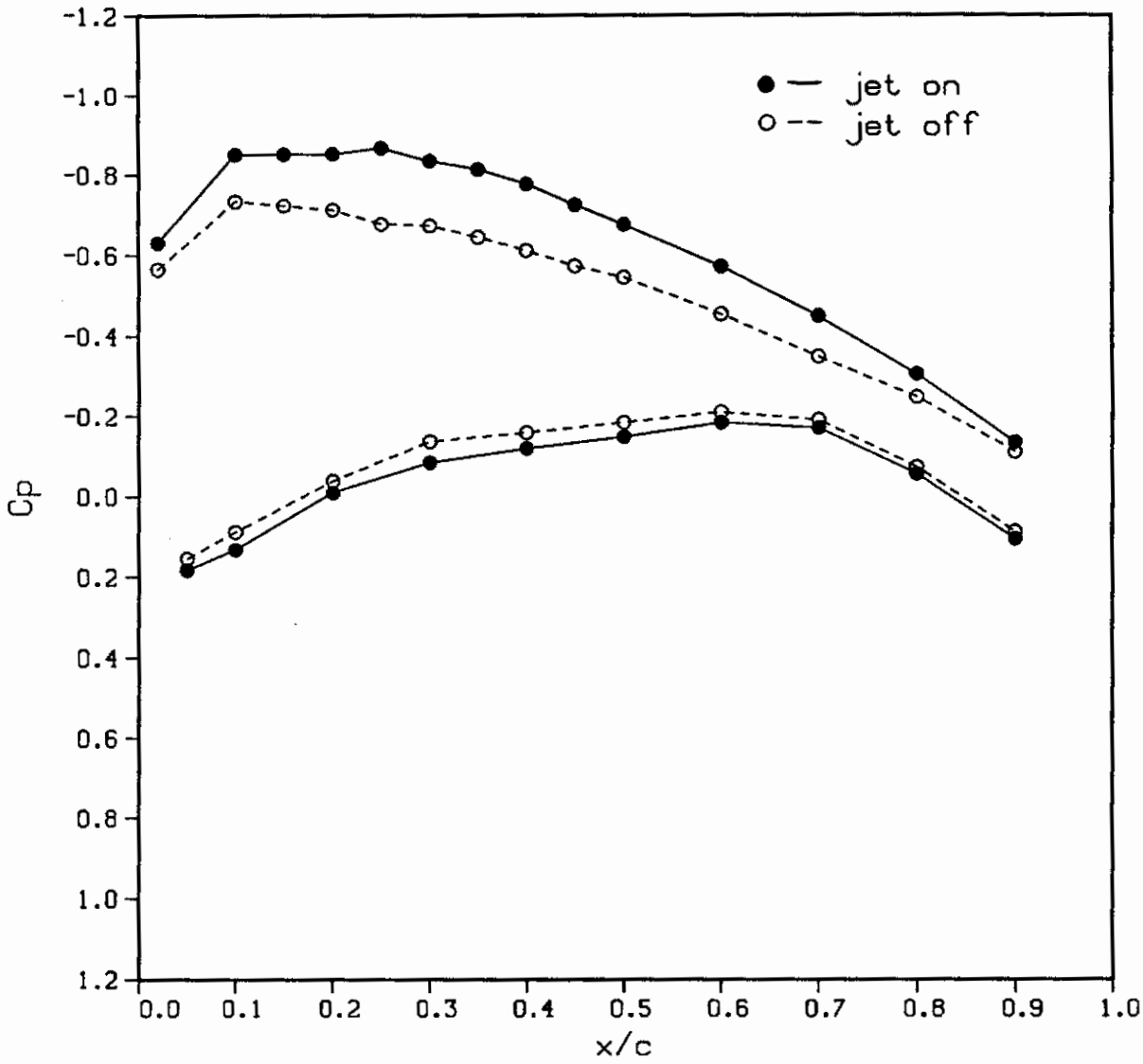

(f) $2y/b = 0.90$

Figure 36.- Continued.

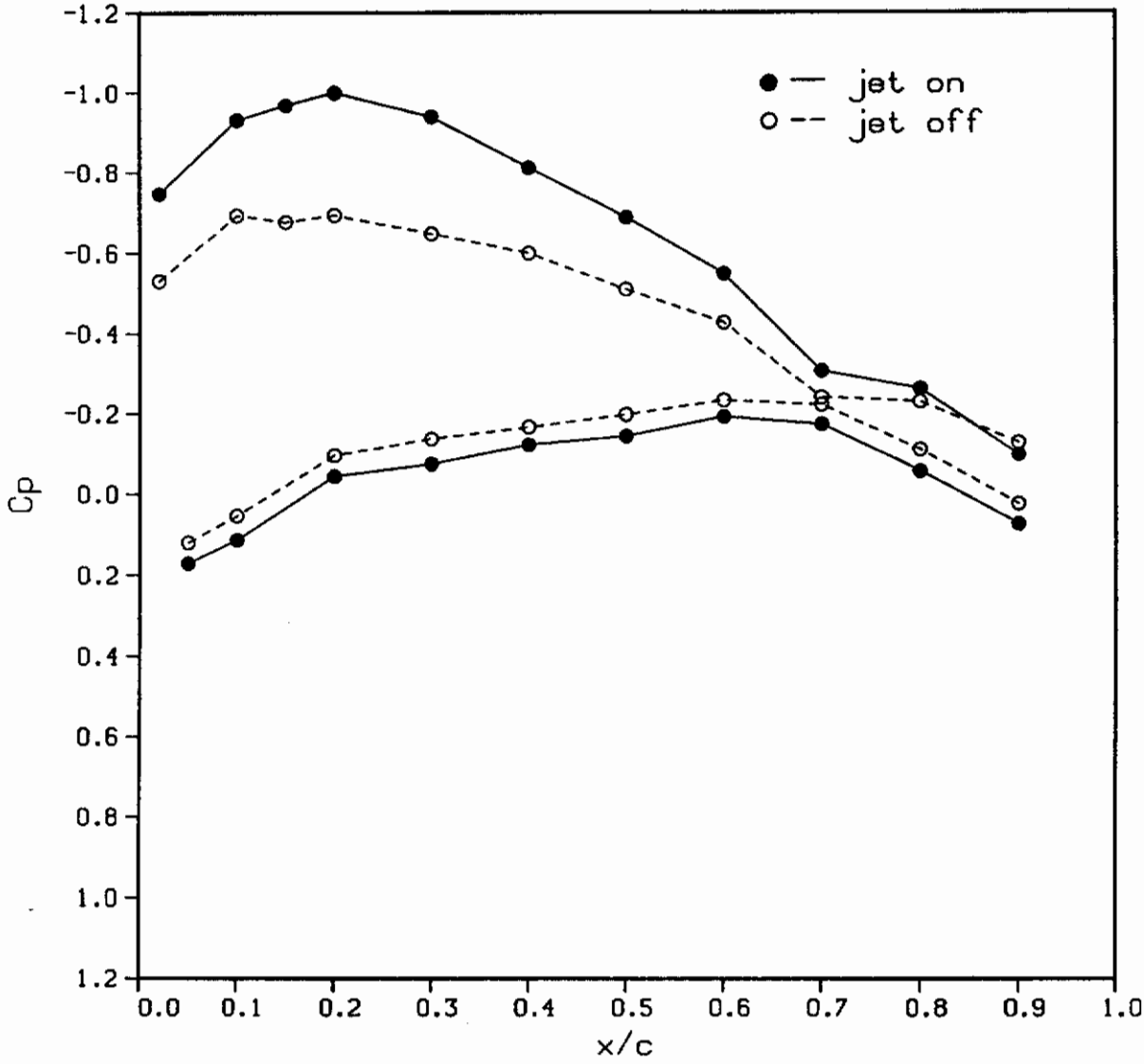

(g) 2y/b = 0.95

Figure 36.- Concluded.

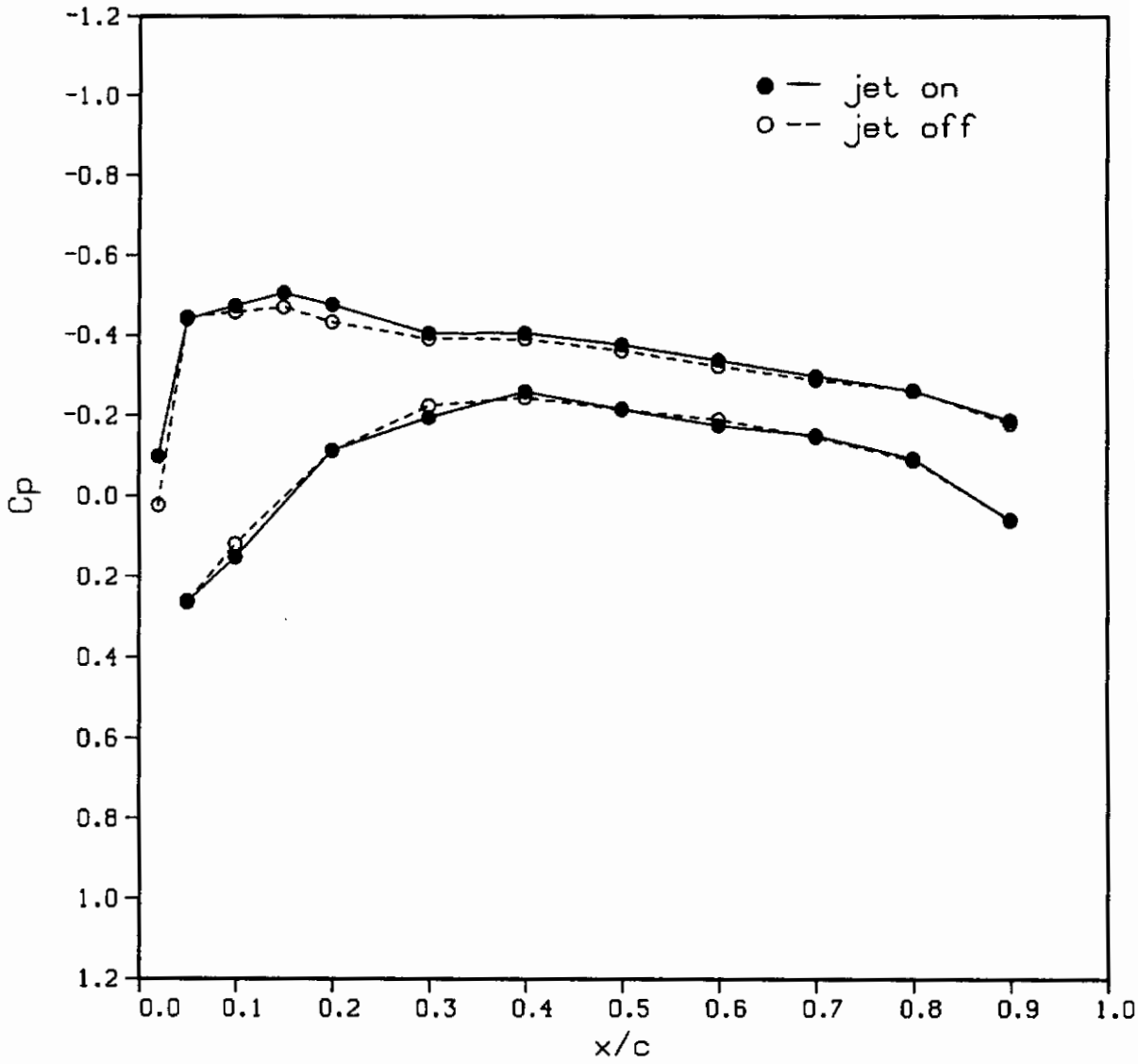

(a) $2y/b = 0.15$

Figure 37.- Effect of tip blowing on the measured pressure distribution on Wing C-BT (Tip No. 4) at $\alpha = 5°$, $C_\mu = 0.02$.

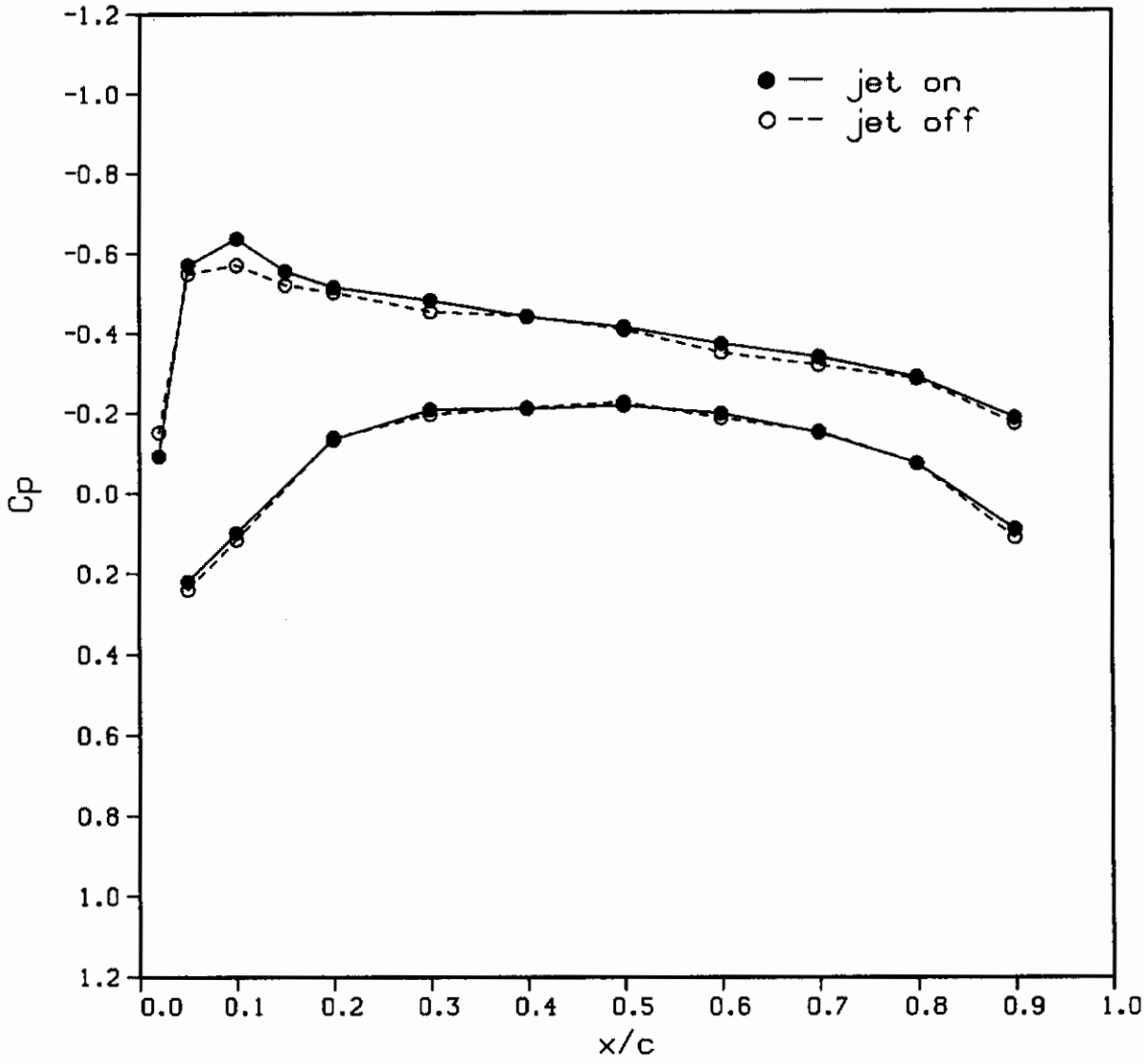

(b) 2y/b = 0.296

Figure 37.- Continued.

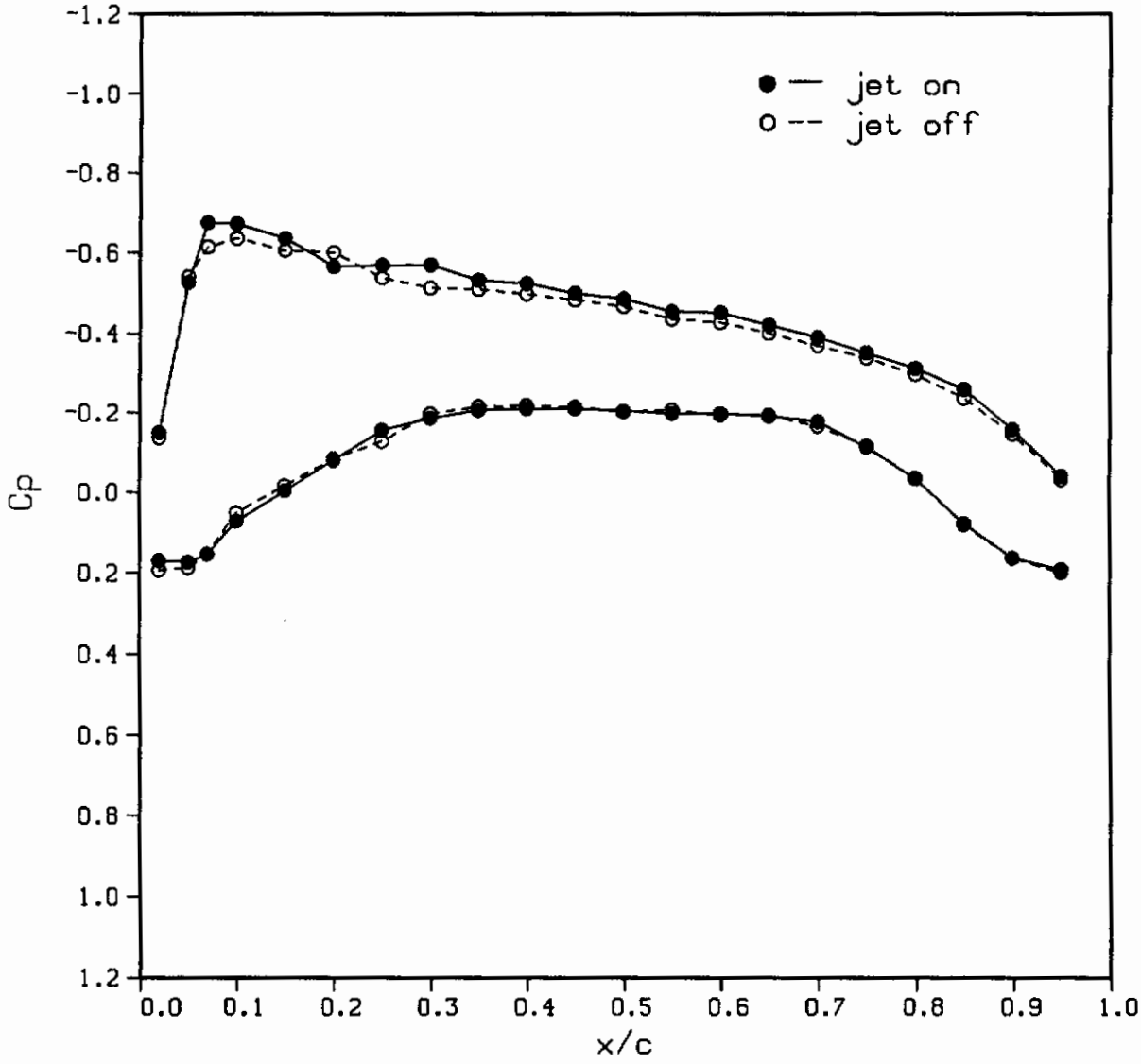

(c) 2y/b = 0.50

Figure 37.- Continued.

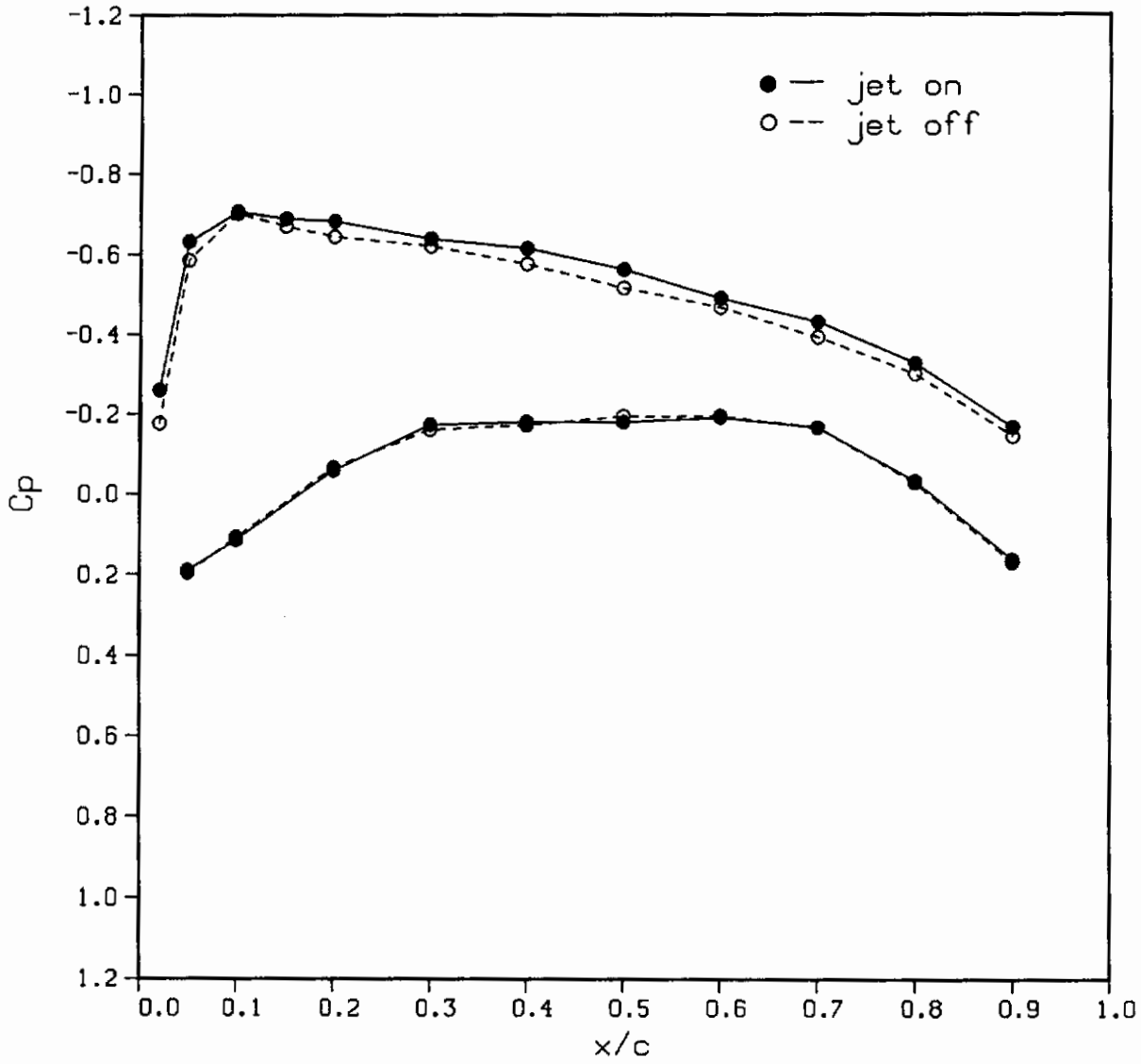

(d) $2y/b = 0.697$

Figure 37.- Continued.

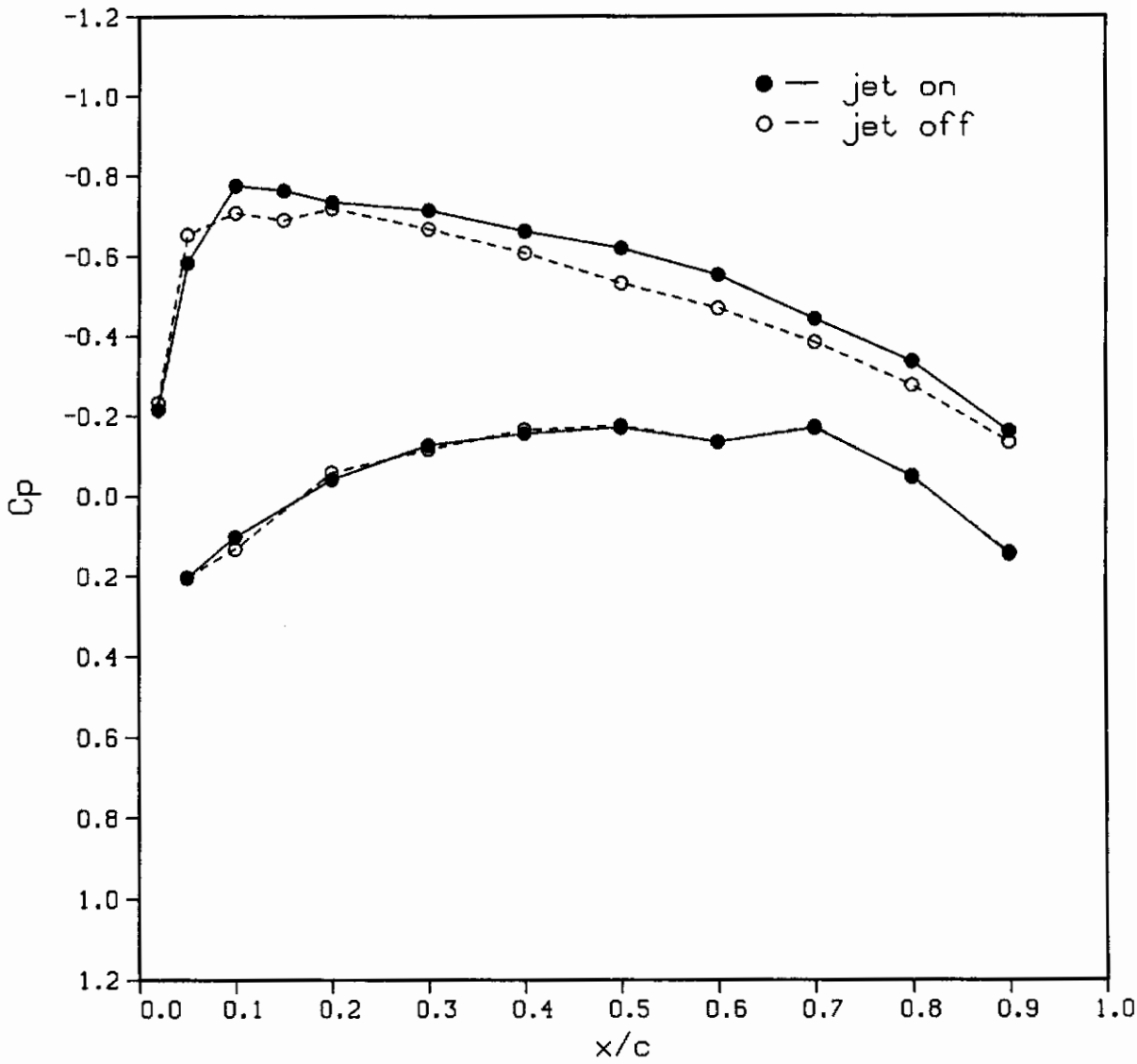

(e) 2y/b = 0.80

Figure 37.- Continued.

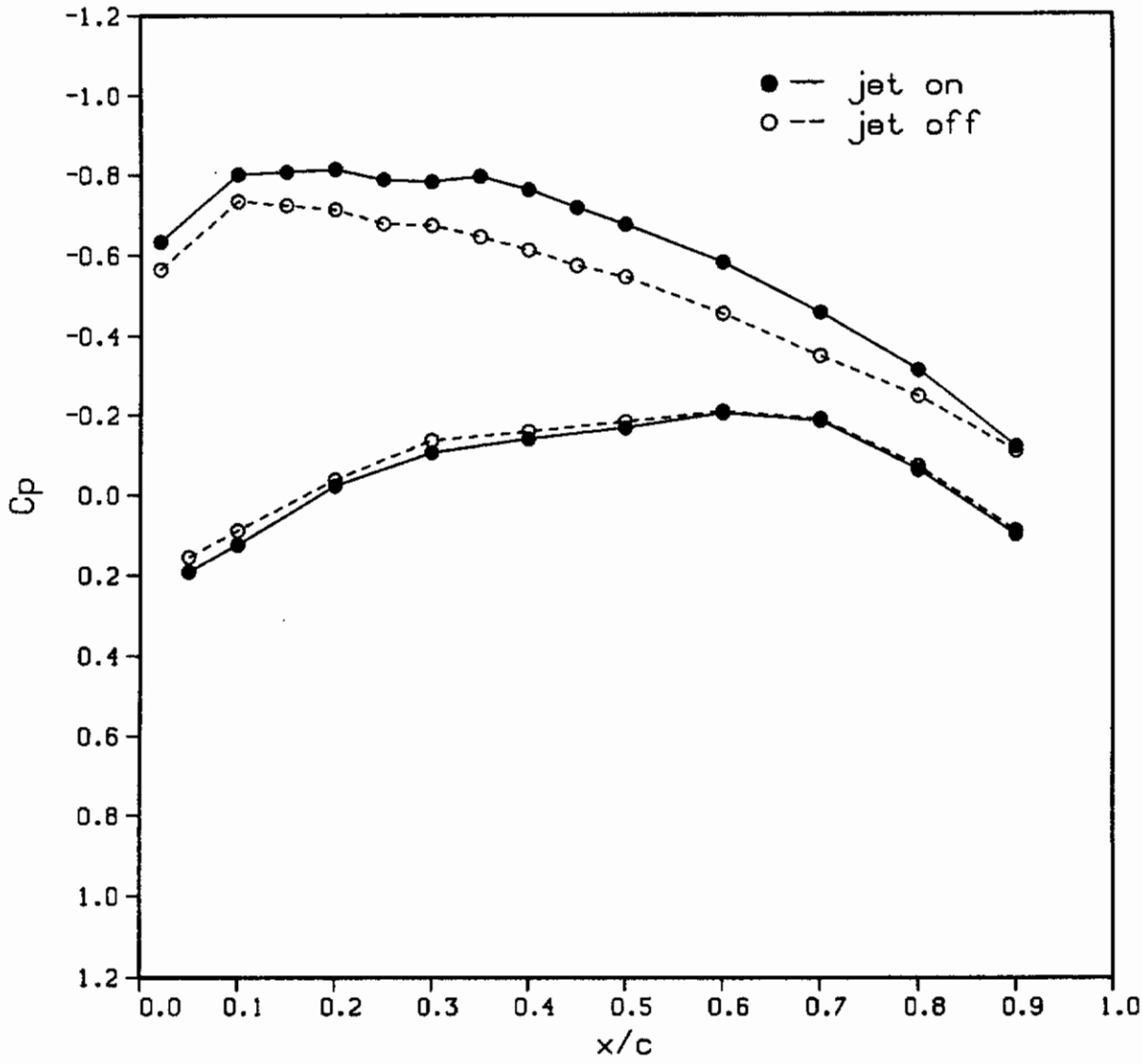

(f) 2y/b = 0.90

Figure 37.- Continued.

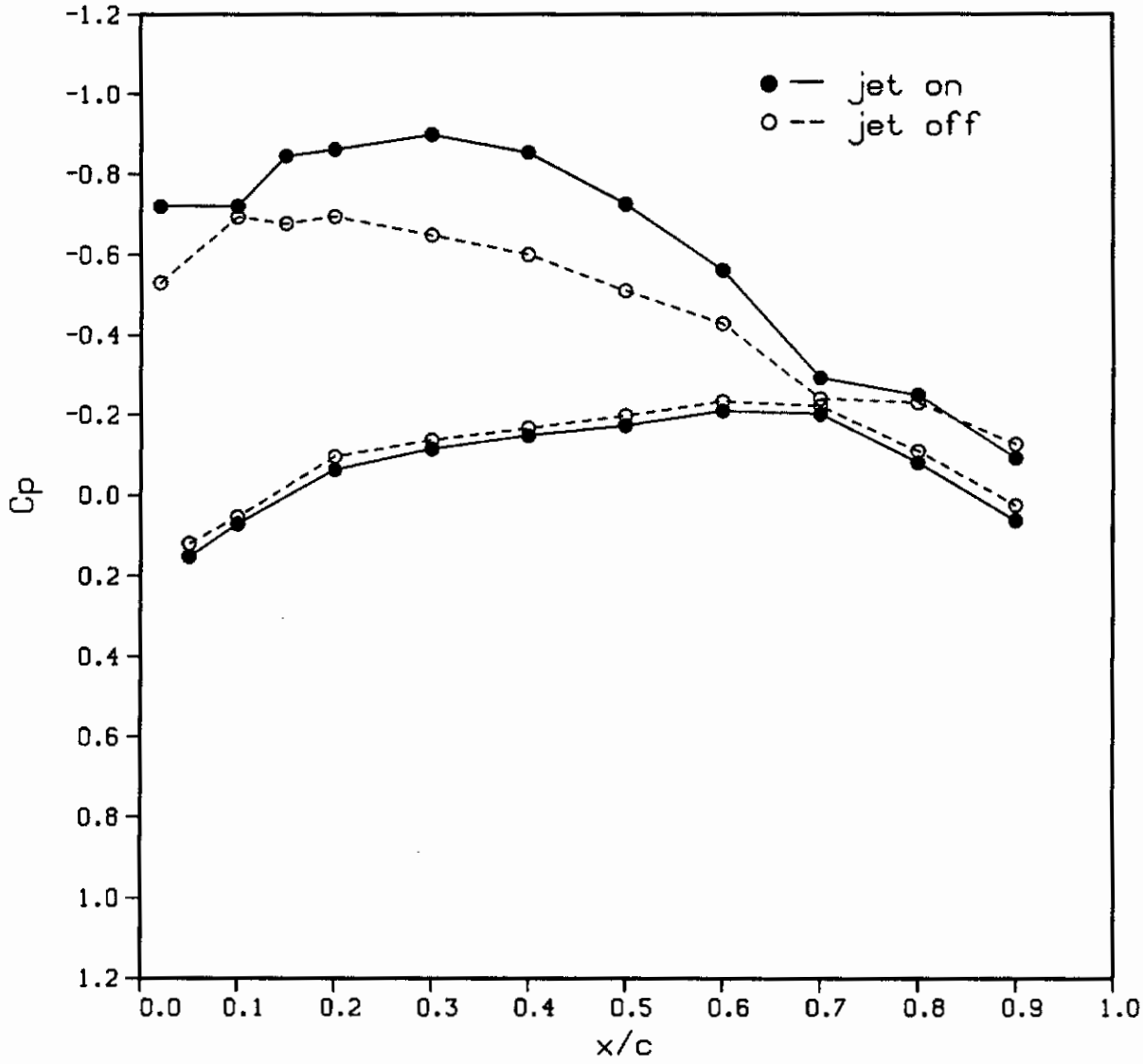

(g) 2y/b = 0.95

Figure 37.- Concluded.

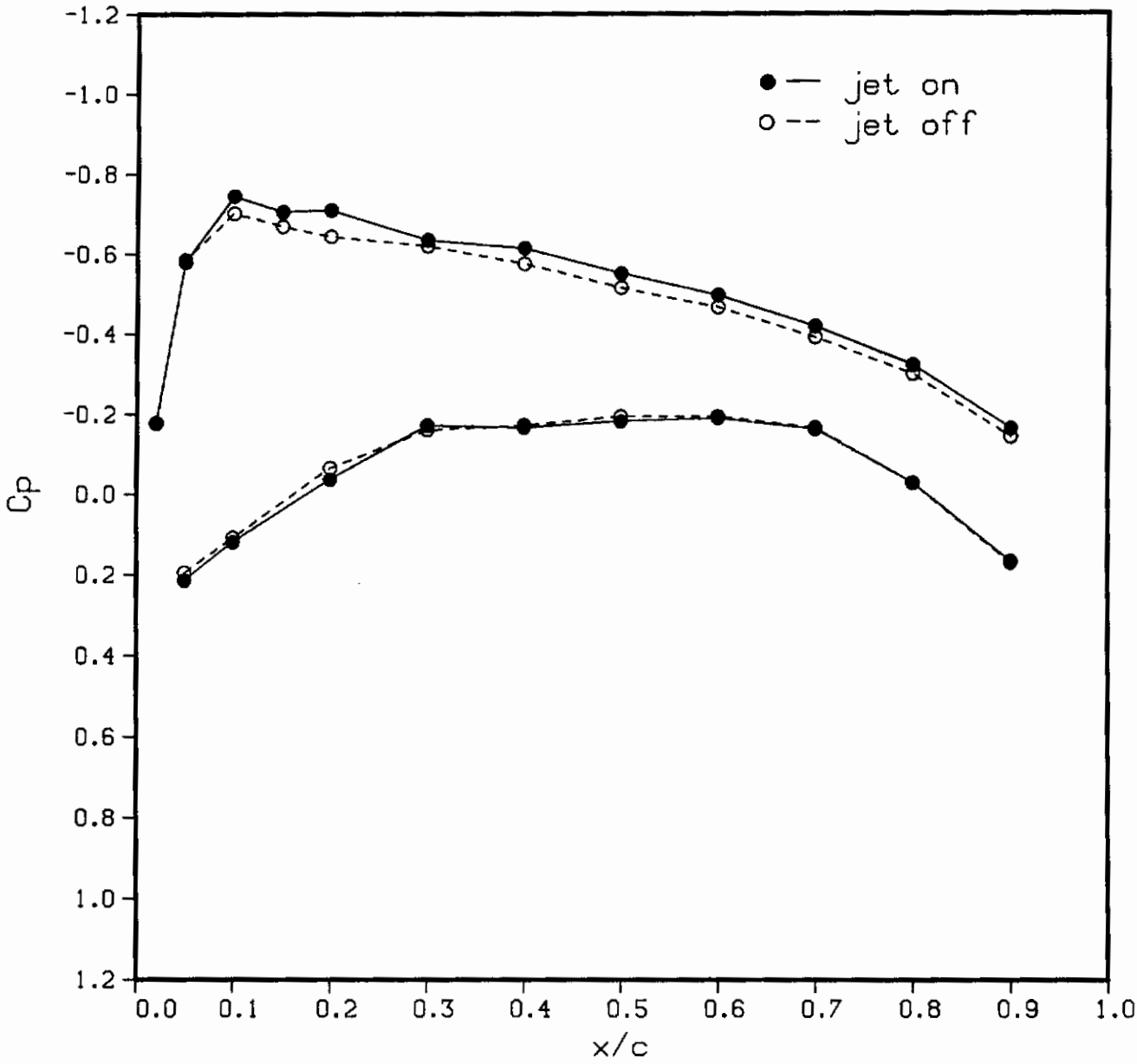

(a) 2y/b = 0.697

Figure 38.- Effect of tip blowing on the measured pressure distribution on Wing C-BT (Tip No. 8) at $\alpha = 5°$, $C_\mu = 0.02$.

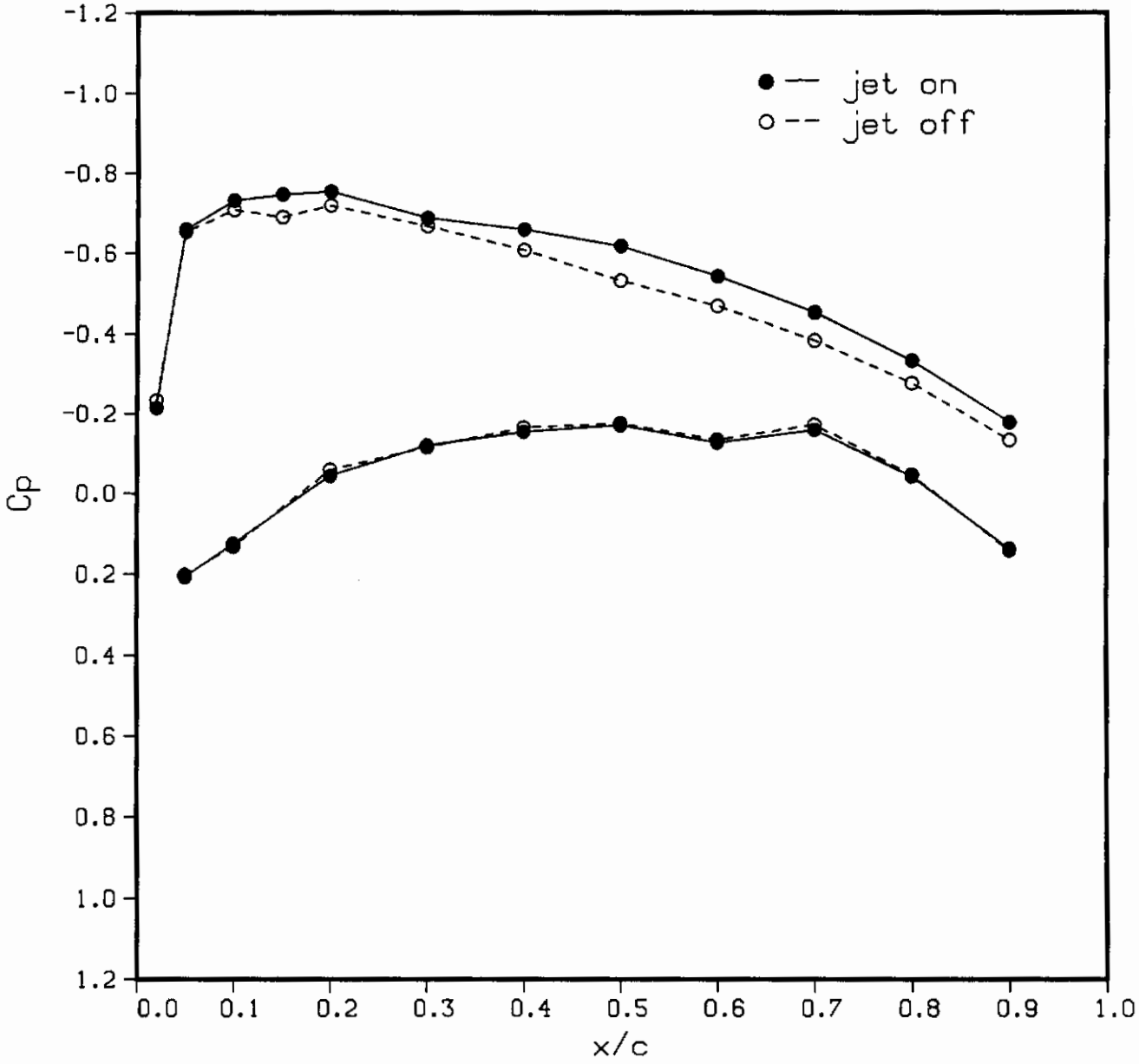

(b) $2y/b = 0.80$

Figure 38.- Continued.

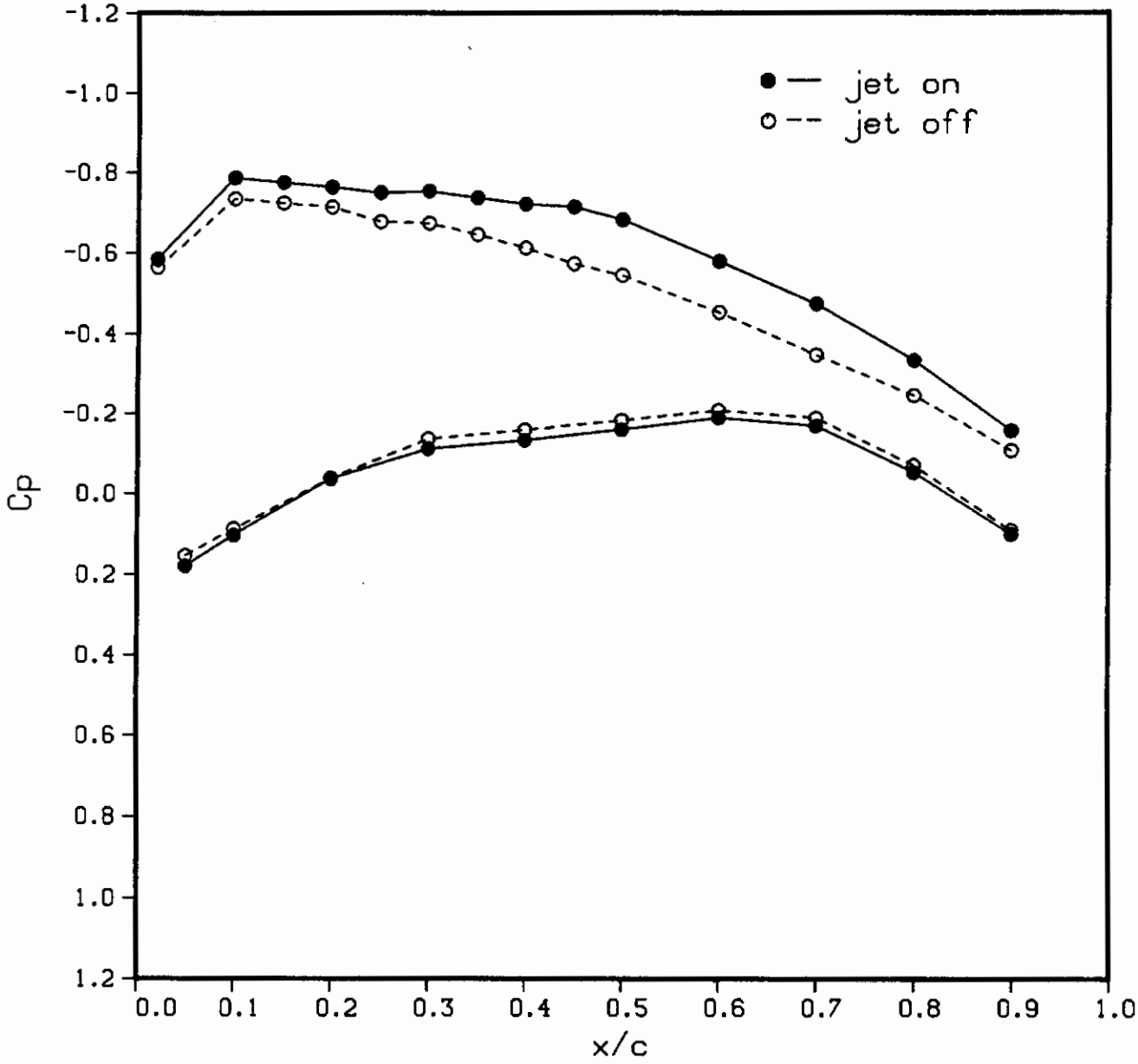

(c) 2y/b = 0.894

Figure 38.- Continued.

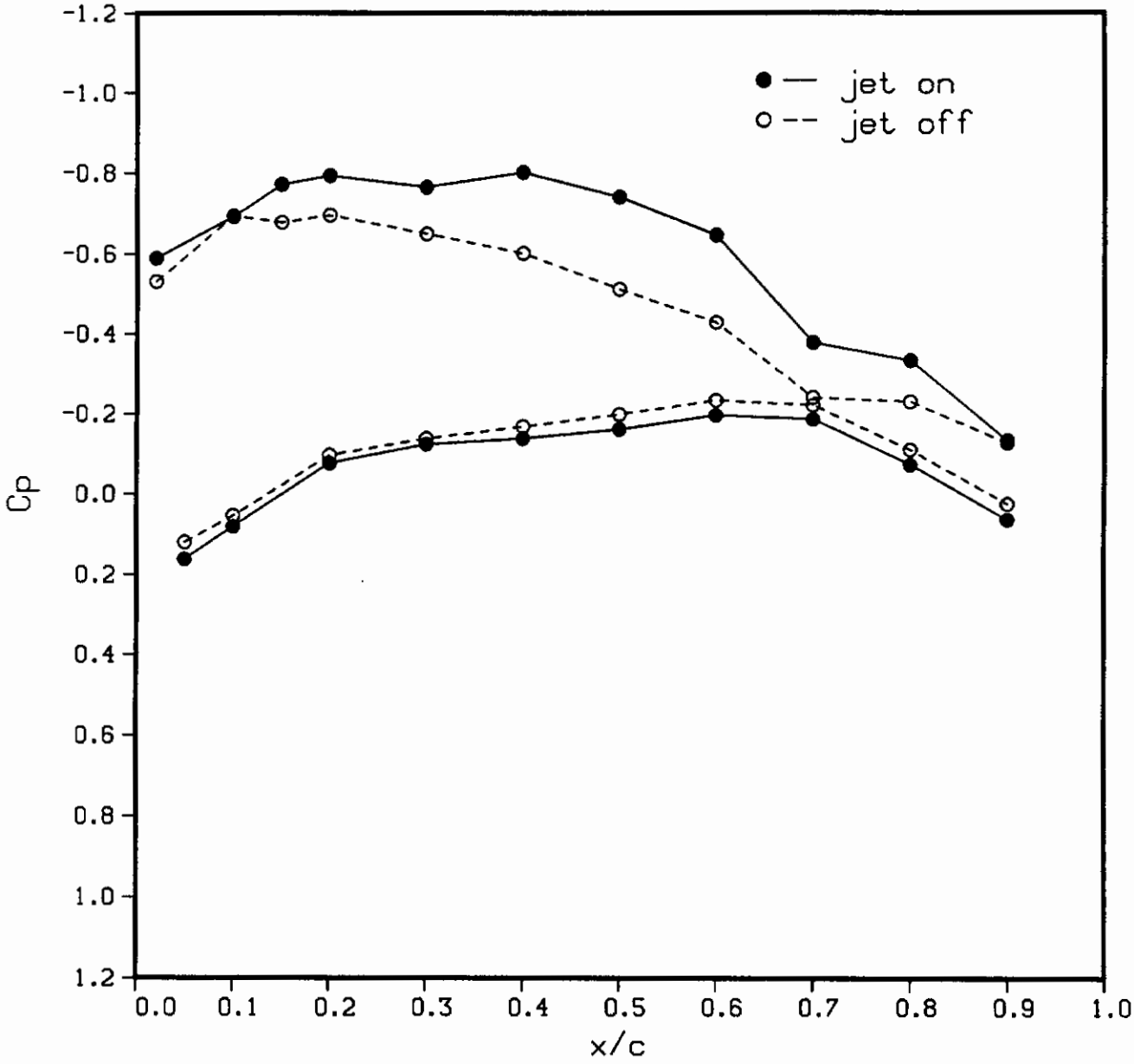

(d) 2y/b = 0.95

Figure 38.- Concluded.

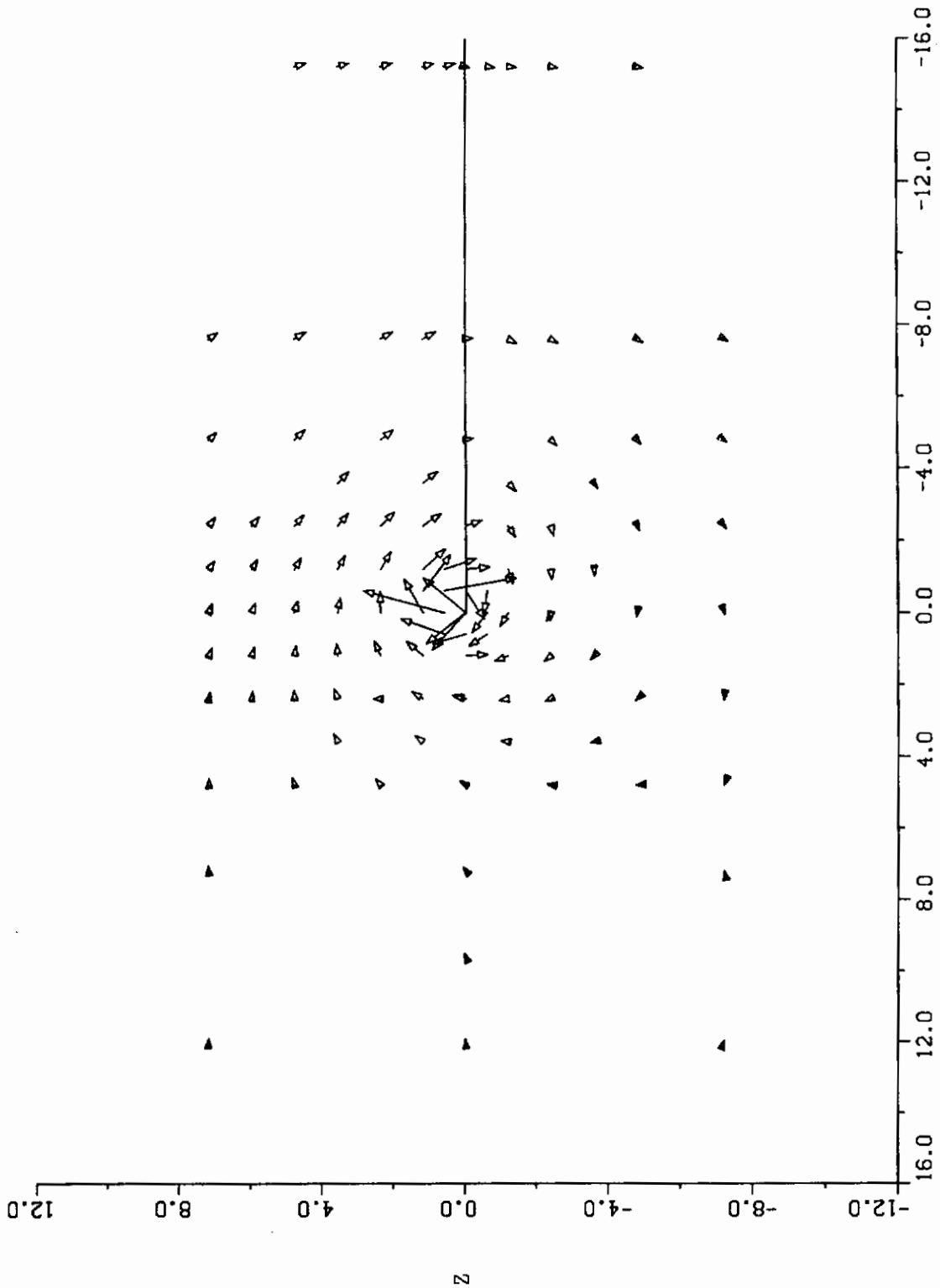

(a) x = 1 inch, C_μ = 0.0

Figure 39.- Flow field surveys aft of wing C-BT at α = 8°.

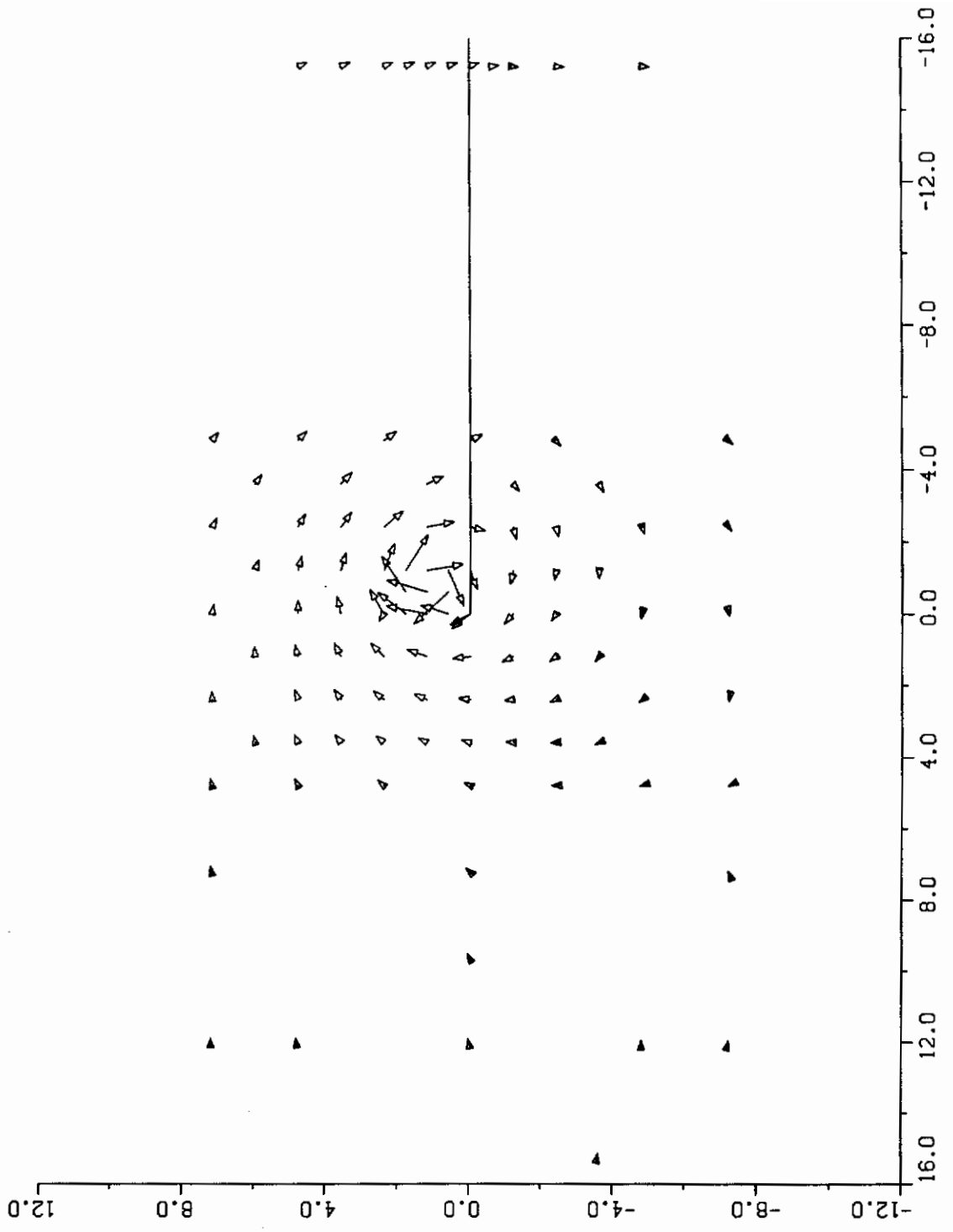

(b) x = 10 inches, C_μ = 0.0

Figure 39.- Continued.

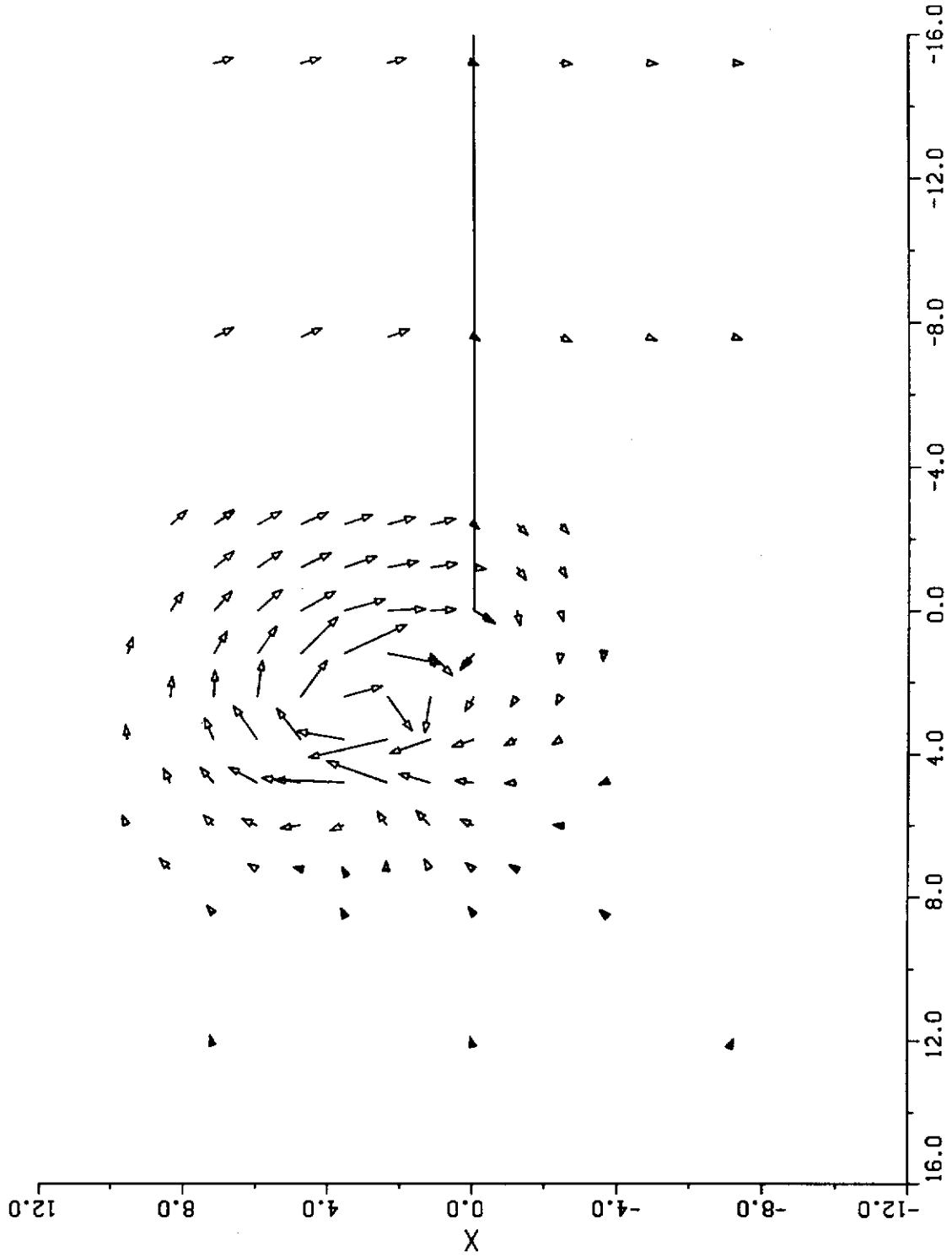

(c) x = 1 inch, C_μ = 0.02, Tip No. 2

Figure 39.- Continued.

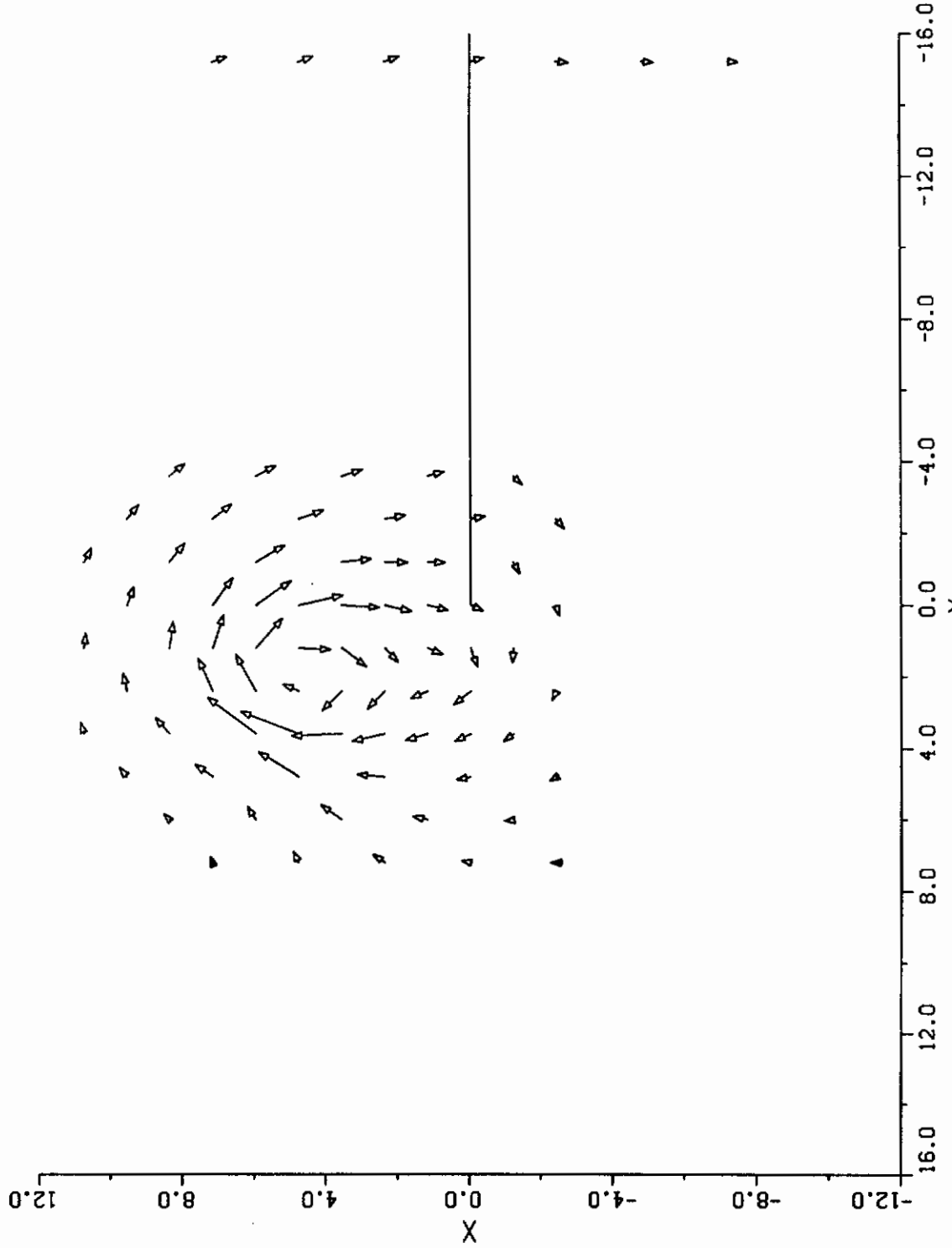

(d) x = 10 inches, C_{μ} = 0.02, Tip No. 2

Figure 39.- Concluded.

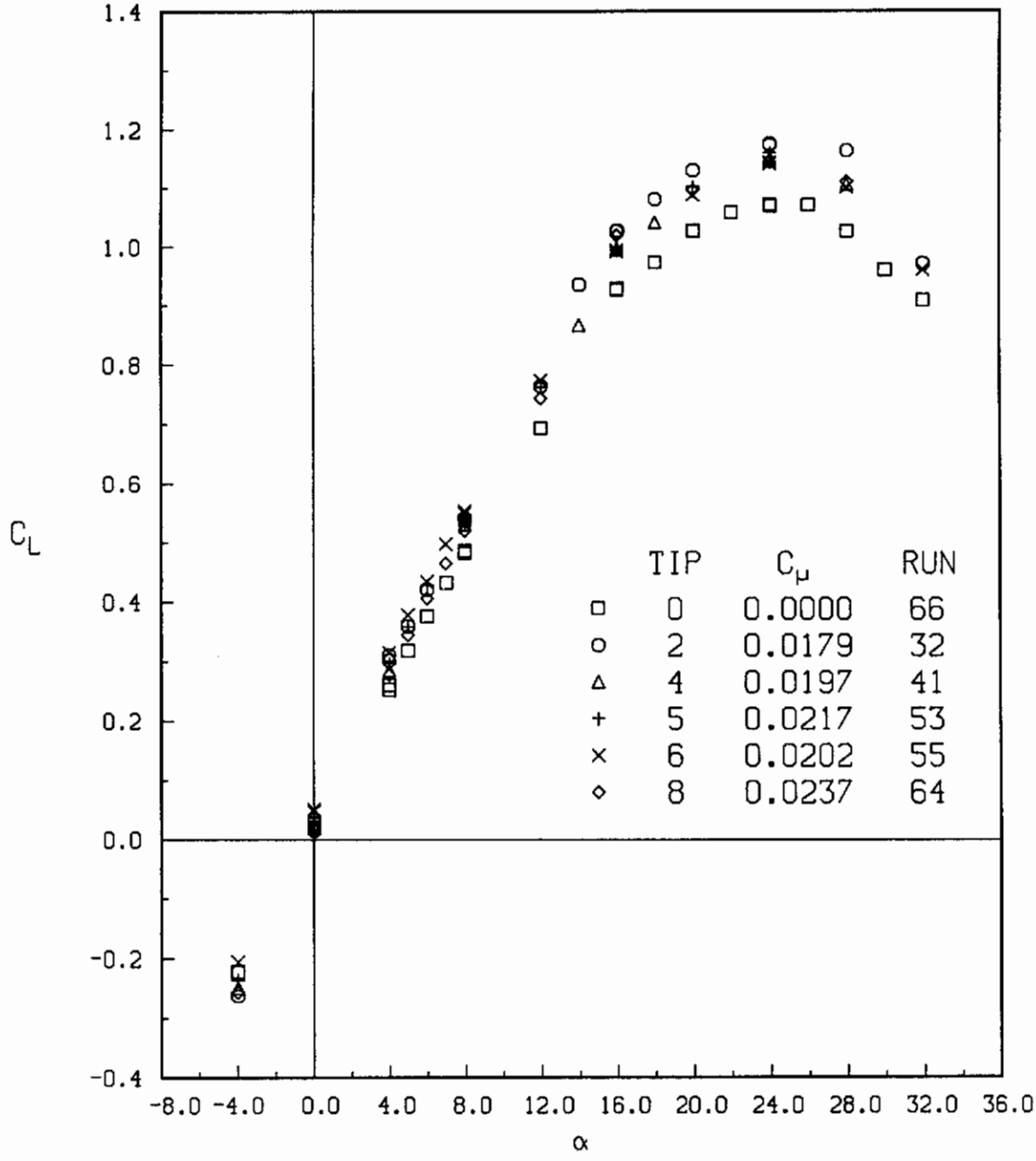

(a) Lift coefficient

Figure 40.- Effect of tip nozzle geometry on measured lift and drag coefficients on Wing C-BT, C_μ = 0.02.

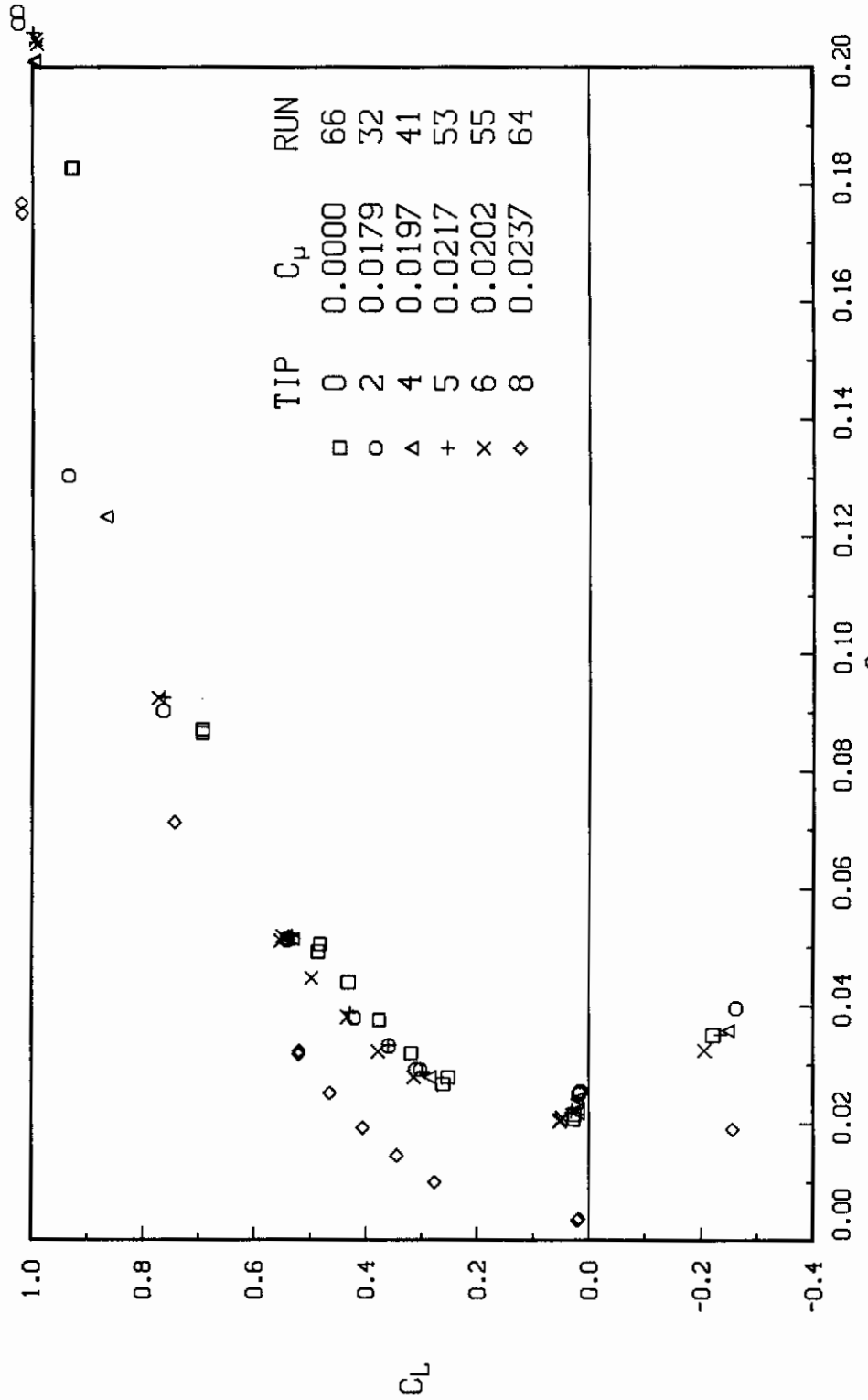

(b) Drag coefficient

Figure 40.- Concluded.

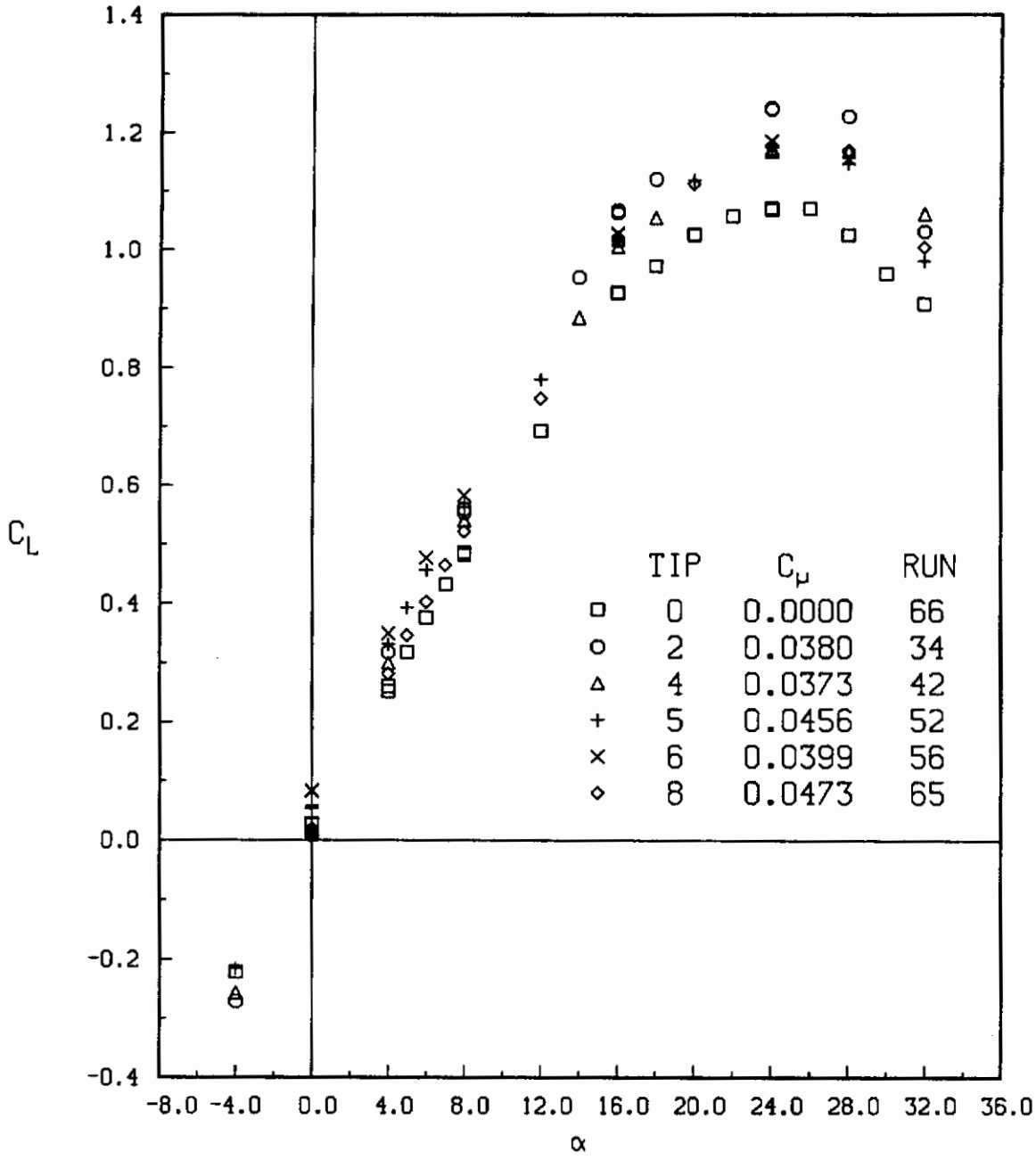

(a) Lift coefficient

Figure 41.- Effect of tip nozzle geometry on measured lift and drag coefficients on Wing C-BT, C_μ = 0.04.

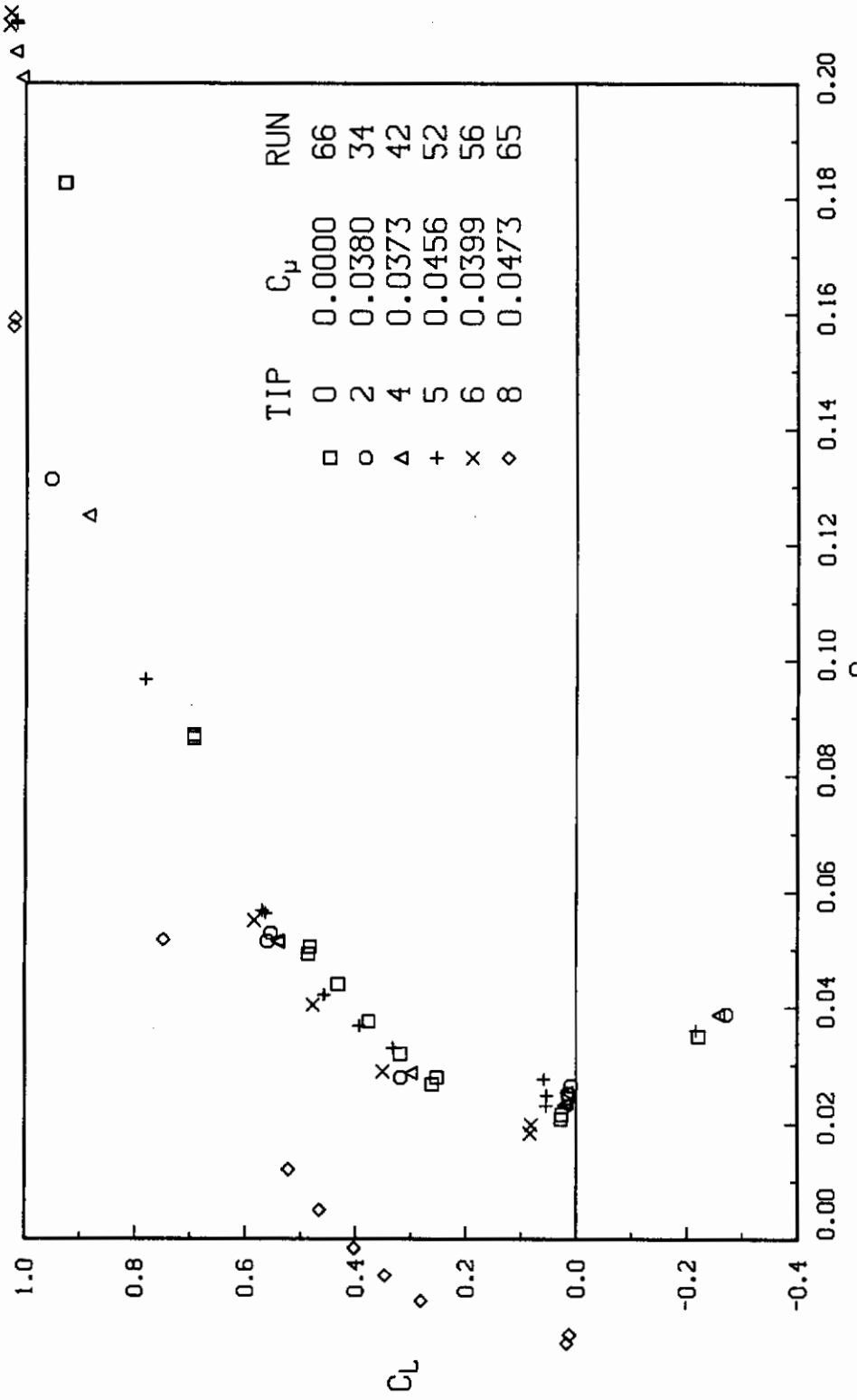

(b) Drag coefficient

Figure 41.- Concluded.

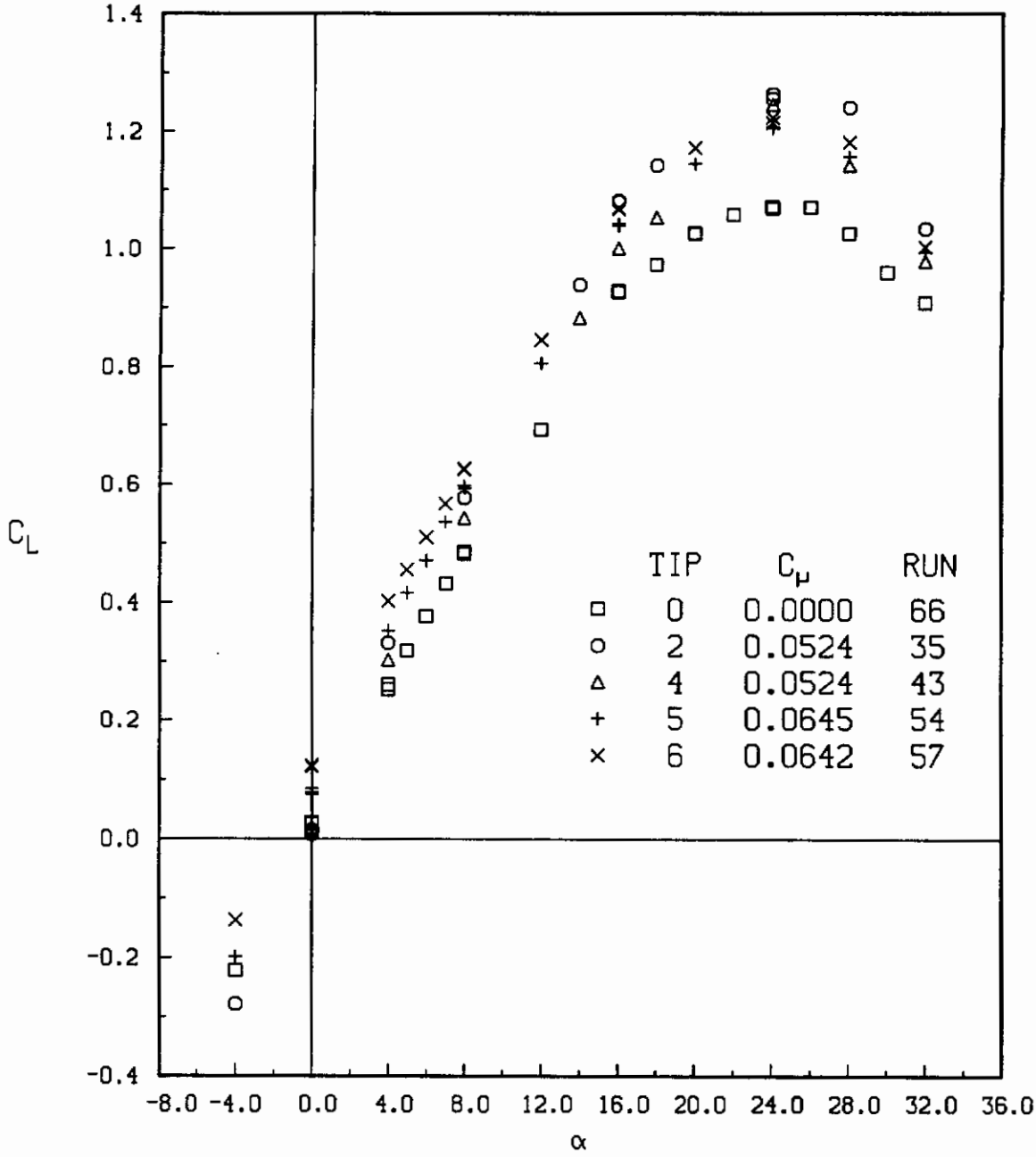

(a) Lift coefficient

Figure 42.- Effect of tip nozzle geometry on measured lift and drag coefficients on Wing C-BT, C_μ = 0.05.

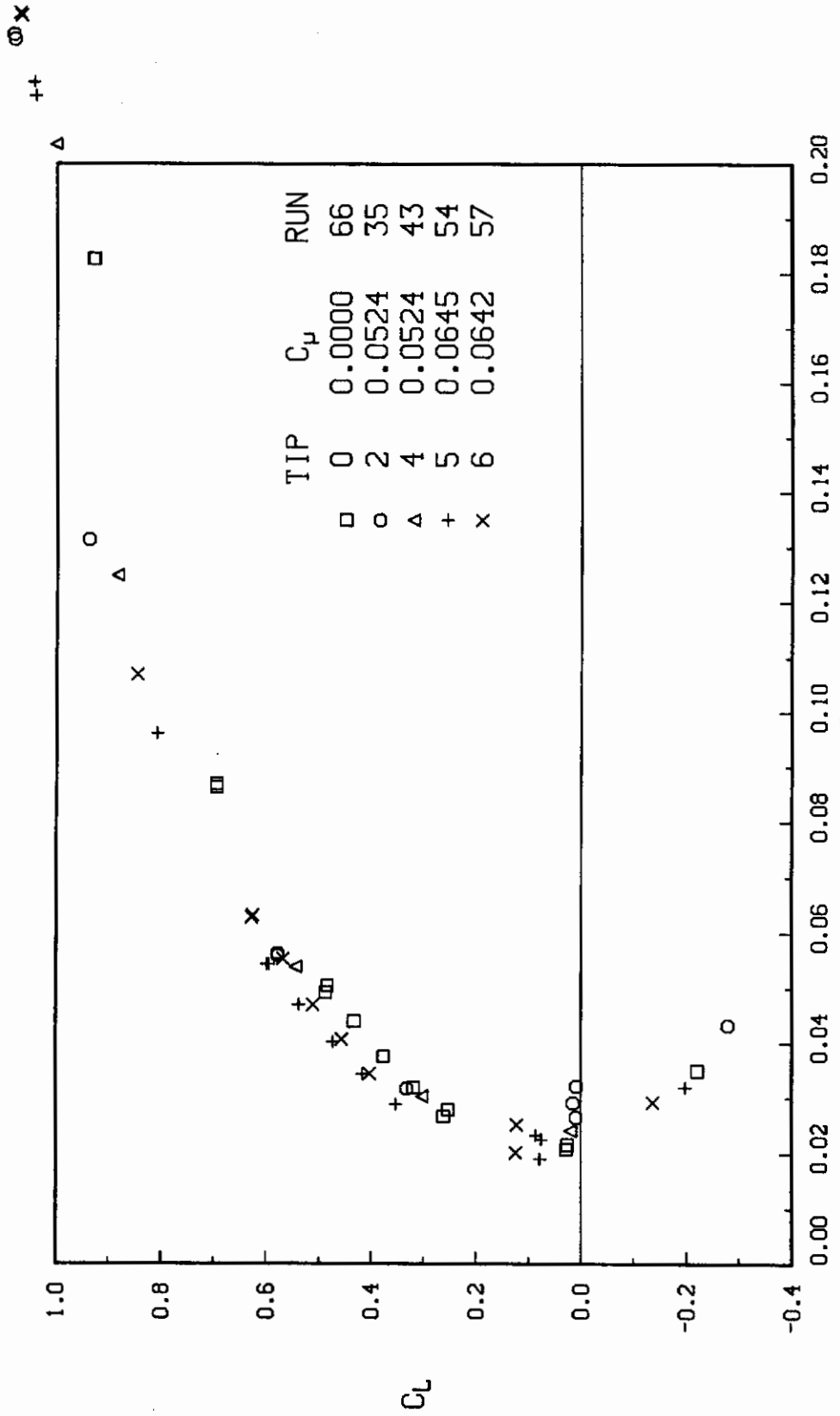

(b) Drag coefficient

Figure 42.- Concluded.

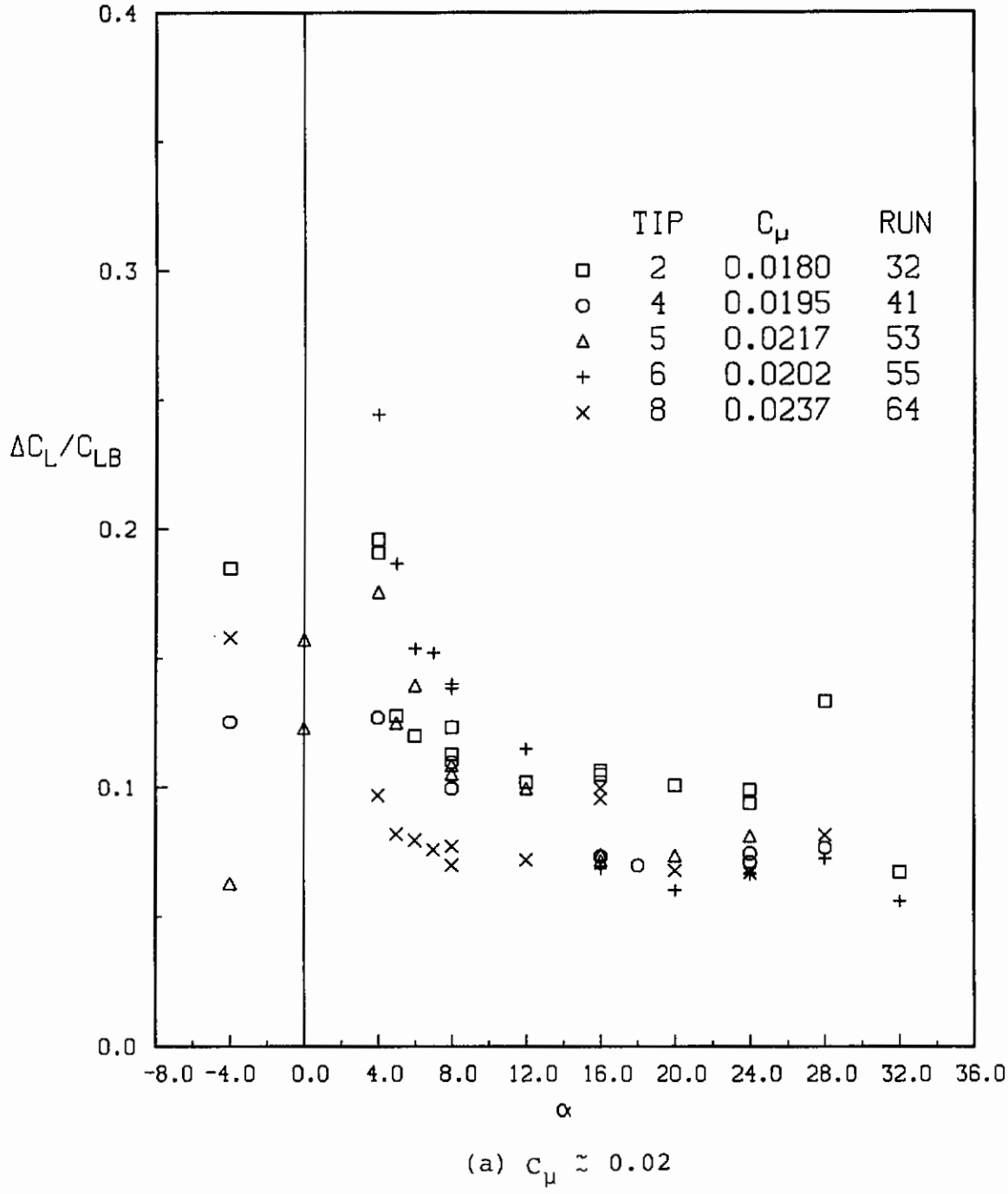

(a) $C_\mu \simeq 0.02$

Figure 43.- Effect of tip geometry and blowing rate on lift augmentation of Wing C-BT.

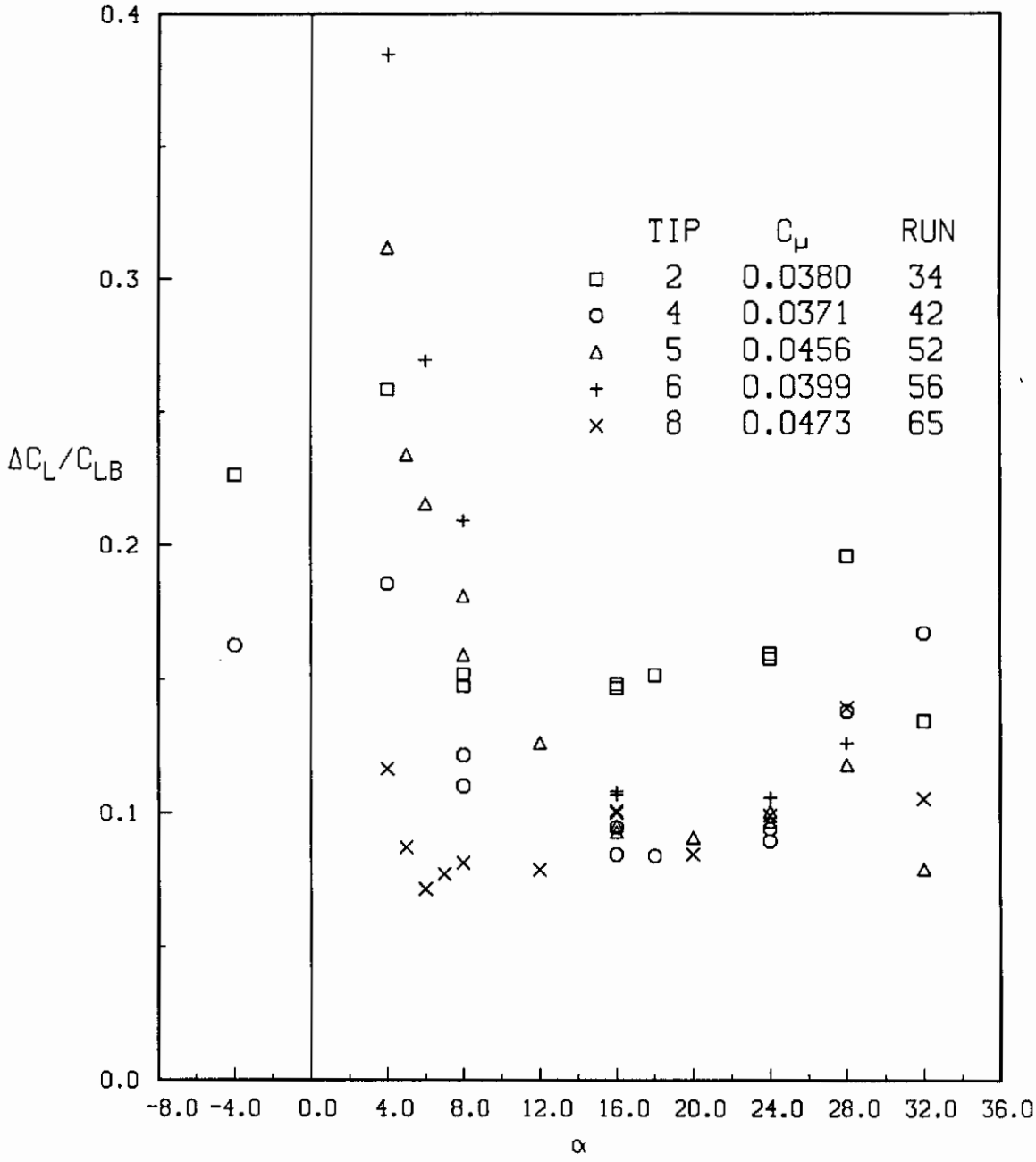

(b) $C_\mu \simeq 0.04$

Figure 43.- Continued.

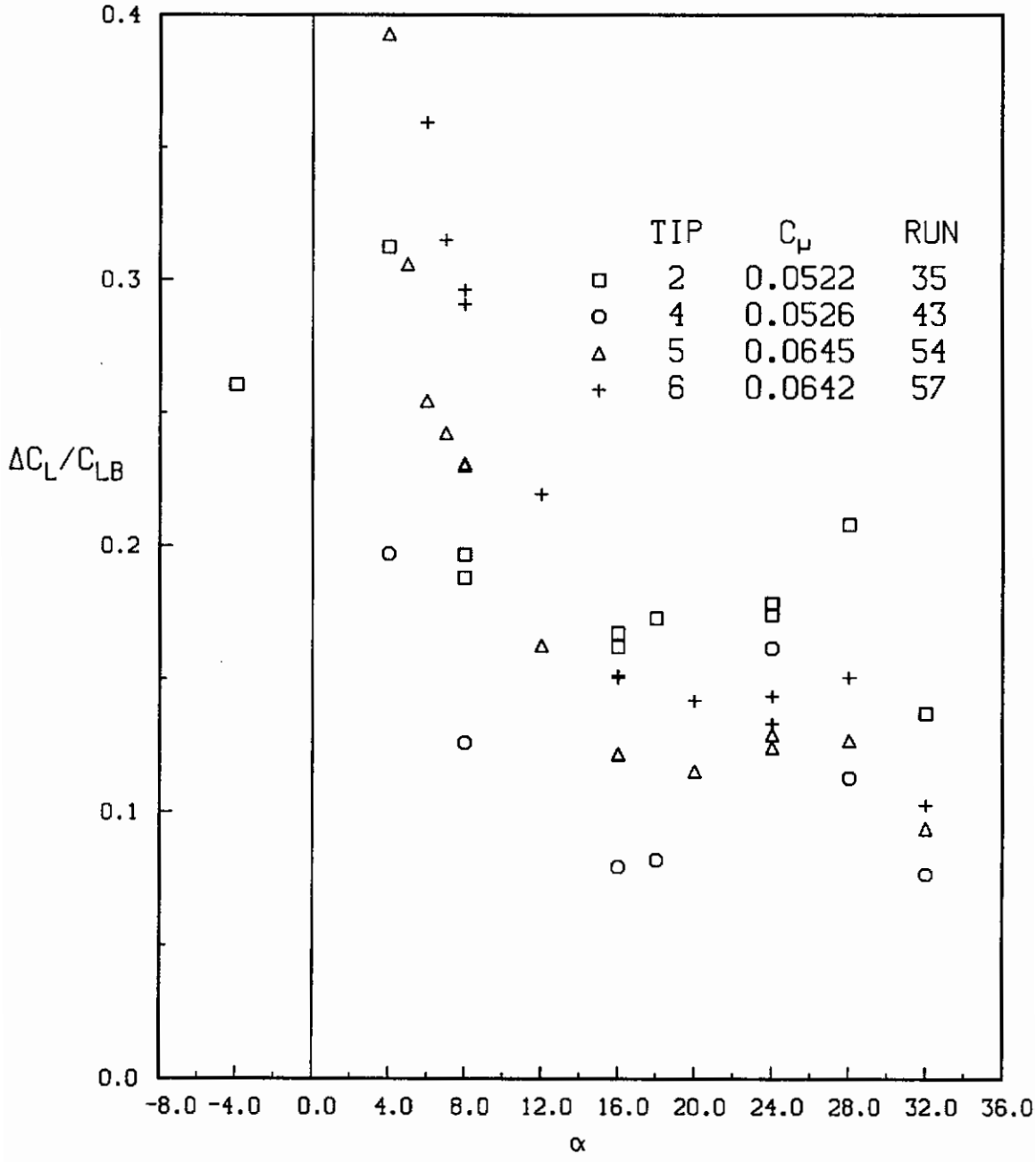

(c) $C_\mu \simeq 0.05$

Figure 43.- Concluded.

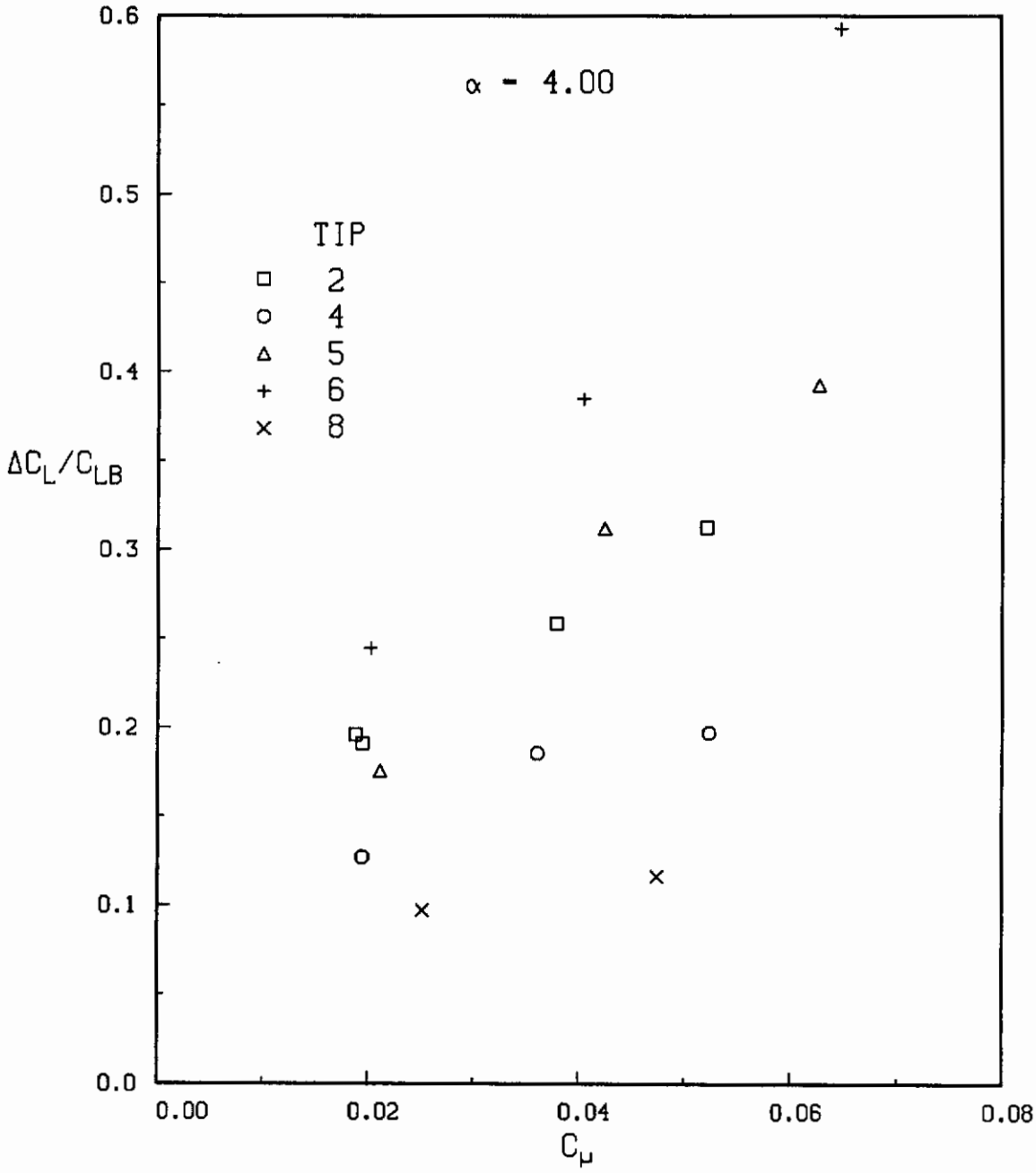

(a) $\alpha = 4°$

Figure 44.- Effect of tip geometry and blowing rate on lift augmentation of Wing C-BT.

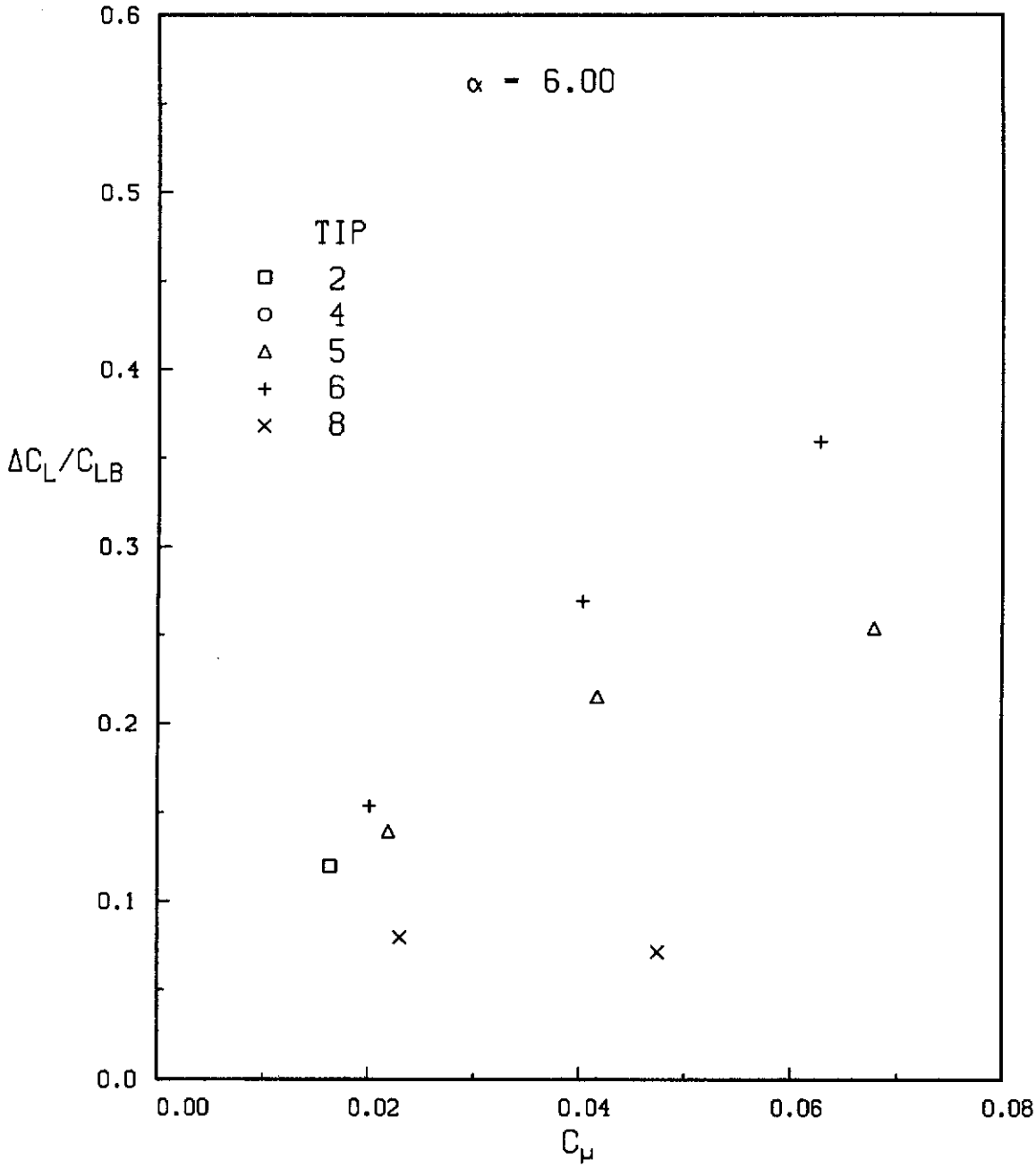

(b) α = 8°

Figure 44.- Continued.

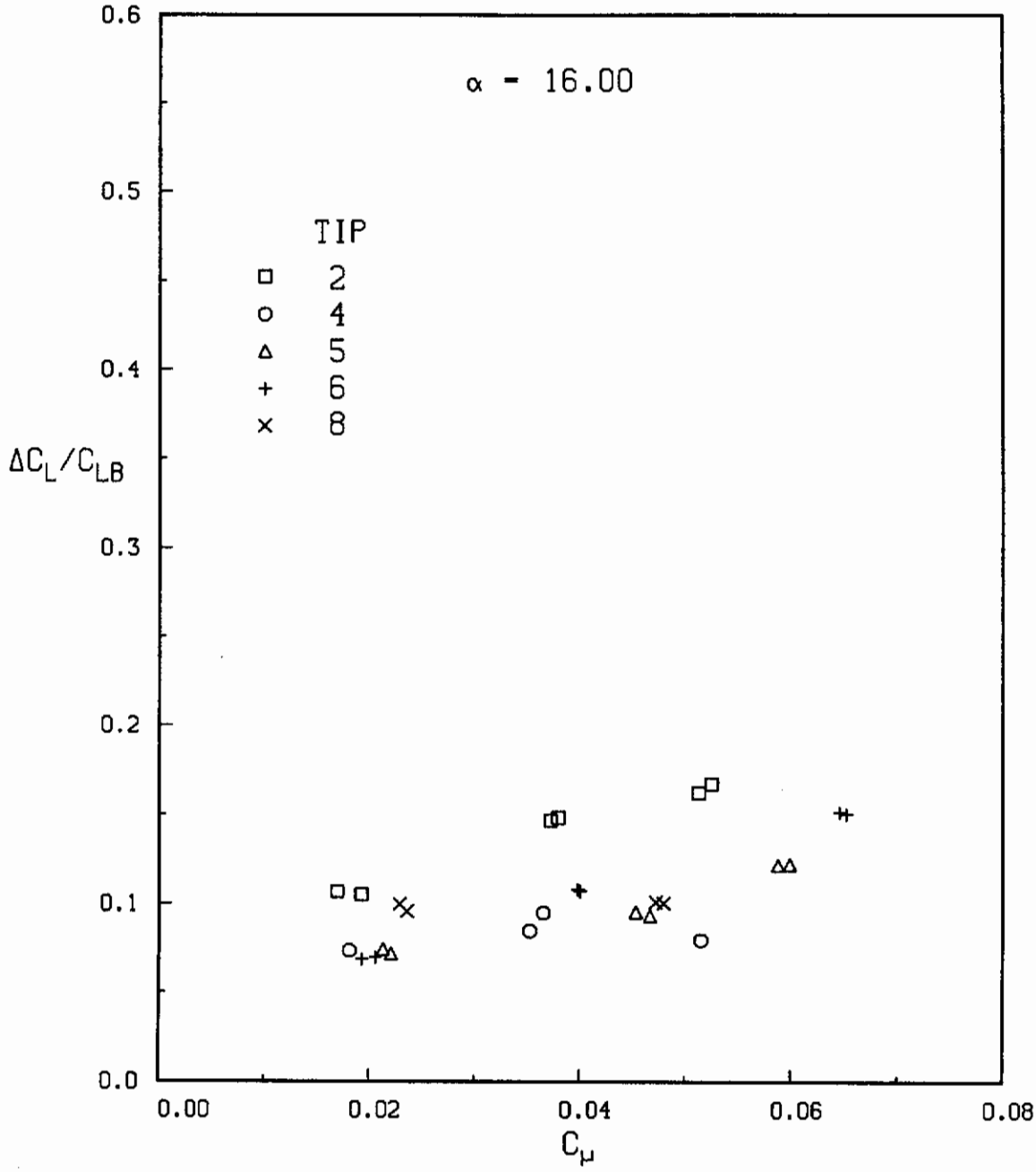

(c) $\alpha = 16°$

Figure 44.- Continued.

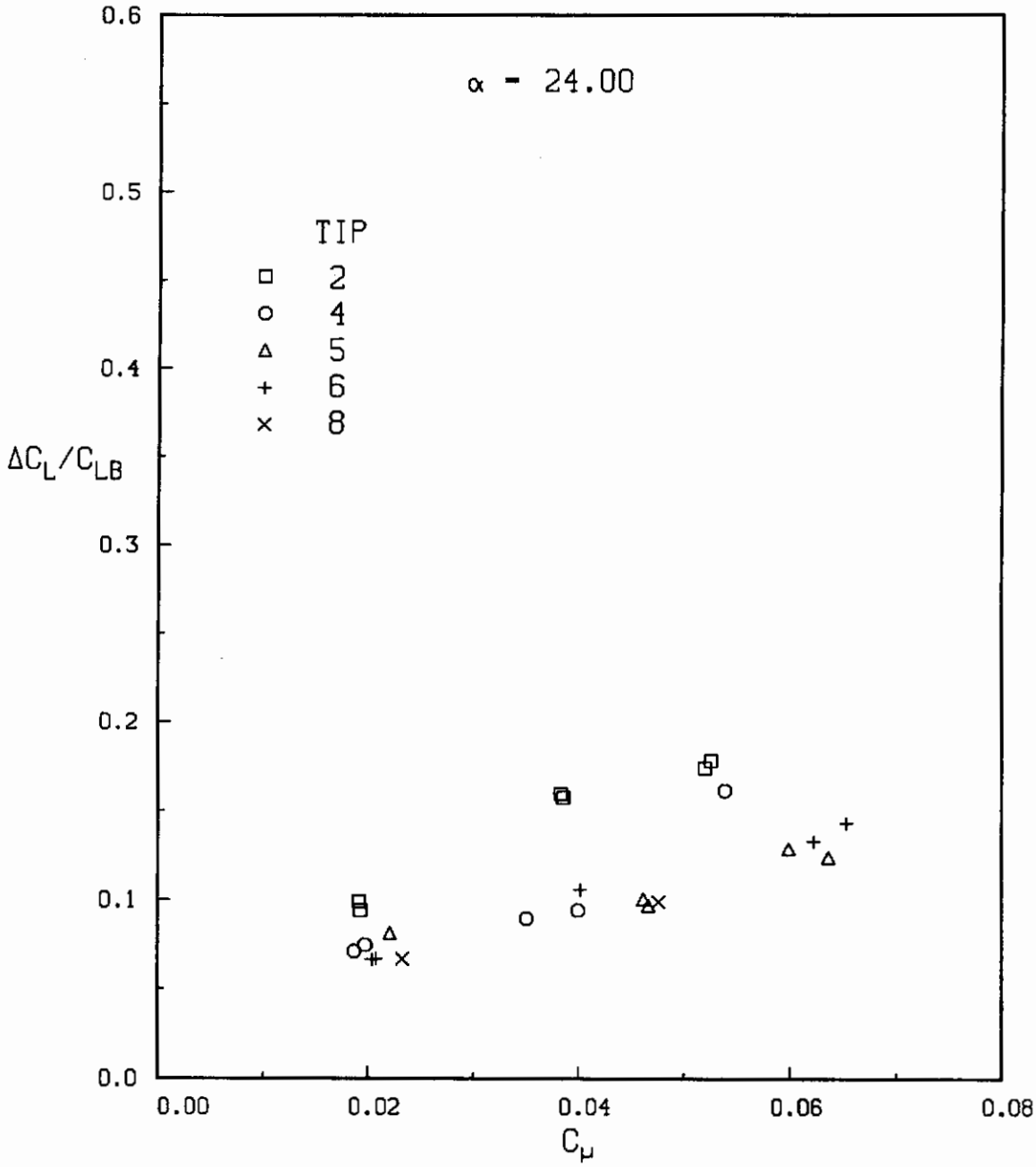

(d) $\alpha = 24°$

Figure 44.- Concluded.

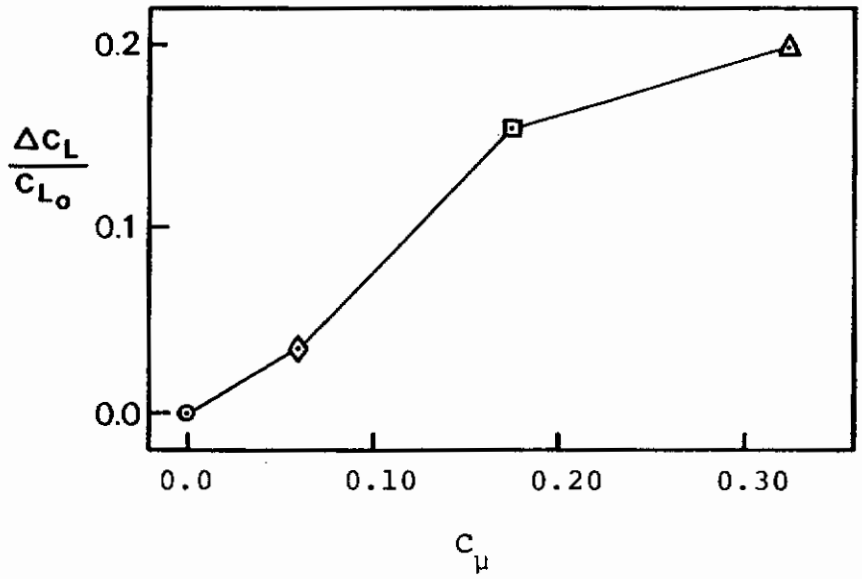

(a) α = 4°

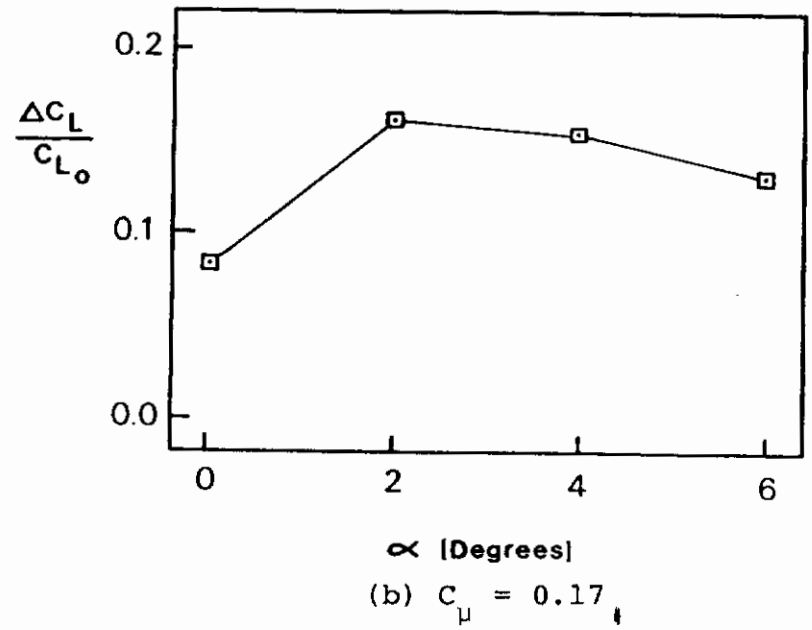

(b) C_μ = 0.17

Figure 45.- Predicted lift increments on a rectangular wing with tip blowing.

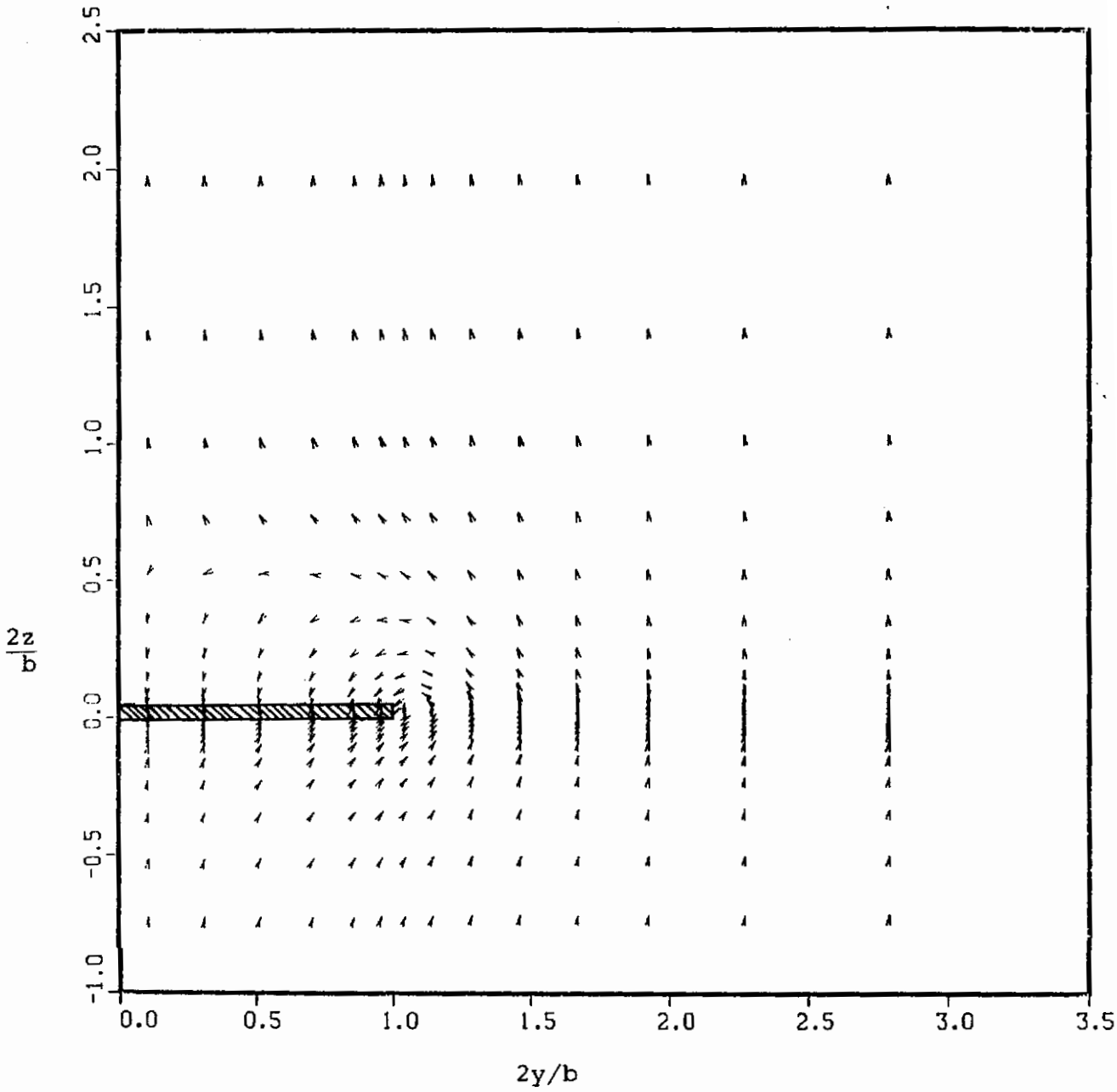

(a) $C_\mu = 0.0$

Figure 46.- Predicted velocity field rectangular wing with tip blowing, x/c = .80, $\alpha = 4°$.

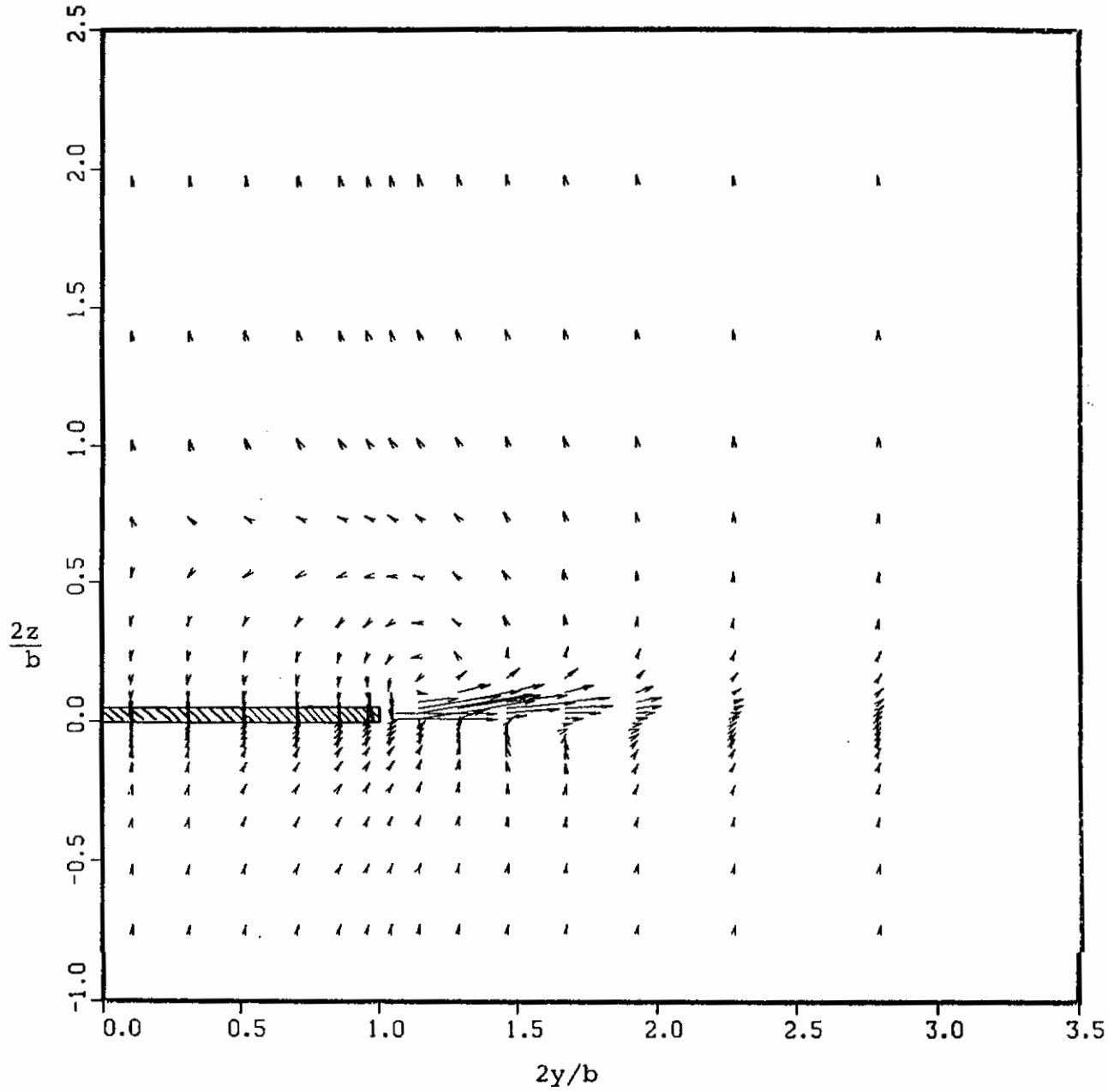

(b) $C_{\mu} = 0.17$

Figure 46.- Concluded.

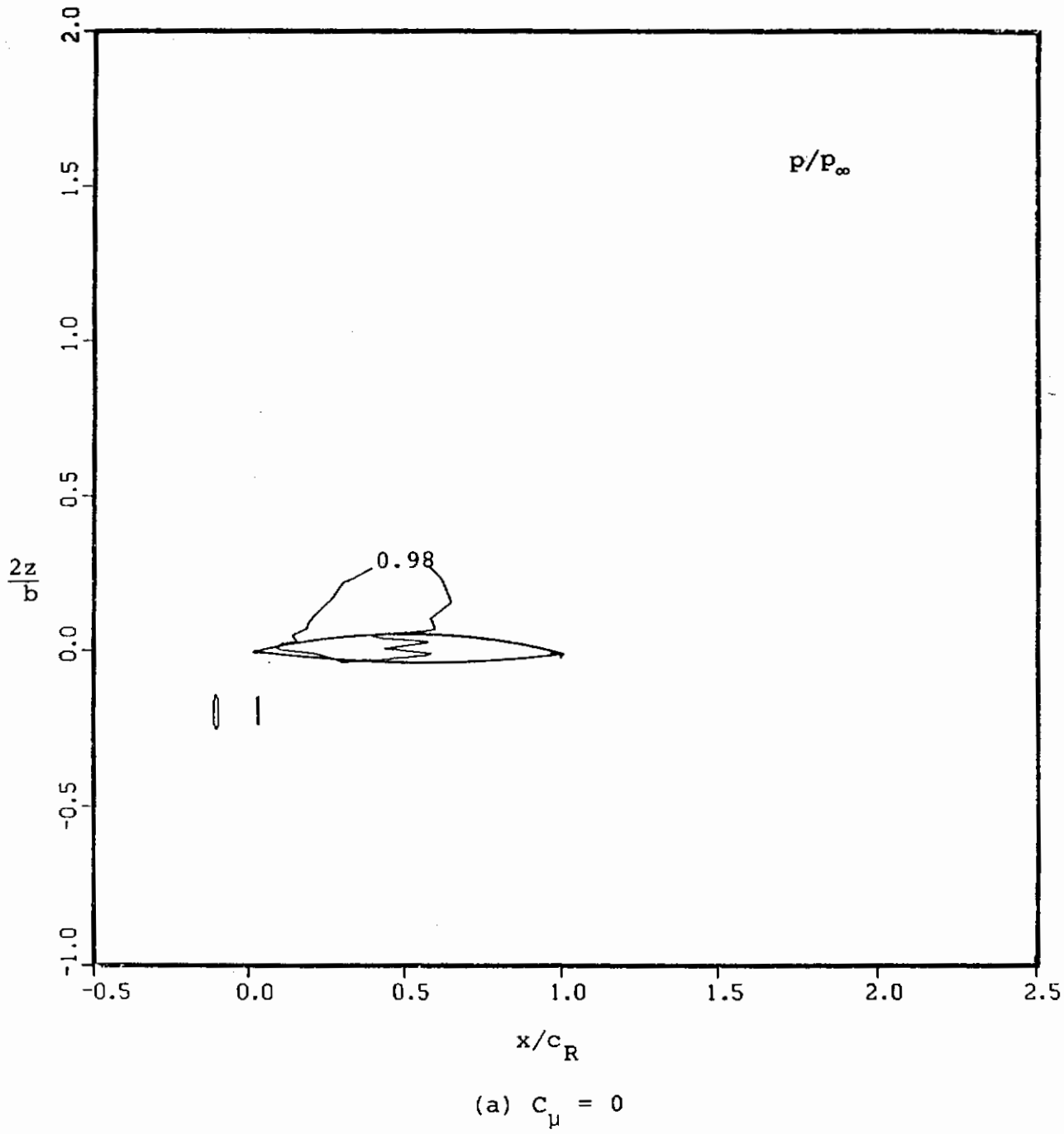

(a) $C_\mu = 0$

Figure 47.- Predicted pressure contours near a rectangular wing with tip blowing, $2y/b = 1.04$, $\alpha = 4°$.

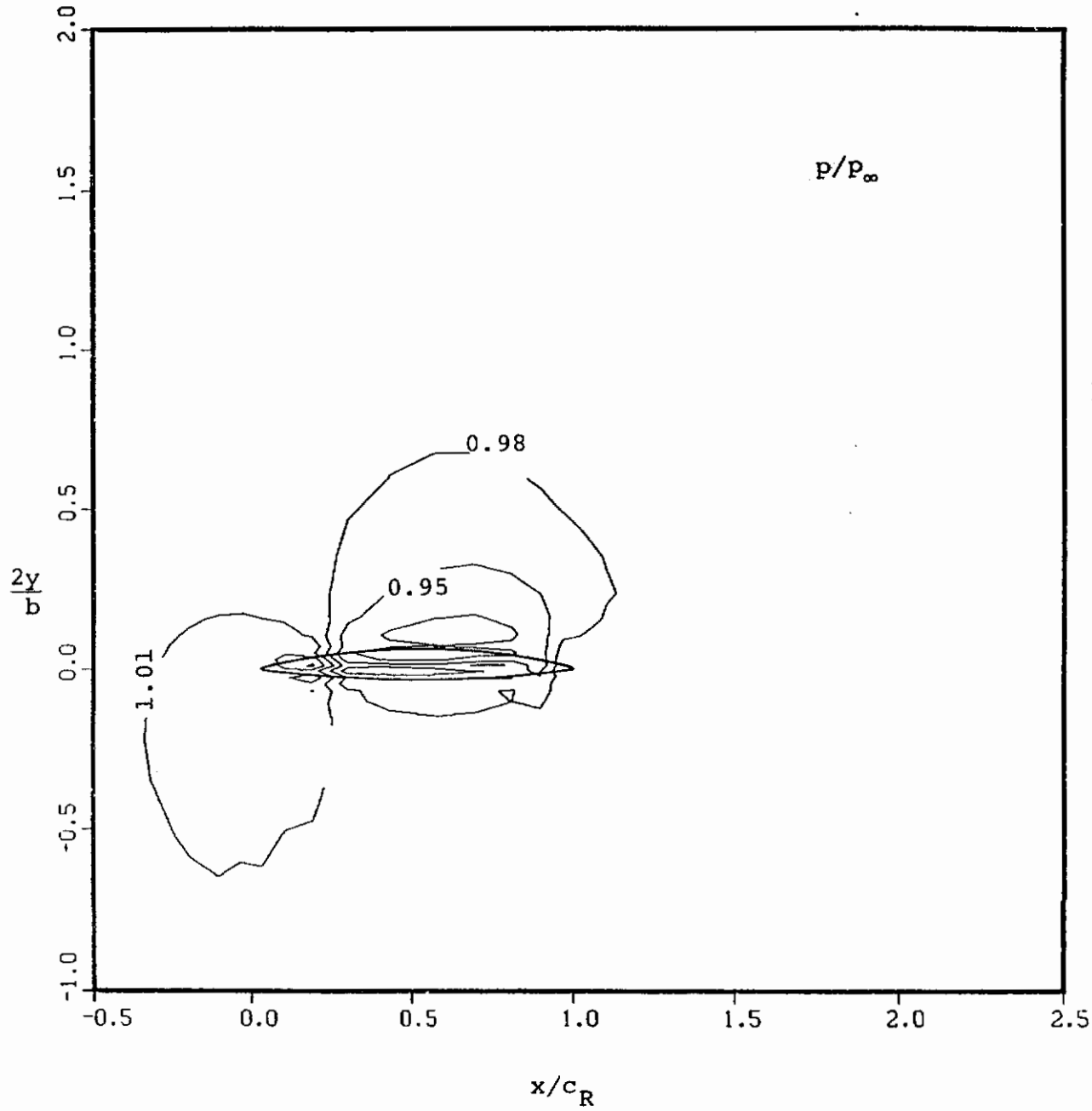

(b) $C_\mu = 0.17$

Figure 47.- Concluded.

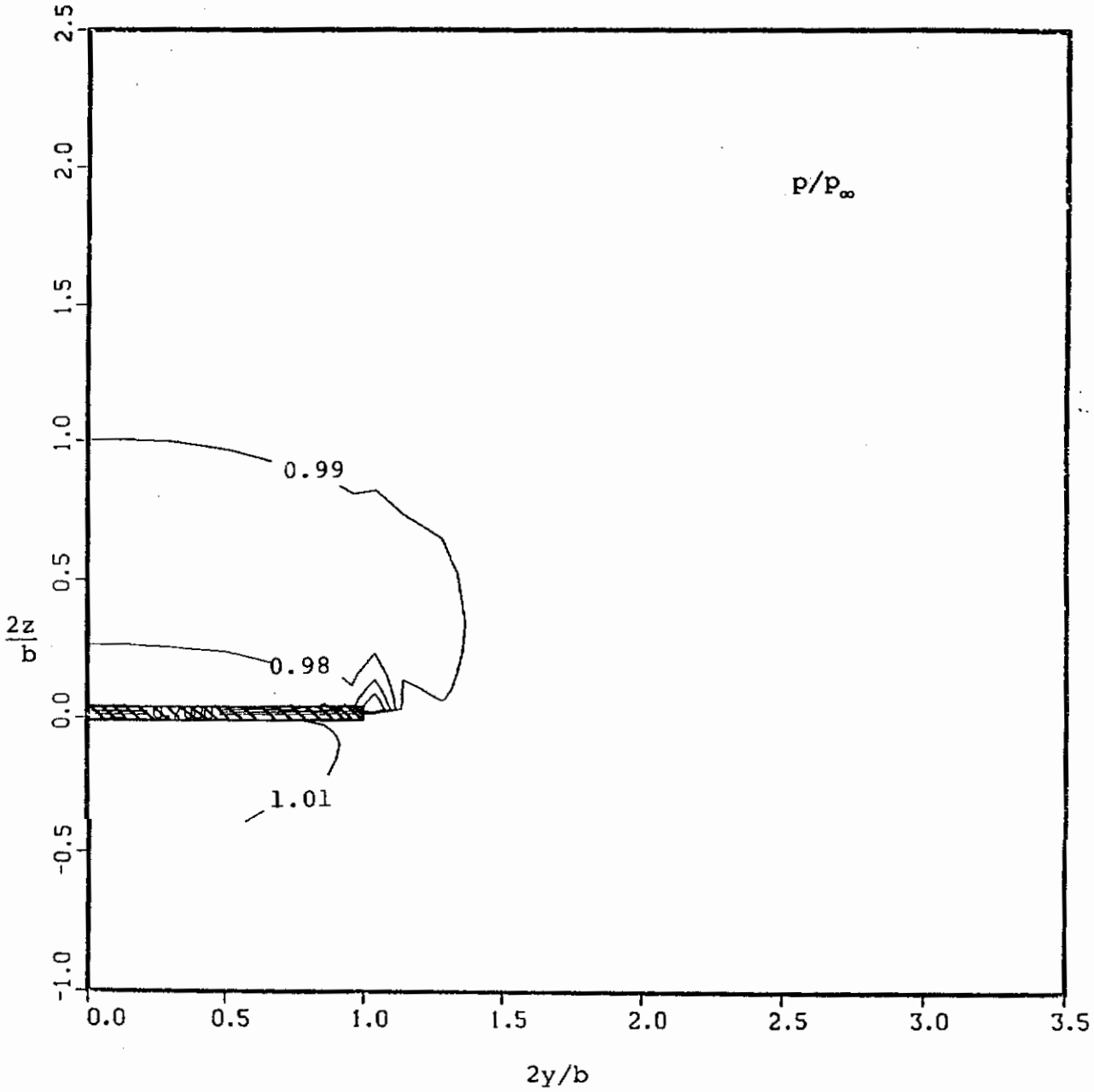

(a) $C_\mu = 0.0$

Figure 48.- Predicted pressure contours near a rectangular wing with tip blowing, x/c = .80, α = 4°.

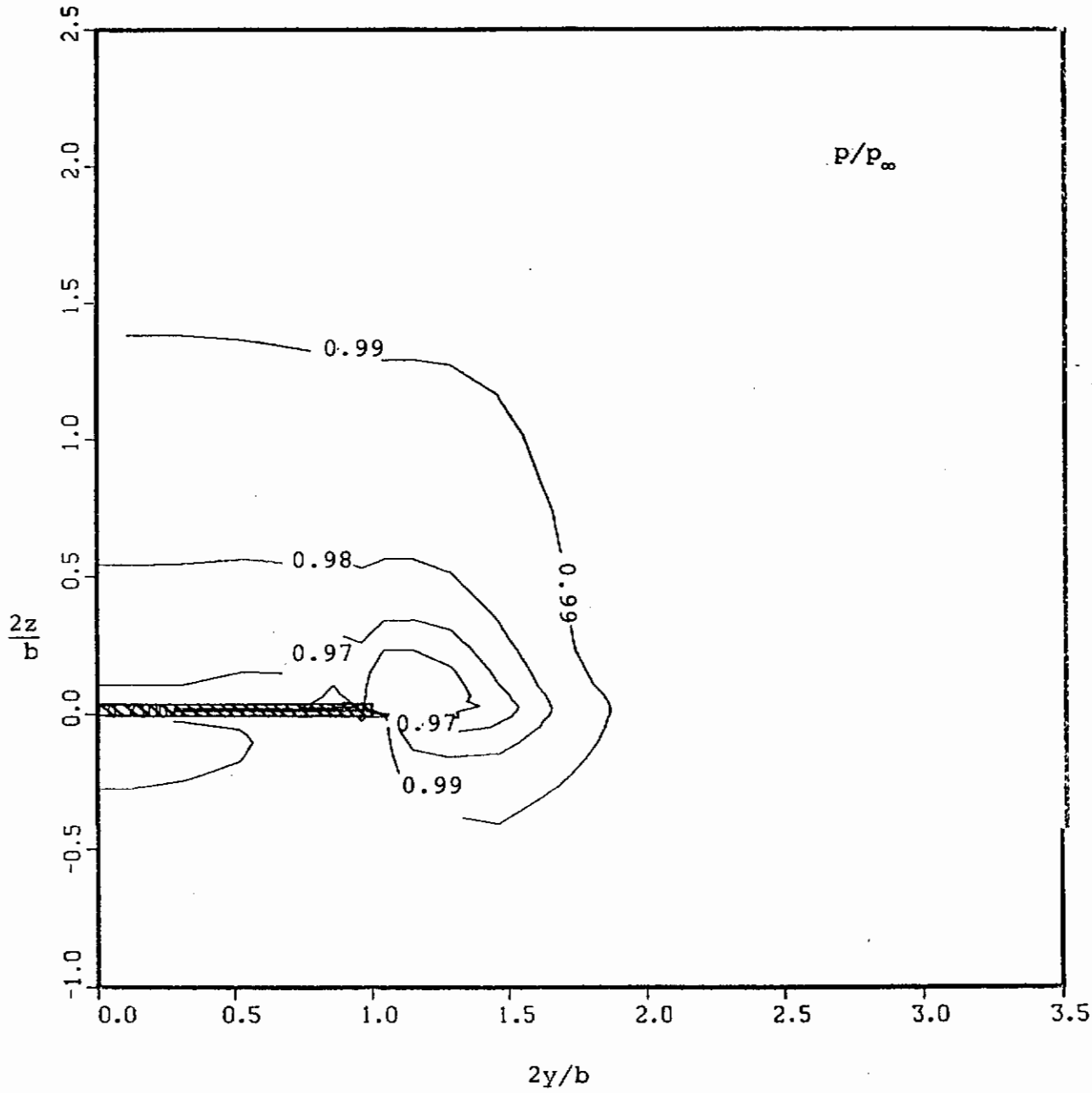

(b) $C_\mu = 0.17$

Figure 48.- Concluded.

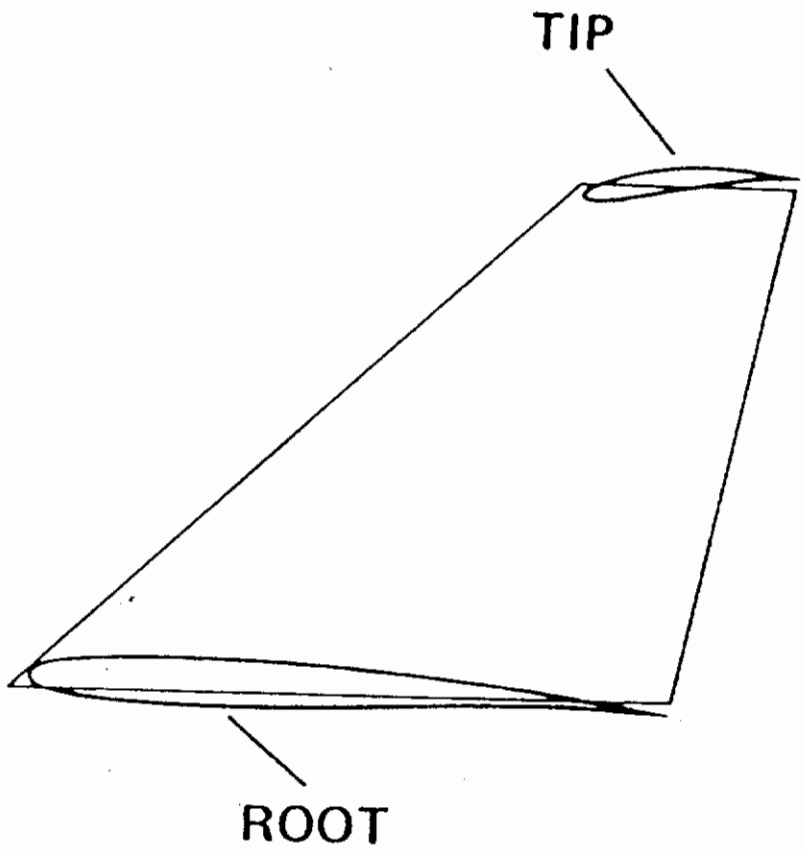

AR = 2.6	λ = 0.3
$\Lambda_{L.E.}$ = 45°	$\Lambda_{T.E.}$ = 9.7°
t_R/c_R = 0.06	t_T/c_T = 0.10
$\alpha_{O,R}$ = 2.38°	$\alpha_{O,T}$ = -5.79°

Figure 49.- WING C geometry.

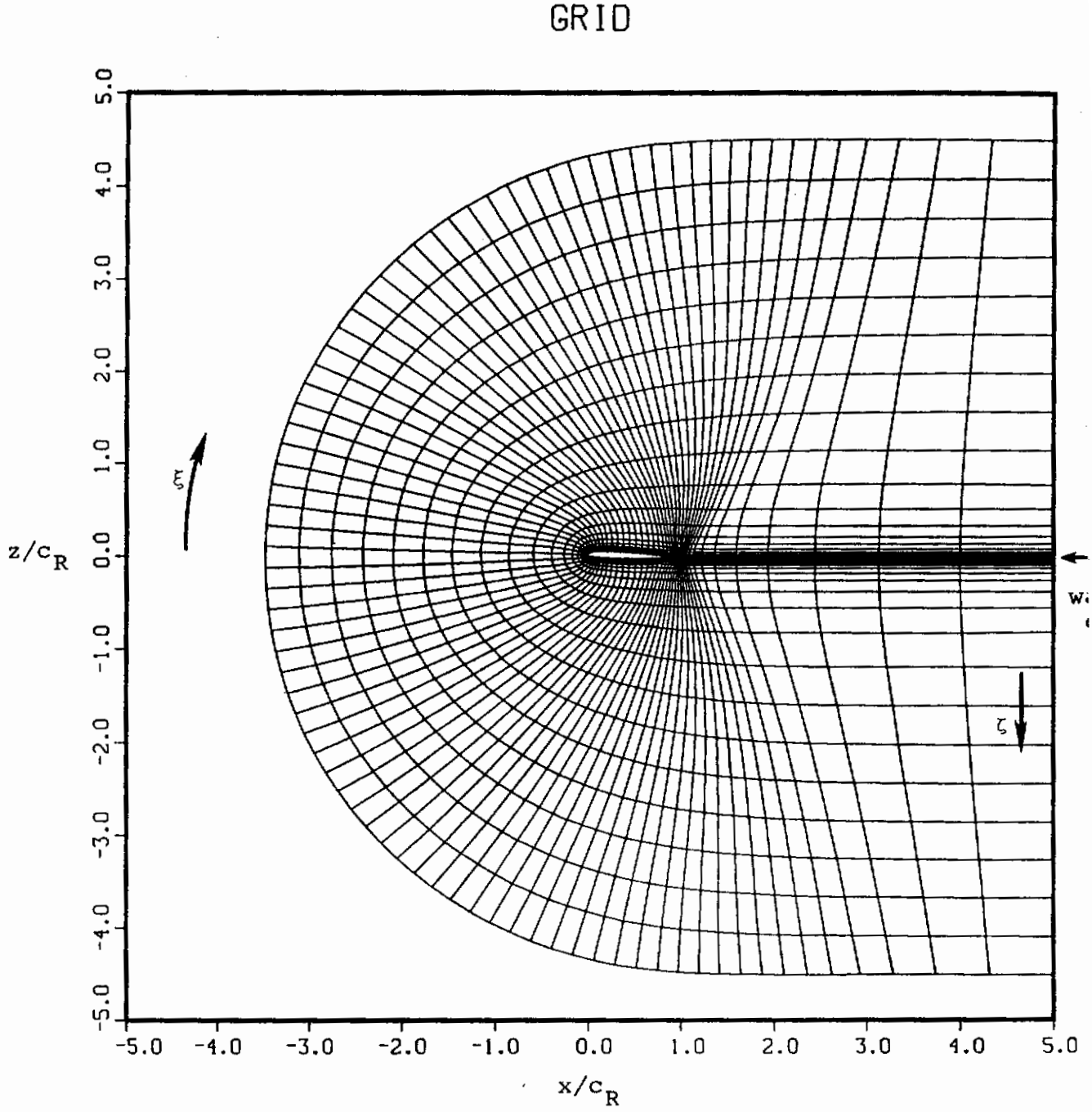

(a) "C" grid at root.

Figure 50.- Computational grid for WING C.

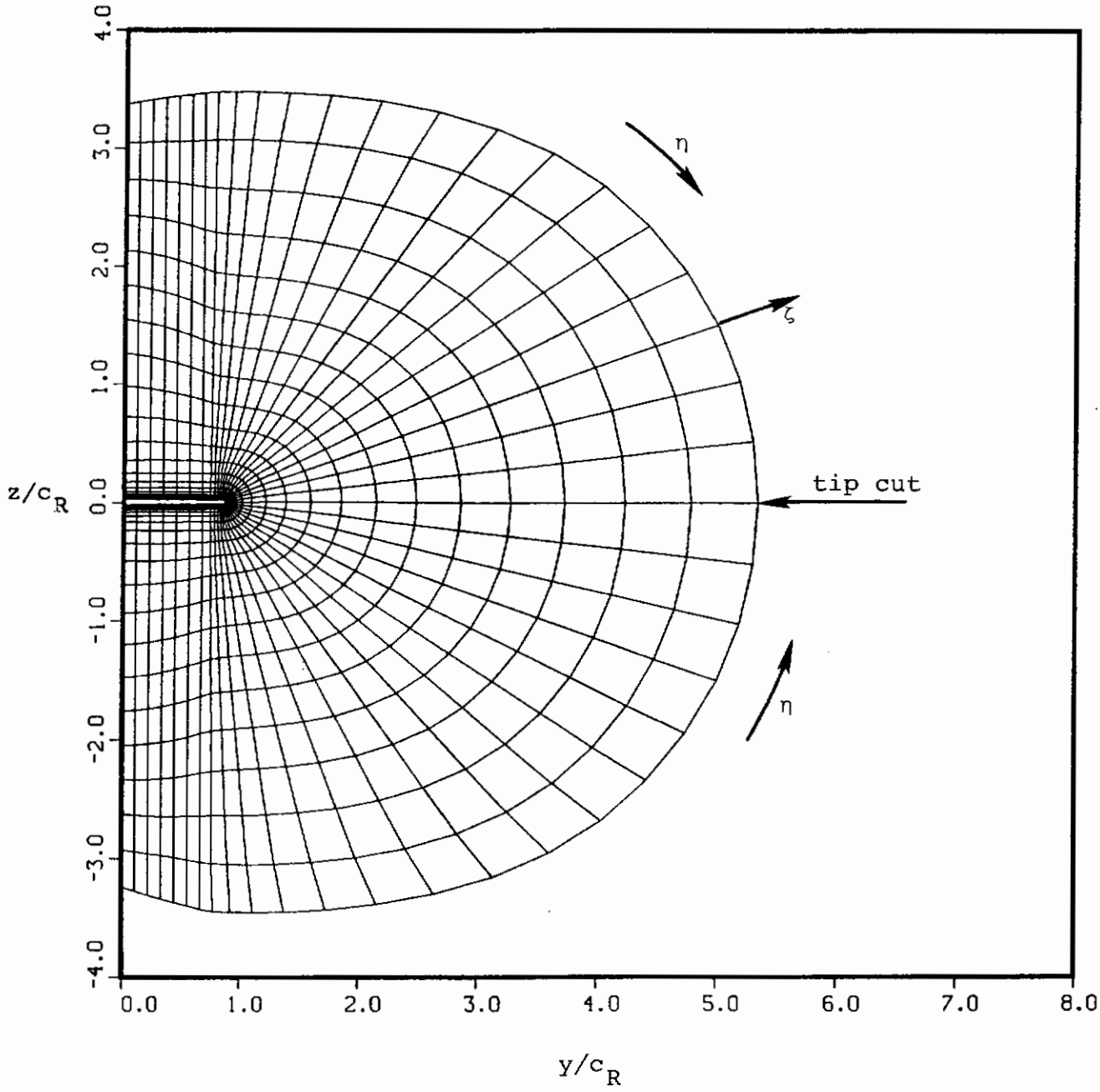

(b) "O" grid at 50% chord.

Figure 50.- Continued.

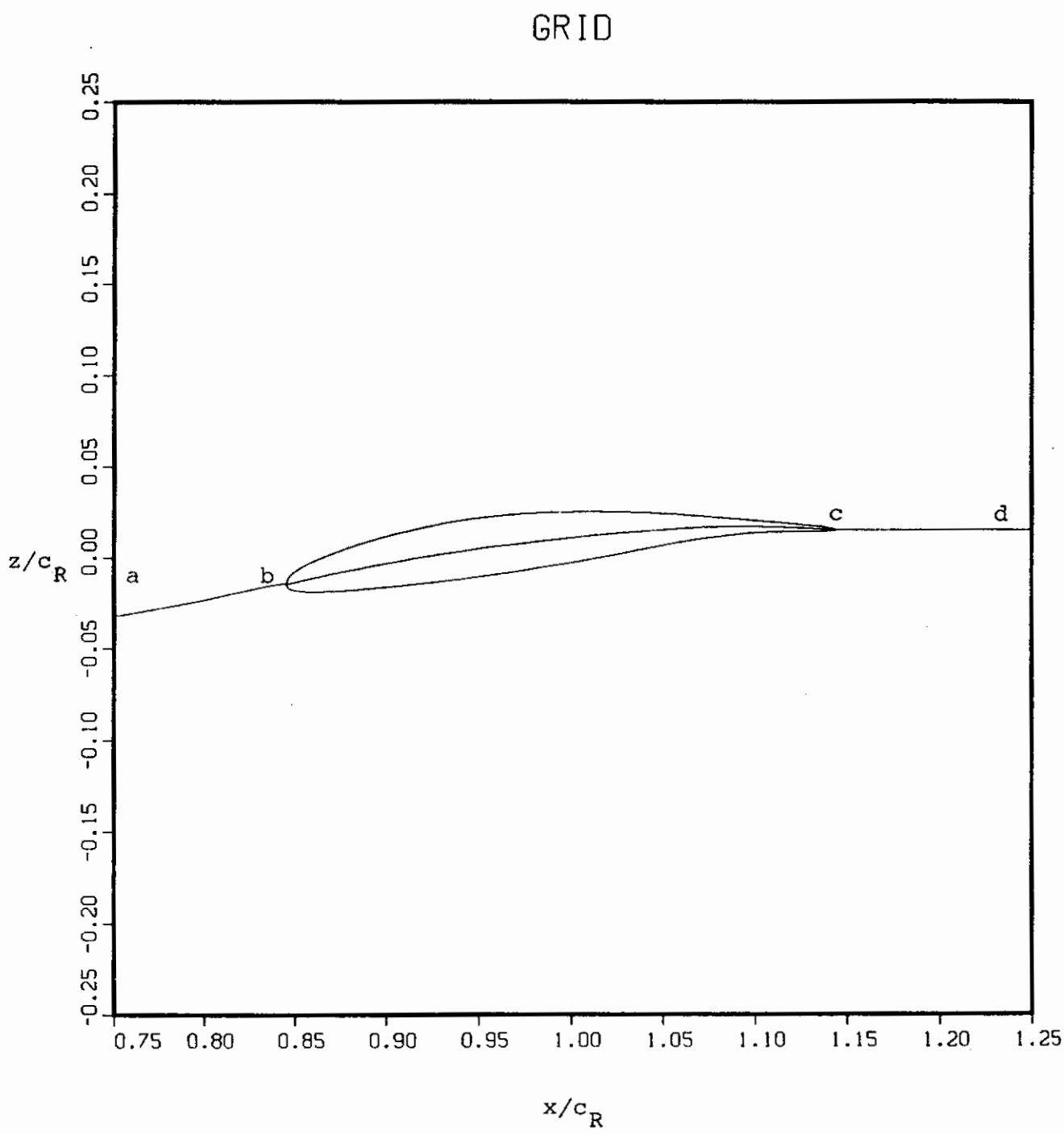

(c) Axis of rotation for tip wrap.

Figure 50.- Concluded.

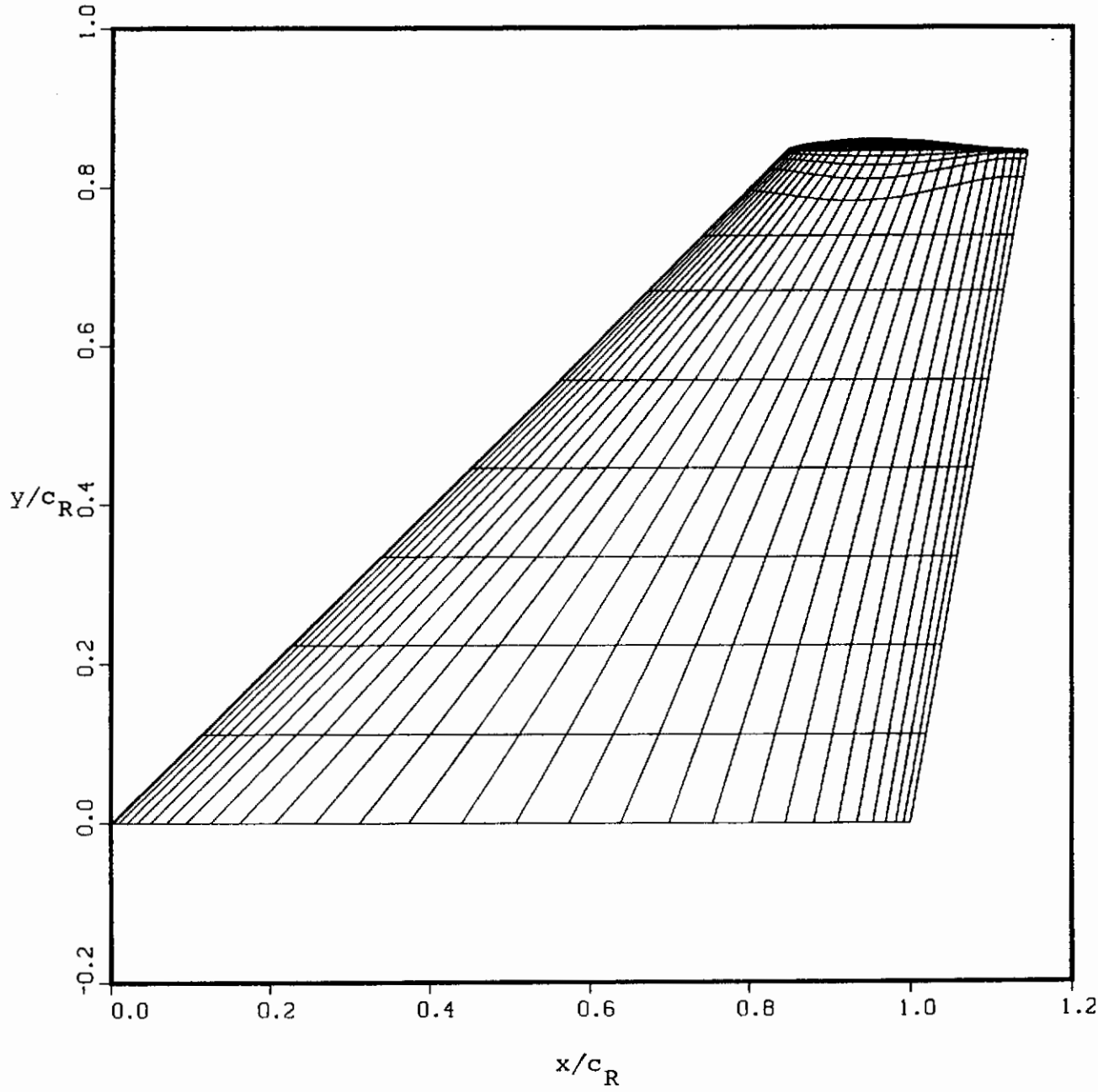

(a) Wing-surface mesh.

Figure 51.- Surface grid distribution on WING C.

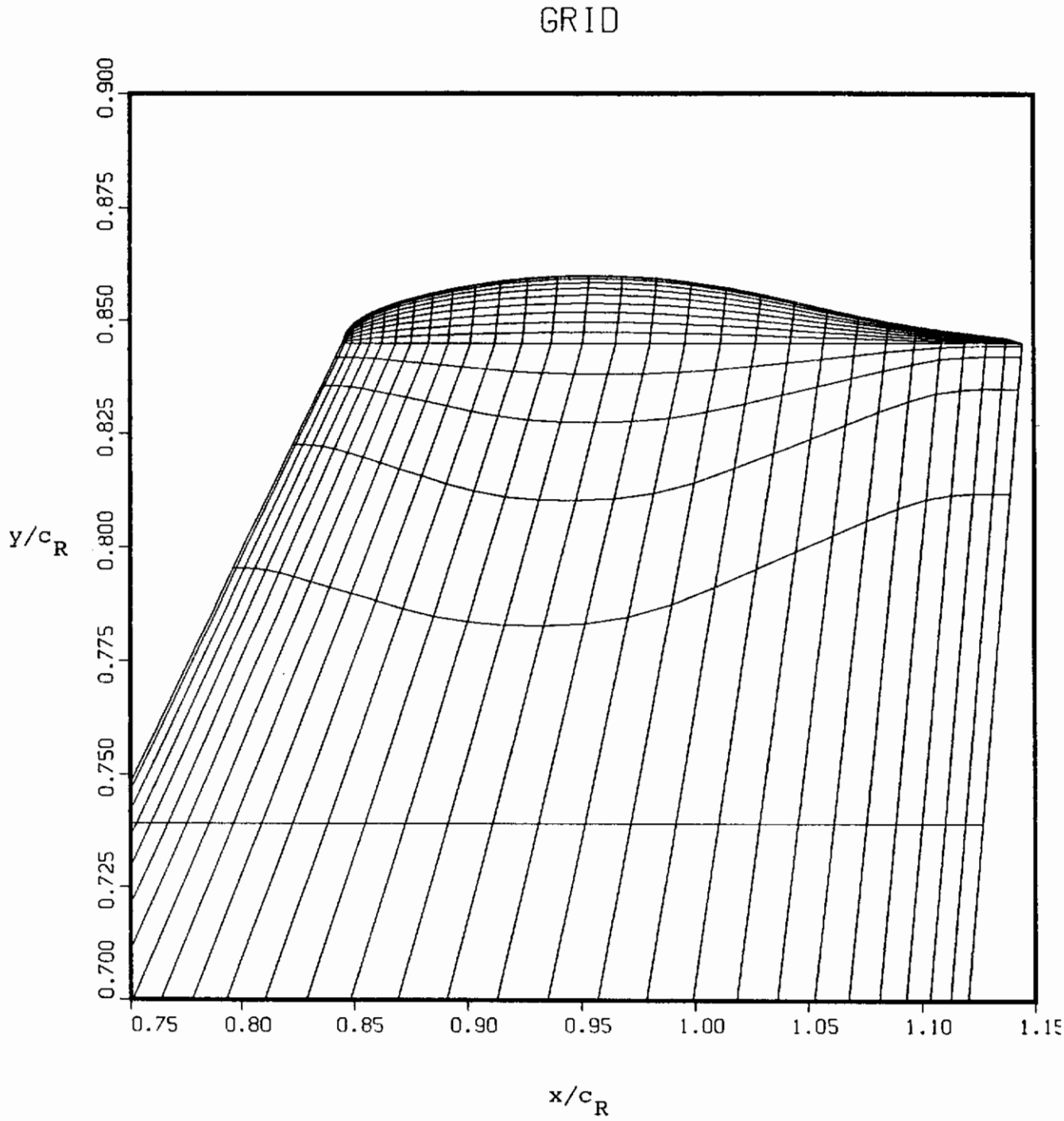

(b) Wing-surface mesh near tip.

Figure 51.- Concluded.

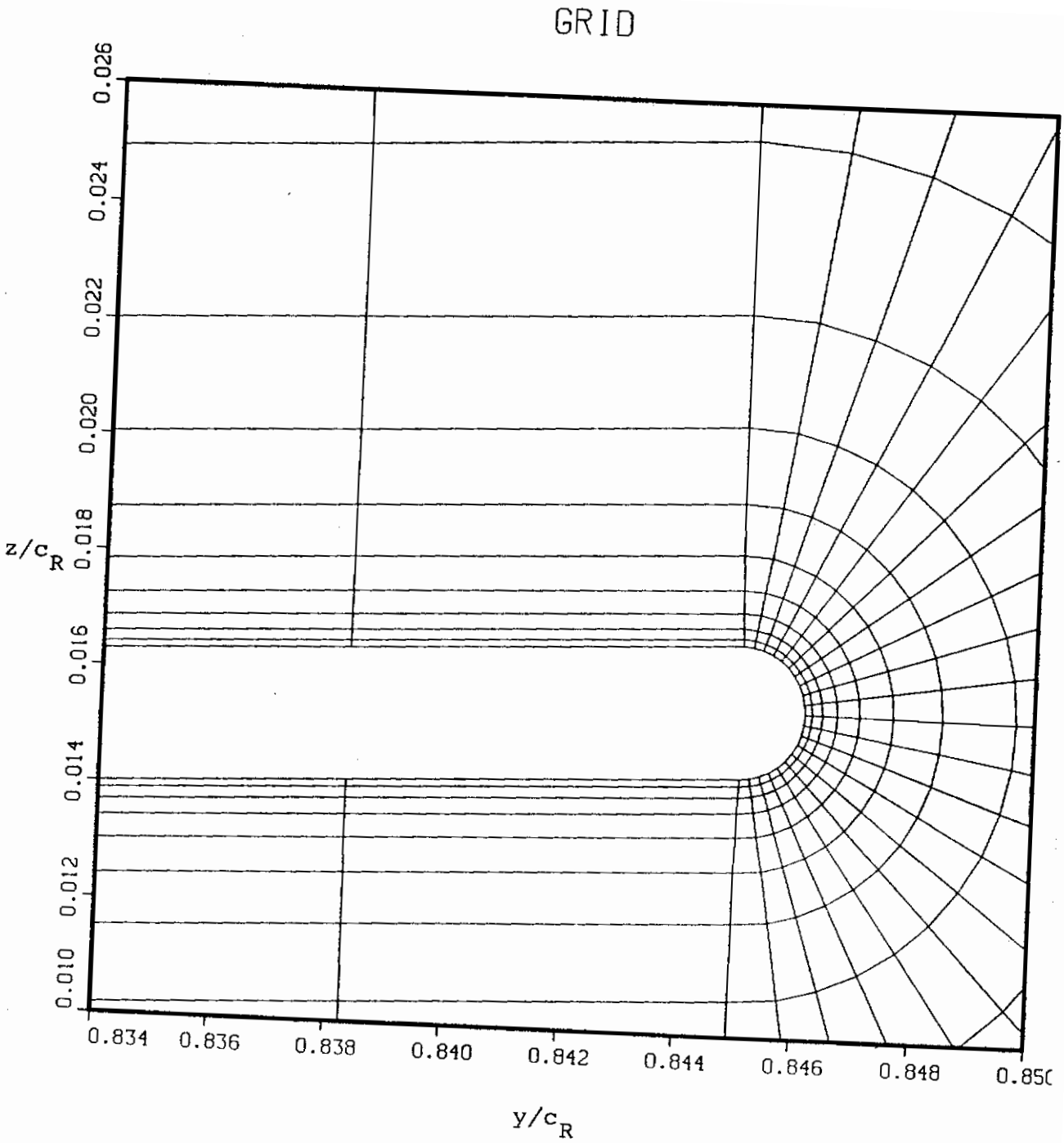

(a) Without bending.

Figure 52.- Mesh at 97% chord.

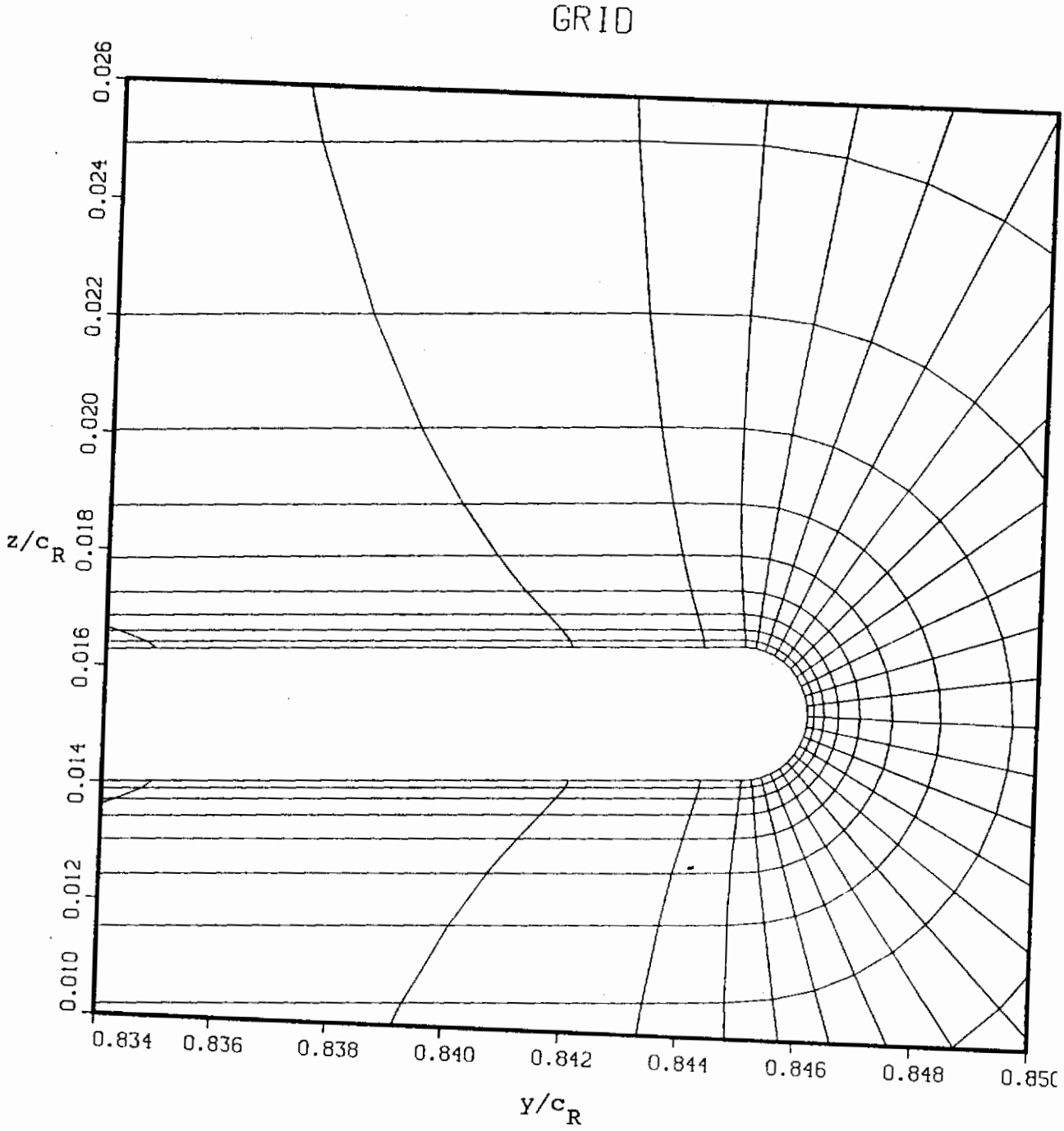

(b) With bending.

Figure 52.- Concluded.

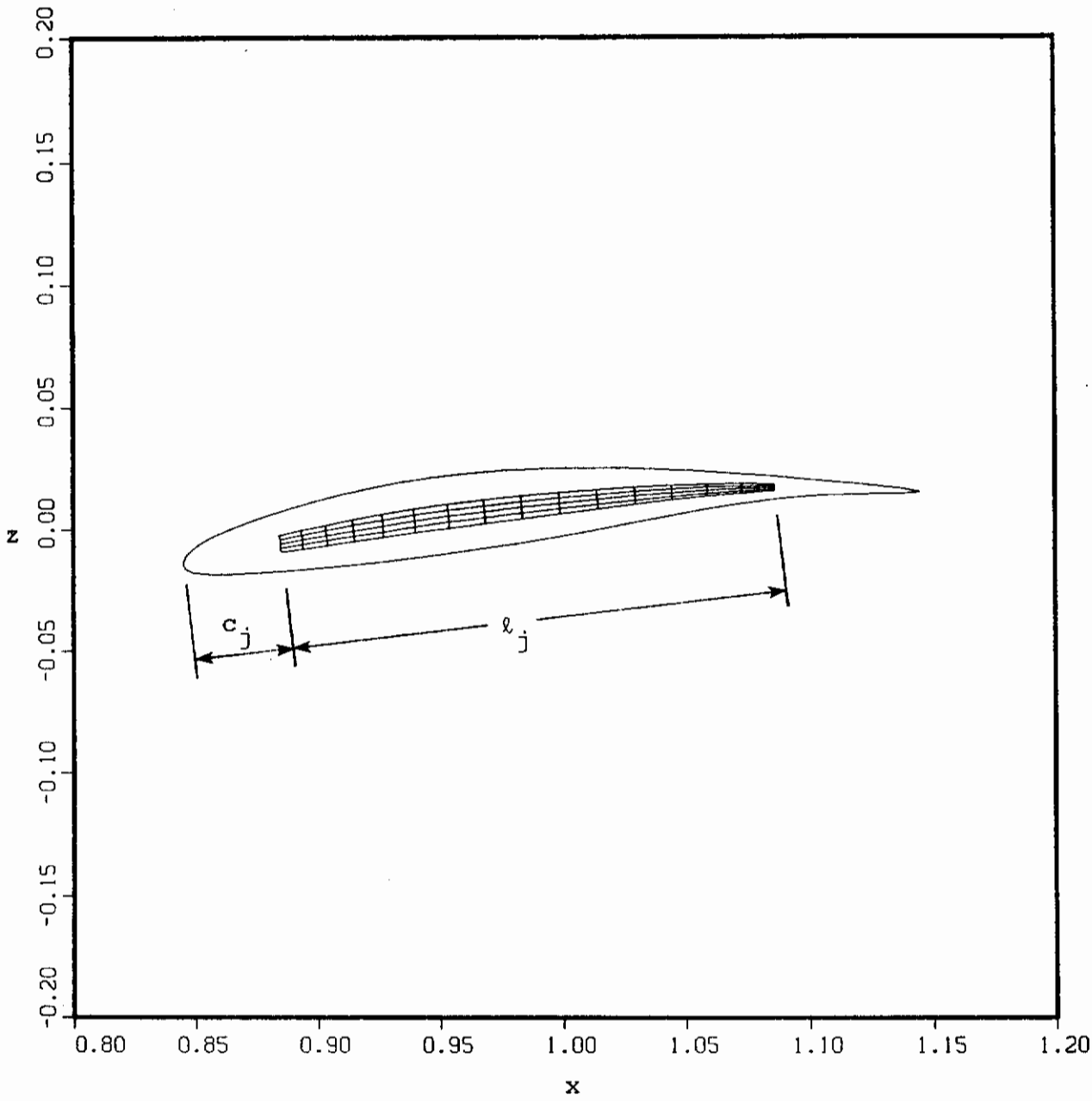

Figure 53.- Tip-jet model.

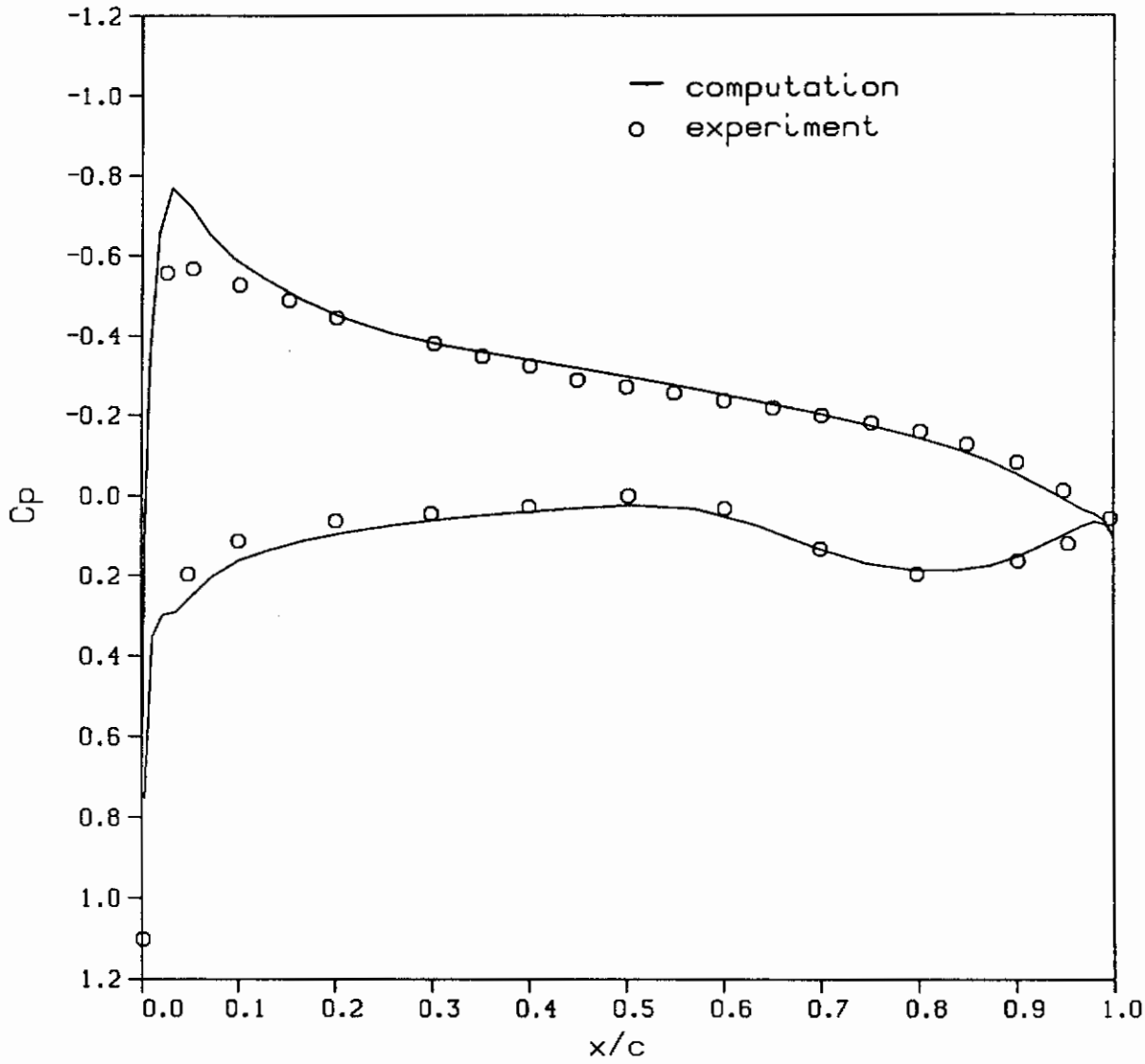

(a) 2y/b = 0.1

Figure 54.- Measured and predicted chordwise pressure distributions on WING C, α = 5°, M_∞ = 0.7.

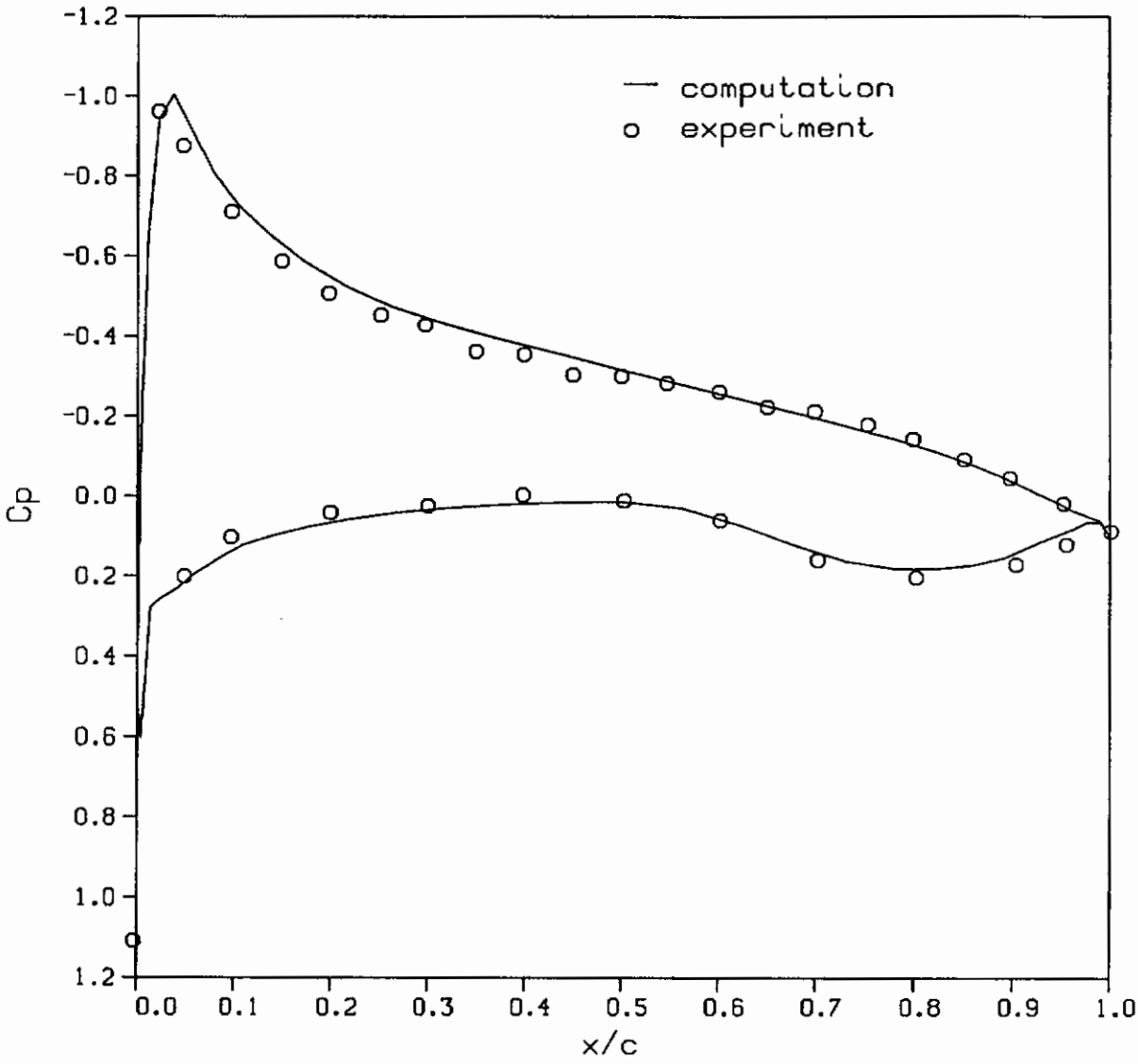

(b) 2y/b = 0.3

Figure 54.- Continued.

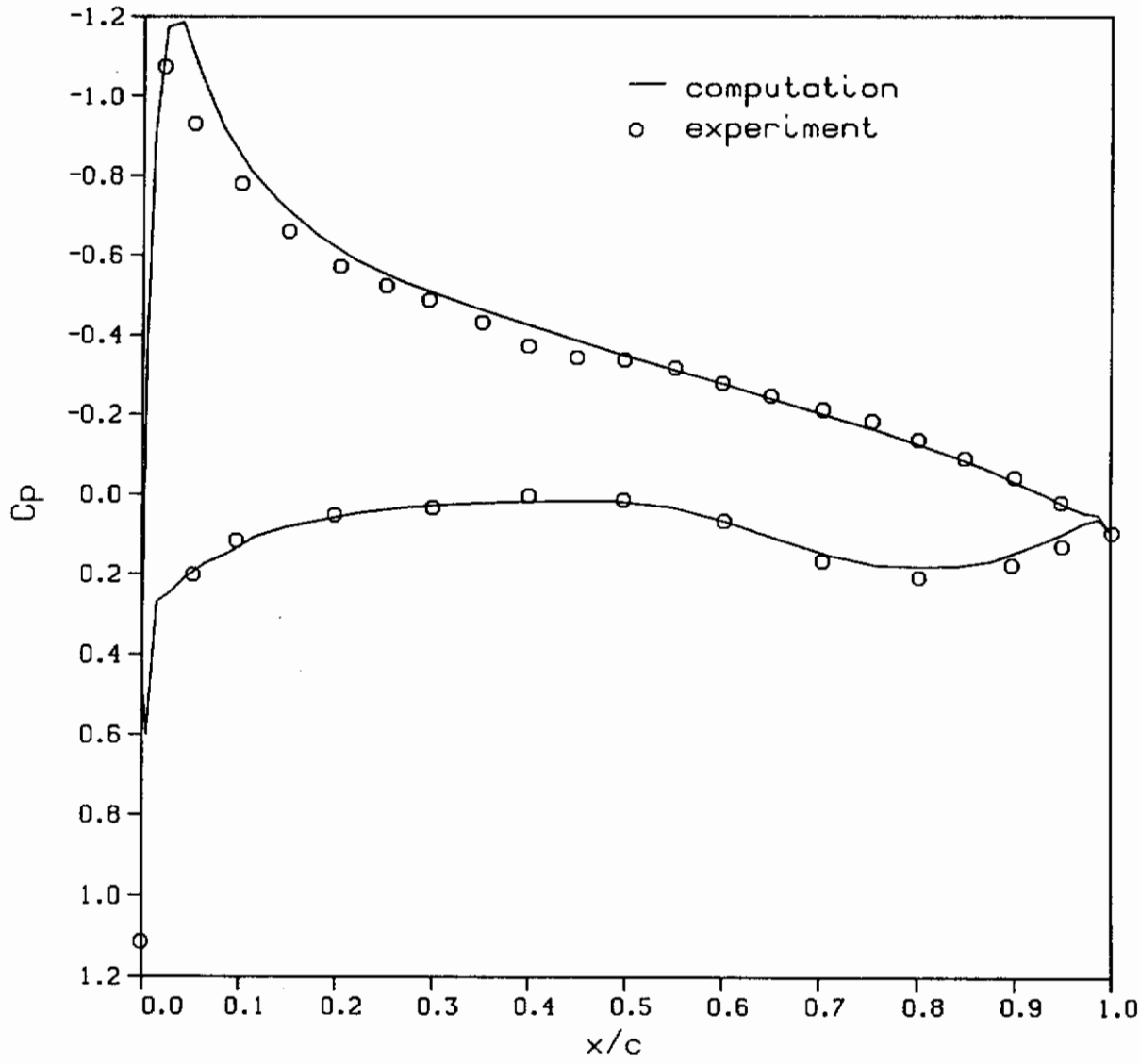

(c) 2y/b = 0.5

Figure 54.- Continued.

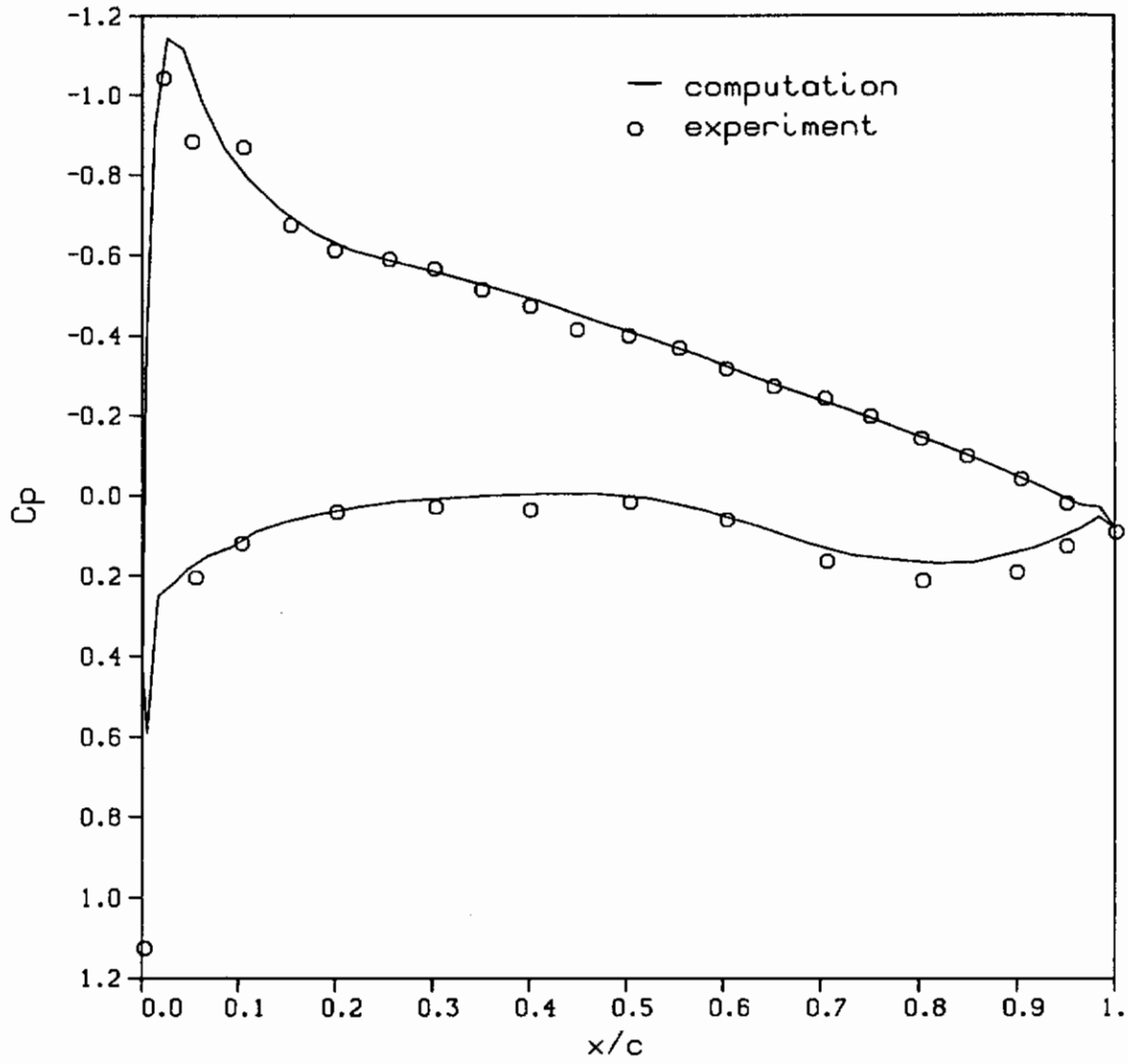

(d) 2y/b = 0.7

Figure 54.- Continued.

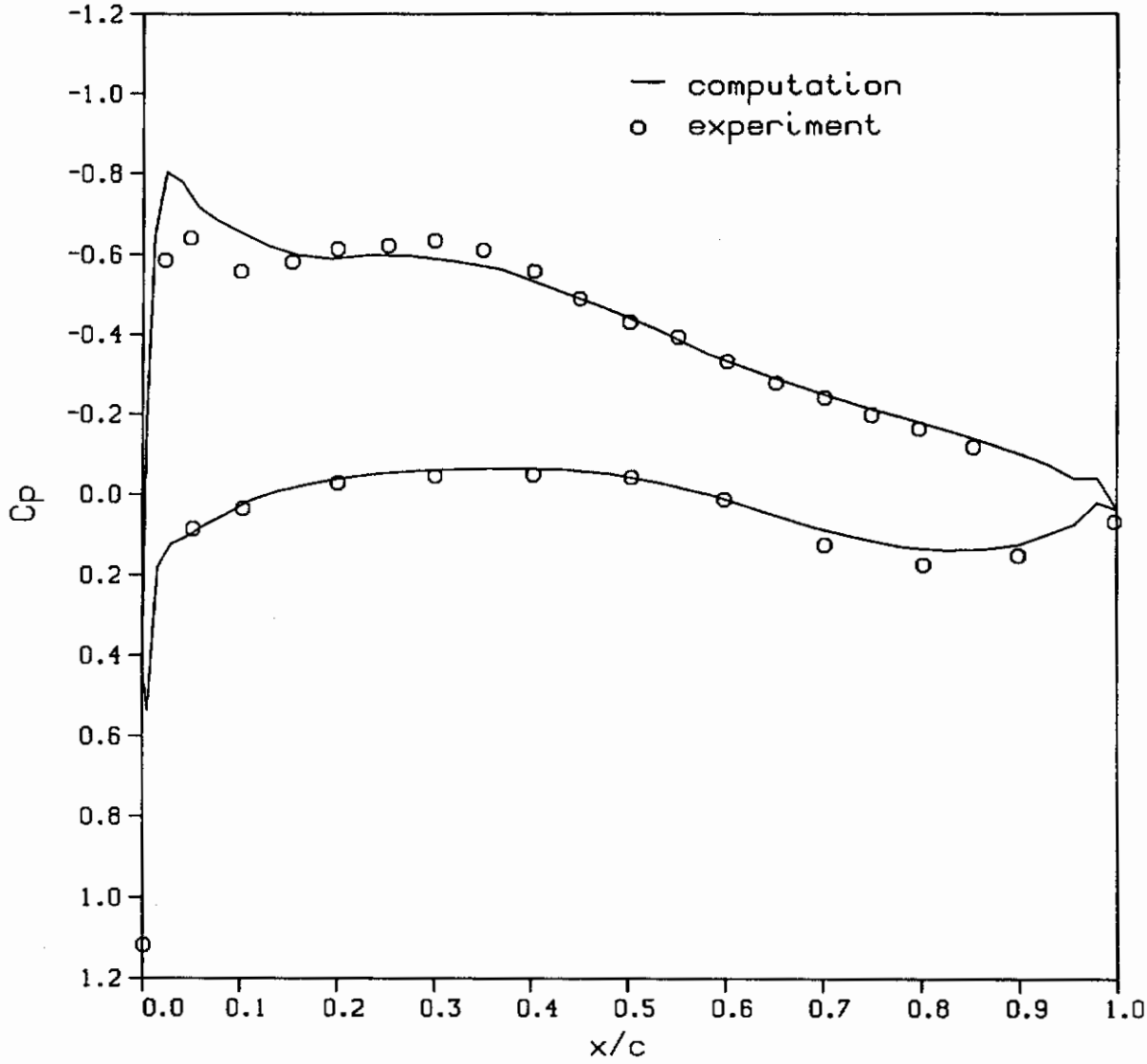

(e) 2y/b = 0.9

Figure 54.- Concluded.

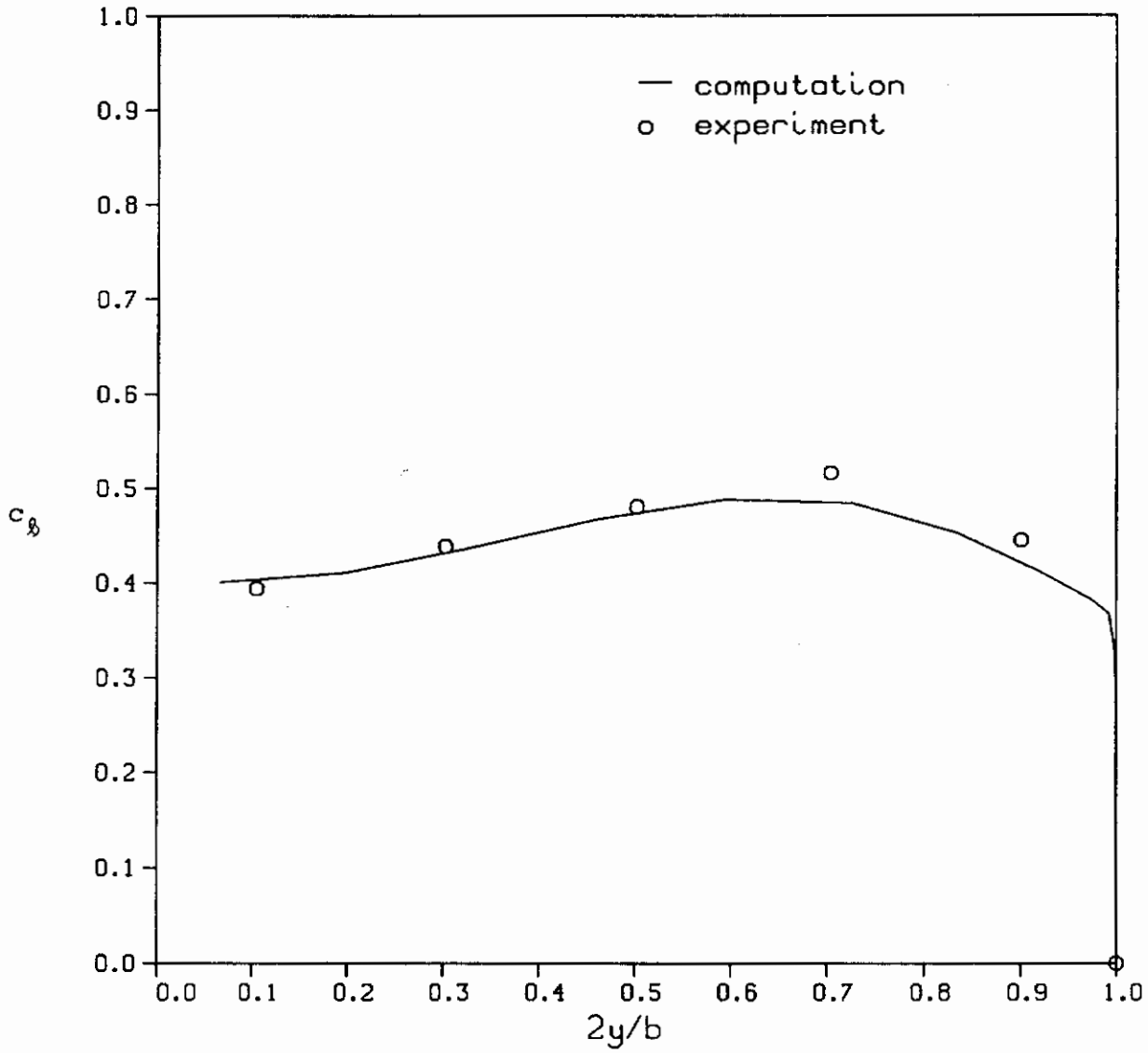

Figure 55.- Measured and predicted spanwise lift distributions on WING C, $\alpha = 5°$, $M_\infty = 0.7$.

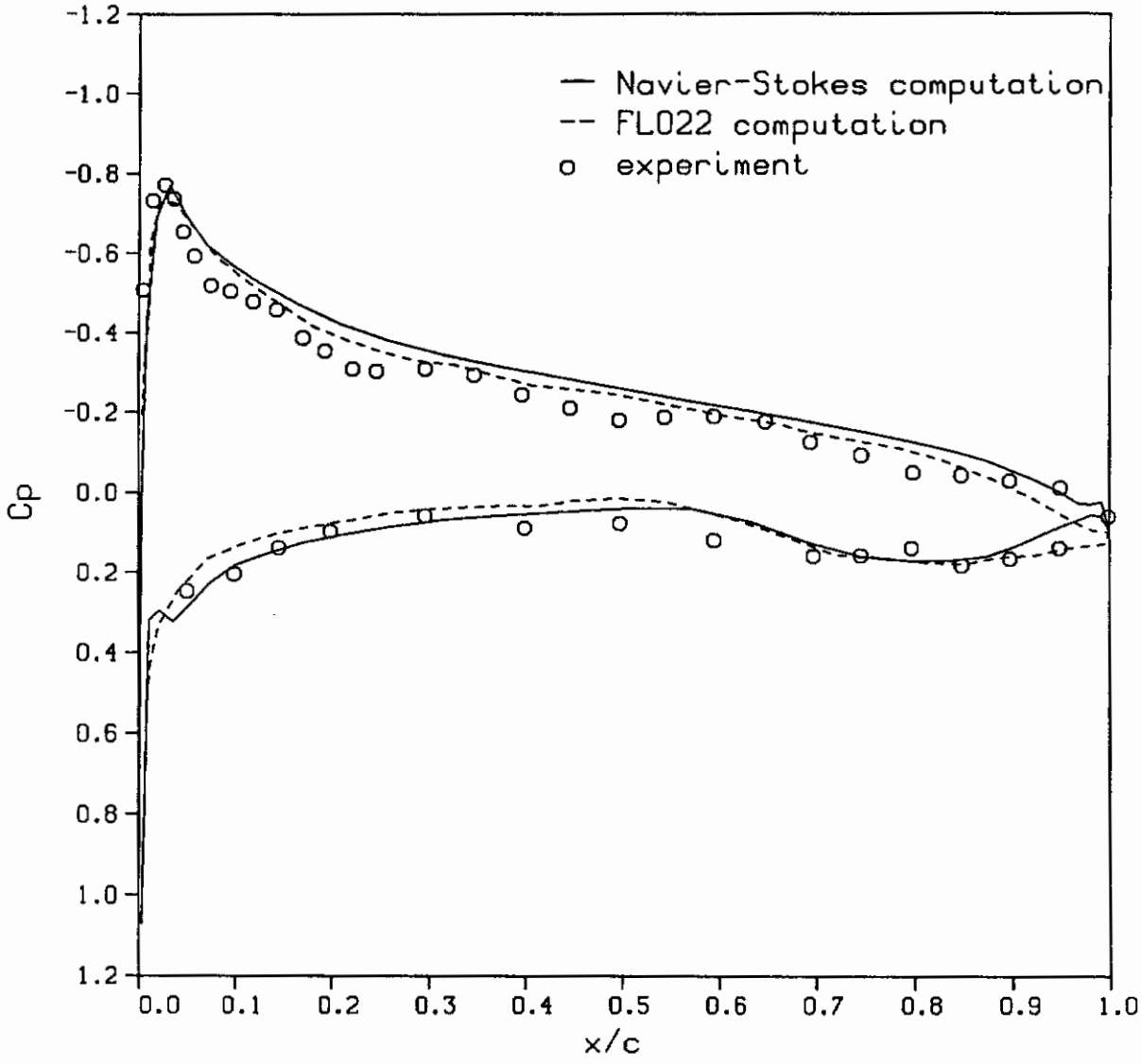

(a) 2y/b = 0.1

Figure 56.- Measured and predicted chordwise pressure distributions on WING C, $\alpha = 5°$, $M_\infty = 0.25$.

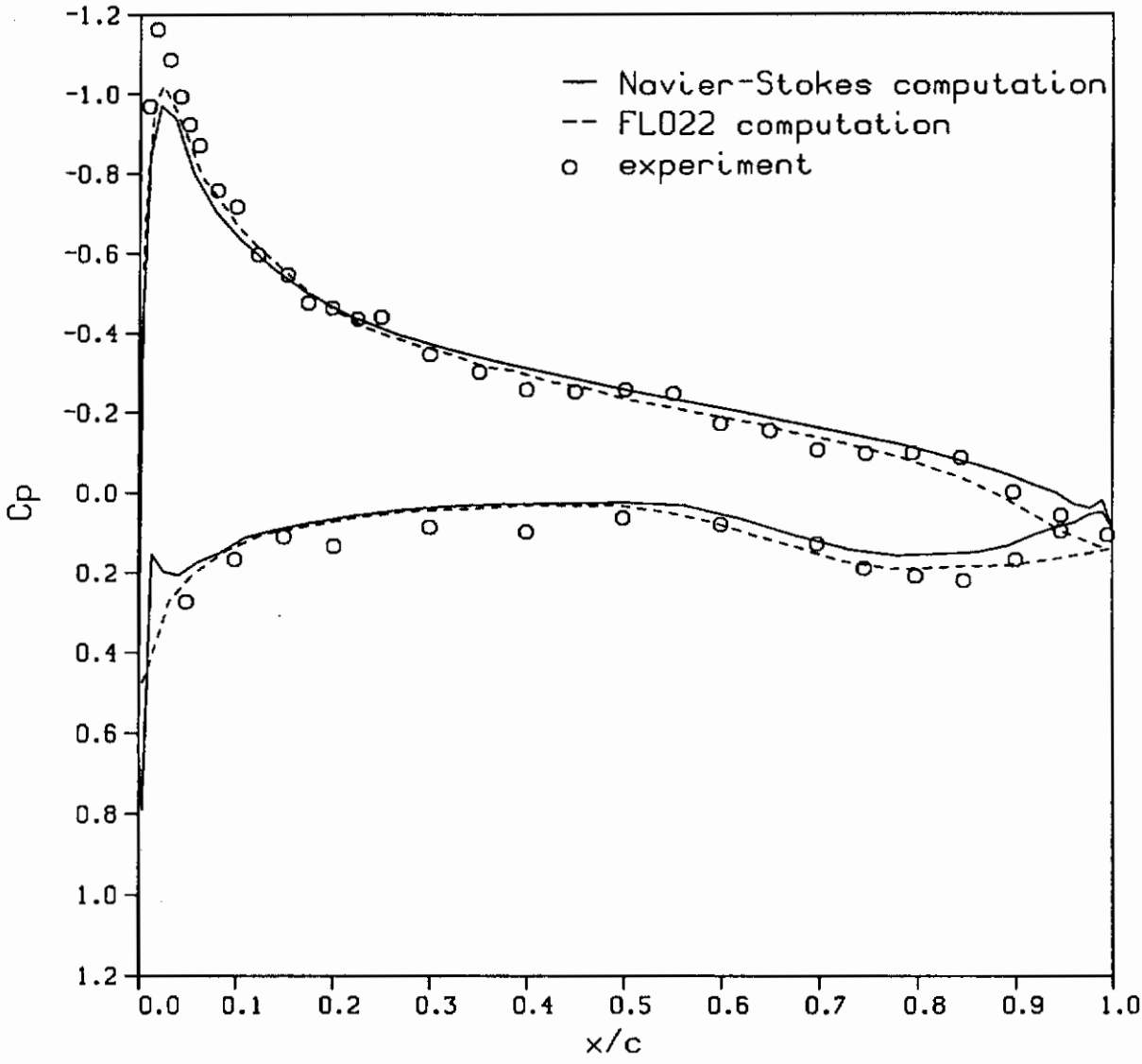

(b) 2y/b = 0.3

Figure 56.- Continued.

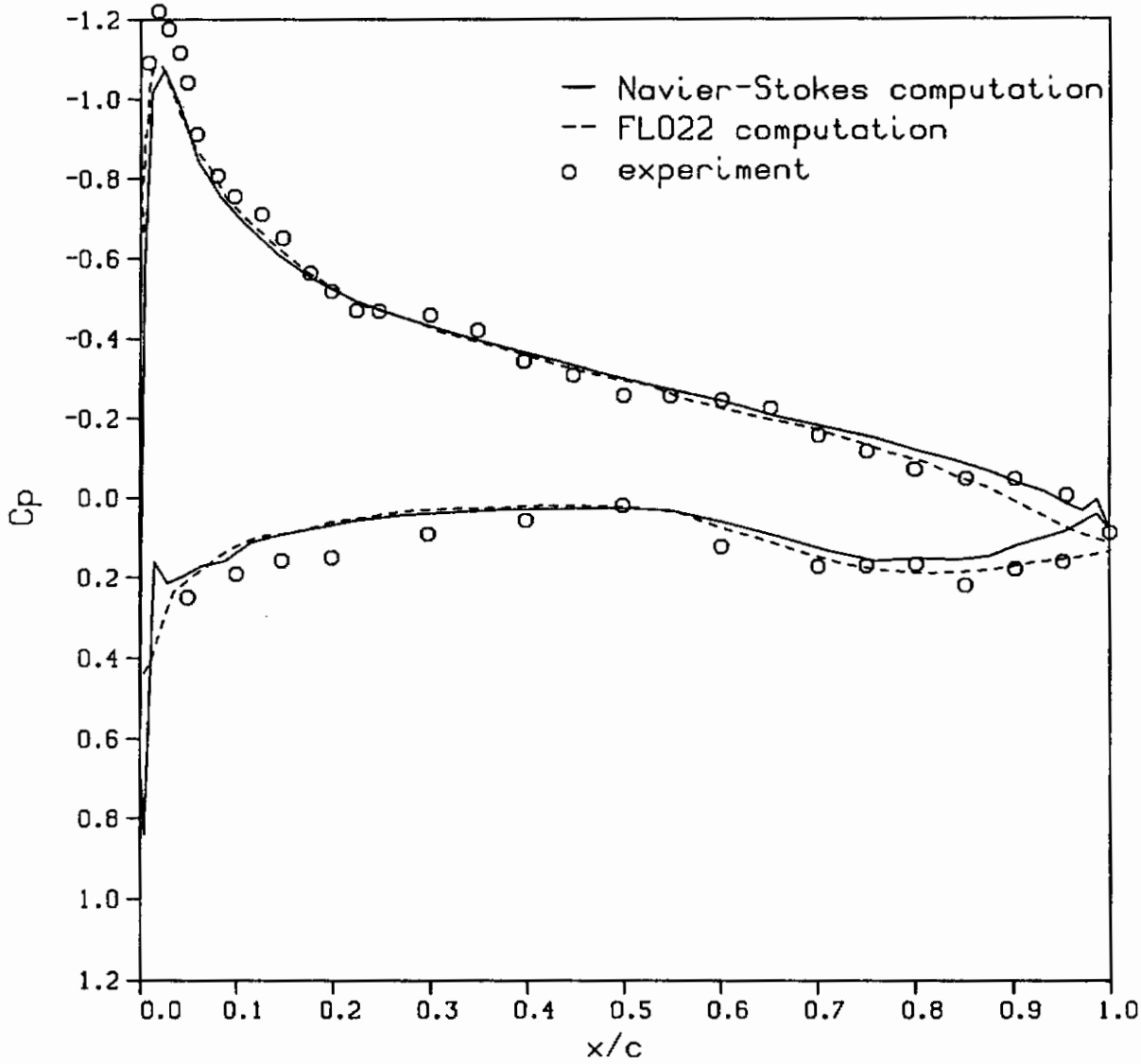

(c) 2y/b = 0.5

Figure 56.- Continued.

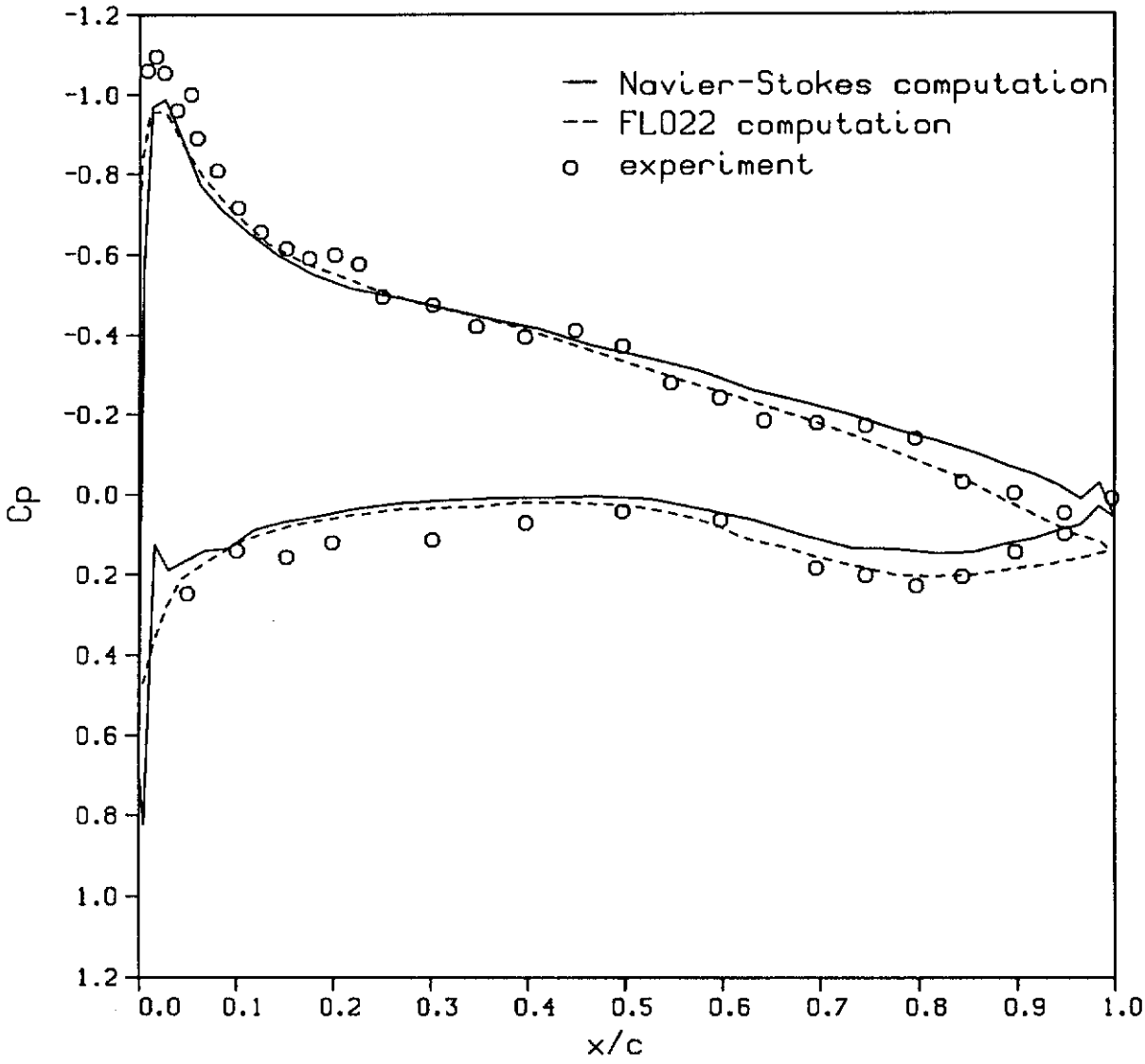

(d) 2y/b = 0.7

Figure 56.- Continued.

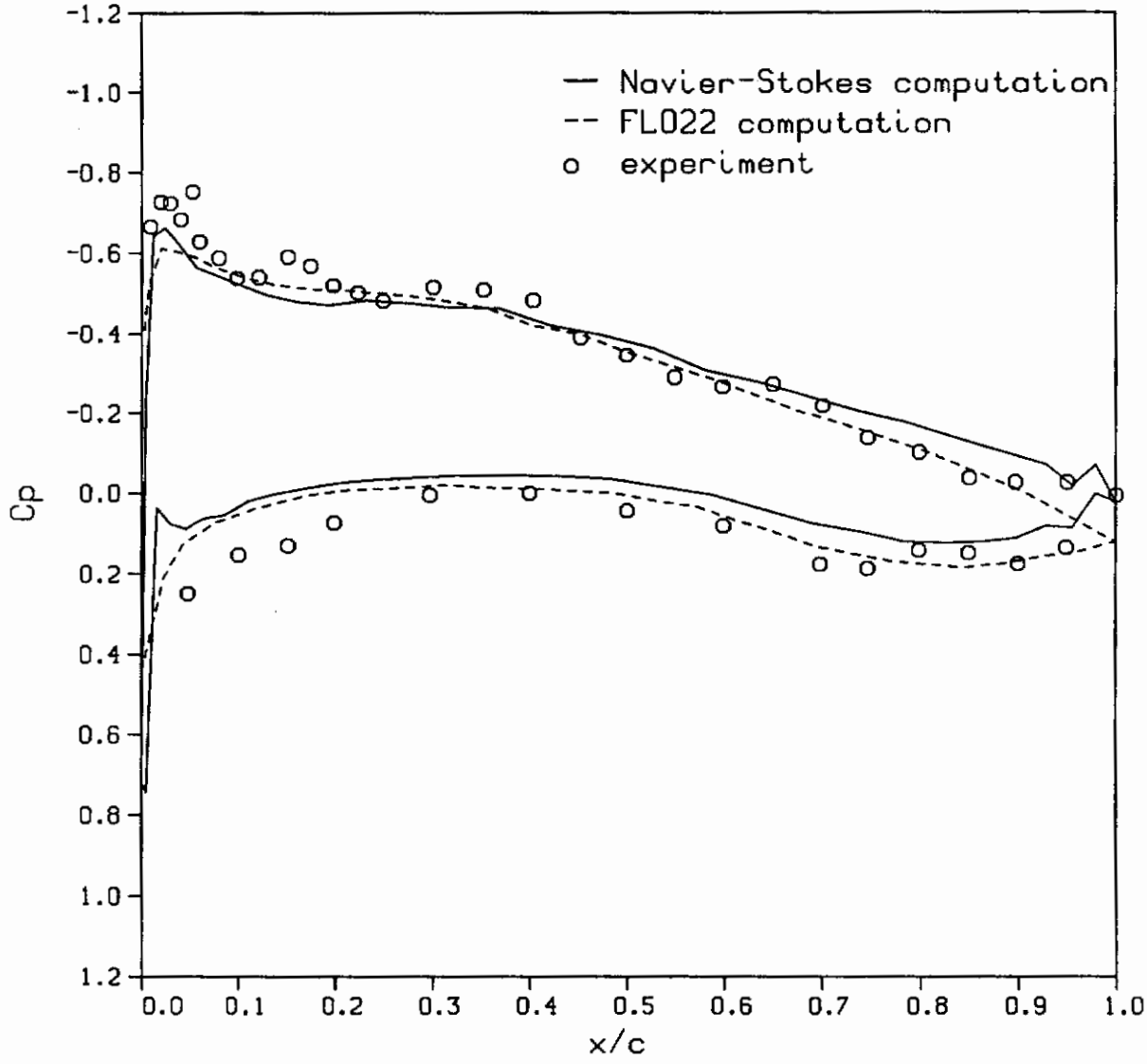

(e) 2y/b = 0.9

Figure 56.- Concluded.

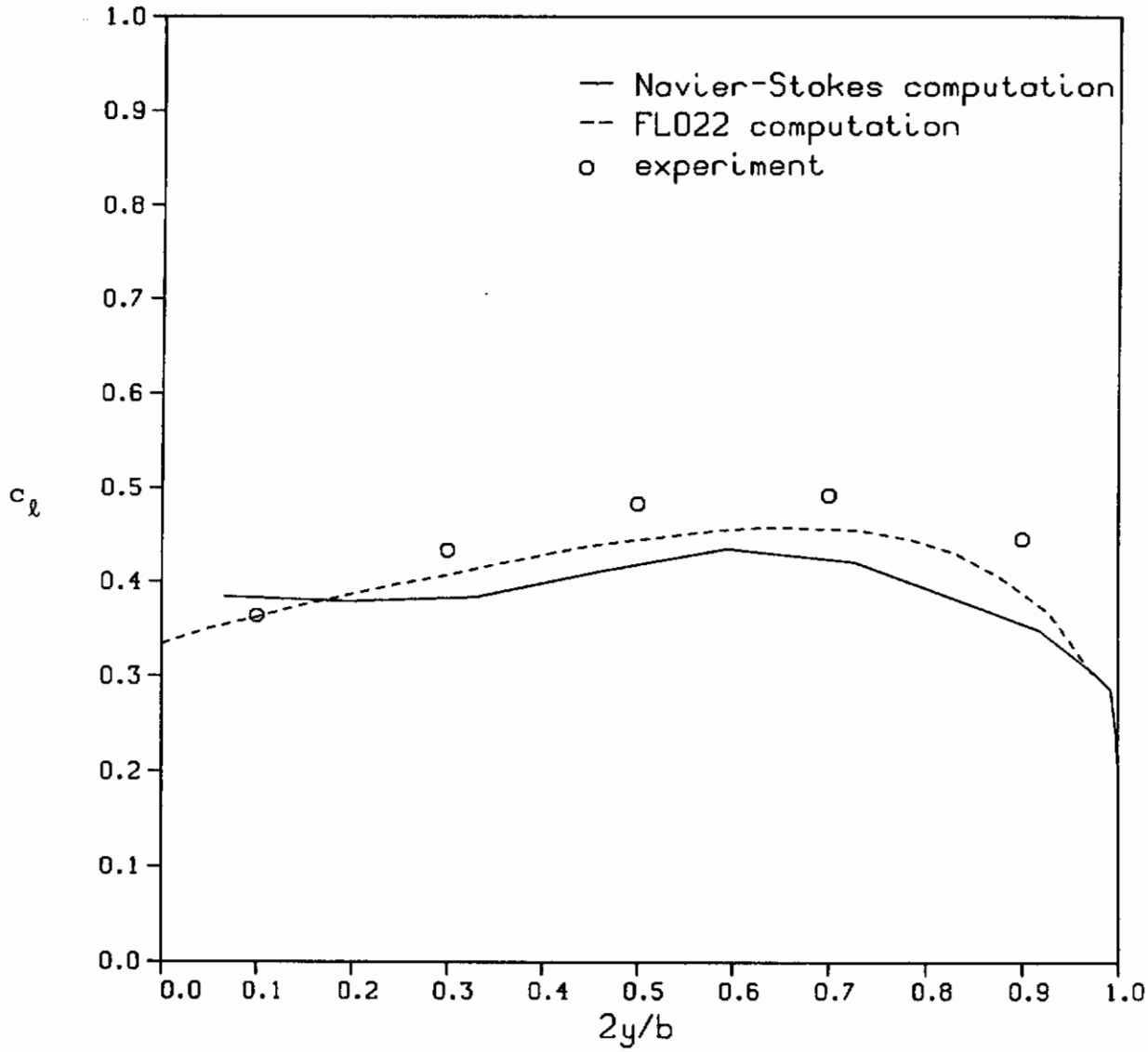

Figure 57.- Measured and predicted spanwise lift distributions on WING C, $\alpha = 5°$, $M_\infty = 0.25$.

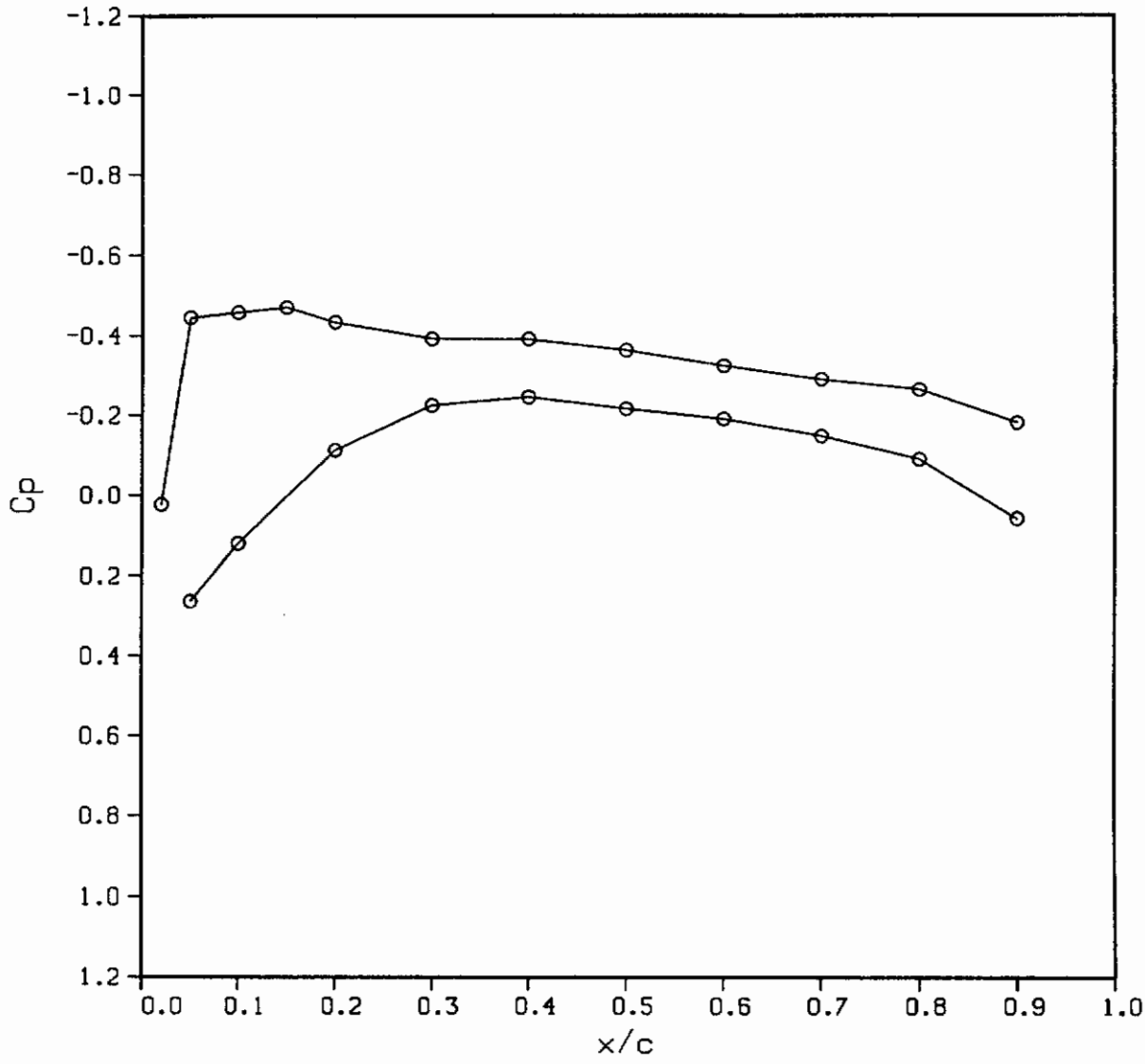

(a) 2y/b = 0.15

Figure 58.- Measured chordwise pressure distributions on large-scale WING C-BT, $\alpha = 5°$, $M_\infty = 0.25$.

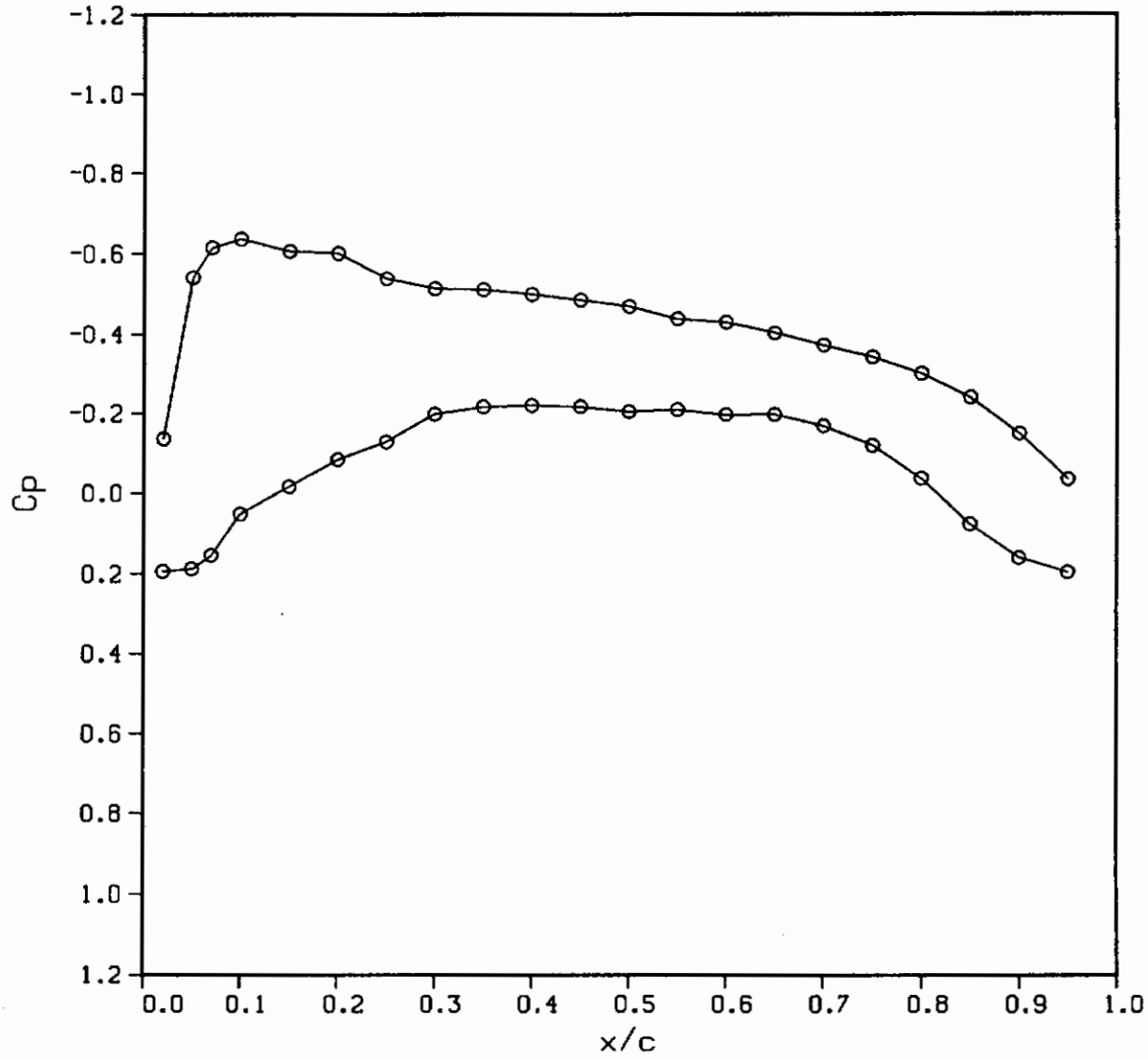

(b) 2y/b = 0.5

Figure 58.- Continued.

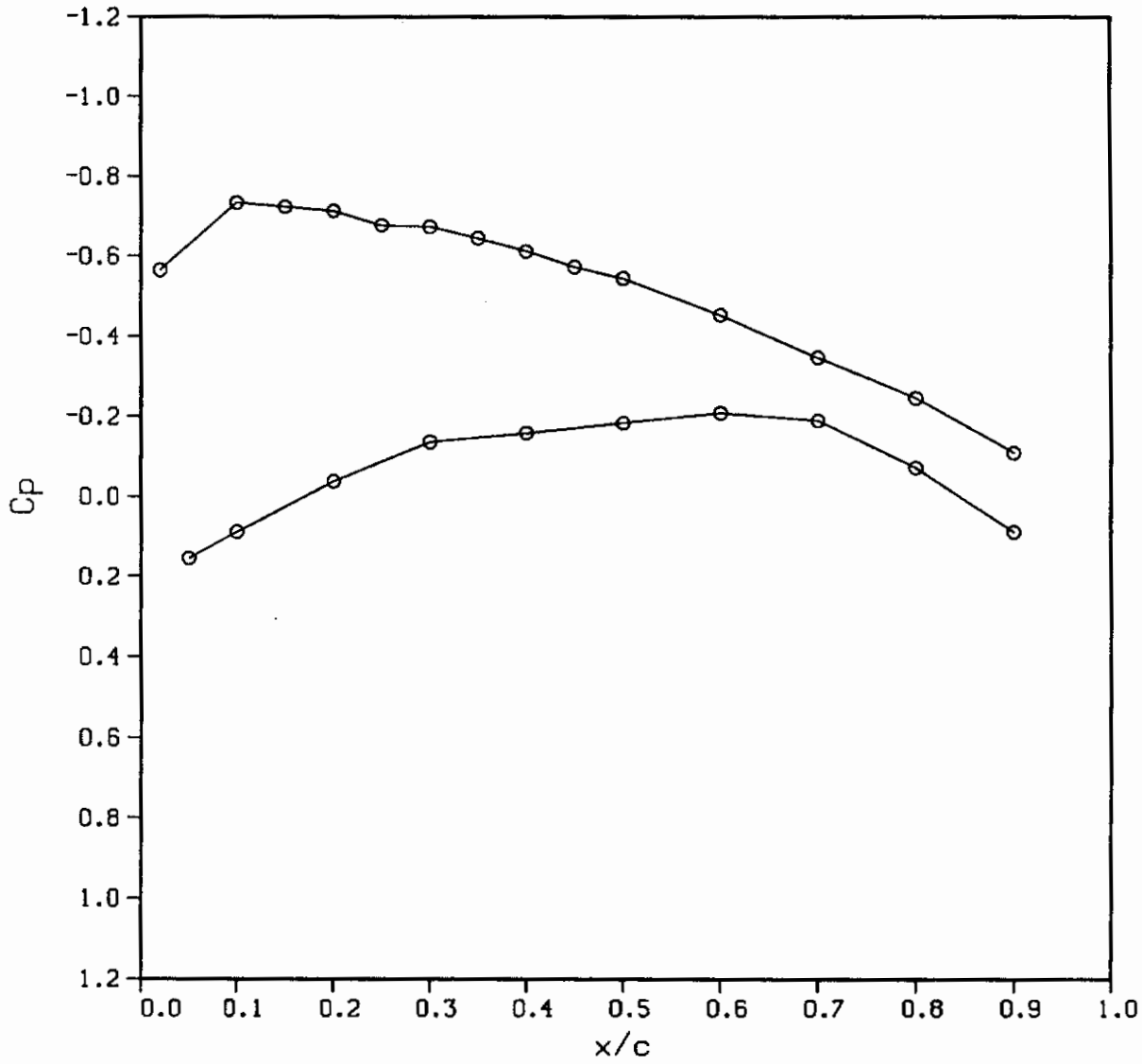

(c) 2y/b = 0.9

Figure 58.- Concluded.

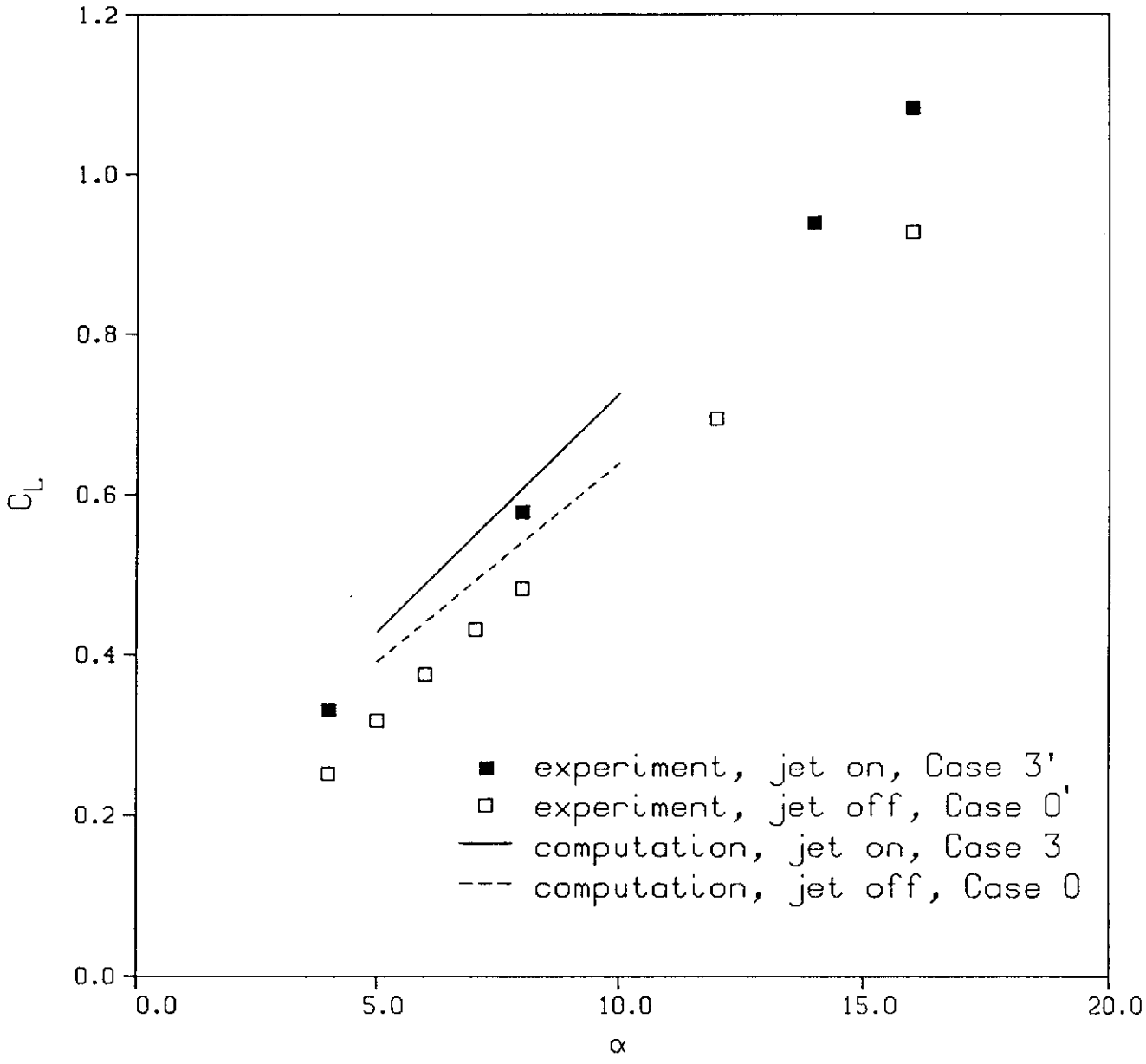

Figure 59.- Effect of tip blowing on measured and predicted lift coefficients.

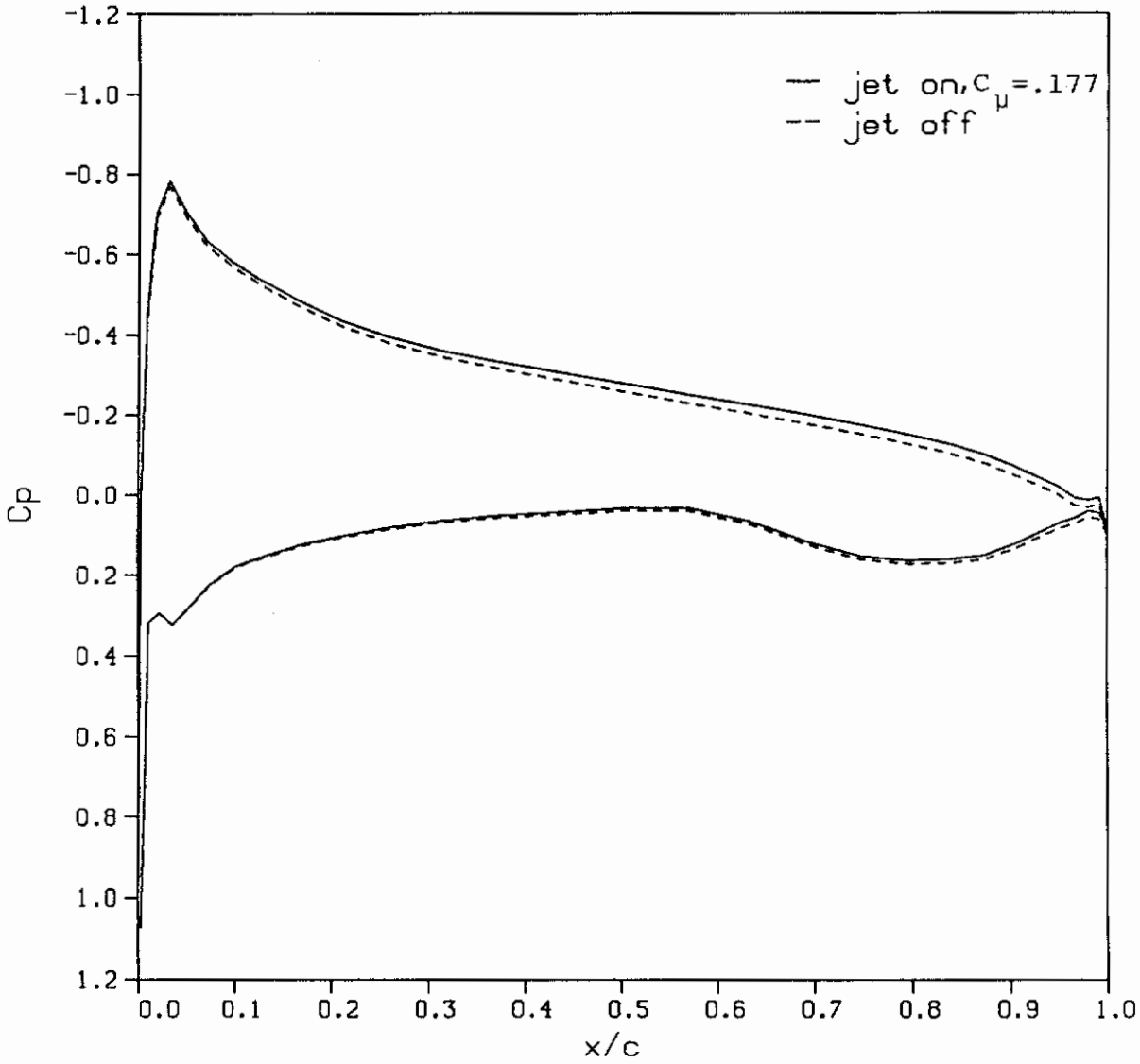

(a) 2y/b = 0.1

Figure 60.- Comparison of computed chordwise pressure distributions with and without tip blowing, $\alpha = 5°$, $M_\infty = 0.25$.

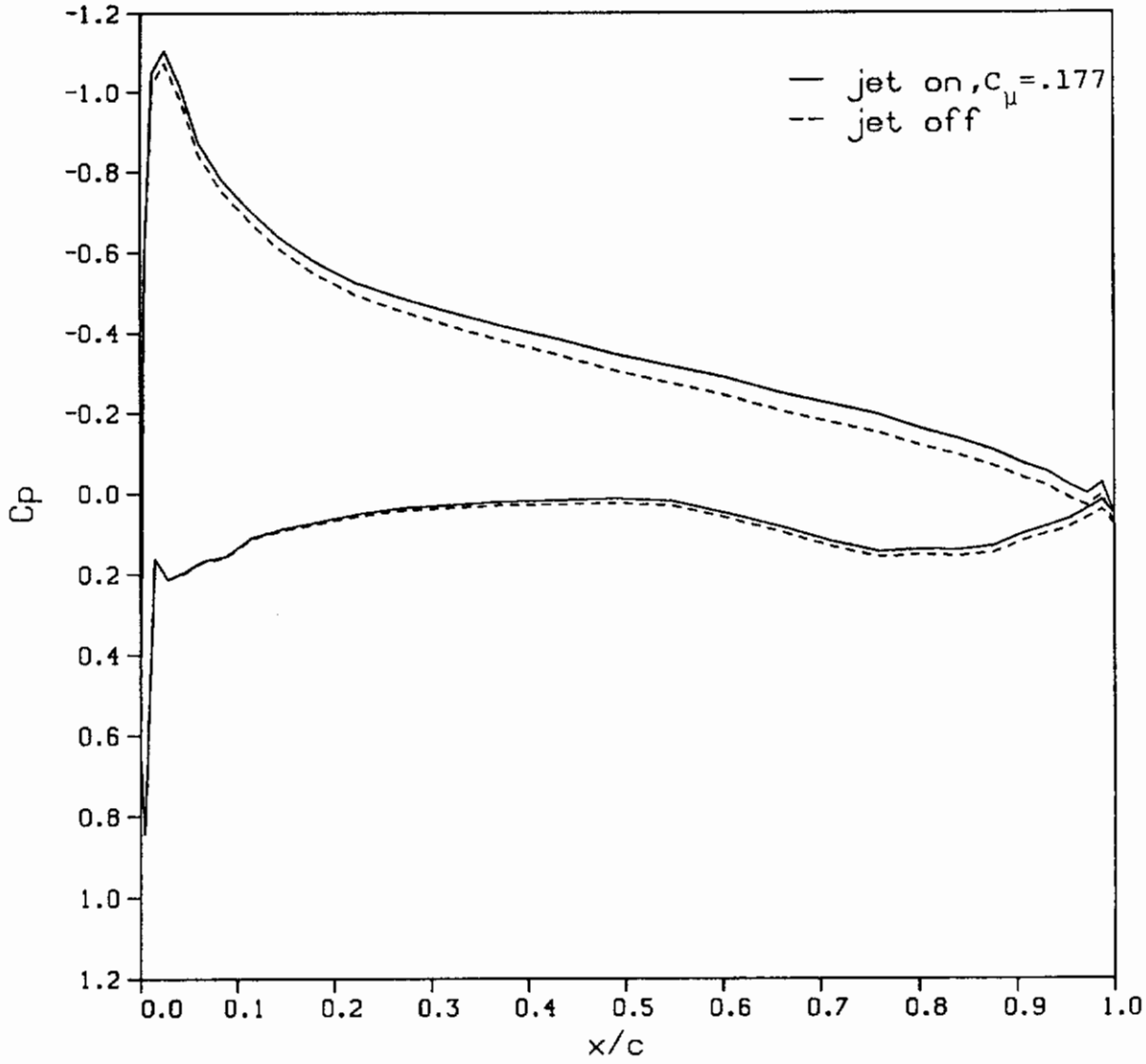

(b) 2y/b = 0.5

Figure 60.- Continued.

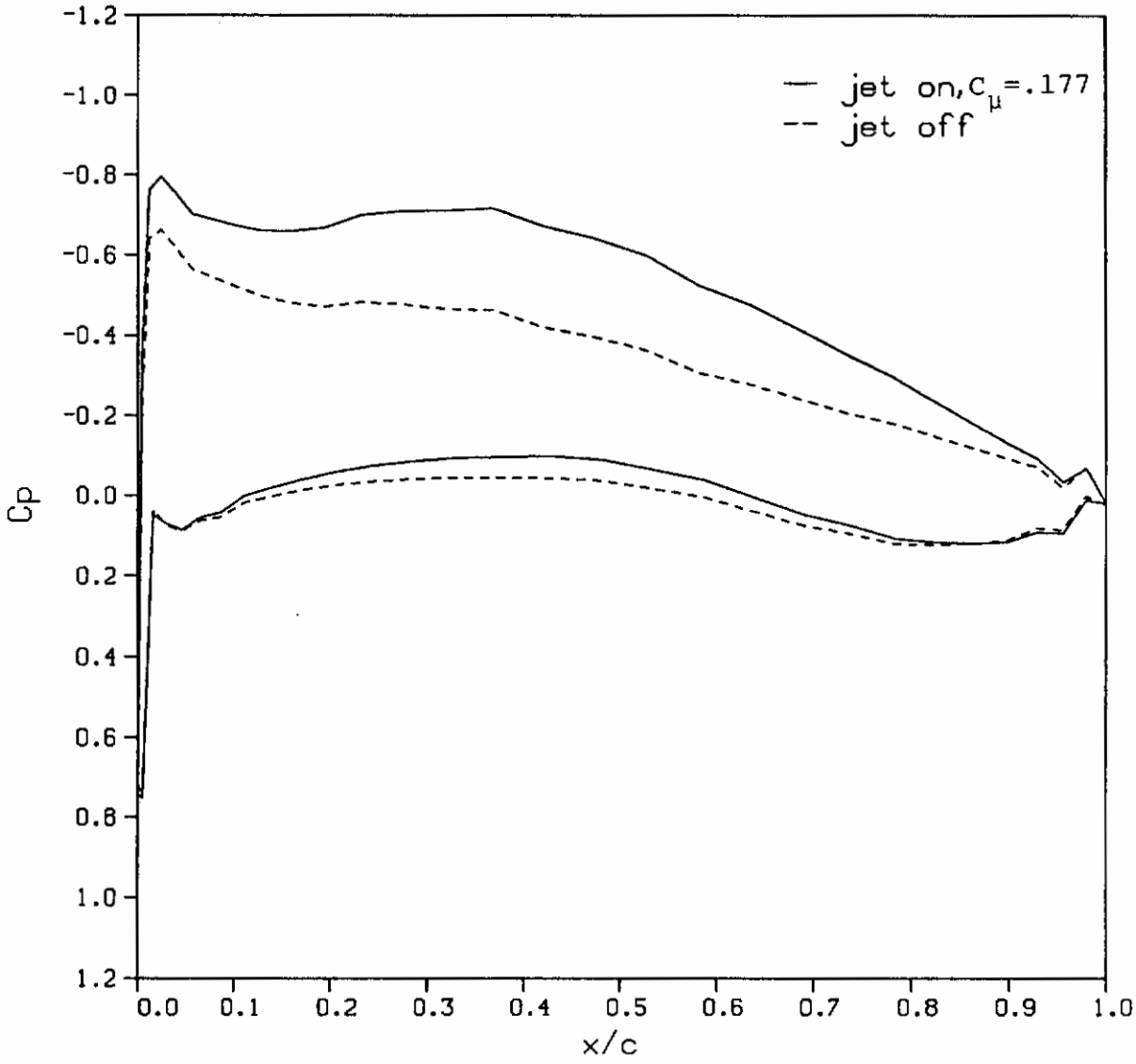

(c) 2y/b = 0.9

Figure 60.- Concluded.

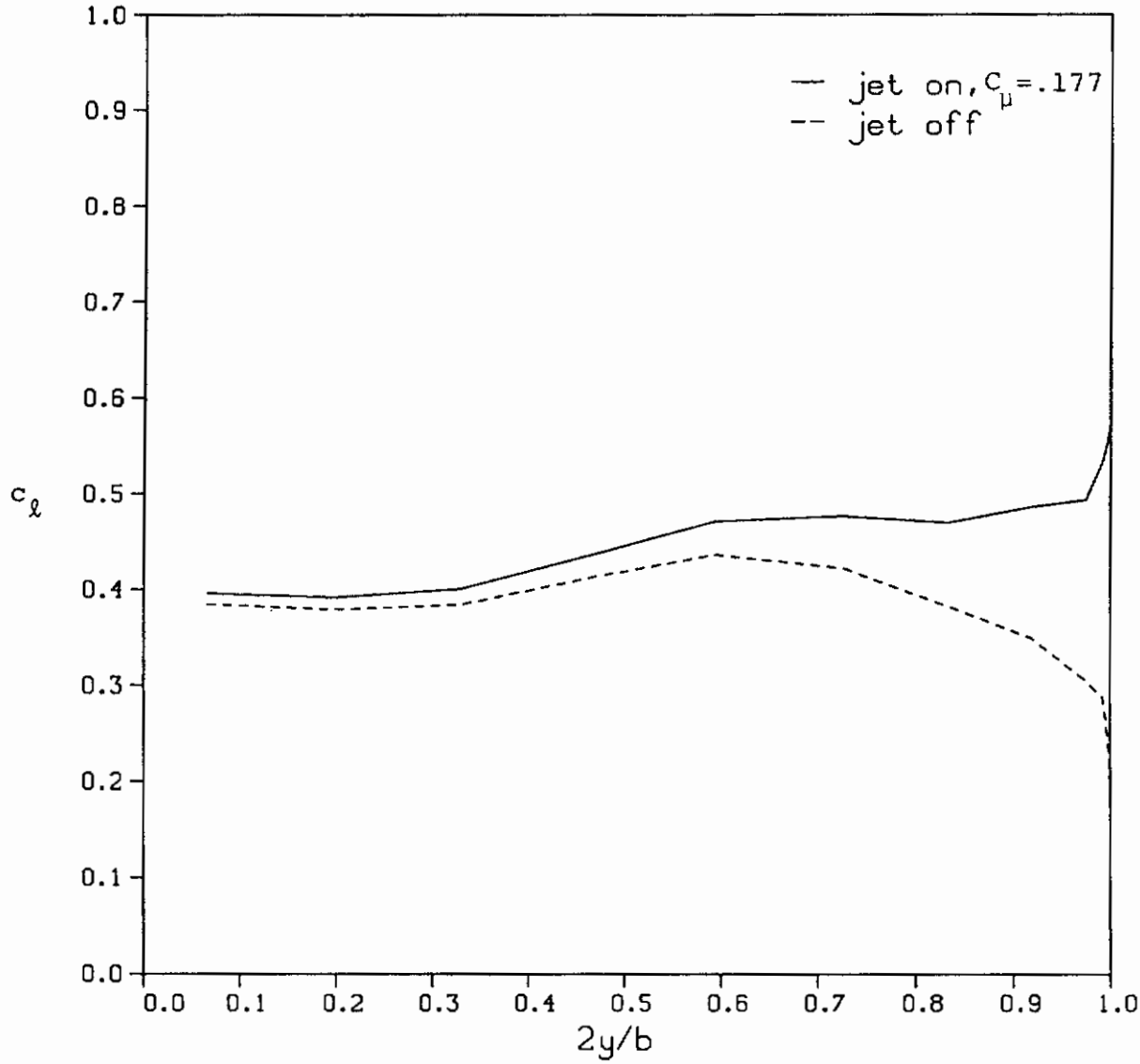

Figure 61.- Comparison of predicted spanwise loading with and without tip blowing, α = 5°, M_∞ = 0.25.

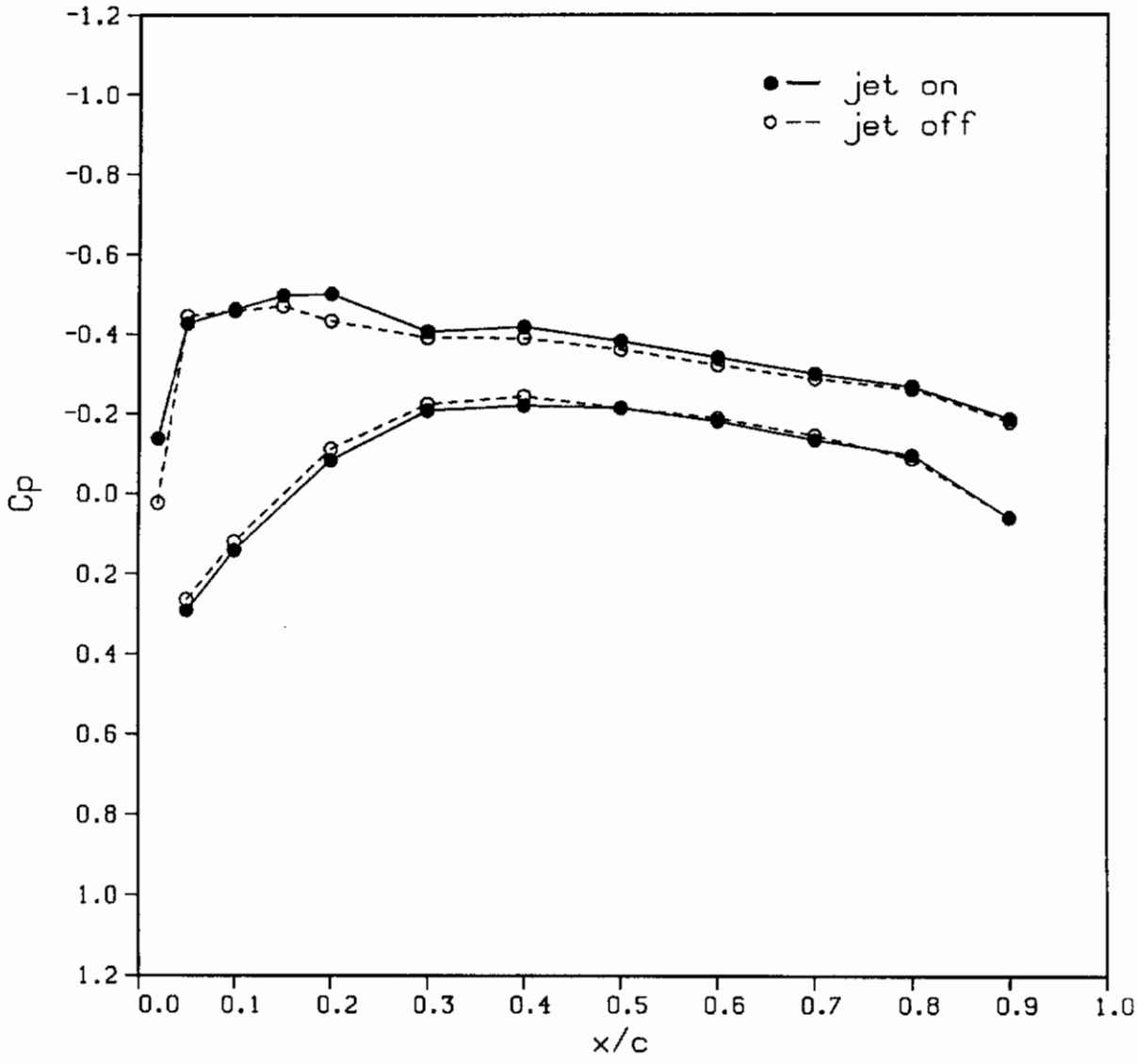

(a) 2y/b = 0.15

Figure 62.- Comparison of typical measured chordwise pressure distributions with and without tip blowing for large-scale wing.

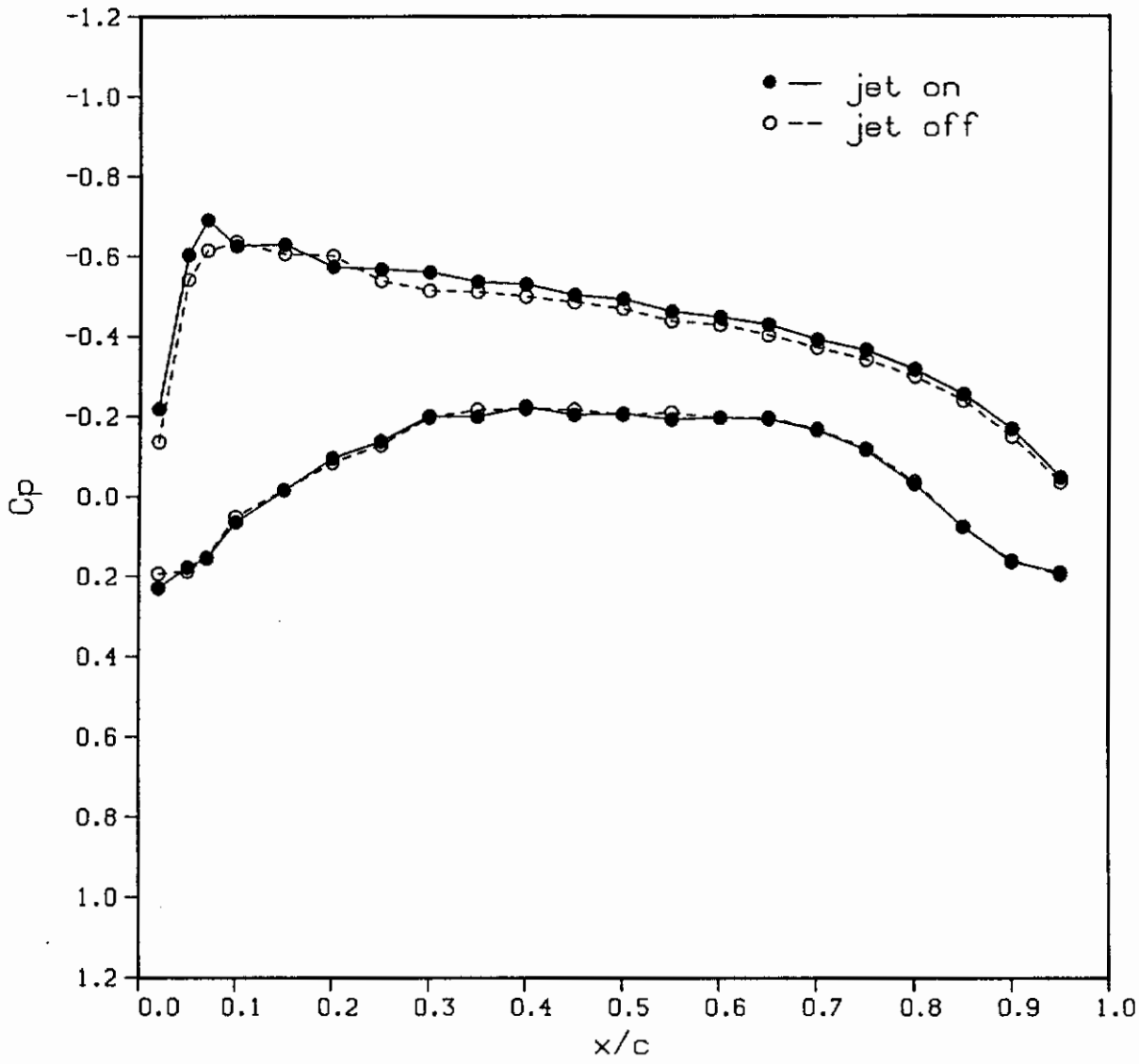

(b) 2y/b = 0.5

Figure 62.- Continued.

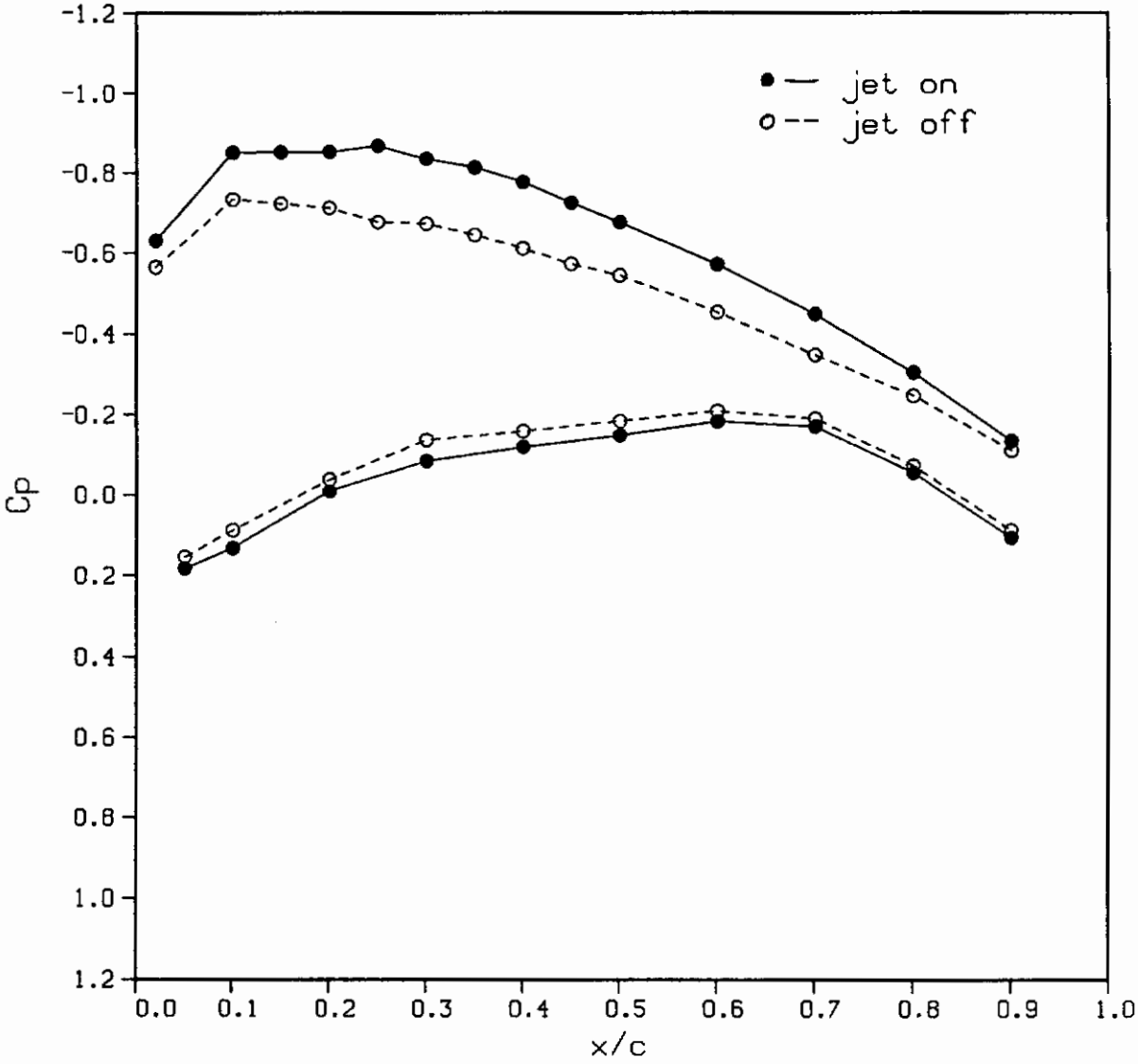

(c) 2y/b = 0.9

Figure 62.- Concluded.

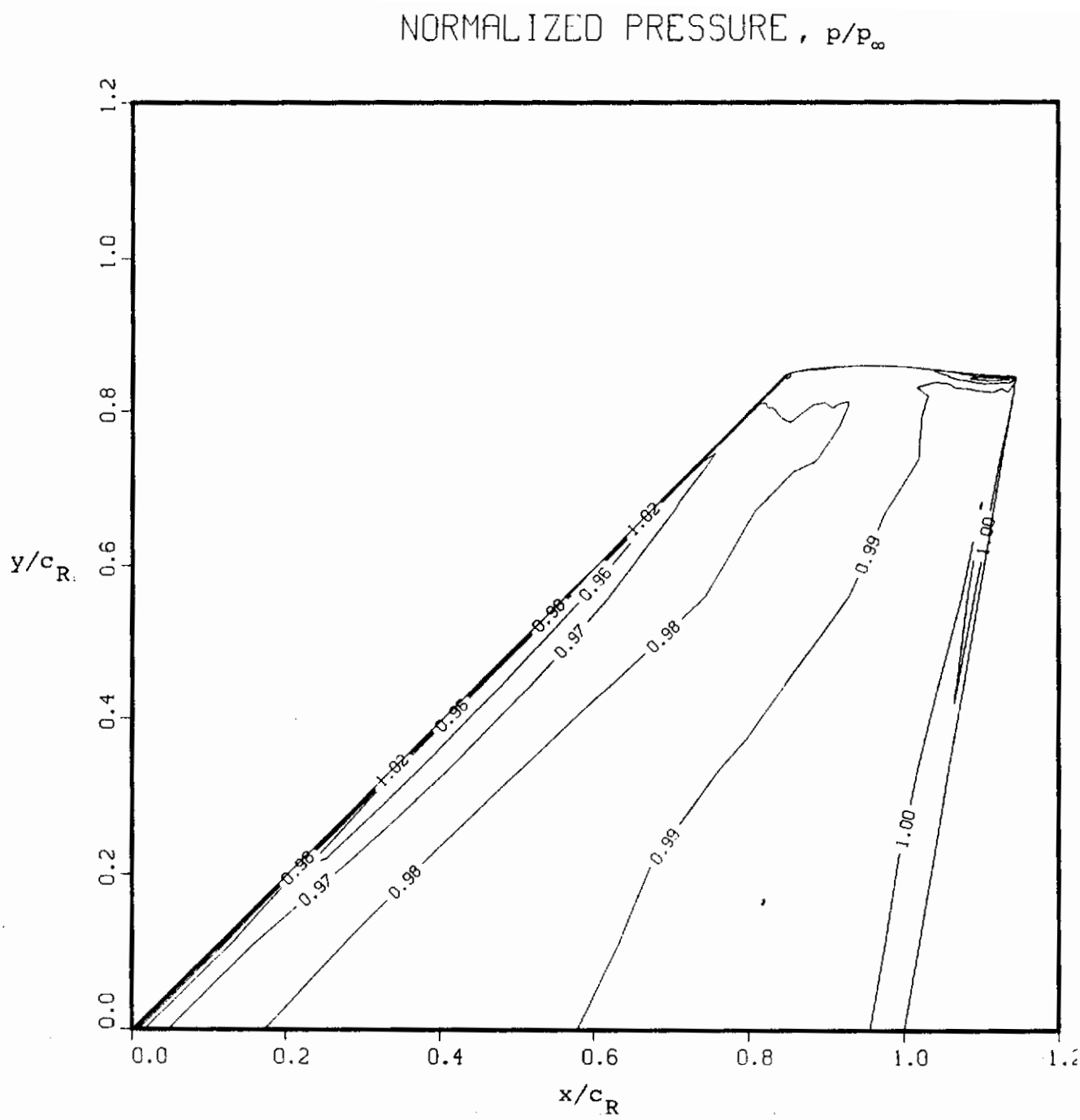

(a) No blowing, upper surface

Figure 63.- Computed wing surface pressure contours, $\alpha = 5°$, $M_\infty = 0.25$.

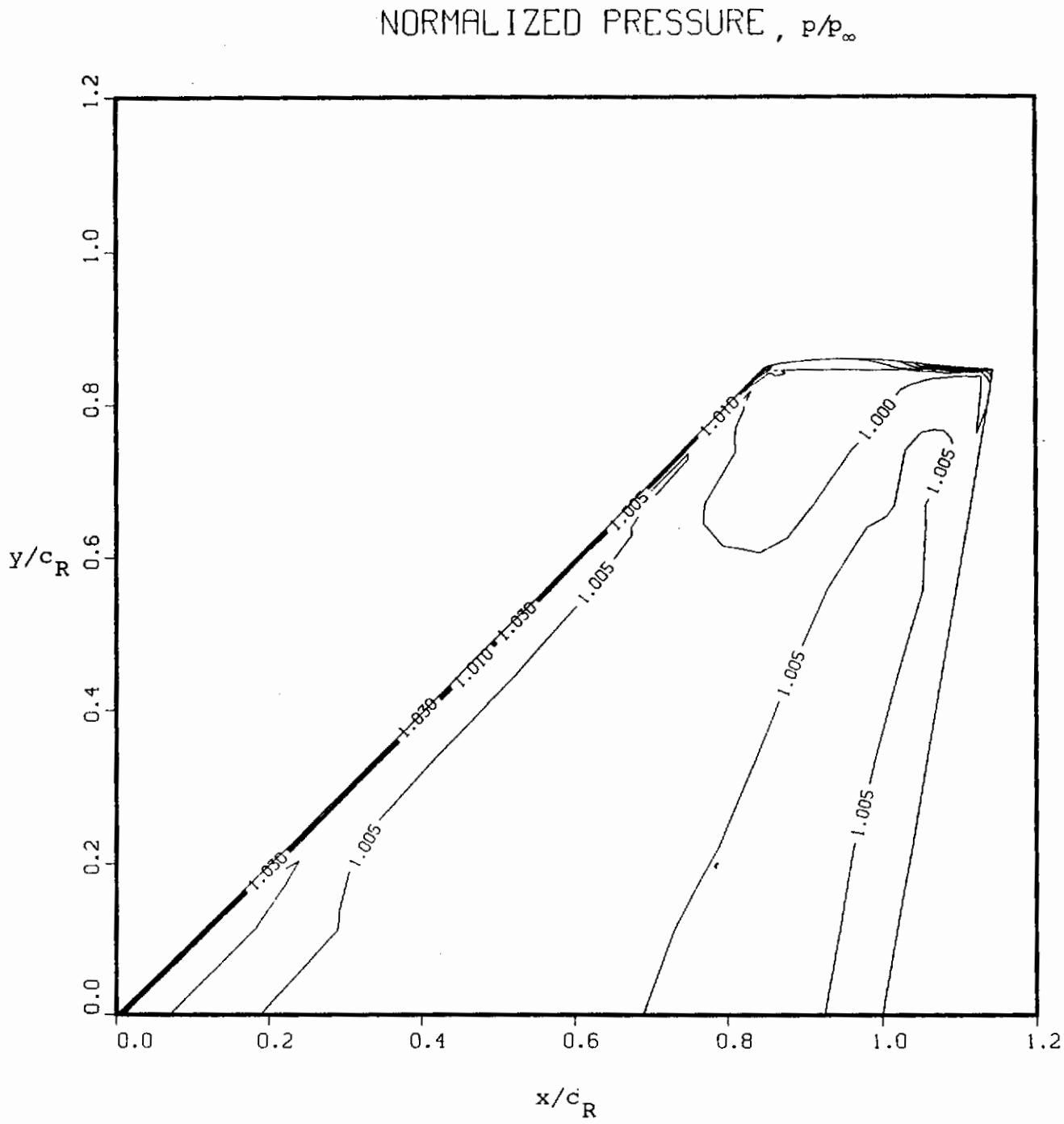

(b) No blowing, lower surface

Figure 63.- Continued.

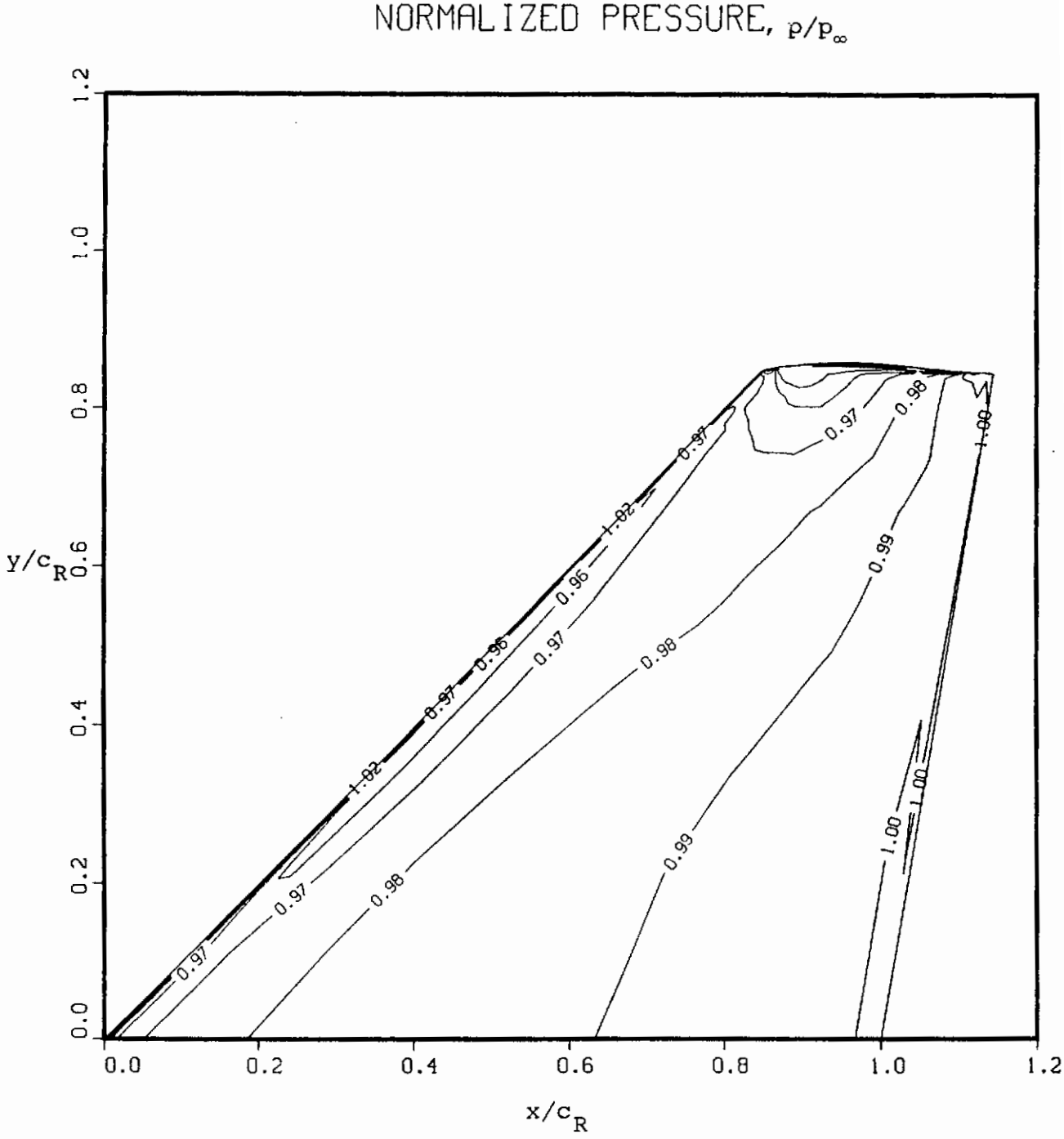

(c) C_μ = 0.177, upper surface

Figure 63.- Continued.

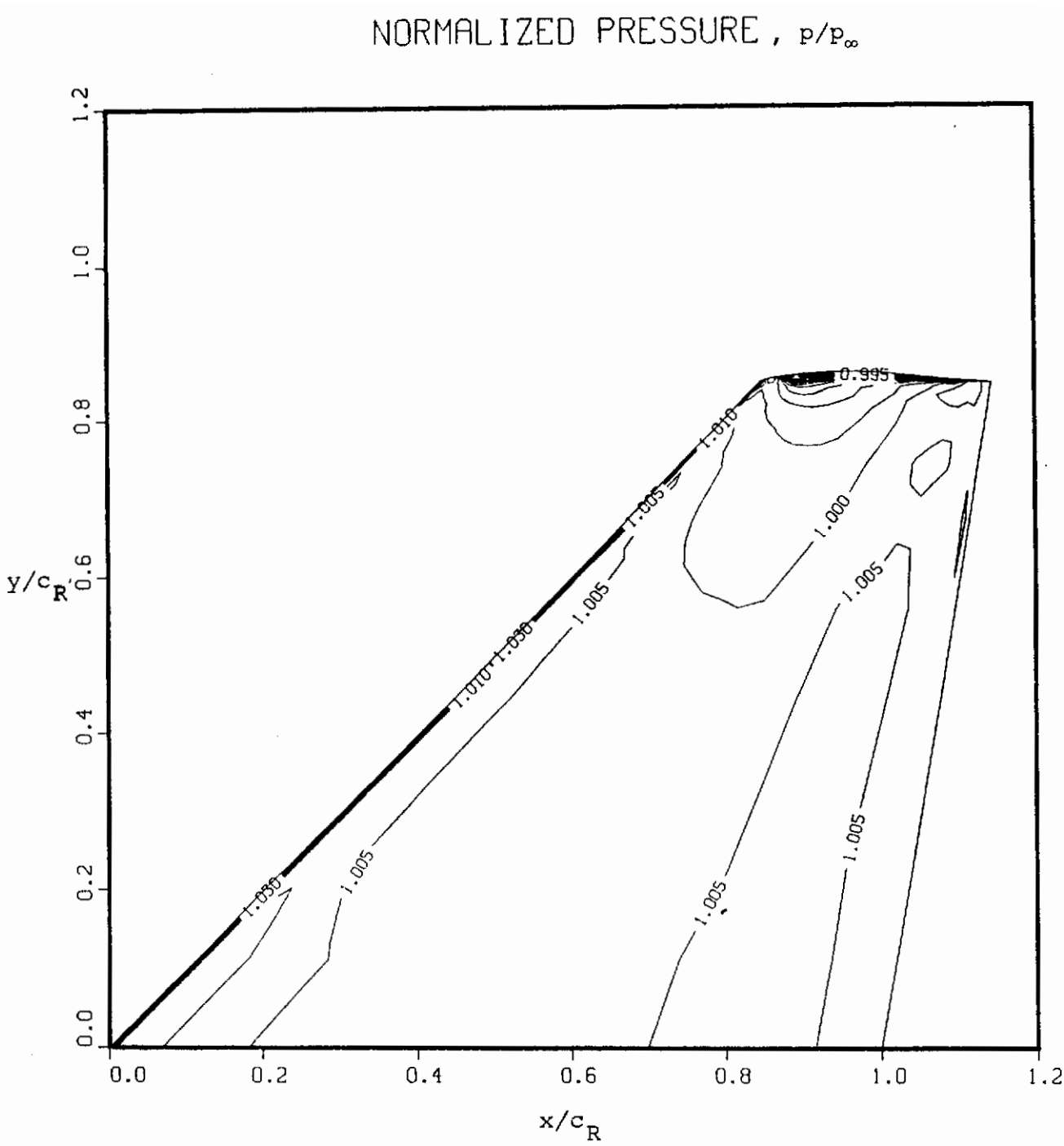

(d) C_μ = 0.177, lower surface

Figure 63.- Concluded.

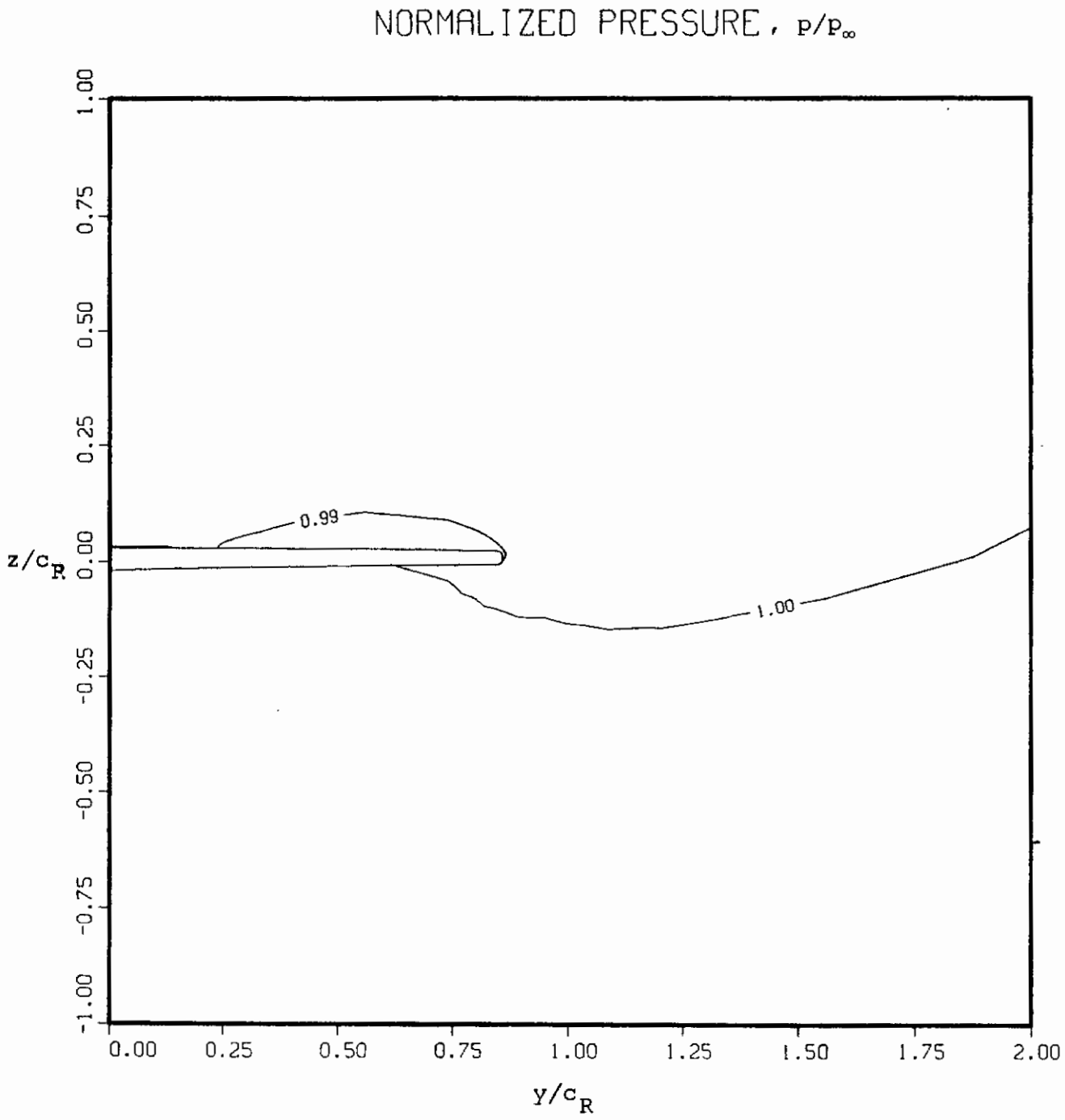

(a) No blowing

Figure 64.- Computed pressure contours at 35-percent chord, $\alpha = 5°$, $M_\infty = 0.25$.

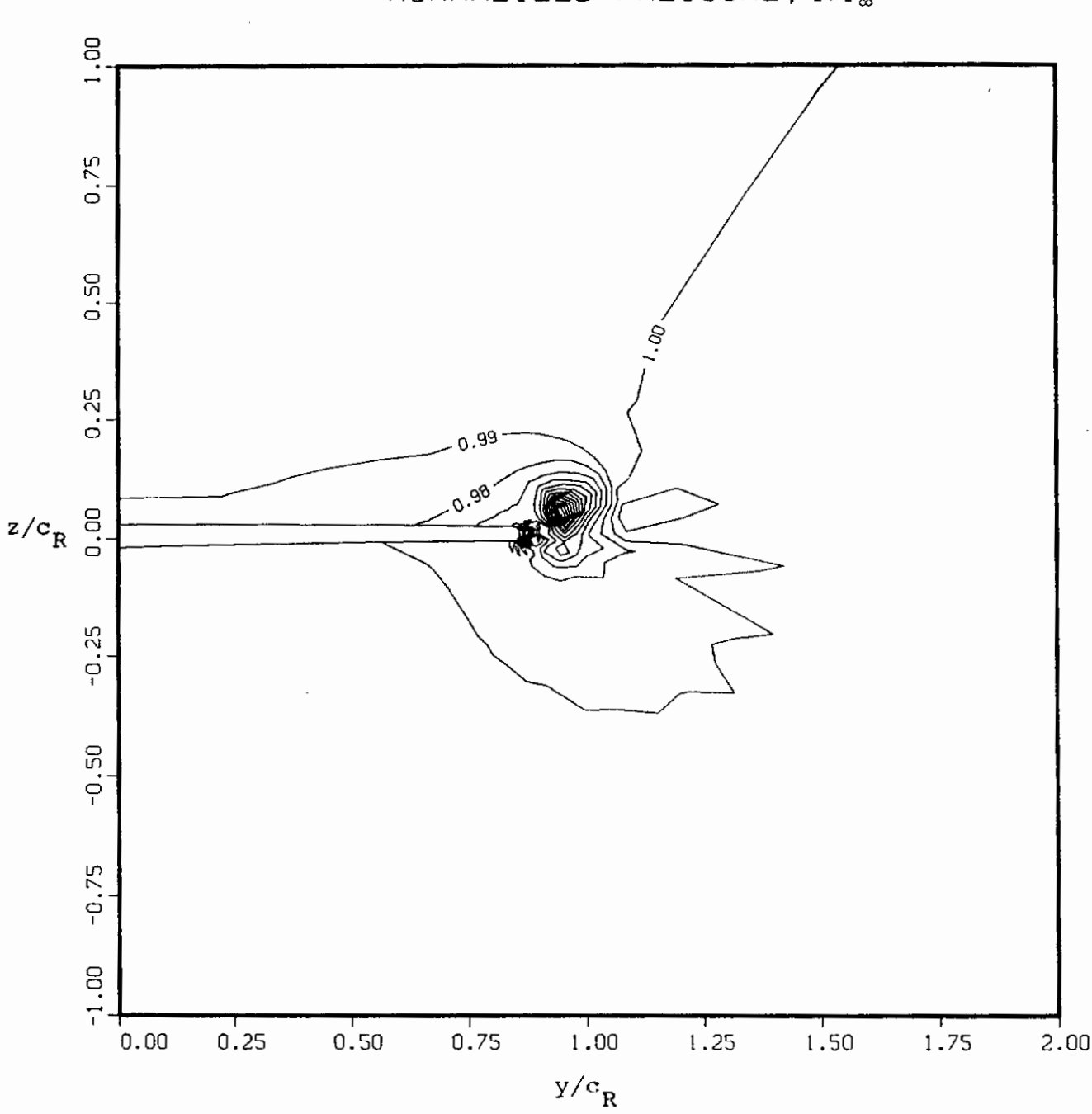

(b) Tip blowing, $C_\mu = 0.177$

Figure 64.- Concluded.

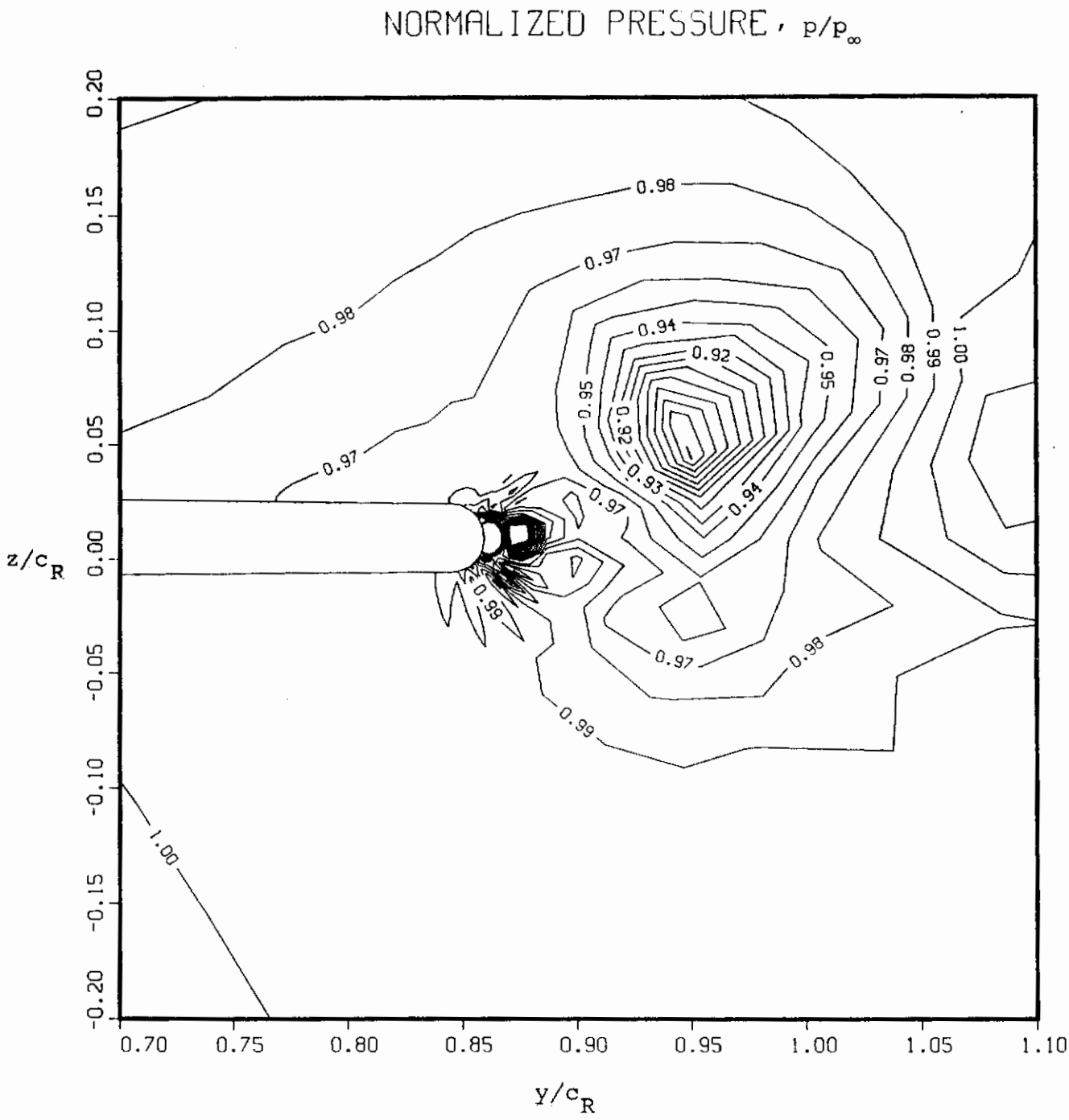

(a) Pressure field

Figure 65.- Close-up of tip flowfield with tip blowing at 35-percent chord, $\alpha = 5°$, $M_\infty = 0.25$, $C_\mu = 0.177$.

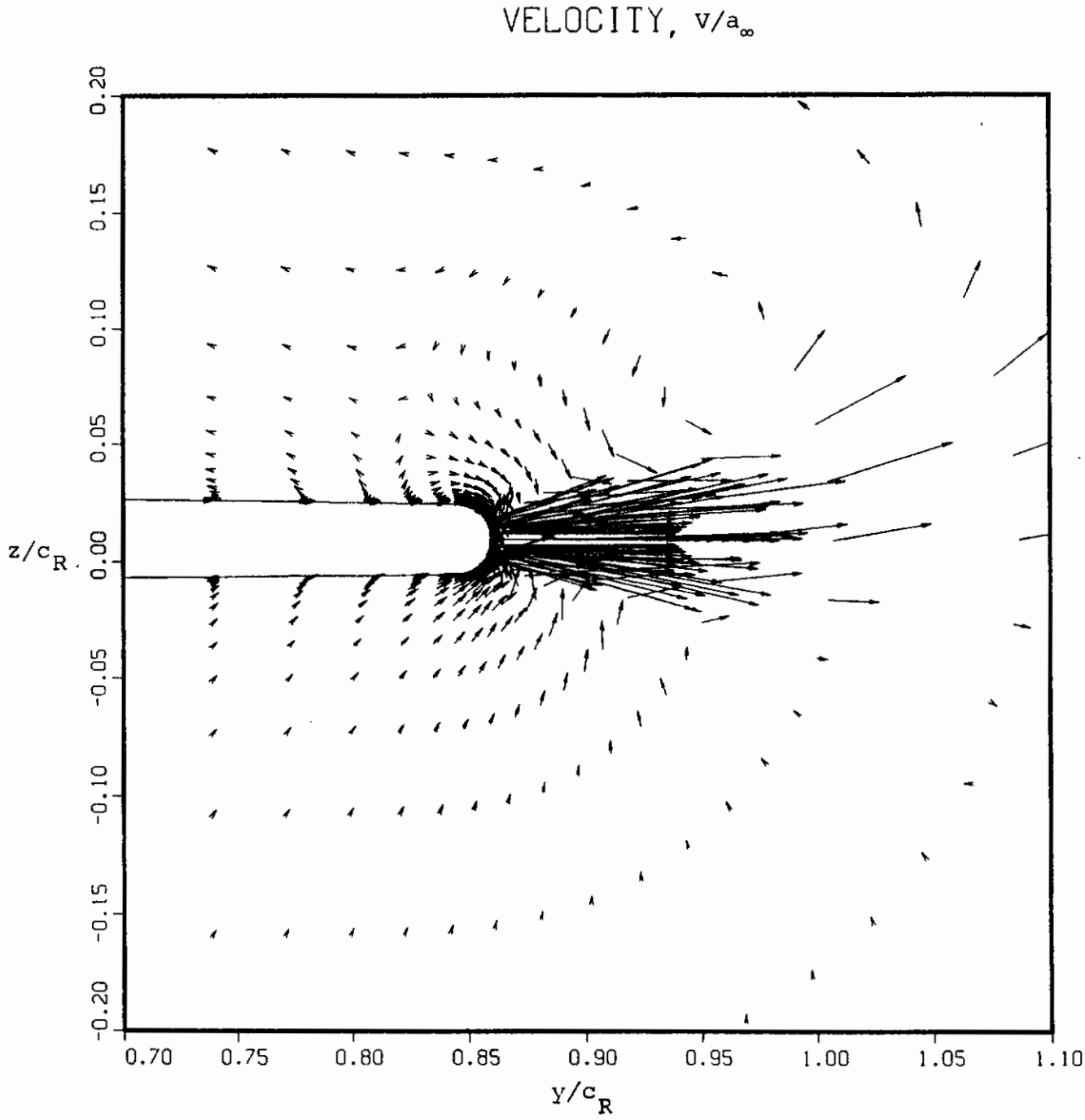

(b) Velocity field

Figure 65.- Concluded.

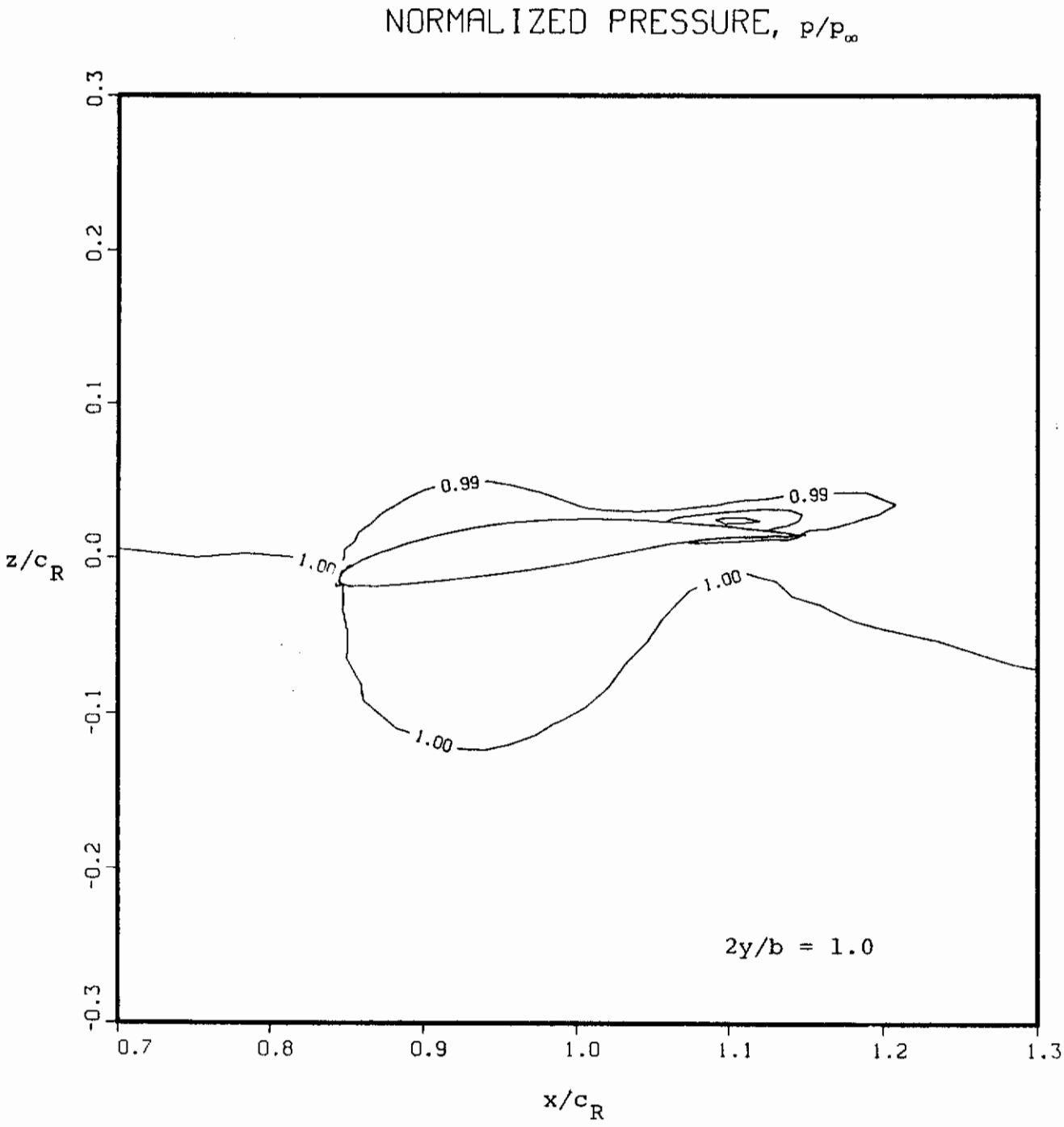

(a) No blowing

Figure 66.- Pressure field in the tip plane, $\alpha = 5°$, $M_\infty = 0.25$.

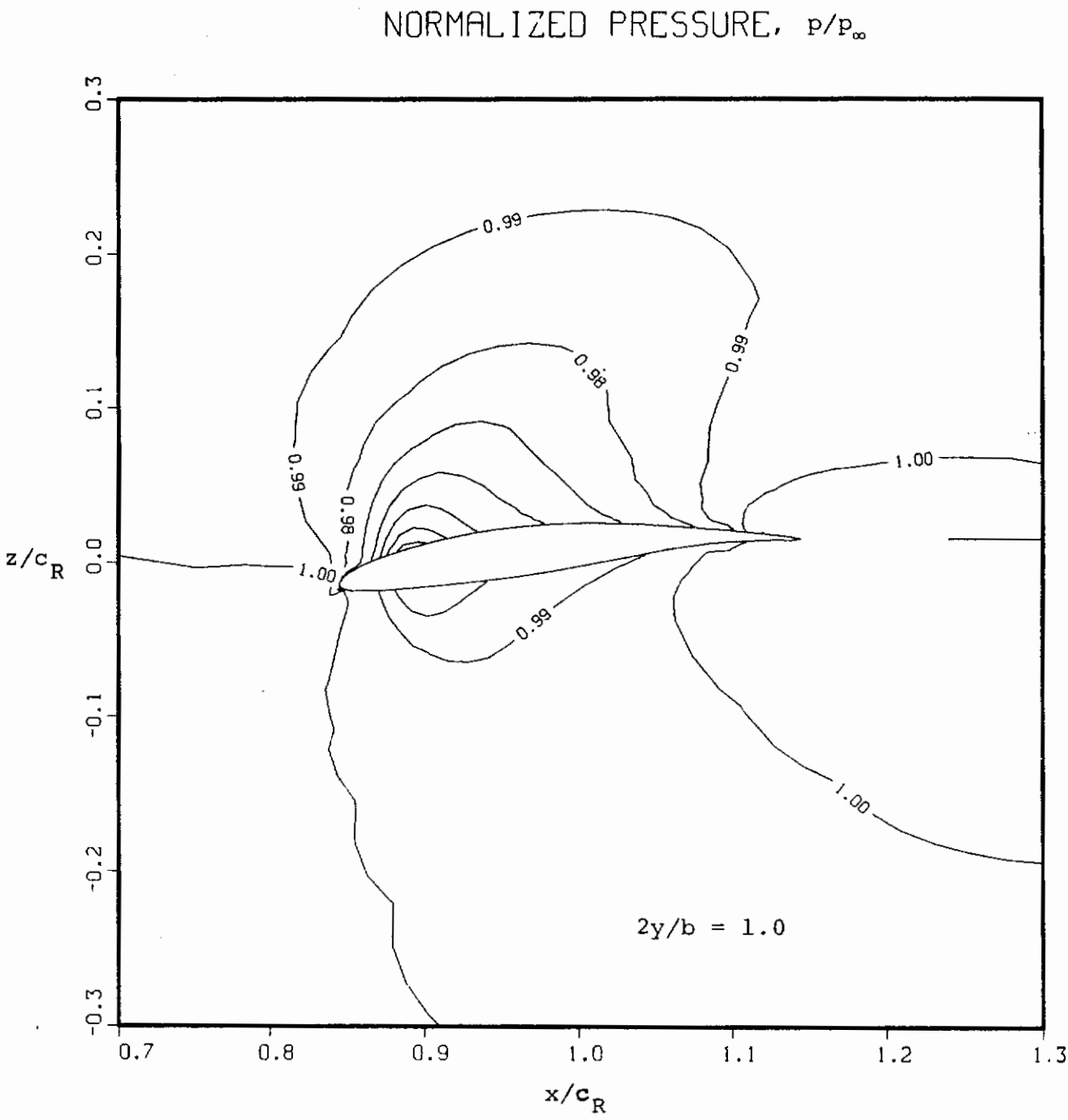

(b) Tip blowing, $C_\mu = 0.177$

Figure 66.- Concluded.

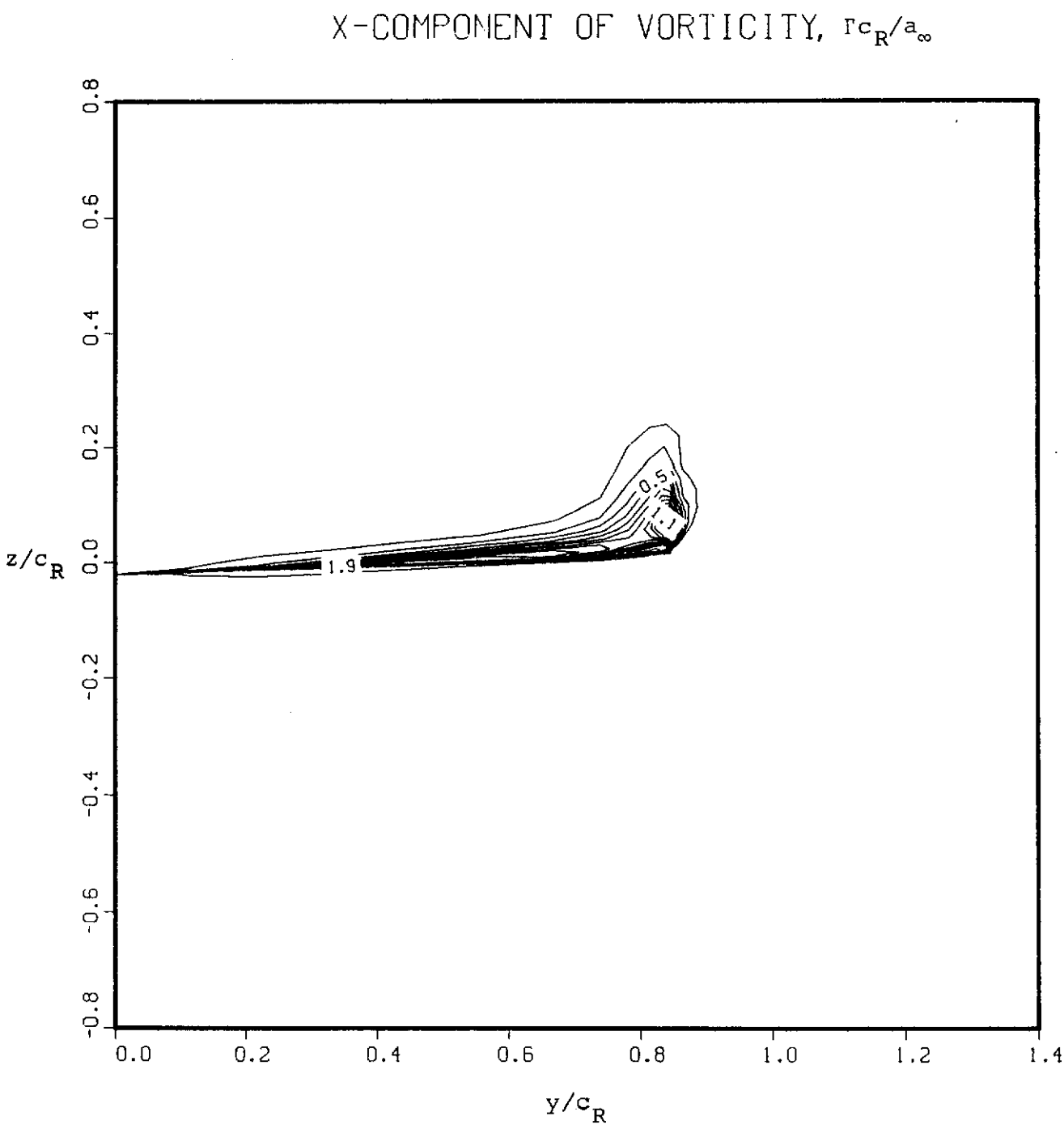

(a) No blowing

Figure 67.- Streamwise vorticity field at 150-percent chord, $\alpha = 5°$, $M_\infty = 0.25$.

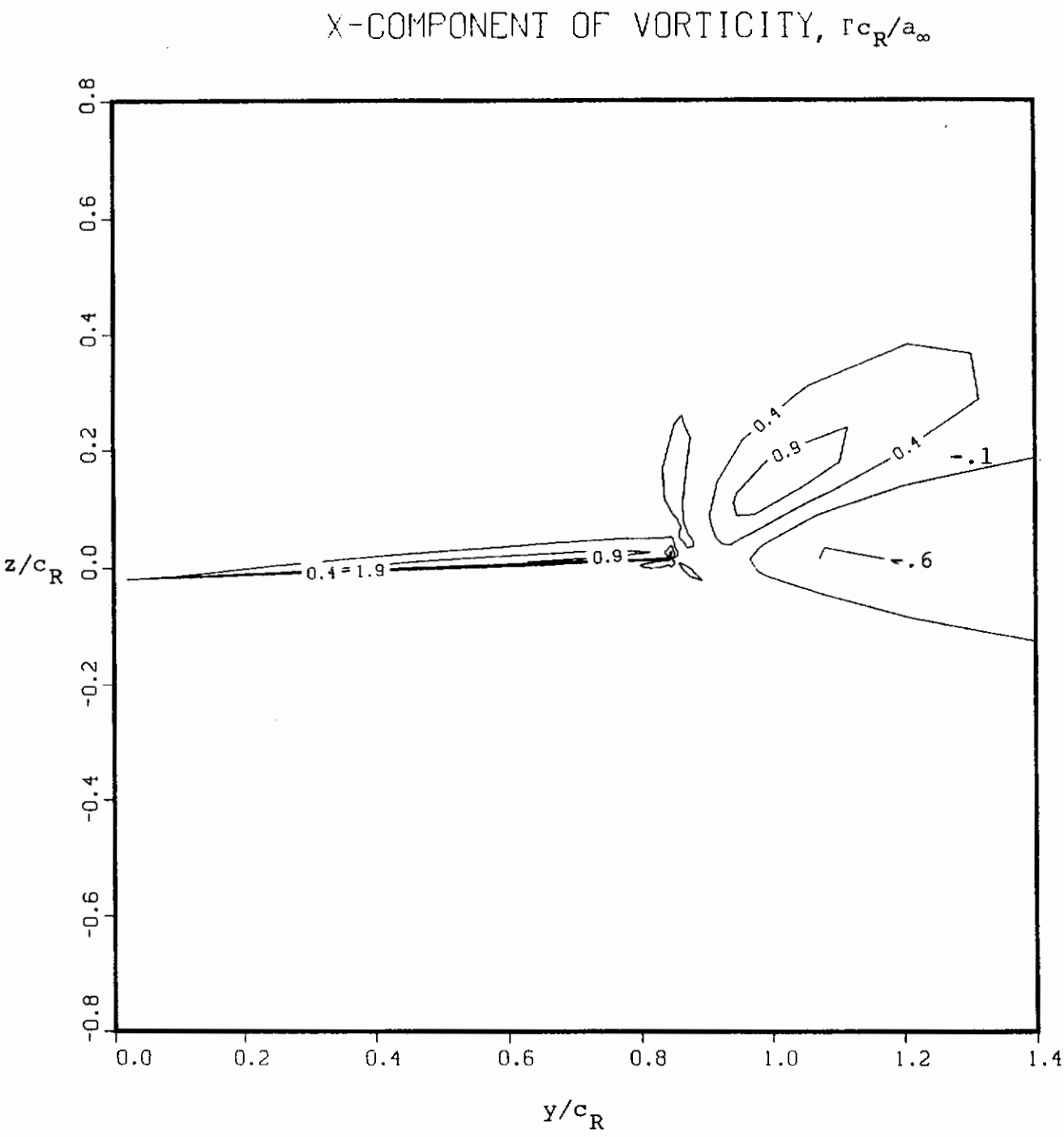

(b) $V_{jet}/V_\infty = 4$

Figure 67.- Continued.

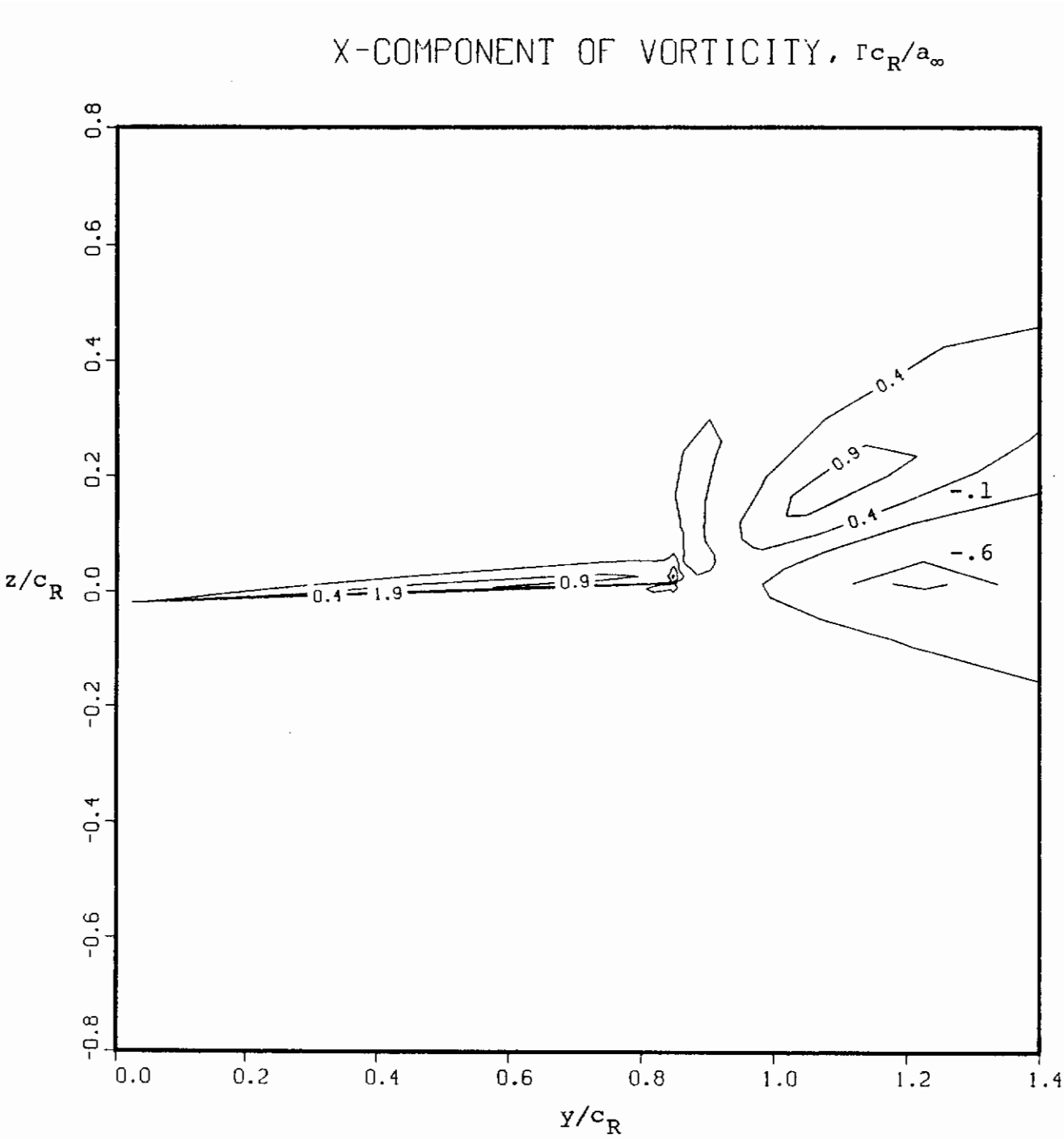

(c) $V_{jet}/V_\infty = 8$

Figure 67.- Concluded.

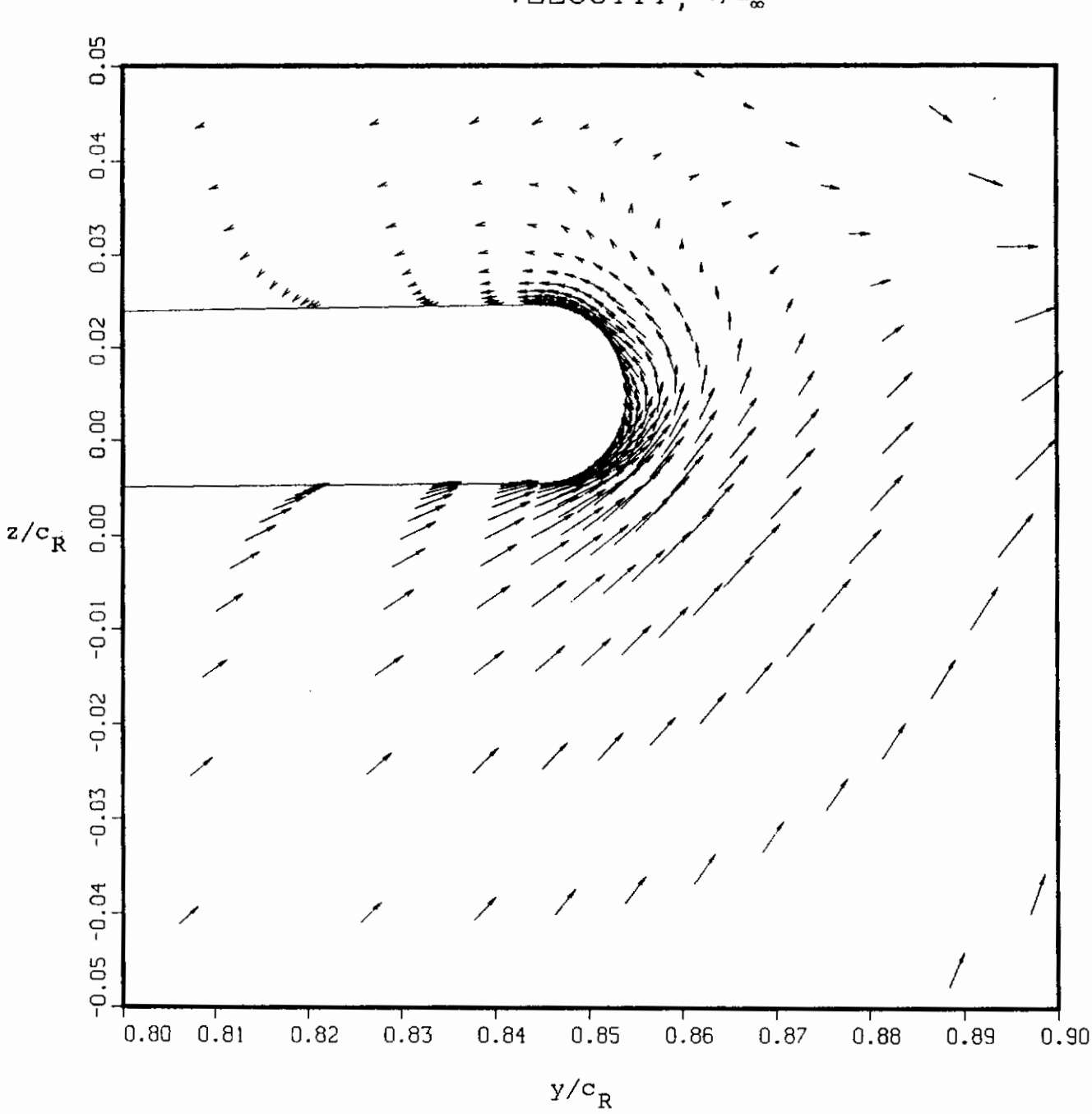

Figure 68.- Velocity field at 67-percent chord for short tip jet, $\alpha = 5°$, $M_\infty = 0.25$, $C_\mu = 052$.

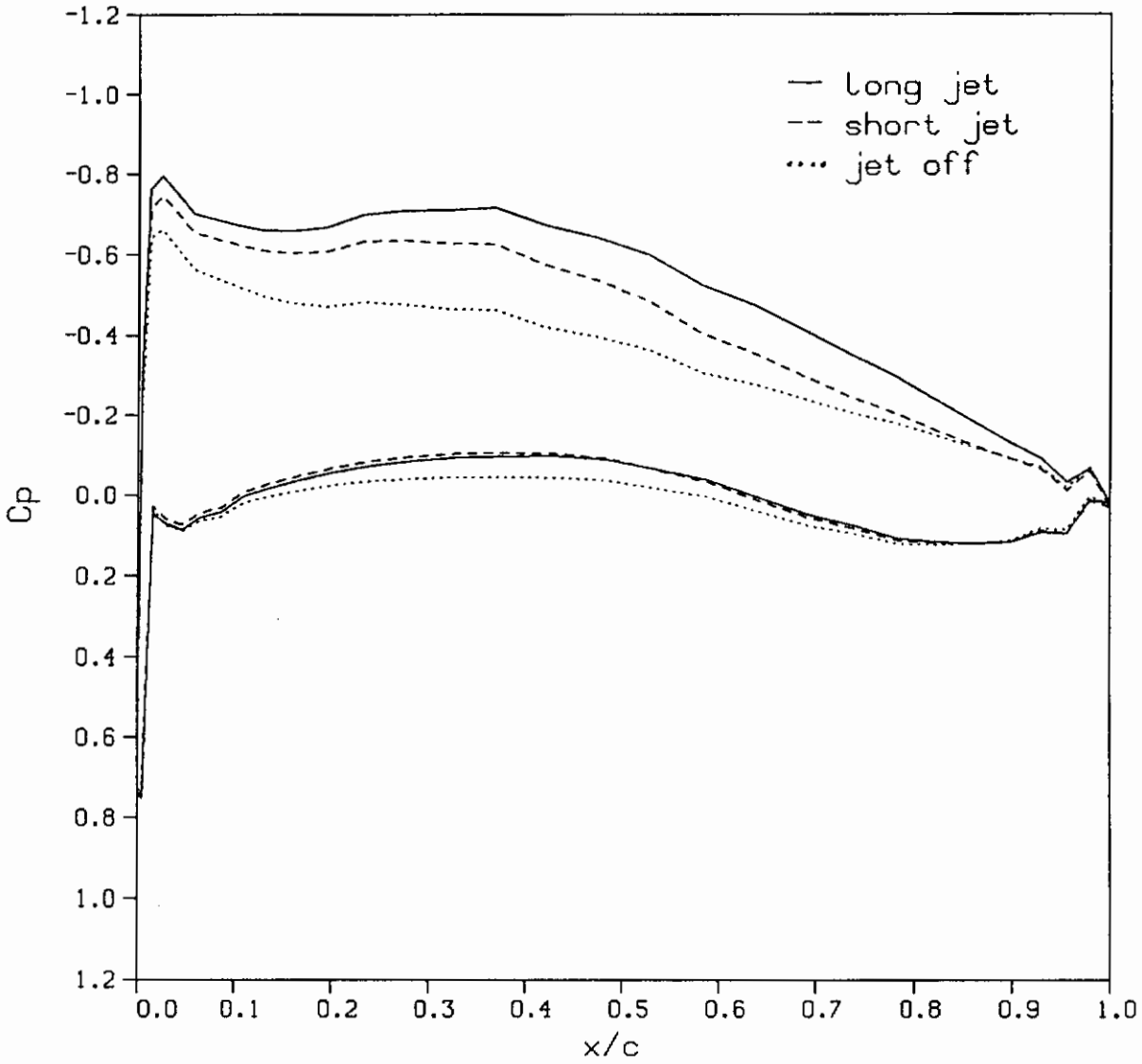

Figure 69.- Effect of jet length on predicted chordwise pressure distribution at 2y/b = 0.9, α = 5°, M_∞ = 0.25, v_j/V_∞ = 4.

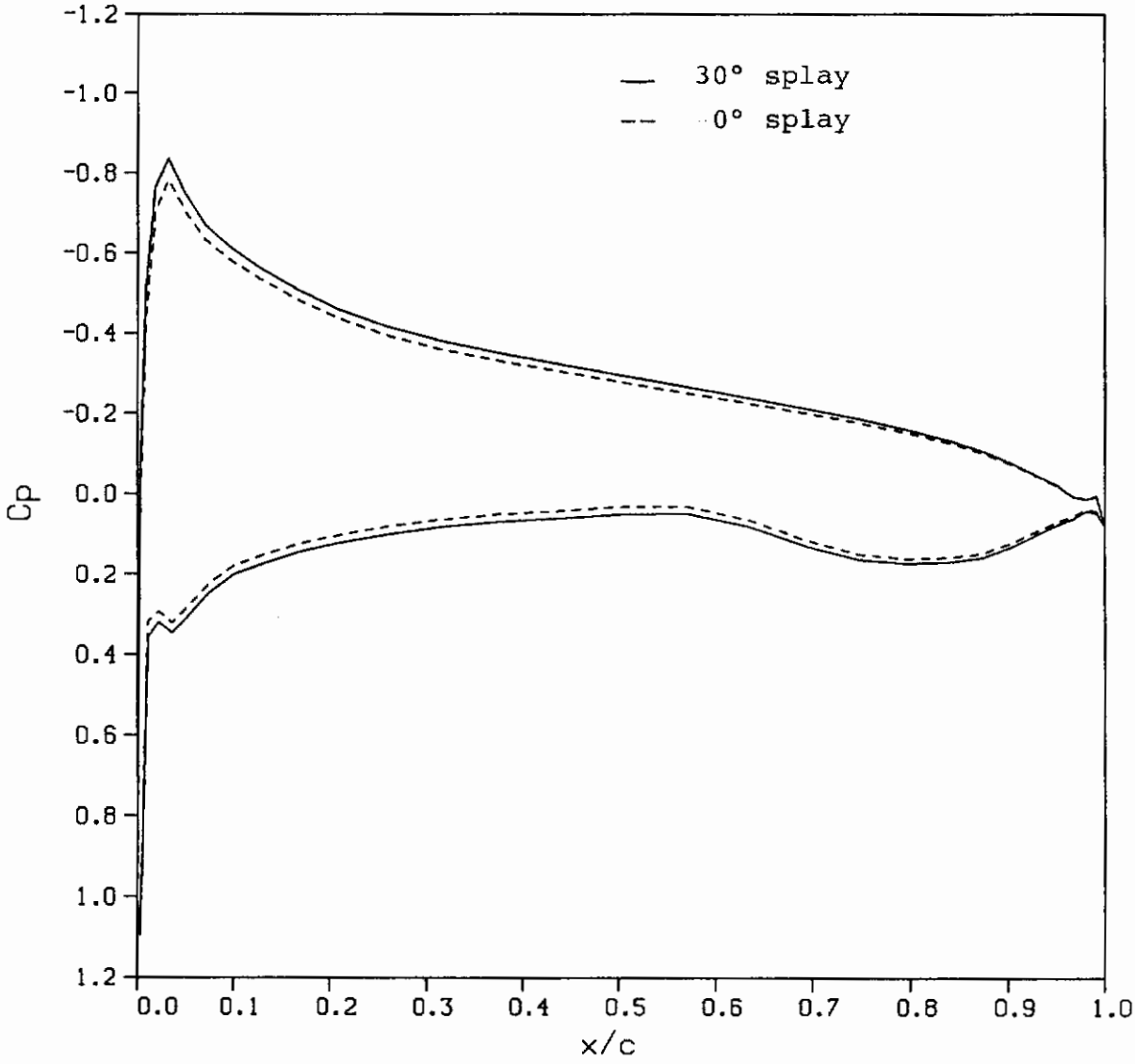

(a) 2y/b = 0.1

Figure 70.- Comparison of chordwise pressure distribution for blowing with and without splay angle; $\alpha = 5°$, $M_\infty = 0.25$, $C_\mu = 0.177$.

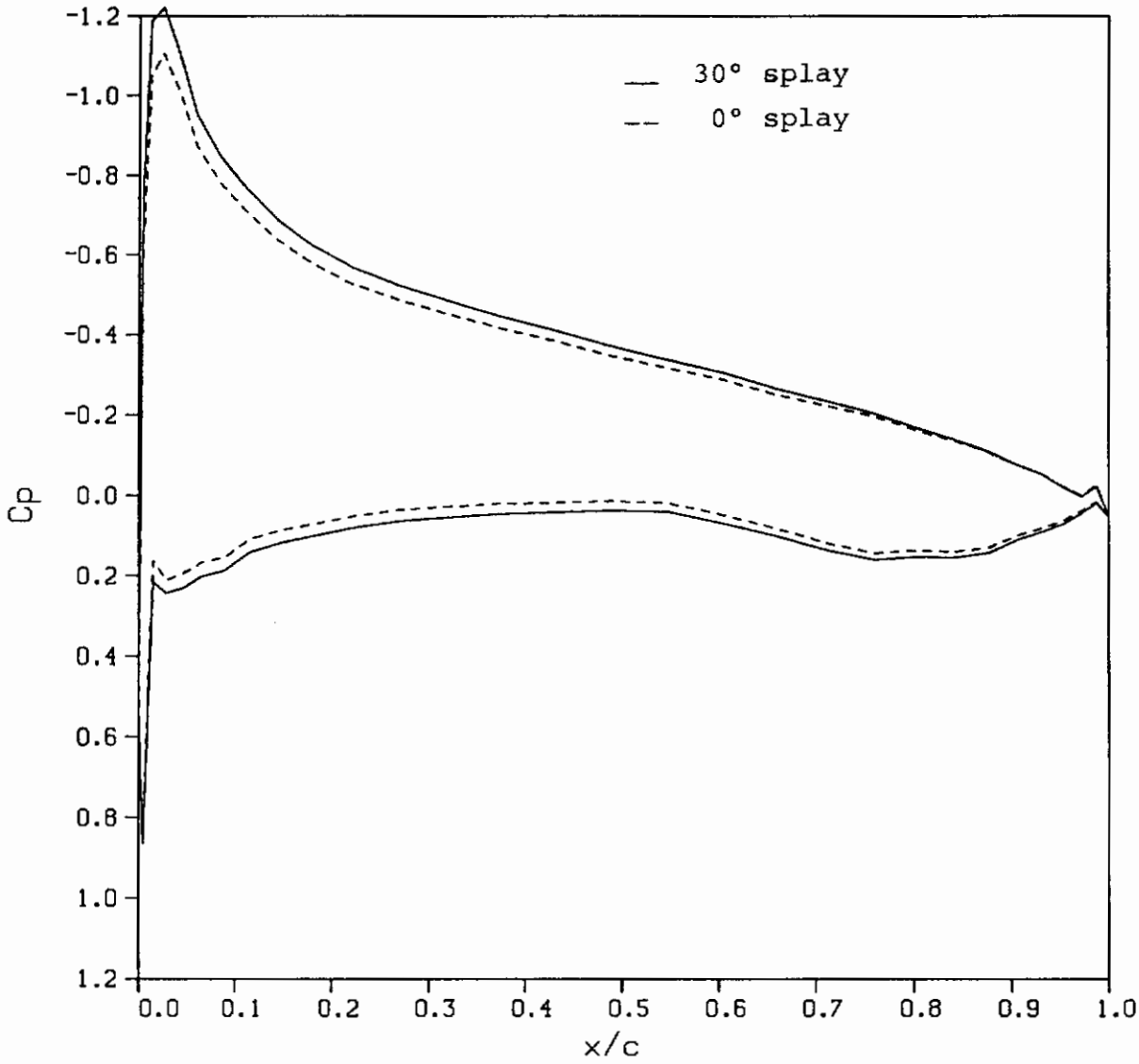

(b) 2y/b = 0.5

Figure 70.- Continued.

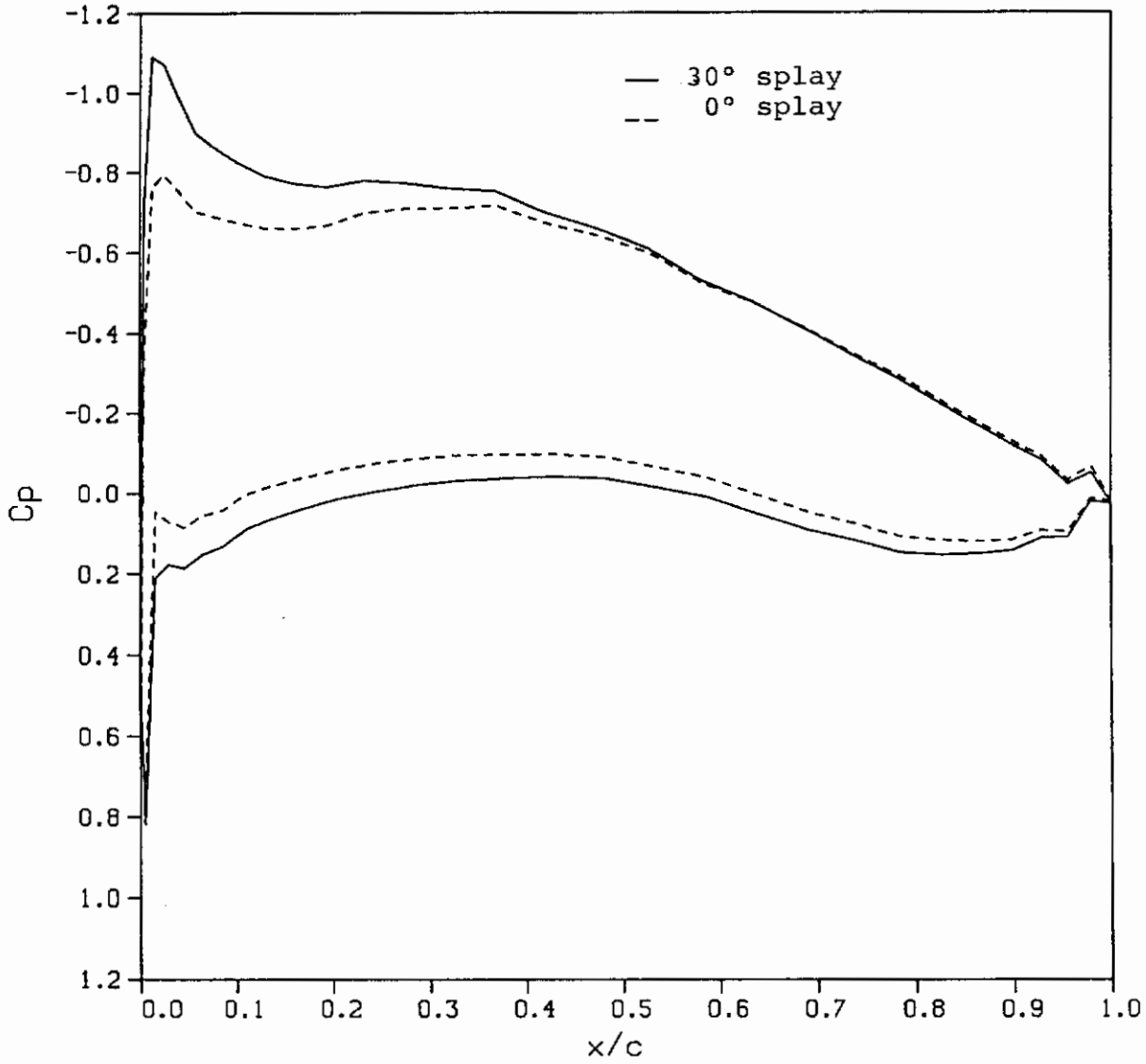

(c) 2y/b = 0.9

Figure 70.- Concluded.

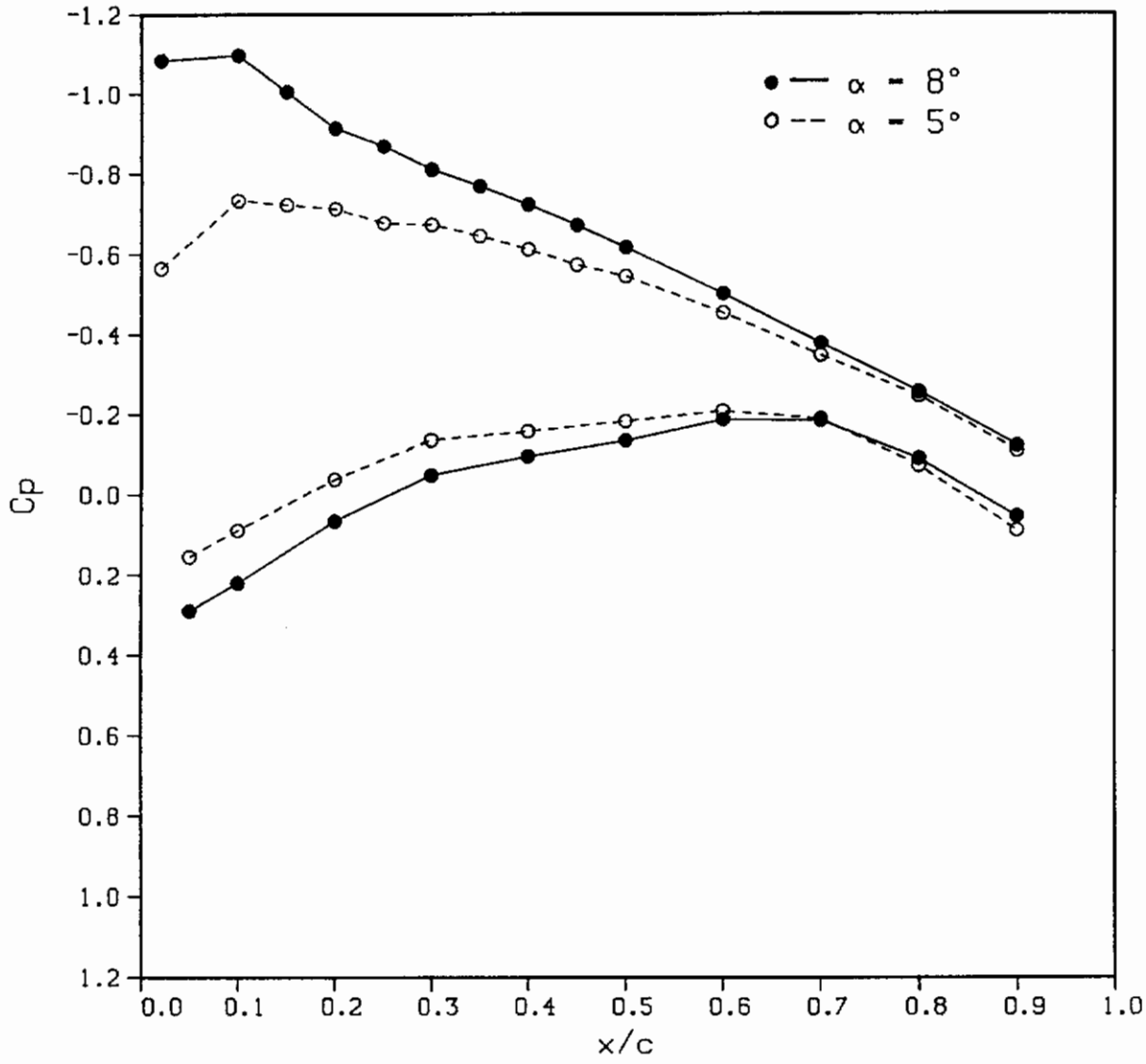

Figure 71.- Experimental chordwise pressure distributions for large-scale WING C-BT, M_∞ = 0.25, 2y/b = 0.9, jet off.

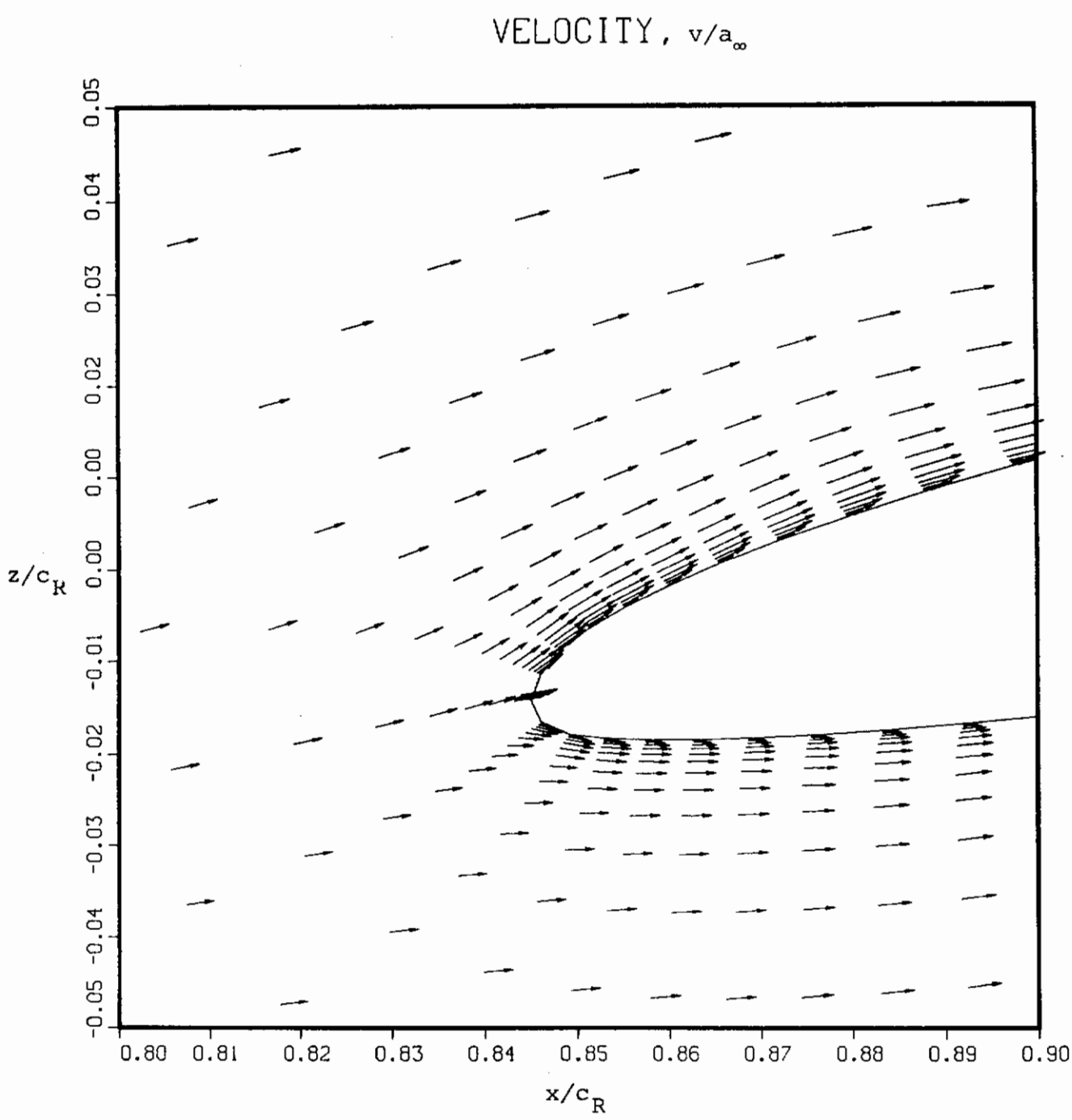

(a) 0° splay

Figure 72.- Computed velocity field at 2y/b = 1.0, α = 5°, M_∞ = 0.25, C_μ = 0.177.

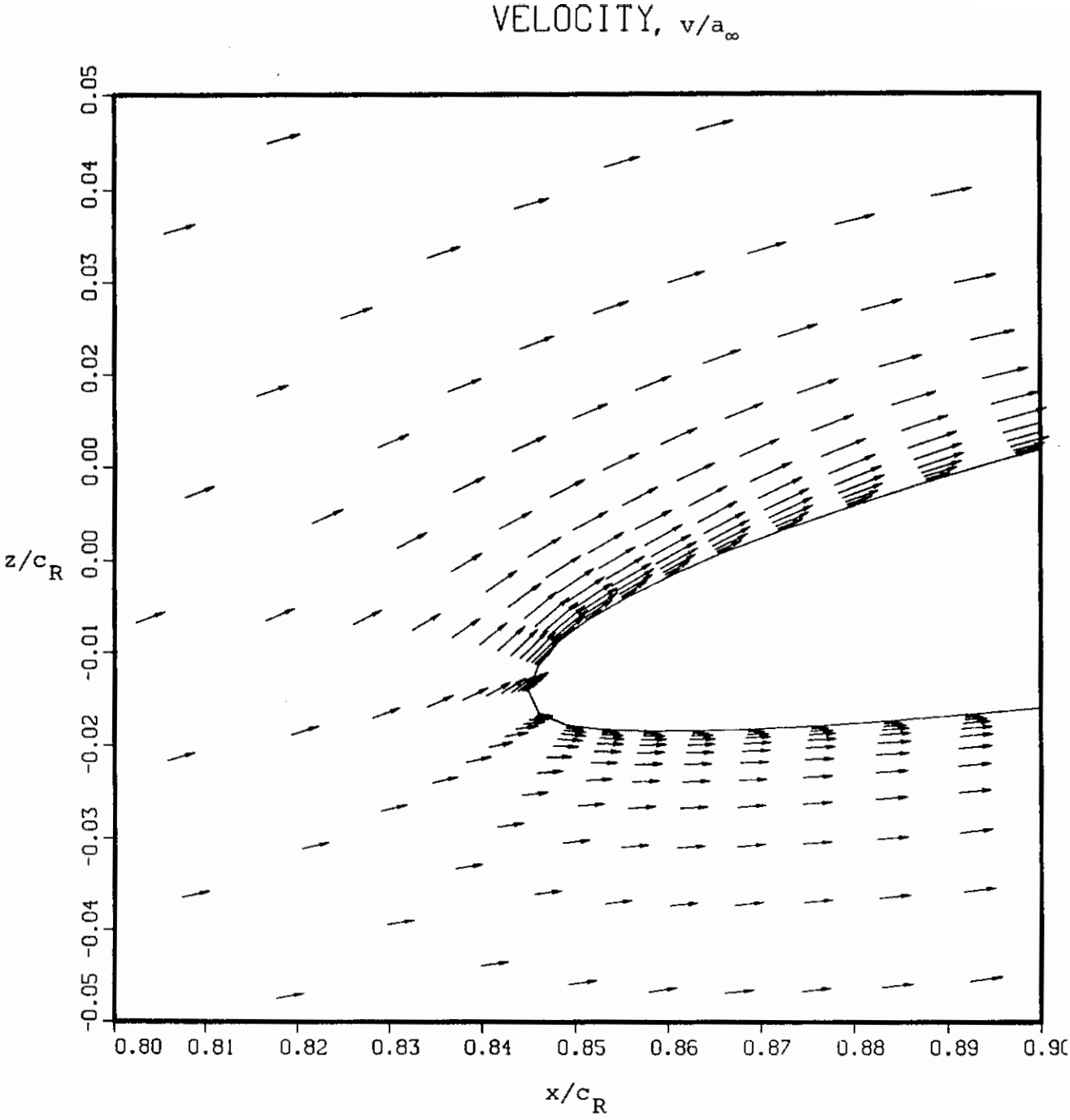

(b) 30° splay

Figure 72.- Concluded.

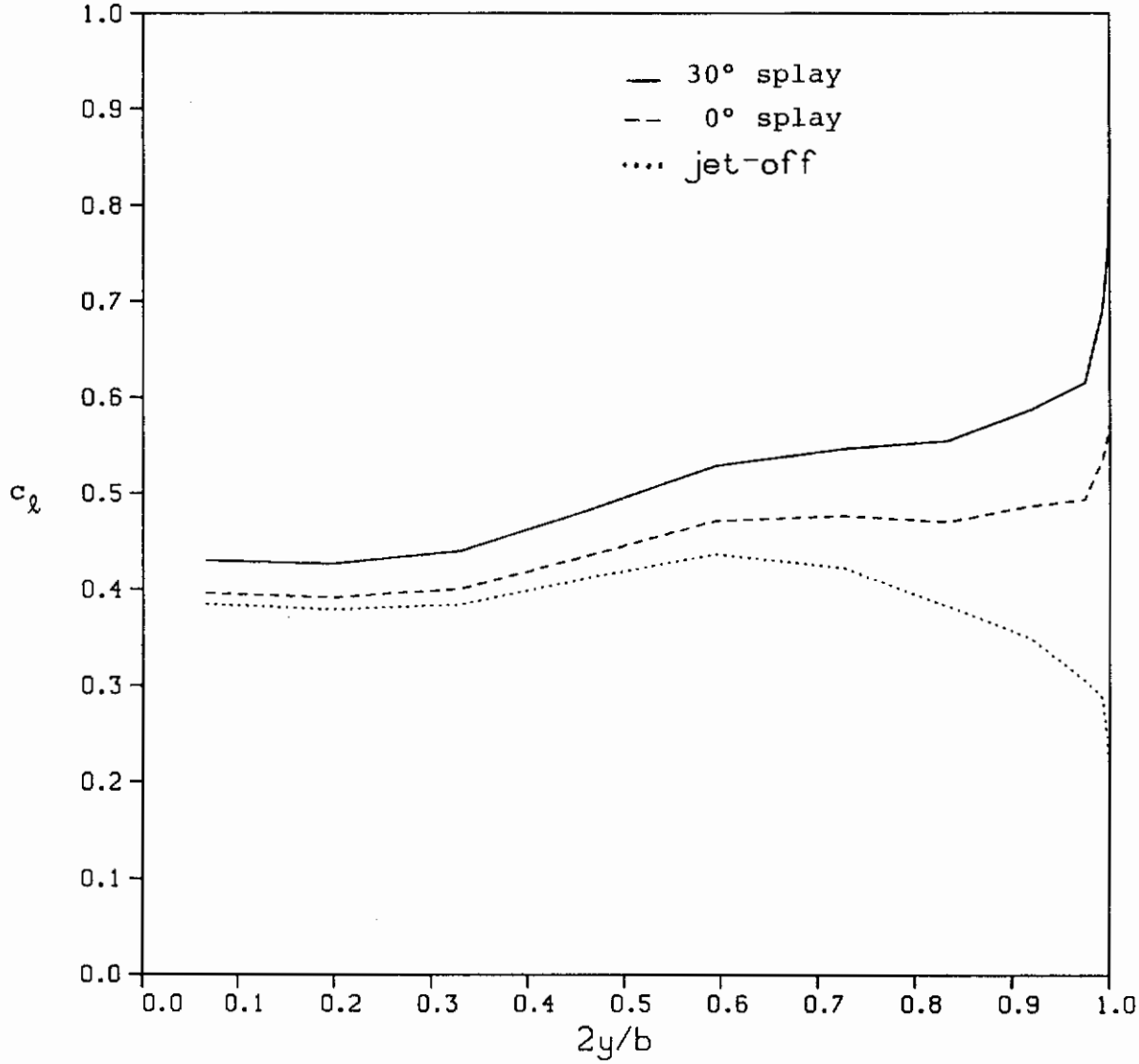

Figure 73.- Comparison of spanwise loading for tip blowing with and without splay angle, $\alpha = 5°$, $M_\infty = 0.25$, $C_\mu = 0.177$.

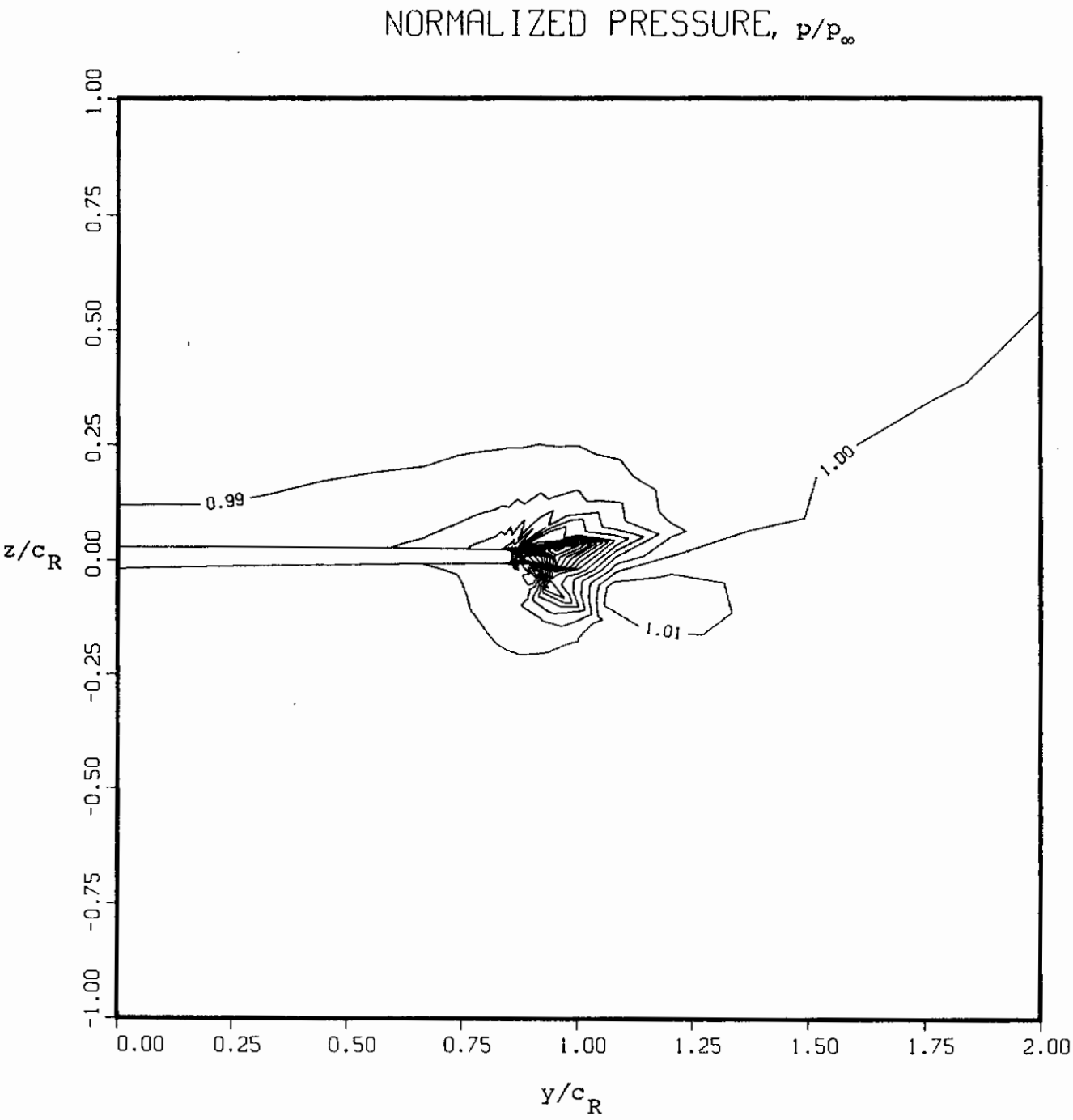

(a) pressure field

Figure 74.- Flowfield at 35-percent chord with blowing at 30° splay angle, α = 5°, M_∞ = 0.25, C_μ 0.177.

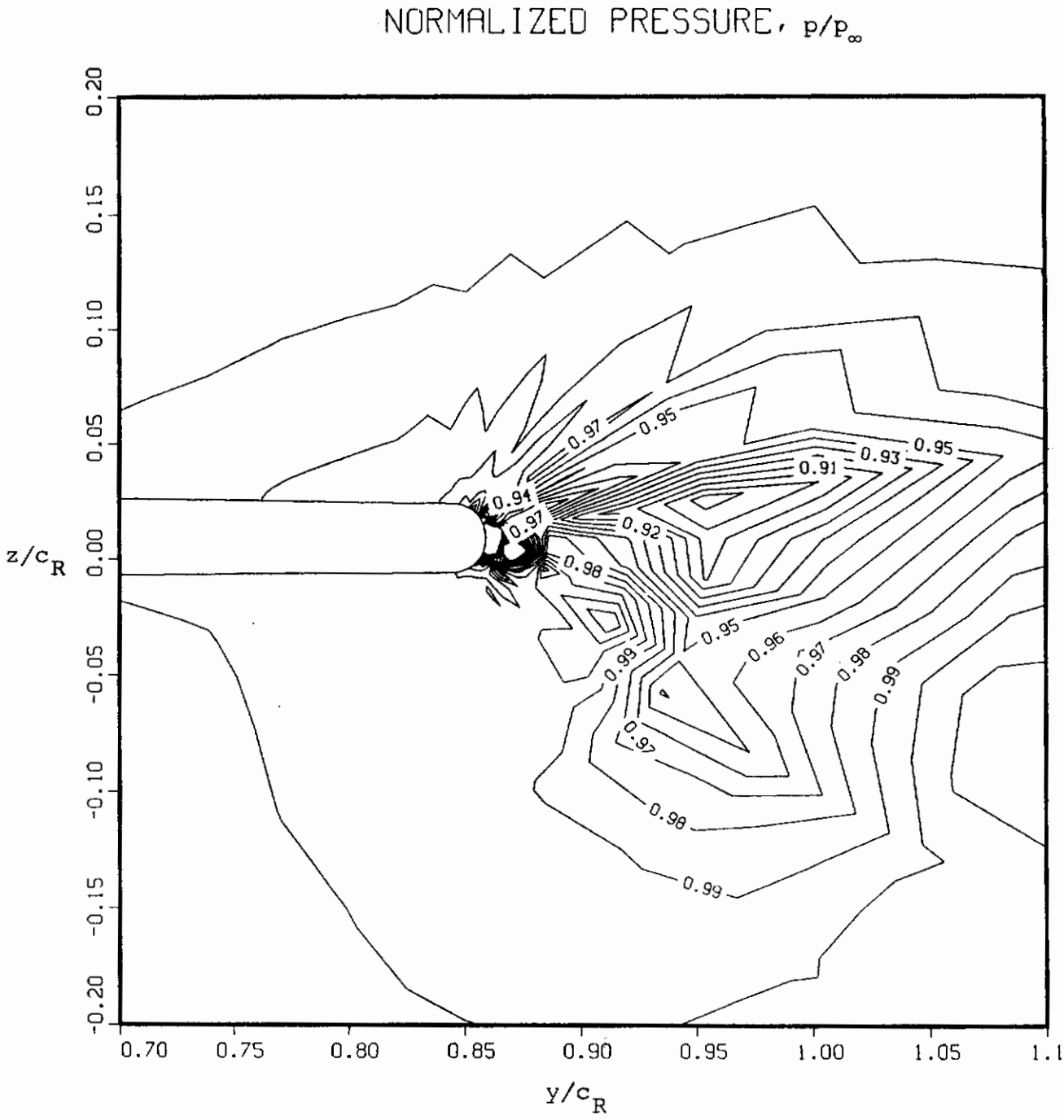

(b) Close-up of pressure field

Figure 74.- Continued.

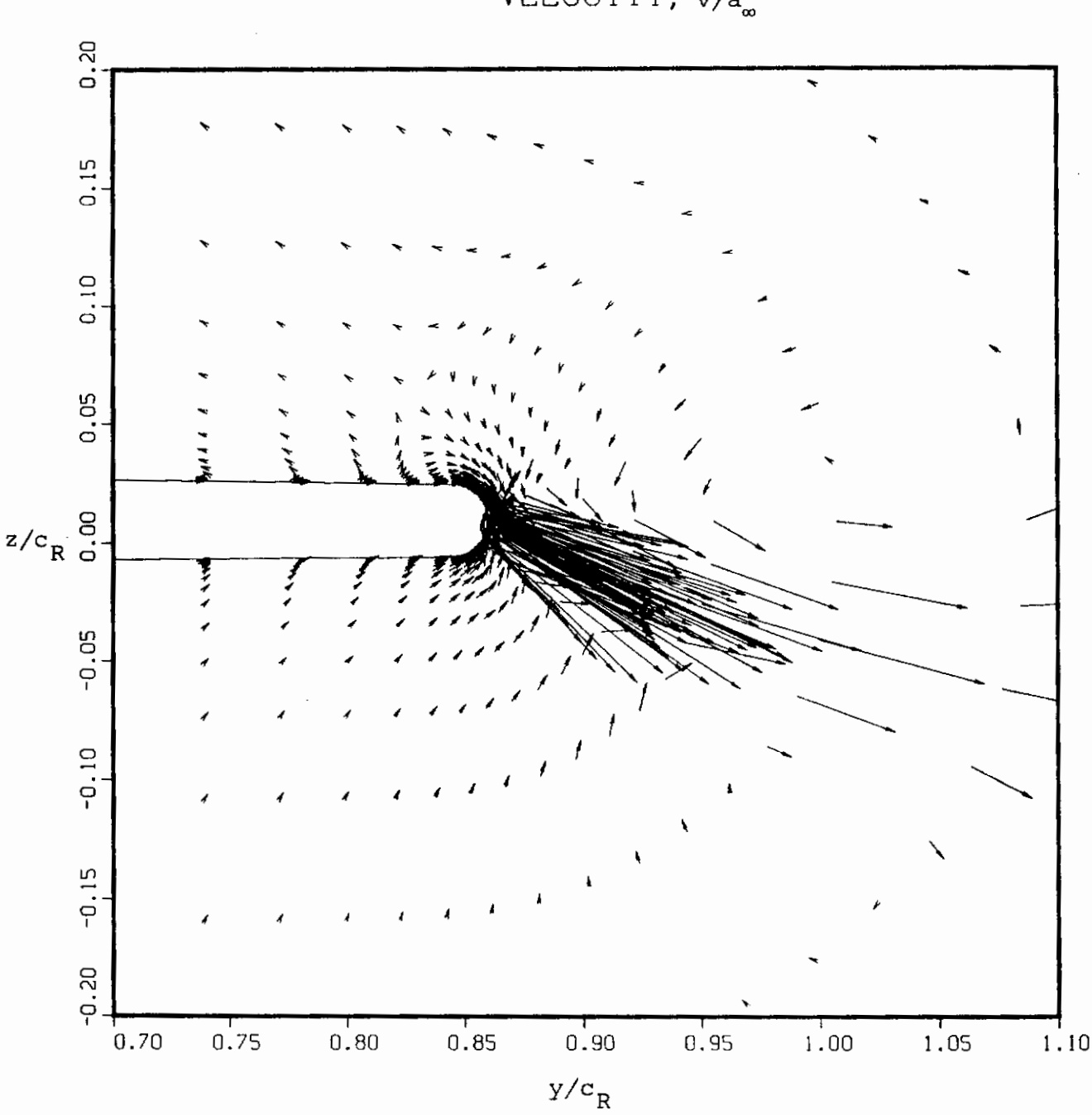

(c) Velocity field

Figure 74.- Concluded.

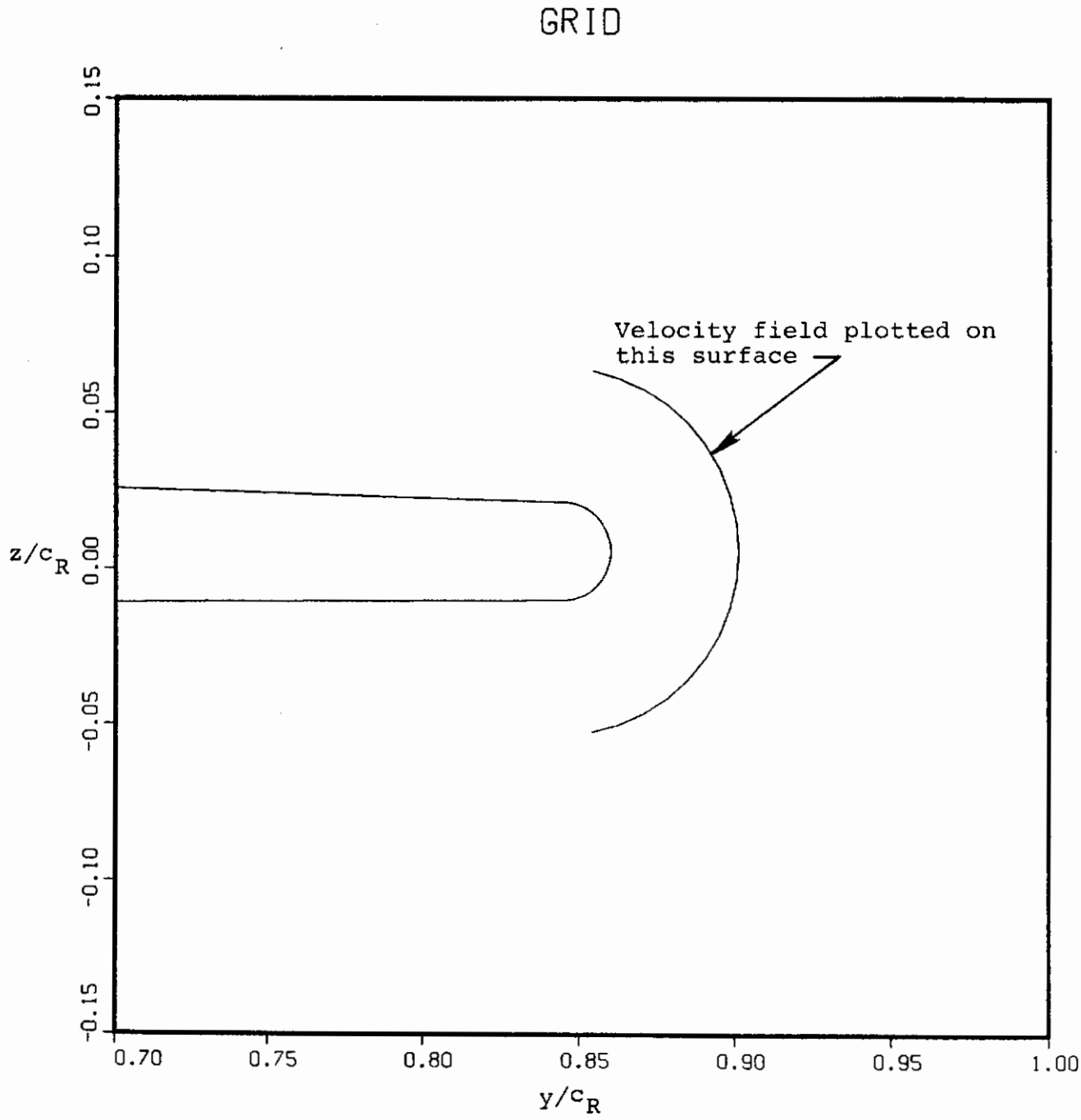

Figure 75.- Reference surface for velocity field at $x/c_T = 0.35$.

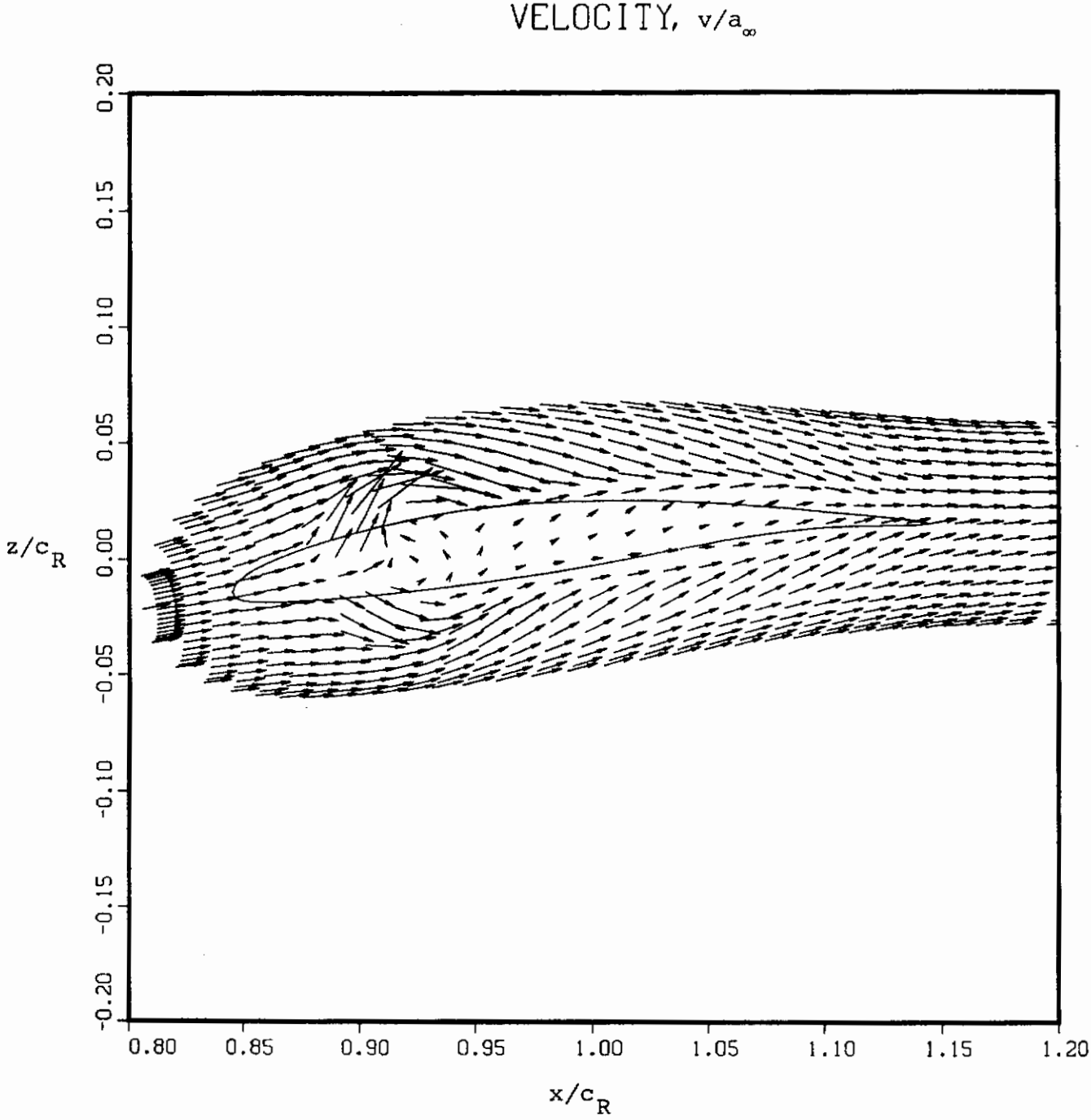

(a) 0° splay

Figure 76.- Effect of jet splay angle on the velocity field beyond the wing tip, α = 5°, M_∞ = 0.25, C_μ = 0.177.

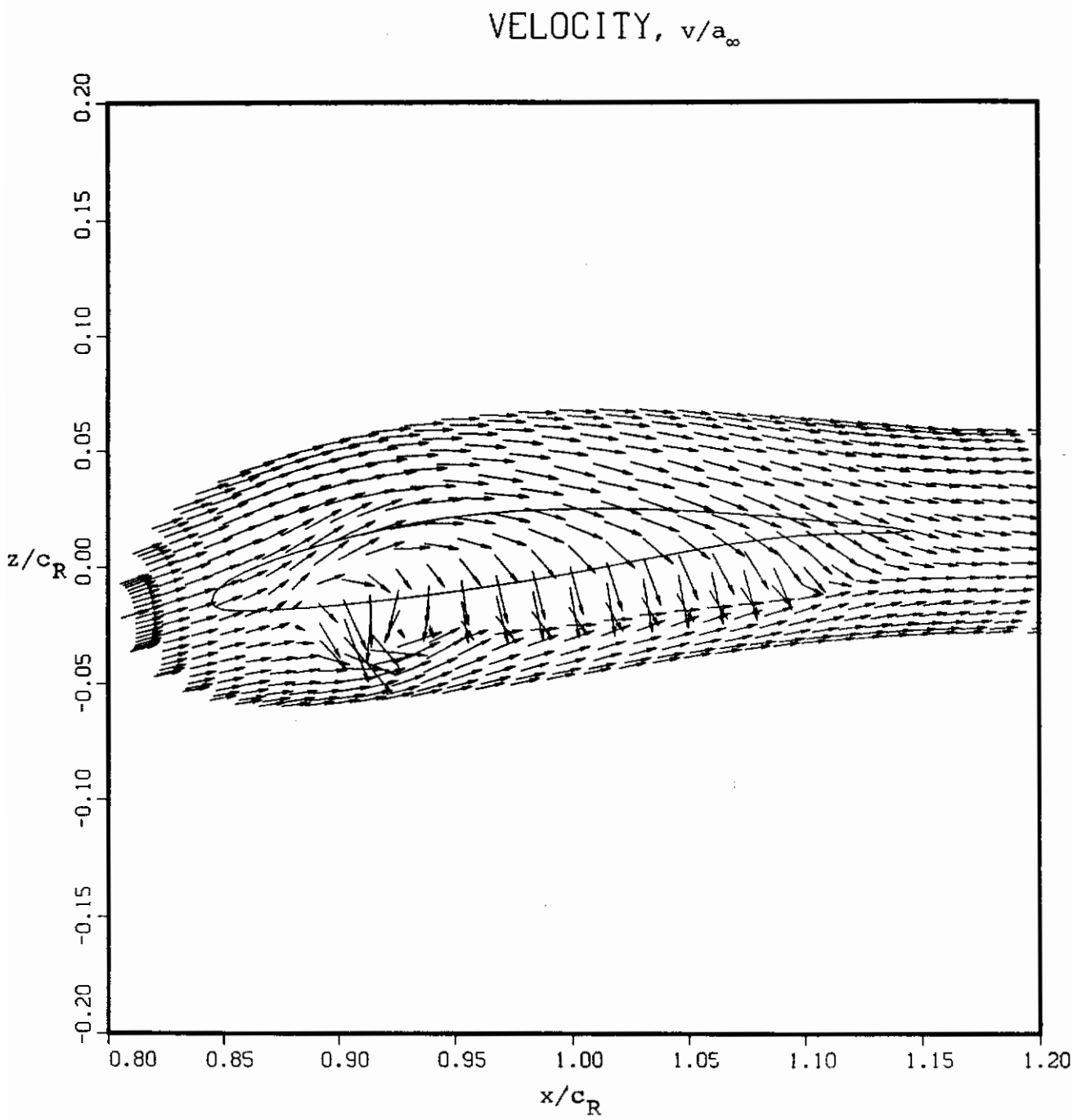

(b) 30° splay

Figure 76.- Concluded.

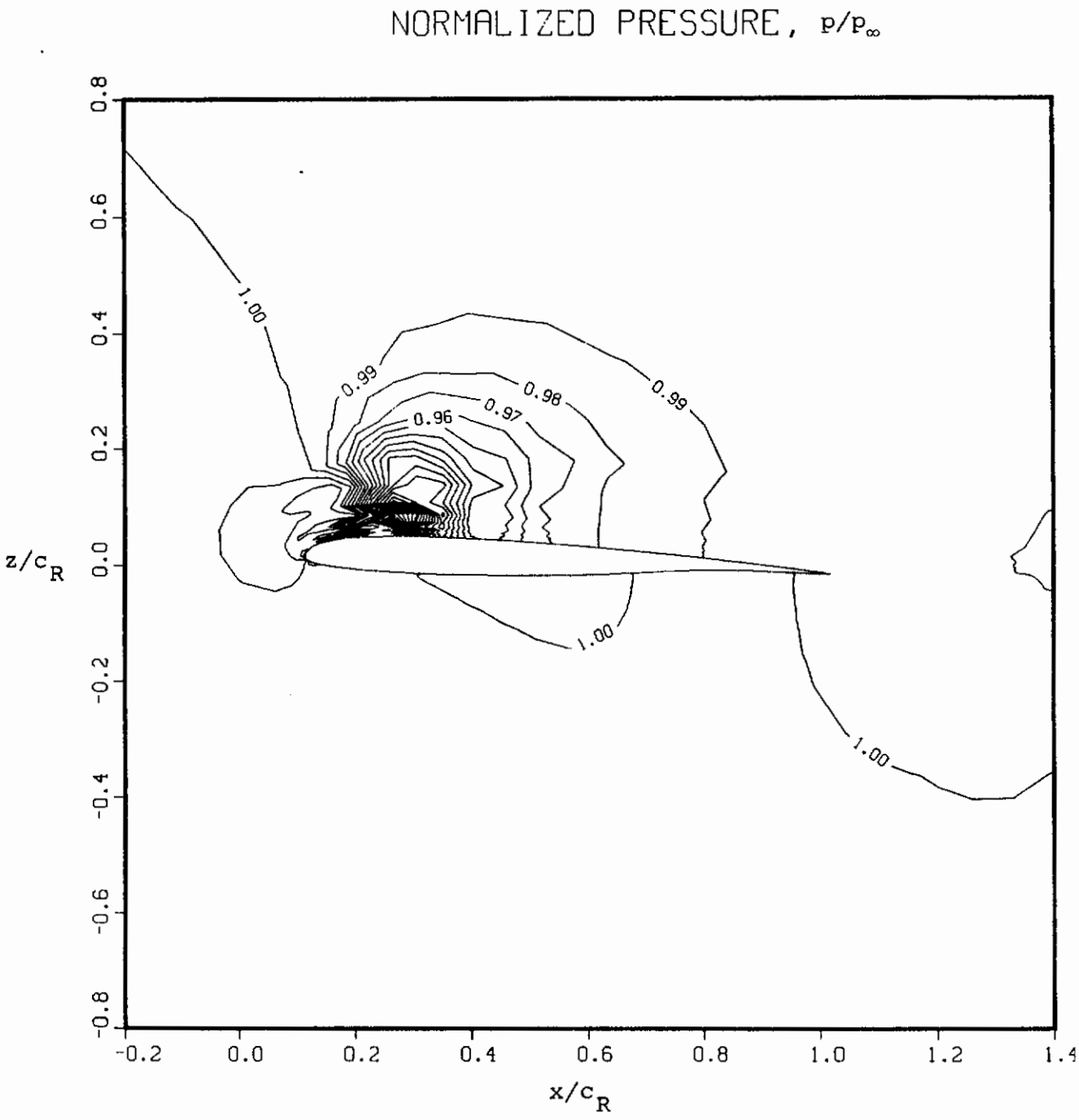

(a) Pressure

Figure 77.- Predicted flowfield at 2y/b = 0.3 with spanwise blowing, $\alpha = 5°$, $M_\infty = 0.25$, $C_\mu = 0.14$.

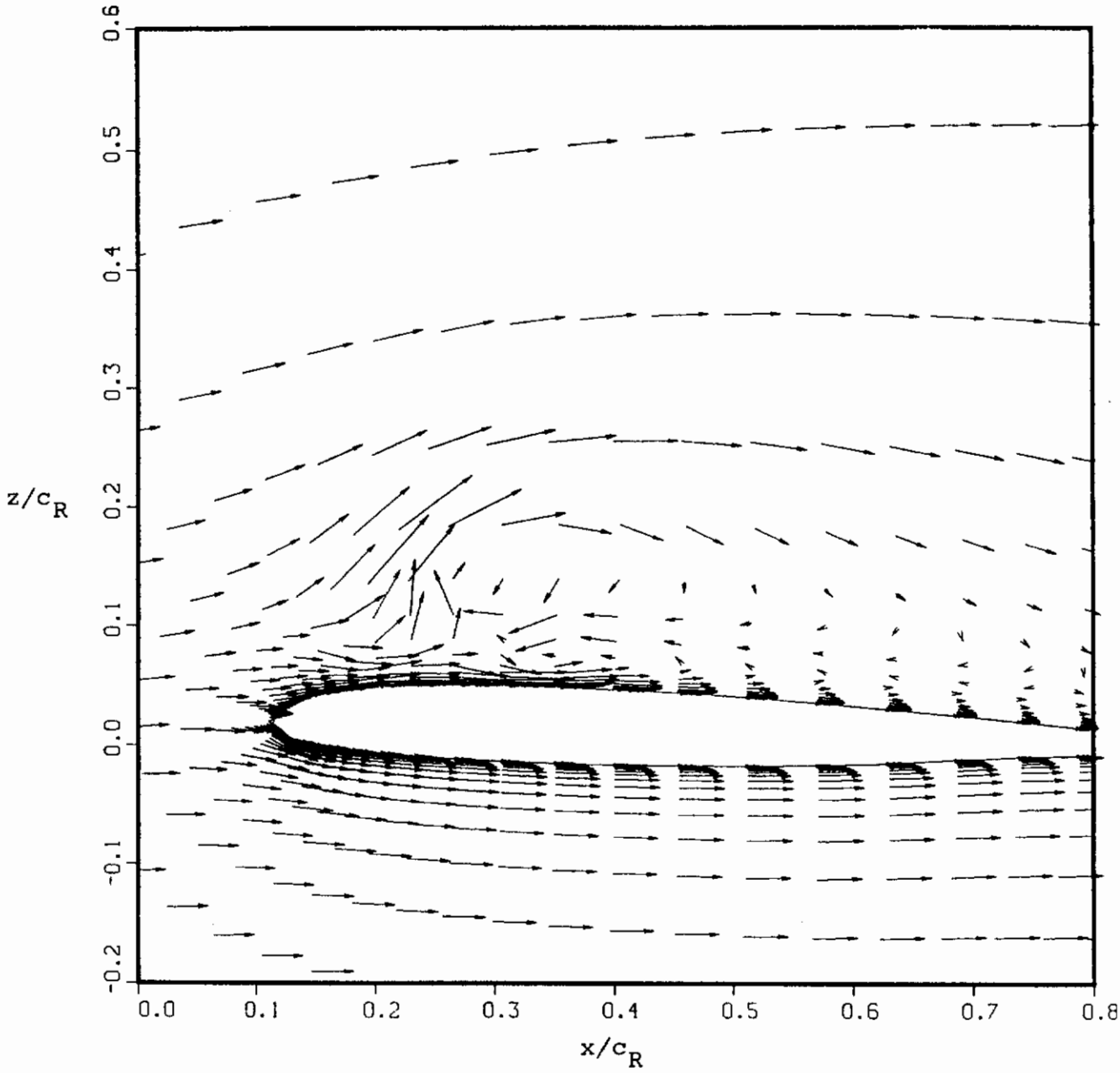

(b) Velocity

Figure 77.- Concluded.

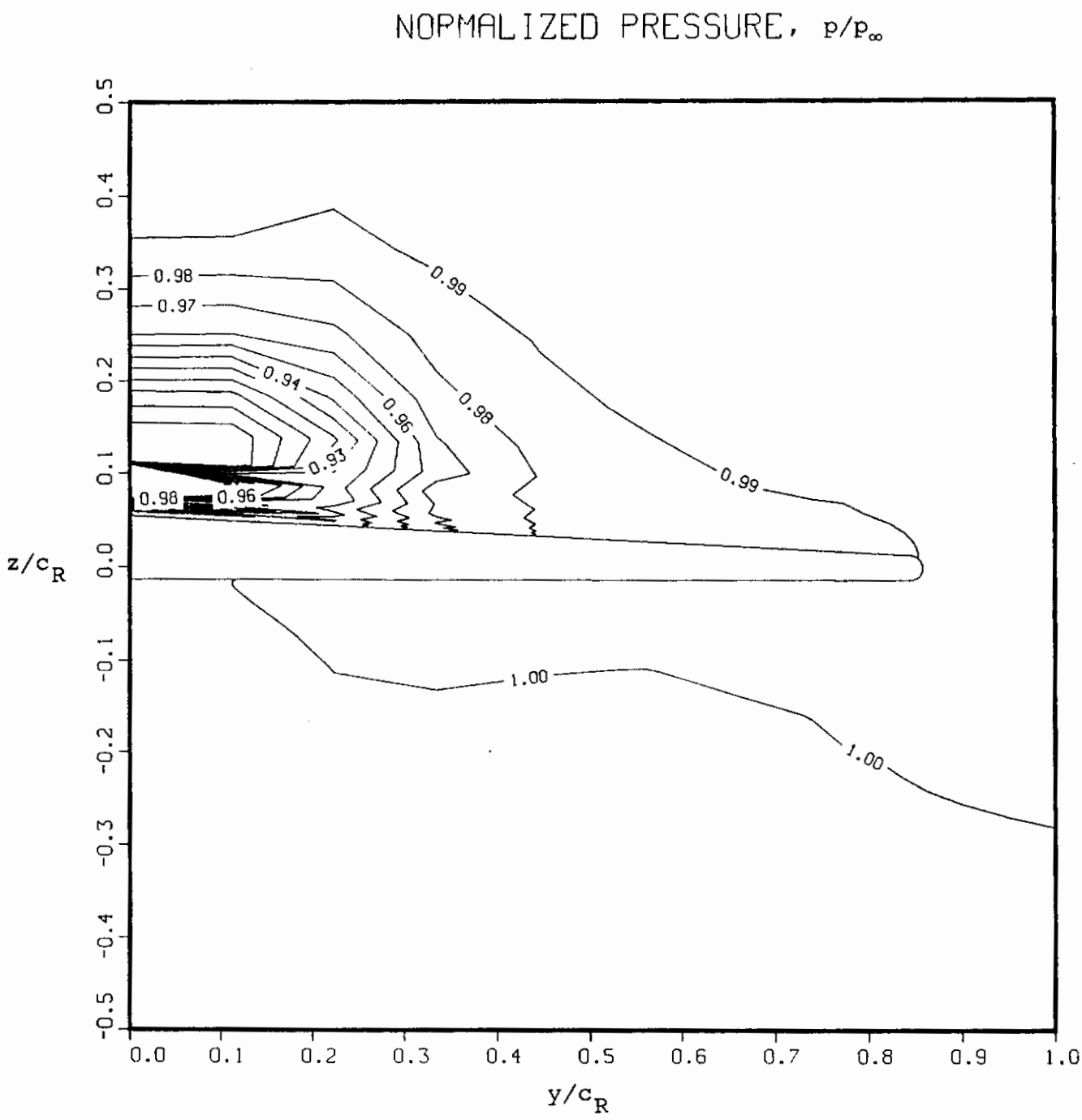

(a) Pressure

Figure 78.- Predicted flowfield at x/c = 0.20 with spanwise blowing, α = 5°, M_∞ = 0.25, C_μ = 0.14.

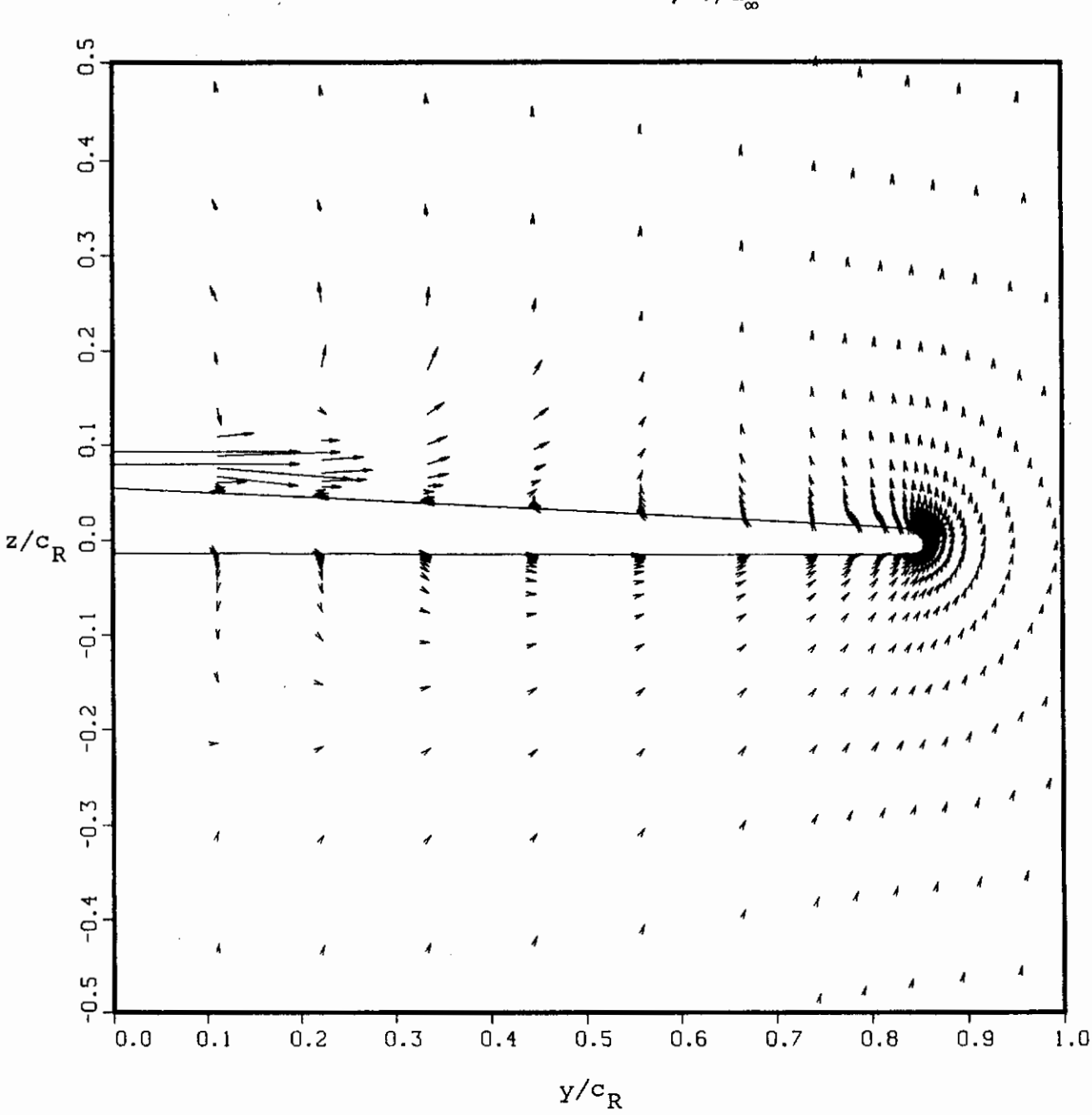

(b) Velocity

Figure 78.- Concluded.

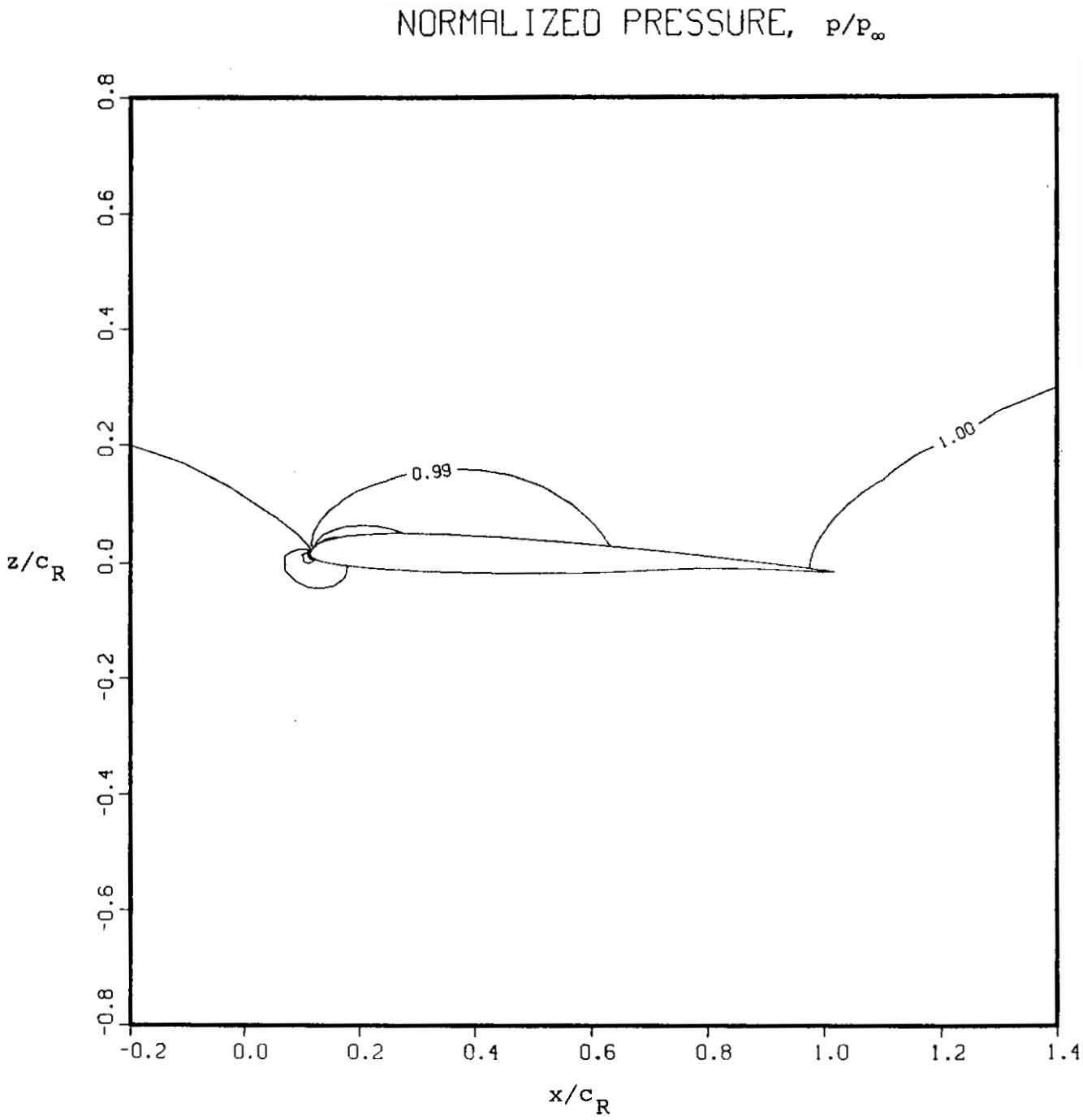

(a) 2y/b = 0.13

Figure 79.- Pressure field with no blowing, $\alpha = 5°$, $M_\infty = 0.25$.

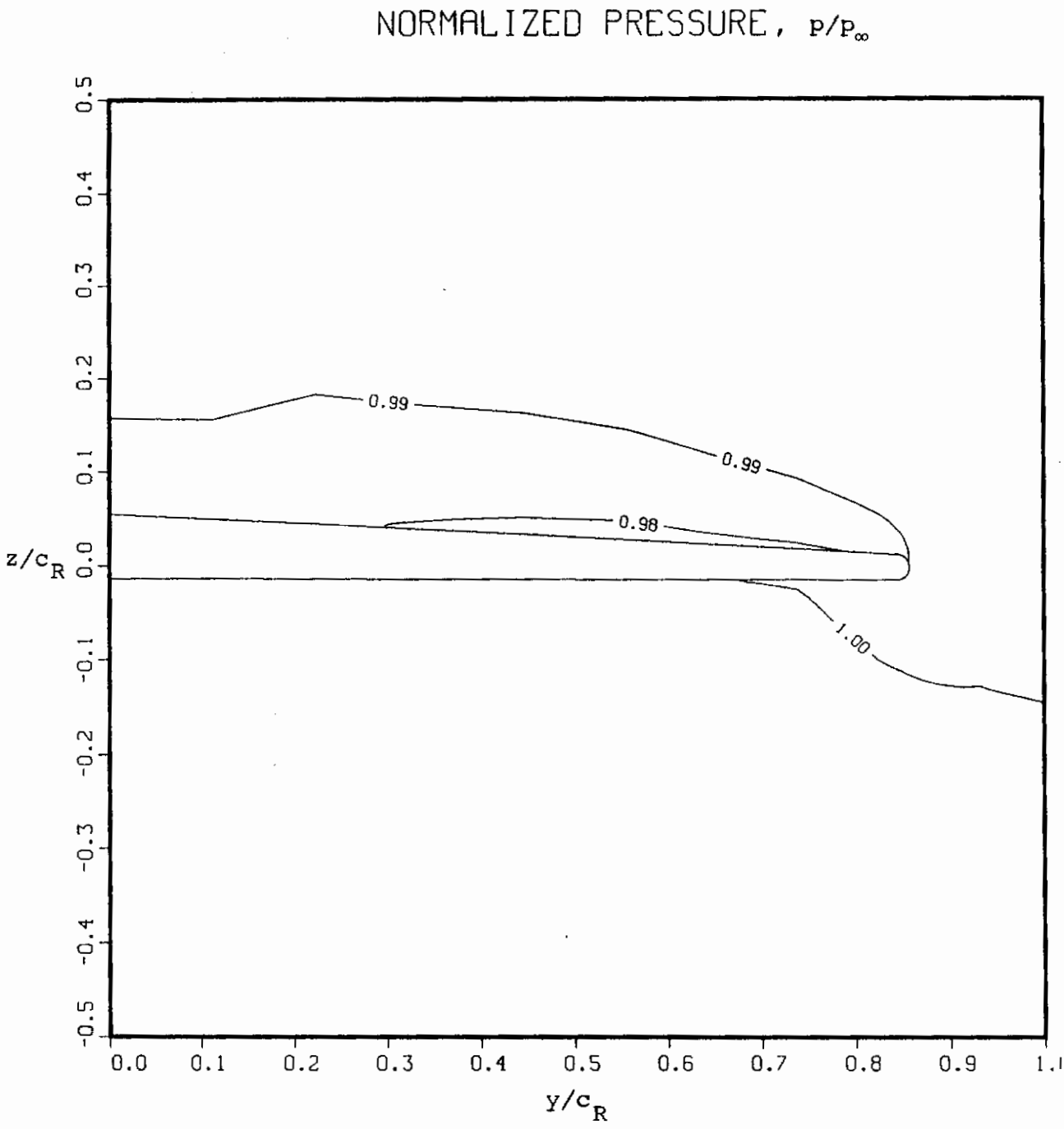

(b) x/c = 0.30

Figure 79.- Concluded.

☆ U.S. GOVERNMENT PRINTING OFFICE: 1988—548-054-80807